Non-linear registration of thoracic and abdominal CT and 18-FDG whole-body emission PET images: methodological study and application in clinical routine

Oscar Camara-Rey

To cite this version:

Oscar Camara-Rey. Non-linear registration of thoracic and abdominal CT and 18-FDG whole-body emission PET images: methodological study and application in clinical routine. domain_other. Télécom ParisTech, 2003. English. NNT : . pastel-00000903

Thèse

en vue de l'obtention du grade de

Docteur de l'Ecole Nationale Supérieure des Télécommunications
Spécialité : Signal et Images

Non-linear registration of thoracic and abdominal CT and 18-FDG whole-body emission PET images: methodological study and application in clinical routine

Recalage non linéaire d'images TDM thoraciques et abdominales et d'images TEP au FDG-18 d'émission corps entier : étude méthodologique et application en routine clinique

par

Oscar Camara Rey

Cette thèse a été soutenue le vendredi 19 décembre 2003.
Le jury était constitué de :

Dirk Vandermeulen	Rapporteurs
Pierre Grangeat	
Juan José Villanueva	Examinateurs
Fabrice Heitz	
Philippe Cinquin	Président du jury
Isabelle Bloch	Directrice de thèse
Vincent Frouin	Invités
Hervé Foehrenbach	
Jean François Stévenet	

Abstract

The aim of this work is to implement a software-based algorithm in order to achieve a robust, fast enough and good quality registration of thoracic and abdominal CT and 18F-FDG whole-body emission PET images. The proposed algorithm may be applied to register CT and PET images acquired on separate devices or to refine hardware registration provided by combined PET/CT scanners.

The proposed registration methodology is based on the incorporation of prior anatomical information in an intensity-based non-linear registration algorithm. The incorporation of this prior information is performed in an explicit way, by initializing the intensity-based registration stage with the solution obtained by a non-linear registration of corresponding anatomical surfaces segmented through a hierarchically ordered set of anatomy-specific rules. Then, we only use general anatomical knowledge instead of any kind of geometrical or morphological model of the structures such as atlases of phantoms, permitting to work with any kind of unexpected situations, which are common in pathological images. Therefore, the general scheme of the registration approach we propose is divided in two stages: a structure registration phase in which homologous structures are segmented in both CT and emission PET grey-level images and registered with a non-linear transformation; and a grey-level registration phase in which a non-linear registration technique is applied to the whole set of image intensities of the images. The second registration stage is initialized with the transformation provided by the structure registration stage and it furnishes the final non-linear transformation. Non-linear deformations are modeled in both registration steps by means of a FFD technique. Mutual Information is used as the similarity criterion at the grey-level registration step.

A set of 20 pairs of thoracic and abdominal CT and whole-body emission PET images obtained by separate devices and 3 provided by a combined PET/CT machine have been processed. Five of these pairs of images have been evaluated by the visual assessment protocol we have also designed. In all 15 thoracic cases, the registrations were successful as visually assessed, notably at the diaphragmatic wall. In the abdominal cases, very good results are obtained on liver and kidneys structures, but some small errors are found at the stomach. With respect to combined PET/CT scanners, some improvements using our algorithm are found on the cardiac region for 1 case. The visual assessment protocol has been used by three independent physicians, confirming visual results. Registration errors provided by the evaluation protocol are less than 1cm on lungs, heart, liver and kidneys structures but up to 1.5cm on the stomach. The average computational time was less than 2 hours to furnish good quality results.

La deformación deja de serlo
cuando está sujeta a una matemática perfecta.

Max Estrella en *Luces de bohemia*, de Valle-Inclán

Al yayo,
y a mis tios Toni y Agustin,
y Mari Carmen y Amador.

Remerciements

Je souhaite tout d'abord exprimer mes sincères remerciements à Isabelle Bloch, ma directrice de thèse. Je voudrais saluer ici sa disponibilité (jamais un non de sa part), son enthousiasme et ses compétences scientifiques, mais surtout pour son optimisme et sa manière d'affronter la vie, sa gentillesse et sa patience infinie avec moi.

Je souhaite également exprimer toute ma gratitude à Dirk Vandermeulen, pour avoir relu le manuscrit avec objectivité, rigueur et intérêt, en apportant une précieuse contribution à l'amélioration de ce travail. Je suis reconnaissant à Pierre Grangeat, d'avoir aussi accepté la tâche fastidieuse d'être rapporteur de cette thèse. Je tiens également à remercier Philippe Cinquin pour avoir accepté de présider ce jury de thèse. A Juan José Villanueva, qui m'a fait l'honneur de participer à ce jury, je souhaite témoigner mon respect et toute ma reconnaissance. Je remercie également Fabrice Heitz d'avoir accepté d'examiner ce travail de thèse.

Ce travail à été possible grâce à la création d'un cadre multidisciplinaire unique qui a convergé vers le projet *ONCOMATCHING*, me permettant de connaître les différents points de vue, priorités et nécessités des milieux académique, industriel et clinique :

- Milieu académique
  - Ecole Nationale Supérieure des Télécommunications (ENST) de Paris, France. I. Bloch, O. Camara, G. Delso, O. Colliot.
  - Service Hospitalier Frédéric Joliot (SHFJ), DRM, DSV, CEA, Orsay, France. V. Frouin, T. Delzescaux, R. Maroy.
- Milieu clinique
  - Hôpital d'Instruction des Armées du Val de Grâce, Paris, France. Dr Foehrenbach, O. de Dreuille, Y. Martelli, M. Soret.
  - Centre Hospitalier Régional Universitaire de Lille, France. Dr X. Marchandise, J. Rousseau.
  - Centre Hospitalier Universitaire de Liège, Belgique. C. Bernard.
  - Centre Hospitalier Princesse Grâce de Monaco. Dr P. Rigo.
- Milieu industriel
  - Segami Corporation. P. Briandet, J.F. Stévenet, S. Hammer, J.Y. Roul.

Je tiens à témoigner mon respect et mes remerciements à tous les partenaires du projet avec lesquels j'ai eu la chance et le plaisir de travailler. Je tiens à remercier tout particulièrement Hervé Foehrenbach pour son enthousiasme, ses suggestions et sa disponibilité malgré un emploi du temps ayant besoin de 30 heures par jour. Que le reste de son équipe soit également remercié. Un grand merci à Vincent Frouin pour sa patience et pour m'avoir guidé au début de ces travaux. Je tiens également à exprimer ma reconnaissance à Philippe Briandet et en particulier à Jean-François Stévenet, qui ont accepté de me faire confiance pendant ces trois ans et m'ont accueilli chaleureusement au sein de la Société SEGAMI, toujours dans une ambiance très professionnelle, mais décontractée (merci, Jean-Yves, j'ai bien rigolé). Merci enfin à tous les membres non-thésards du département TSI pour l'aide qu'ils m'ont apportée. J'adresse de chaleureux remerciements à Francis Schmitt, Michel Roux, Florence Tupin, Sophie-Charlotte (si tu étais arrivée auparavant, j'aurais eu moins de problèmes informatiques et plus de conversations à coté de la machine du café) et Patricia (toujours gentille, malgré les maux de tête causés par mes missions).

Si je pouvais mettre plus d'un nom sur la couverture de ce manuscrit, je serais ravi d'inclure Yves Martelli, Gaspar Delso et Olivier Colliot. Les trois savent qu'au moins 1/4 de ces travaux leur appartient à chacun. Mais plus important que leur boulot a était leur amitié au cours de ces années, qui va rester dans ma mémoire pour toujours. Merci, conn…, pardon, collègues.

Merci beaucoup aux thésards du département TSI, pour avoir fait de ces années à l'ENST des moments inoubliables. J'associerai toujours ma thèse avec le groupe bière-Butte aux Cailles francophone (Stéphane, ou comment se faire des copains au bar, Najib, ou comment me faire comprendre sa culture avec une tolérance et amitié sans limites, Saïd, très bon collègue de bureau, François, mais t'est tatoué ou pas?, Olivier), ses discussions politiques et sa patience pour m'expliquer les blagues de Nuls ou les Inconnus, et avec le groupe tour de Babel (Alex, ou comment manger pendant 3 heures sans arrêter de dire n'importe quoi, Sveta et son humeur radioactive, Antonio, le gagnant du prix de la personne la plus gentille du monde, Tony-faux-chinois, t'est beau mais sans poils, Dalila, ou comment réussir à comprendre que nos blagues étaient innocentes, Ferdaous, un doux bonjour chaque matin, Riadh, inshala, inshala, Carlos, ou comment parler toujours de sujets pas politiquement corrects, Arantxa, Pau, ueeeee, quan fan el Barça?, Silvia, Eve, Saïd, Celine, Yu) qui montait au resto de l'école pour y passer deux heures chaque jour. Vous êtes tous des lumières découvertes à Paris qui tarderont à s'éteindre dans ma mémoire.

Estos tres años de tesis me han permitido disfrutar de una gran ciudad (aunque sin taxis a partir de las dos de la mañana), pero si por algo será especial cada vez que vuelva a París, es porque cada esquina, cada puente, cada barrio, me recordará un amigo, una cara, unas risas. Necesitaría un buen uso de las palabras y muchos manuscritos como éste para agradecer como se merecen todos los personajes que han jugado un papel importante en mi cuento parisino. Me contentaré con garabatear algo sobre ellos. Sobre el clan mexicano, sobresaliendo Gabriel-cadaver Campusano, ese caballero y genio norteño, compañero de viajes astrales, con esas ideas descabelladas y con una biografía digna de best-seller, y su primo Haroun, y Totoro, reconócelo, no tienes ni idea de la NBA a pesar de medir 2 metros. O sobre el manresà Edu (aupa TDK). O sobre esos italianos, Simone (poeta, bohemio, artista de nuestro tiempo), Fabio (jumeau espirituel de Simone), Giorgio (longue vie a Advent et au Metal!!!), Davide (et sa liste d'appels téléphoniques), Peppe (crack poliglota, fins i tot català!!!), todos tan italianos, pero todos tan diferentes. O sobre el clan Montparnasse formado por Marc, Davides, Jordis, Susanas y los que me olvido, siempre organizando fiestas con más de 30 personas. O sobre los Erasmus, fundadores de Juerga, que resistieron o resisten en París después del increíble primer año (Mauro, Nano, Maria, Marcos, Fernandito, Joel, Gabis, Jesus, Marta, Karim, Gloria, Sonia, Esteban, . . .), o sobre las sucesivas generaciones de Juerguistas (Guillermo, Fede-Eva, Felipe, Javier de Santiago, Toti, Raúl, Satán, Javi, Manel, Joses, Ramón, María, Angie, Mara, Eugenia, Antonios, Enric, Pedro, Mirko, Gemma, Felicita, y los que seguro me olvido) con los que compartí aventuras que sólo contaré a mis nietos cuando sean mayores, y que nunca creyeron que hacía una tesis. O sobre cualquier miembro del Club del Pendejómetro, cuya sede oficiosa era la siempre limpia casa de Dani, y cuyo objetivo no era tan intelectual como el de Rayuela, sino batir records de pendejadas, reírse hasta tener dolores estomacales y catar cualquier cosa que los biólogos nos propusieran en esas imborrables sesiones de cine en la comuna okupada de chez Dani. No puedo escribir nada en particular sobre vosotros, no me salen palabras que aproximen a describir lo unido, lo bien y lo privilegiado que me he sentido con vosotros. Gracias Carlos. Gracias Ro. Gracias Dani. Gracias Clara. Gracias Manel, Gracias Jorge. Gracias Pluvia. Gracias Maite.

Si algo ha sido duro de estos tres años, aparte de la falta de sol, de la simpatía parisina, los acueductos, las termas, las carreteras, narizotas, . . . , ha sido estar lejos de la familia en los momentos difíciles que ha habido. Tuve la suerte de tener a Timoteo, Virginia, Paco, Jérémie, Isabel, Juan, que apaciguaron mi morriña familiar a base de amistad, batallitas de Huélamo y sobretodo paellas. Muchas gracias, vous êtes ma famille adoptive française. De todas maneras, ese sacrificio se vio recompensado por la alegría que me invadió al ver la felicidad llorosa y radiante de mis padres en la soutenance, el sentirlos juntos y orgullosos por ver a su hijo alcanzar un nivel de estudios al que ellos le dan más importancia de la que tiene, y disfrutar de la complicidad de los suegros (muchas gracias por venir, y por las tortillas de patata!!!). Elena, has de saber que en esos días, me sentí más realizado como hermano mayor que por acabar la tesis. Javi, a pesar de toda la gente que hubo, no estabas tú, y por lo tanto, la dicha no fue completa.

He dejado, como mandan los cánones, lo más importante para el final. Las dos niñas con las que he tenido el inmenso placer de convivir estos tres años: Melian y Maite. Para la primera, tan sólo decir que a pesar de los 500 euros, me ha producido más satisfacciones que dolores de cabeza, que ya es decir. Maite, como un ex-thesard sin doctorado, así estaría yo sin tí. Pero eso no es lo primordial. El lanzarse a por esta tesis me demostró lo valiente que eres, nadie había hecho tanto por mí, y provocó que haya disfrutado de los tres anõs más felices de mi vida. Dichosa la hora en que decidí hacer la tesis!!! Afortunadamente, esto sólo es el principio, aunque en nuestros recuerdos, siempre nos quedará Paris. Yo te I loviu.

Table of Contents

List of Figures

Résumé

Introduction

Dans le domaine de l'oncologie, la combinaison des images anatomiques et fonctionnelles prend de plus en plus d'importance, grâce au développement de nouveaux appareils d'acquisition, de nouvelles méthodes algorithmiques et grâce à la complémentarité des modalités. En imagerie fonctionnelle, le développement des acquisitions TEP (Tomographie à Émission de Positons) avec le traceur fluorine 18 fluorodeoxyglucose (18-FDG) donne accès à une information très riche pour le diagnostic et le suivi thérapeutique de cancers primitifs et métastasiques. L'inconvénient de cette modalité est que l'information anatomique est réduite, rendant difficile la localisation de tumeurs avec une haute précision par rapport aux organes. Cette information anatomique est fournie par la tomodensitométrie (TDM ou *Computed Tomography* ou CT) ou l'Imagerie par Résonance Magnétique (IRM) et permet au clinicien d'obtenir une localisation des lésions très précise, ainsi que des mesures de taille et de forme. Malheureusement, ces modalités ne fournissent pas une information suffisante sur la malignité de la lésion. La combinaison de ces deux modalités peut donc avoir un impact significatif sur les décisions médicales pour le diagnostic, la thérapie et la planification de traitements [294]. Du point de vue du traitement d'images, le problème s'exprime essentiellement comme un problème de recalage, de mise en correspondance entre les informations issues des deux modalités.

Le but de ces travaux est de proposer une contribution au recalage d'images TDM-TEP dans les régions thoraciques et abdominales. Les fortes déformations existant entre les images excluent d'emblée toute solution de recalage rigide entre les deux modalités et il faut développer des méthodes de recalage non linéaire (plus de 12 degrés de liberté dans la transformation). Ces déformations sont principalement dues aux protocoles d'acquisition et à la nature élastique des organes considérés.

Le problème du recalage

L'objectif d'un algorithme de recalage est de trouver la transformation mettant en relation l'information contenue dans une image et sa correspondance anatomique sur l'autre image. Les méthodes de recalage peuvent être classées selon plusieurs critères : région d'intérêt, modèle physique de déformation, mesure de similarité et méthode d'optimisation utilisée. Des synthèses exhaustives des méthodes de recalage peuvent être trouvées dans [177 ; 11].

Plusieurs transformations non linéaires sont disponibles dans la littérature du traitement d'images. Les Déformations de Forme Libre à base de B-splines (B-spline Free Form Deformations ou FFD) constituent un modèle paramétrique qui fournit une transformation non linéaire souple car aucune supposition n'est faite quant aux images ou aux structures à recaler. Ce modèle a été utilisé avec succès dans différentes applications d'imagerie médicale, comme pour le recalage de mammographies [242], le recalage de régions cérébrales [113] ou pour la segmentation de régions cardiaques [167 ; 178]. En général, une transformation linéaire est calculée avant la phase non linéaire pour s'approcher suffisamment de la solution finale. Cependant, la plupart de ces applications travaillent avec des données monomodalités, où le rapport entre les intensités dans les images à recaler est plus simple que dans le cas des applications multimodales. En outre, les images fonctionnelles introduisent des difficultés supplémentaires liées au bruit important et aux artefacts. Mattes et al. [190] ont tout de même appliqué le modèle FFD pour recaler des images TDM-TEP (avec des images TEP de transmission) des régions thoraciques, en utilisant un schéma hiérarchique et multi-résolutions pour éviter les minima locaux et pour éviter d'avoir à fournir une initialisation très précise. Un inconvénient de cette méthode est qu'elle considère une relation fonctionnelle entre les acquisitions des images TEP de transmission et d'émission. En outre, les auteurs signalent que les résultats ne sont pas complètement satisfaisants dans les régions avec des déformations plus importantes à compenser, comme le diaphragme et l'abdomen.

Une solution à ce problème est de contraindre ces déformations pour éviter la convergence vers des minima locaux et pour réduire le coût de calcul de l'algorithme. Ces contraintes nous conduisent à proposer une méthodologie divisée en une phase d'initialisation recalant les structures segmentées dans les deux images, et une deuxième phase de recalage à niveaux de gris, raffinant l'étape précédente de l'algorithme. Les transformations sont modélisées dans les deux étapes à partir de Free Form Deformations (FFD), gérées par une grille de plusieurs points de contrôle par dimension. La segmentation est réalisée en appliquant un modèle déformable 3D à base de maillages simplexes sur les régions d'intêret dans une procédure hiérarchique de reconnaissance des formes.

Segmentation de structures anatomiques

Schéma de la procédure La phase initiale de recalage nécessite une étape de segmentation des structures thoraciques et abdominales dans les deux images. Ce premier recalage sera raffiné en utilisant l'information de niveaux de gris. Les éventuelles erreurs de segmentation ne seront pas propagées vers le résultat final car la seconde phase de recalage pourra les corriger.

Les différents niveaux de difficulté dans la segmentation de structures suggèrent l'utilisation d'une procédure hiérarchique : l'extraction d'une structure donnée utilisera des informations dérivées des structures plus simples. Ces informations sont composées de contraintes spatiales déduites à partir de structures segmentées précédemment et sont exprimées sous la forme de Régions d'Intêret (ROI), dans lesquelles la recherche des nouvelles structures aura lieu. Cette stratégie a été aussi utilisée dans une application concernant la segmentation des structures cérébrales internes sur des images IRM [64 ; 62]. Dans le présent travail, les structures à segmenter pour le recalage sont les poumons, les reins et le foie (dans cet ordre). Bien qu'ils ne soient pas employés dans le processus de recalage, la peau et le squelette sont également extraits et constituent les premières étapes de la procédure hiérarchique dans le cas des images TDM.

Les poumons, les reins et le foie sont traités en deux étapes différentes. Une première étape est composée d'un seuillage automatique et d'opérations de morphologie mathématique dans la région d'intérêt définie par les objets déjà segmentés. La deuxième étape consiste à raffiner le résultat en utilisant un modèle déformable 3D. La peau et le squelette sont segmentés en employant seulement la première étape.

Première étape : segmentation grossière Pour contraindre la segmentation, une région d'intérêt est définie en utilisant des relations spatiales par rapport aux autres structures. Ces relations incluent des directions (par exemple, le foie est en-dessous des poumons) et des contraintes d'exclusion (les structures segmentées auparavant sont soustraites de la région d'intérêt pour éviter la superposition de deux objets). La région d'intérêt pour chaque structure est définie comme suit :

- peau et squelette : ils constituent les premiers pas de la procédure pour les images TDM et il n'y donc pas de région d'intérêt ;
- poumons : dans les images TDM, la région d'intérêt est calculée à partir de la peau. Dans les images TEP, nous segmentons les poumons dans les images de transmission et nous dilatons le résultat pour produire une région d'intérêt dans l'image TEP d'émission;
- reins : dans les images TDM, la région est limitée en utilisant les dimensions du thorax déterminées à partir de la segmentation du squelette. Une limite supérieure dans la direction z est déterminée à partir des poumons : la région d'intérêt est définie en-dessous d'une ligne liant la limite inférieure droite du poumon gauche et la limite inférieure gauche du poumon droit (une ligne est automatiquement tracée sur chaque coupe coronale). Une limite inférieure est calculée en utilisant la partie haute du bassin, extrait à partir du squelette. Dans les images TEP, nous utilisons seulement la limite supérieure calculée à partir des poumons car le squelette n'est pas disponible;
- foie : la région d'intérêt est la même que dans le cas des reins, mis à part ces derniers qui ont été soustraits. La région d'intérêt a été particulièrement utile pour séparer le foie des structures proches comme le cœur et les reins.

Dans cette région, nous réalisons une succession d'opérations : seuillage automatique par k-moyennes, érosion binaire, sélection des composantes connexes, dilatation binaire et remplissage de trous en 3D. Dans le cas des poumons et du foie, nous sélectionnons la plus grande composante connexe, alors que pour les reins, les deux composantes les plus symétriques par rapport au plan de symétrie du corps sont choisies, en utilisant un algorithme proposé dans [63].

Deuxième étape : raffinement avec un modèle déformable 3D La première étape ne peut pas être considérée comme une segmentation finale. Le principal problème vient de l'absence de régularisation, en particulier dans le cas des structures fines qui peuvent être détectées dans une modalité mais pas dans l'autre, introduisant ainsi une différence que la procédure de recalage interpréterait à tort comme une déformation et essaierait de compenser. Un modèle déformable 3D a été implanté pour résoudre ce problème.

Nous avons choisi d'implanter un modèle discret fondé sur les maillages simplexes (introduits par Delingette [75]). Le fait d'avoir une bonne initialisation est très utile pour atteindre une convergence rapide du modèle, et c'est pour cette raison que nous utilisons pour chaque structure une surface initiale dérivée de la première phase de segmentation. La segmentation obtenue dans la première étape est érodée pour assurer que l'initialisation est à l'intérieur de l'objet. Ensuite, elle est transformée en une triangulation par un algorithme d'isosurfaces [165]. Elle est alors décimée et convertie en un maillage simplexe par l'opération duale. Cette conversion est valable quelles que soient la complexité et l'irrégularité des maillages.

L'évolution d'une surface déformable peut est décrite par une équation de force dynamique composée d'une force interne qui spécifie la régularité de la surface et d'une force externe qui mène la surface vers les contours de l'image. Dans notre cas, la force externe n'est pas seulement dérivée à partir des contours de l'image, mais contraint également le modèle à rester dans la région d'intérêt. Elle peut être écrite comme une combinaison linéaire d'un champ Gradient Vector Flow (GVF) (introduit par Xu et al. [308]) et d'une force liée à la région d'intérêt. Un champ GVF est calculé par diffusion du vecteur gradient d'une carte de contours donnée.

La carte de contours est obtenue à partir du gradient après diffusion anisotrope. Cette technique [100] est une méthode efficace pour enlever du bruit dans des régions homogènes tout en préservant et même en renforçant les contours. Elle s'est révélée particulièrement utile pour les images TEP.

Le deuxième terme de la force externe est utilisé pour éviter que le modèle déformable ne sorte de la région d'intérêt. Ce terme est une force potentielle de distance [56], cette distance étant, dans notre cas, une carte distance à la région d'intérêt (la force est nulle dans la région d'intérêt). De plus, nous utilisons aussi la région d'intérêt comme masque pour le GVF et ainsi le GVF est nul hors la région d'intérêt. Finalement, nous employons aussi la région d'intérêt comme masque pour la segmentation obtenue pour assurer que les objets ne se superposent pas.

Procédure de recalage non linéaire

Schéma La procédure de recalage non linéaire est séparée en deux phases: une première étape de recalage entre les structures segmentées dans les deux images et une deuxième étape, initialisée avec la transformation calculée précédemment, qui réalise un recalage raffiné utilisant les intensités des deux images.

Modèle de déformation Plusieurs transformations non linéaires sont disponibles dans la littérature du traitement d'images, comme par exemple les splines de plaque mince (Thin-Plate Splines ou TPS) [27], les modèles élastiques [7] ou les modèles de viscosité [34]. Notre application impose les restrictions suivantes : un nombre suffisamment élevé de degrés de liberté pour recaler les déformations plus locales ; un coût calculatoire limité pour pouvoir utiliser l'algorithme en routine clinique ; l'impossibilité d'utiliser des repères externes pour aider la procédure de recalage.

Les B-splines Free Form Deformations (FFD), introduites par Sederberg et al. [253], sont une technique paramétrique qui fournit des transformations non linéaires souples. Dans cette technique, les déformations de l'objet 3D sont calculées via l'optimisation d'une grille sous-jacente de points de contrôle. Le nombre de points de contrôle définira la localité des déformations permises par le modèle FFD. Cependant, avec une grille densément peuplée, les temps de convergence seront notablement accrus. Ainsi, un compromis doit être effectué concernant ces deux aspects. Nous avons choisi une grille de 10 points de contrôle par dimension.

Le choix de cette méthode par rapport à d'autres modèles paramétriques contraints est dû à la grande variabilité des structures dans notre application. En fait, il est extrêmement difficile de fournir un modèle anatomique approprié qui puisse être appliqué automatiquement sur n'importe quel patient et qui puisse tenir compte de tout type de déformation. Pour cette raison, nous préférons la souplesse des FFD qui est liée au fait qu'aucune hypothèse n'est faite sur les structures à recaler. De plus, les conditions de vitesse du système font que les FFD sont plus appropriées que d'autres méthodes de déformation plus réalistes mais plus coûteuses en temps de calcul, comme les modèles élastiques [7] ou les modèles fluides [34].

Le modèle FFD a été utilisé dans les deux étapes de la méthode de recalage, celle des structures segmentées et celle à niveaux de gris. Cette implantation nous a permis d'intégrer facilement les deux phases dans la même procédure, le recalage de structures étant considéré comme un pas de plus dans la chaîne multi-résolutions utilisée dans la plupart des techniques iconiques. Ainsi, le recalage à niveaux de gris commence avec la grille trouvée lors de la phase des structures segmentées, laquelle fournit une transformation initiale très proche de la solution finale, tout au moins dans le voisinage des structures segmentées.

La procédure d'optimisation est fondée sur une technique itérative de descente de gradient sur la totalité de la grille de points de contrôle. A chaque itération, nous calculons une estimation locale du gradient pour chaque point de contrôle par la méthode des différences finies. De plus, un terme de régularisation composé d'une force molle locale a été introduit pour éviter l'intersection entre les nœuds, ce qui pourrait produire des modifications non souhaitées de la topologie des structures.

Recalage de structures Le but de cette étape est de fournir une initialisation au recalage à niveaux de gris aussi proche que possible du résultat final souhaité. Cette transformation contraindra la recherche de la solution globale qui sera effectuée dans la prochaine étape.

Avant la réalisation du recalage non linéaire entre les structures, nous calculons une approximation initiale de la transformation entre les deux images. Cette approximation est composée d'un mouvement rigide, d'un changement d'échelle indépendant dans les trois axes et d'une élimination des parties des volumes qui n'ont pas d'intérêt pour notre application. Cette élimination est réalisée à partir de la boîte englobant les structures à recaler et elle est complètement automatique, à la différence des méthodes classiques de recalage qui nécessitent un recalage manuel (principalement dans la direction z) avant de pouvoir être appliquées sur les images TDM et TEP corps entier.

Le recalage de surfaces 3D a été traité largement dans les domaines du traitement d'image et de la vision. Des synthèses de ces techniques peuvent être trouvées dans [5 ; 177]. Une des méthodes les plus performantes est l'ICP (Iterative Closest Point), proposée par Besl et al. [16], et qui a été utilisée avec de bons résultats pour différentes applications. Cet algorithme optimise itérativement une transformation rigide qui minimise la distance entre deux ensembles de points (lignes, points, triangles, ...). Les correspondances sont donc déterminées par proximité. Dans un premier temps, nous avons employé la carte de distances calculée avec cette méthode pour réaliser une estimation de la transformation non linéaire entre les surfaces des organes. Cela était utilisé pour initialiser les positions de points de contrôle de la FFD du recalage à niveaux de gris. Cependant, l'interaction entre les deux phases de recalage pouvait conduire à une perte d'informations.

Pour ces raisons, nous avons décidé d'appliquer à l'étape du recalage de structures le même modèle de déformation FFD que dans la phase de recalage avec l'ensemble des intensités de l'image, simplifiant l'interaction entre les deux étapes. Nous proposons donc deux approches fondées sur les FFD pour réaliser le recalage de structures. La première méthode emploie le critère d'Erreur Quadratique Moyenne (EQM) comme mesure de similarité, en calculant une estimation locale du gradient à chaque point de contrôle de la grille, et en utilisant une procédure de descente itérative de gradient. La deuxième méthode calcule un champ Gradient Vector Flow (GVF) sur les structures segmentées sur l'image TDM pour guider l'optimisation des points de contrôle.

- Déformations de Forme Libre guidées par l'Erreur Quadratique Moyenne (EQM-FFD) :

  La méthode de déformation FFD nécessite l'optimisation des points de contrôle de la grille pour minimiser un critère de similarité donné. Le choix de ce critère est simple dans notre cas, puisque nous travaillons avec des images segmentées qui possèdent un rapport linéaire entre leurs intensités. Ainsi, l'Erreur Quadratique Moyenne (EQM) des niveaux de gris de voxels homologues sur l'ensemble du volume sera utilisée pour déterminer les paramètres optimaux de la déformation. Nous aurions pu utiliser des mesures de similarité plus simples, mais nous avons choisi l'EQM parce qu'elle nous permet de travailler avec plusieurs structures en même temps. Les résultats obtenus en appliquant cette méthode montrent une bonne performance de l'algorithme de recalage non linéaire dans les cas des poumons et du foie.

- Déformations de Forme Libre guidées par le Gradient Vector Flow (GVF-FFD) :

  Un inconvénient de la méthode EQM-FFD est la nécessité d'optimiser tous les points de contrôle avec l'estimation locale de gradient calculée à chaque itération. Les approches multi-résolutions accélèrent la convergence de l'algorithme, mais l'estimation du gradient reste un problème en termes de temps de calcul.

  Nous proposons une approche originale pour accélerer l'optimisation de la déformation, en calculant un champ de vecteurs sur les structures de référence (dans notre cas, celles segmentées sur les images TDM) pour guider l'optimisation des FFD. Ce champ est appliqué aux structures anatomiques (dans notre cas, celles segmentées sur les images TEP).

  Le Gradient Vector Flow, proposé par Xu et al. [308] est une méthode élégante pour obtenir ce champ de vecteurs et fournit en chaque point de l'image la direction vers la structure anatomique de référence. Cette technique est normalement utilisée pour guider les modèles déformables dans des applications de segmentation, mais à notre connaissance, elle n'a pas encore été utilisée pour contrôler les algorithmes de recalage fondés sur les FFD.

  Un champ GVF $\mathbf{u}$ est défini comme la solution d'équilibre d'une equation de diffusion composée de deux termes. Le premier terme de l'équation est appelé *terme de régularisation*, et il tend à uniformiser le champ de vecteurs résultant. Le deuxième terme est le *terme de données*, et il amène le champ de vecteurs à rester proche du gradient de contours calculé à partir des données. Les fonctions de pondération qui sont appliquées aux termes de régularisation et de données déterminent le compromis entre le lissage du champ de vecteurs et la fidélité aux contours de l'image. Nous choisissons une formulation classique permettant la diffusion du vecteur gradient seulement là où il n'y a pas de forts contours, empêchant ainsi l'effet de moyennage quand des gradients opposés sont très proches.

  Après le calcul du champ de vecteurs GVF, nous avons pour chaque point appartenant à la structure TEP la bonne direction pour évoluer vers la structure TDM correspondante. Ainsi, pour chaque point de contrôle, nous trouvons les points du contour des structures TEP sous son influence et nous regardons la valeur du champ de vecteurs GVF pour ces points. Ces valeurs sont pondérées selon leur distance vers le point de contrôle et la moyenne des vecteurs résultants est prise comme la direction optimale de déplacement de chaque point de contrôle. A la fin de chaque itération, un terme de régularisation composé d'une force molle locale est appliqué comme dans l'algorithme EQM-FFD.

  La convergence de l'algorithme dépend de la qualité du champ de vecteurs calculé. De plus, les points de contrôle tendent à osciller au voisinage des contours de structures TDM. Ainsi, plusieurs contraintes sur les points de contrôle ont été implantées pour éviter les oscillations. Nous avons introduit la méthode dans une procédure multi-pas pour aider l'algorithme à trouver les déformations globales dans les premières itérations, en laissant les plus locales pour la fin. Les résultats obtenus en appliquant cette méthode montrent que les déformations sont de qualité inférieure par rapport à celles obtenues avec la méthode EQM-FFD. Cependant, cet algorithme converge plus rapidement vers les bonnes transformations, comme cela est montré dans la suite.

- Comparaison des deux méthodes d'optimisation :

  Nous avons comparé quantitativement la qualité et le coût de calcul des deux méthodes de recalage de structures proposés avec l'algorithme ICP. Nous avons appliqué ces techniques sur une base de données composée de 15 paires de structures déformables (poumons, foie ou reins), précédemment segmentées dans les images TDM et TEP.

  Pour évaluer ces techniques, en plus de l'inspection visuelle de volumes 3D, nous avons calculé deux mesures quantitatives : une mesure de superposition calculée comme le ratio entre l'intersection et la réunion entre les structures (qui vaut 1 si la superposition totale est réalisée); et l'Information Mutuelle (IM) sur les images à niveaux de gris transformées avec les déformations calculées lors du recalage de structures. Nous avons choisi d'utiliser l'Information Mutuelle au lieu de l'EQM directement sur les structures segmentées pour tenir compte de possibles erreurs induites par la phase de segmentation.

  La mesure de superposition et l'IM confirment les résultats visuels, à savoir que l'EQM-FFD est la méthode avec laquelle on obtient les meilleures déformations, alors que le GVF-FFD améliore tout de même significativement les résultats des méthodes de recalage rigide. Il faut remarquer que la mesure de superposition entre les structures n'arrive jamais à 1; cela est dû à la régularisation intrinsèque au modèle de déformation non linéaire choisi. En fait, cela nous convient parce que ces différences sont normalement provoquées par les modalités d'acquisition, pas par les erreurs de recalage, et elles doivent être préservées.

  Nous avons observé que l'EQM-FFD donne de meilleurs résultats que le GVF-FFD dans des régions avec des déformations très locales. Cela est dû au compromis fait dans le calcul du champ de vecteurs GVF entre le rejet des structures non désirées (par exemple les bronches dans les poumons) et la capacité de recaler les déformations locales.

  De plus, la méthode GVF-FFD a de meilleures performances en termes de rapidité de convergence, alors que l'EQM-FFD reste un algorithme très lourd en calcul, ce qui est dû au calcul des estimations locales du gradient à chaque itération, à la différence du GVF-FFD où l'on calcule seulement une fois le champ de vecteurs qui contrôle l'évolution dans toutes les itérations. Finalement, la méthode que nous proposons consiste à initialiser l'EQM-FFD avec la solution fournie par le GVF-FFD, ce qui a donné des résultats de meilleure qualité qu'avec seulement l'EQM-FFD, tout en fournissant des temps de convergence raisonnables pour notre application.

Recalage à niveaux de gris La transformation produite par l'étape d'initialisation n'est pas nécessairement valable dans les régions éloignées des structures segmentées. Le calcul de leur déplacement doit donc être effectué par l'étape de recalage à niveaux de gris. En revanche, dans les zones proches des structures segmentées, cette étape doit seulement corriger les erreurs qui ont pu être introduites par la procédure de segmentation. Une conséquence importante est que l'optimisation des points de contrôle qui sont tombés sur les structures segmentées sera beaucoup plus rapide, car leur valeur initiale de déplacement est déjà très proche de la solution finale, ce qui accélère considérablement cette étape.

Comme la méthode de déformation n'a pas changé, l'algorithme est essentiellement le même que celui utilisé dans l'étape de recalage des structures. Cependant, le fait de travailler avec l'ensemble des niveaux d'intensité nous oblige à changer le critère de similarité à maximiser. Le choix d'une mesure de similarité est directement lié aux modalités d'imagerie à recaler. Une situation particulièrement difficile se présente quand les distributions d'intensités des deux modalités différentes ne suivent pas un rapport fonctionnel, ce qui est le cas des images TEP et TDM. L'Information Mutuelle (*Mutual Information* ou MI), un critère proposé par Viola [292] et Collignon [59], est un outil très performant pour le recalage d'images multimodales avec un rapport non linéaire entre les intensités. L'Information Mutuelle exprime la quantité d'information d'une image I contenue dans une autre image J. Ainsi, l'Information Mutuelle sera maximale si les deux images sont recalées géométriquement. Elle est obtenue à partir des entropies marginales des deux images et de leur entropie conjointe, calculées à partir de leur histogramme conjoint. L'Information Mutuelle Normalisée (*Normalized Mutual Information* ou NMI) est une variante de MI introduite par Studholme [269] pour éliminer l'effet lié à la superposition des images sur la mesure.

Ces calculs nécessitent l'estimation des distributions de probabilités conjointes et marginales des deux images. Nous utilisons une approximation fréquentielle, $p_{ij} = n_{ij}/n$, où p_{ij} est la probabilité estimée d'avoir un niveau de gris i dans une image et j dans l'autre image, n_{ij} étant le nombre de voxels avec ces intensités et n le nombre total de voxels.

Résultats et conclusions

Nous avons testé notre méthode sur un ensemble de 20 acquisitions TEP et TDM de régions thoraciques et abdominales, provenant du LifeScan Louisville, de l'Hôpital de Percy et du H.I.A. du Val de Grâce. Les images CT ont une taille de 512 x 512 pixels dans le plan xy et entre 60 et 125 coupes, avec des dimensions de voxels d'environ 1.0 x 1.0 x 5.0 mm^3. Les images TEP ont une taille de 144 x 144 pixels dans le plan xy et entre 160 et 230 coupes, avec des dimensions de voxels d'environ 4.0 x 4.0 x 4.0 mm^3.

L'évaluation qualitative des méthodes de recalage non linéaire n'est jamais un problème simple à gérer et nous devons normalement nous contenter d'une inspection visuelle qui a ses limites. Une méthode utilisant des marqueurs de référence internes définis par les cliniciens [103], ne serait pas suffisamment précise pour notre application, à cause de l'absence de références anatomiques communes dans les deux images. Une méthode originale d'évaluation a été proposée par Schnabel et al. [249], qui utilisent des techniques d'éléments finis pour développer un simulateur de déformations biomécaniques. Les auteurs ont appliqué leur méthode pour évaluer les résultats de recalage non linéaire sur une application concernant des mammographies IRM avec rehaussement de contraste. Dans notre cas, une telle approche nécessiterait une «verité terrain», une paire de volumes TDM-TEP thoraciques correctement recalés, qui pour le moment n'est pas disponible.

La seule manière d'obtenir des mesures objectives et fiables serait à travers une procédure de validation clinique avec des marqueurs implantés mais cela n'est pas possible dans notre application, seule l'évaluation subjective des résultats par des cliniciens experts peut fournir une idée de la qualité de l'algorithme de recalage. Un protocole d'évaluation pour des méthodes de recalage non linéaire a été développé, sous la supervision du Dr. Foehrenbach (H.I.A. du Val de Grâce), qui permet aux cliniciens et aux spécialistes du recalage de fournir une mesure semi-qualitative de la précision du recalage, sans devoir parcourir le volume 3D complètement. Plusieurs coupes anatomiquement significatives des volumes TDM et TEP recalés sont présentées. Par exemple, pour un volume 256 x 256 x 97, 6 coupes coronales et 6 coupes axiales sont montrées, chaque paire d'images étant marquée avec une règle qui définit quelques points de référence et marque les structures anatomiques significatives. Ces marques permettent aux évaluateurs d'estimer les différences de position des structures mentionnées et de noter le recalage.

Trois médecins (Dr. Foehrenbach, Dr. Rigo et Dr. Marchandise) de trois hôpitaux différents ont utilisé le protocole décrit pour évaluer les résultats du recalage grâce à un formulaire en ligne. La mesure fournie indique une erreur inférieure à 4mm pour les structures les plus significatives (poumons, foie, reins, cœur), ce qui correspond à l'objectif de l'application qui était d'avoir des erreurs plus petites que la résolution des images TEP.

Nous avons vérifié que le recalage est meilleur aux alentours des structures segmentées qui ont été déjà recalées dans la phase d'initialisation, et ce indépendamment de leur appartenance aux zones thoraciques ou abdominales. Une exception est le problème trouvé dans l'estomac. Ce problème est dû à des mouvements très importants entre les deux acquisitions et au fait que nous n'avons pas imposé de contraintes sur cette structure. Le recalage à niveaux de gris n'a donc pas convergé vers le recalage correct. Le fait de contraindre la déformation FFD à travers une étape d'initialisation a largement augmenté la vitesse de convergence du recalage à niveaux de gris : le temps de calcul a été réduit d'environ 80% notamment grâce au plus petit nombre de points de contrôle.

En conclusion, les résultats présentés dans ces travaux indiquent que notre méthode peut fournir un outil valable pour l'analyse de données dans les applications oncologiques pour des régions thoraciques et abdominales. La non rigidité des régions étudiées a été effectivement modélisée grâce aux FFD, et des résultats de recalage satisfaisants peuvent être obtenus en minimisant le critère d'Information Mutuelle Normalisée. Une méthode de segmentation progressive a été proposée pour fournir une initialisation, en l'intégrant comme une première étape dans une procédure multirésolutions. Le fait de pas avoir une segmentation très précise n'a pas été un souci majeur, car seule une approximation est requise, grâce à la stratégie utilisée, où le recalage à niveaux de gris doit corriger ces possibles imperfections.

Les prochains travaux seront focalisés sur la possibilité de permettre dans la phase d'initialisation d'affecter un poids aux points de contrôle de la grille en tenant compte des propriétés mécaniques des tissus sous-jacents.

Introduction

Knowledge about human body, its functioning and its behavior under the influence of external factors has been one of the major concerns of mankind since human beings have reasoning capacity. The fear to death, the love to life and the desire of extending as long as possible its natural limits have induced human beings to dedicate all possible efforts, economic and intellectual, in order to find answers and solutions to mortal diseases. One of these diseases, that is linked to human beings since donkey's years ago, is *cancer*.

Study of cancer through the years has resulted in the actual deep knowledge of this disease, to the point of having developed tools to fight it in a very efficient way, notably reducing its effects and its mortality rate. The apparition of medical image acquisition devices represented an enormous advance in the study of the human body because they allowed, for the first time in history, visualization of the human anatomy without using such drastic means as directly *open and watch*.

Oncology is the branch of medicine that studies cancer disease. Oncology has also taken benefit of the apparition of medical images, allowing strong advances on several medical decisions concerning cancer disease such as diagnosis, therapy and treatment planning. At first, the medical imaging modalities used by oncologists were CT (Computed Tomography) or MRI (Magnetic Resonance Image). These medical imaging modalities are classified as *anatomical* ones because they offer good quality and spatial resolution, providing a good localization of the visualized structures and tumors. On the other hand, they do not give any *functional* or metabolic information. Furthermore, tumors are sometimes not distinguishable from surrounding structures due to their similar intensity values. The apparition of nuclear medicine devices such as PET (Positron Emission Tomography) or SPECT (Single Photon Emission Computerized Tomography) entailed a revolution in oncology because they could provide this metabolic information that was absent. The main drawback of images provided by these functional modalities is their low SNR (Signal to Noise Ratio) quality. As a matter of fact, nuclear medicine images have a high presence of noise and artifacts, preventing a good localization of anatomical structures. An accurate information about structure localization is crucial for several oncology applications such as radiotherapy or surgery to better define radiation area and biopsy starting point respectively.

The combination of information provided by anatomic and functional images allows to have complementary data for a given patient but such a combination is a challenging task. Even if anatomical and functional images for a given patient represent the same reality, the recognition of corresponding zones or structures in different images remains difficult for several reasons. The main problem is the time passed between both image acquisitions and consequently, movements suffered by structures modifying their localization and morphology in the images. Furthermore, structures sometimes appear in only one of both images, thus lacking of correspondences, due to the different nature of acquisition devices.

These difficulties ask for a high knowledge of human body and structure behavior in order to find these correspondences, in a visual way, with a high degree of reliability, therefore, only a expert on the targeted medical application can achieve it.

Until few years ago, these correspondences were computed by the physician in a visual way, studying the 2D slice series from each modality in the traditional light box. Then, the physician should combine the available complementary information in his mind to produce a mapping between homologous structures in different images. This visually obtained mapping strongly depends on physician's knowledge and expertise but it is also influenced by different structure orientations, field of views and image resolutions, making difficult to determine the correspondence between anatomical structures. This procedure, even for expert physicians, remains very rough and time-consuming, and uncertainty in the mental mapping from one image to another may lead to uncertainty in the diagnosis or planning.

Computers and their constant processing capacity improvement have represented an important step towards the objectivity of this mapping computation, allowing to obtain reliable image superimpositions. In image processing, this task involves the spatial transformation of one of the images (this image is then called *floating* or *source* image) in order to put it in the same spatial reference as the other (this image is called *target* or *reference* image), aiming at superimposing homologous structures of the images. This procedure is called *registration* [1]. The nature of this transformation highly depends on the targeted body zone due to the different nature of movements suffered in different anatomical body regions. For instance, brain induces some differences between anatomic and functional images that can be modeled by means of a transformation called *linear*, composed of translations and rotations, because head has a limited range of movements. On the other hand, in other regions such as thoracic and abdominal ones, the structures placed in these zones suffer strong movements due to respiratory and cardiac cycles (between other reasons), inducing differences between the images that require more powerful transformations such as *non-linear* ones.

The main goal of this thesis has been the search of these non-linear transformations in order to guide an objective, robust, fast and as automatic as possible registration software algorithm applied to CT and emission PET images of thoracic and abdominal regions. We have developed a registration methodology in which anatomical prior information is incorporated in an intensity-based non-linear multi-modality registration algorithm. The incorporation of this prior information is performed in an explicit way, by initializing the intensity-based registration stage with the solution obtained by a non-linear registration of corresponding anatomical surfaces segmented through a hierarchically ordered set of anatomy-specific rules. This is the main original point of the proposed registration methodology since we only use general anatomical knowledge

---

[1] For a funny multi-modal registration application, the interested reader is referred to Appendix A.

instead of any kind of geometrical or morphological model of the structures such as atlases of phantoms which application to pathological images is too risky. The results on clinical data are validated using a semi-quantitative assessment protocol.

* *
*

This document is split in two main parts. The first one introduces the medical interest of the application and the algorithmic background on registration. The second part presents the original methodology developed to register CT and emission PET images of thoracic and abdominal regions and the evaluation protocol we have designed to assess registration result accuracy. This part finishes with a conclusion and perspective section. Some appendices are included at the end of the manuscript as complementary information about some aspects of the project. Next, a brief description of each chapter is given.

Chapter 1 presents the medical interest of the application. A brief explanation about CT and PET imaging techniques and their use in oncology applications are given. Afterwards, the interest of the combination of anatomical and functional information provided by these imaging modalities is justified. Finally, the two possible options that can furnish this information combination, hardware and software solutions, are described. This chapter is complemented with **Appendix B**, in which the interested reader can find detailed information about cancer, its origins and causes, statistics of this disease and a historical review of the evolution on the knowledge about it.

Chapter 2 presents the algorithmic background of registration methods. First, basic concepts of a registration method are described, followed by an explanation of the particular conditions of a CT-PET registration application in order to establish its constraints and its requirements. In this chapter, a classical division of a registration system is used, separating it in four phases: image representation, transformation, similarity criterion and optimization. A section of the chapter is dedicated to the description of each one of these phases, including their different possible choices. The second part of this chapter aims at making an exhaustive overview of the published methods for registering CT and emission PET images, emphasizing those ones applied to thoracic and abdominal regions. Finally, a discussion about the different registration options is presented in order to distinguish which approaches are well-suited for our application.

The second part of the manuscript begins with **Chapter 3**, which presents the proposed registration methodology. First, some results obtained applying linear and Free-Form Deformation registration techniques found in the literature are shown and discussed. The poor quality of the results obtained by these methods justifies the development of a new registration approach dedicated to our application. The original proposed registration methodology is based on an explicit incorporation of prior anatomical information in the registration procedure. This methodology is divided into an *initialization* phase registering segmented homologous structures from both CT and emission PET images and a second registration working with the whole set of image intensities, called *fine* registration. This strategy has allowed to take benefit of the advantages associated to both feature-based and voxel-based techniques while canceling some drawbacks of each approach. The initialization phase is then separated into two steps: a segmentation phase in which common structures in both images are recognized; and a structure registration phase that computes an initial transformation between segmented organs in order to initialize close to the final solution the refinement registration phase.

Therefore, **Chapter 4** describes the proposed procedure for the segmentation of the main and discernible homologous CT and emission PET structures of the thorax and abdomen. The segmentation of these structures is not a simple problem, in particular in functional images. For this reason, we propose an original hierarchical segmentation strategy in which organ-specific prior information complements distinct photometric properties of the structures. The developed procedure delineates organs in a hierarchical order, from simple to more complex to segment. Then, the extraction of a given structure is driven by information derived from anatomical objects which have been previously segmented. This information is composed of spatial constraints (directions, exclusions) inferred from the previously segmented structures and expressed by the means of Regions Of Interest (ROI) in which the search for new structures will take place. Structures are treated in two different stages: a first stage is composed of automatic thresholding and other low level operations in the ROI defined by previously segmented objects; a second stage employs a 3D deformable model to refine and regularize results provided by the former step. In **Appendix C**, numerical implementation details of some parts of the proposed segmentation procedure are described. A similar segmentation procedure has been successfully used in a brain internal structure segmentation application, described in **Appendix E**. Initial results on a semi-interactive tumor segmentation procedure we are developing are shown in **Appendix D**. The main goal of this procedure is to include tumor information on the initial registration phase, thus imposing some constraints on the tumor transformation.

Chapter 5 presents three different methods we have developed for registration of structures recognized during the previous segmentation phase. This structure-based registration should provide a good initial non-linear deformation for the fine-grained intensity-based registration phase. The first method is an extension of the well-known Iterative Closest Point (ICP) technique to non-linear transformations. The second algorithm (RMS-FFD) employs a B-spline Free-Form Deformation (FFD) model in conjunction with a Root Mean Squared (RMS) difference similarity criterion to align both labeled segmentation structures. The third method (GVF-FFD) computes a deformation field over CT segmented structures by means of the Gradient Vector Flow (GVF) technique in order to make corresponding PET structure surfaces evolve towards CT ones. The transformation is also modeled by means of a FFD and its control point displacements are optimized according to the GVF field. The final section of the chapter compares and evaluates the three developed structure registration methods, in terms of registration accuracy and computational cost.

Chapter 6 describes the *fine* registration phase which works with the whole set of CT and emission PET image intensities. The transformation is also modeled by means of a FFD model, thus making easier the interaction between both stages of the proposed registration methodology. Normalized Mutual Information (NMI) has been employed as similarity criterion to guide the optimization of the control points displacements of the FFD grid.

Chapter 7 is devoted to the assessment of the registration result accuracy. First, a review of the evaluation techniques frequently used in medical image processing, and in particular in registration applications, is given. Afterwards, the visual assessment protocol we have developed in collaboration with the physicians involved in the project is described and the study of its inter-observer consistency proves that it can be used to obtain an objective enough estimation of the registration result accuracy provided by the proposed methodology.

Chapter 8 shows statistics furnished by the visual evaluation protocol on some final registration results provided by the proposed registration methodology. Several snapshots of three final registration results are also shown, illustrating the good performance of the proposed methodology.

In **Chapter 9**, conclusions about the general proposed methodology and its different stages are presented, together with some perspectives of our work.

Part I

Application context

CHAPTER 1

Medical framework

Contents

In this chapter, we present the medical interest of the combination of anatomical and functional information provided by CT and PET images in oncologic applications. First, some definitions and statistics are given in Section 1.1. In Appendix B, detailed medical and biologic information about cancer, statistics and other information related to this disease are available. Thereafter, in Section 1.2 we introduce CT and PET imaging modalities, their physics principles and their contribution in oncologic applications. In Section 1.3, the combination of anatomical and functional data in oncology is studied. First, the benefit of this combination is presented and proved with a review of several published clinical studies about this subject. Then, we enumerate the difficulties to overcome in order to combine information provided by CT and PET images of thoracic and abdominal regions. Finally, current techniques that can be used to perform this combination are described. The development of a software-based registration algorithm is then justified and some particular requirements of our application are also presented.

1.1 Cancer disease

Cancer is a term used to describe a group of illnesses all having in common the lack of regulated cell growth, which results in serious health problems. Cancer has afflicted humans throughout recorded history. Nowadays, worldwide, there are over 10 million new cases of cancer and more than 6 million deaths from cancer annually. In approximately 20 years time, the number of deaths annually due to cancer will increase from about 6 million to 10 million. Detailed information about cancer, its origins and causes, statistics of this disease and a historical review of the evolution of knowledge about it can be found in Appendix B.

The study of this disease is one major trend in medical research in which imaging modalities and their image processing play a significant role.

1.2 Imaging modalities

In these days, medical decisions are rarely taken without the use of imaging technology. Imaging allows us to explore inside the body in a non-invasive way. Not only more comfortable and safe to the patient, imaging allows views of anatomy and physiology that cannot be obtained by any other means.

Since the discovery of *X-rays* by W.C. Roentgen (1845-1923) in 1896, the last 100 years has seen a veritable boom in medical imaging methods and technology. The original X-ray is only one of the many methods in a radiologist's arsenal of imaging modalities. Together with Computed Tomography (CT), Magnetic Resonance Imaging (MRI), Single Photon Emission Computed Tomography (SPECT), Positron Emission Tomography (PET) and Ultrasound (US), the physician can examine the patient in a manner which was beyond imagination only 50 years ago. In general, imaging can address two issues: structure and function. One can either view structures in the body and image anatomy or view chemical processes and image biochemistry. Structural imaging techniques include X-rays, CT, MRI and US. It is the role of SPECT and PET imaging to view the biochemical processes inside.

In the particular case of cancer, both structural and functional imaging modalities decisively contribute to medical tasks such as diagnosis, benign and malignant tumor distinction, staging [1] of malignant lesions, cancer spread assessment, survival prediction, monitoring and treatment planning, surgical intervention guiding, therapeutic follow-up or treatment response evaluation. In these days, CT and PET are the imaging modalities usually employed in oncology applications involving thoracic and abdominal regions.

1.2.1 Computed Tomography (CT)

The CT scan is a natural progression from X-rays. The method is based on the principle that a three-dimensional object can be reconstructed from its two dimensional

---

[1] After cancer has been diagnosed, doctors assign a *stage* to the cancer to determine how far the disease has progressed.

projections. The mathematics are based on the Radon transform which is a map from an n-dimensional space to an (n-1)-dimensional space.

The scanner rotates an X-ray tube around the patient in an arc and the emergent radiation beam is measured by photo-electric detectors, taking X-ray pictures from various angles and then combining them together to reconstruct the three-dimensional structures in the body. A computer is used to display the measurements as a grey-level image representing a cross-sectional slice of the patient, based on the density (or attenuation value) of tissues to X-rays. Dense structures such as cortical bone appear bright, whereas low density areas like air appear dark, as is the case with conventional radiographs.

The main advantage of CT scans (MRI as well) is that they provide exquisite anatomical detail, i.e., about the localization and the morphology of structures and tumors, as shown in Figure 1.1. Therefore, diagnosis, staging and re-staging of cancer, as well as monitoring and planning of cancer treatments have traditionally relied on this anatomical imaging modality. Furthermore, information provided by CT images is indispensable specifically for guiding intervention techniques, in which a high level of precision is required in order to exactly define tumor position with respect to surrounding structures. It permits the operator to situate an instrument with confidence and safety, even in relatively inaccessible areas of the body.

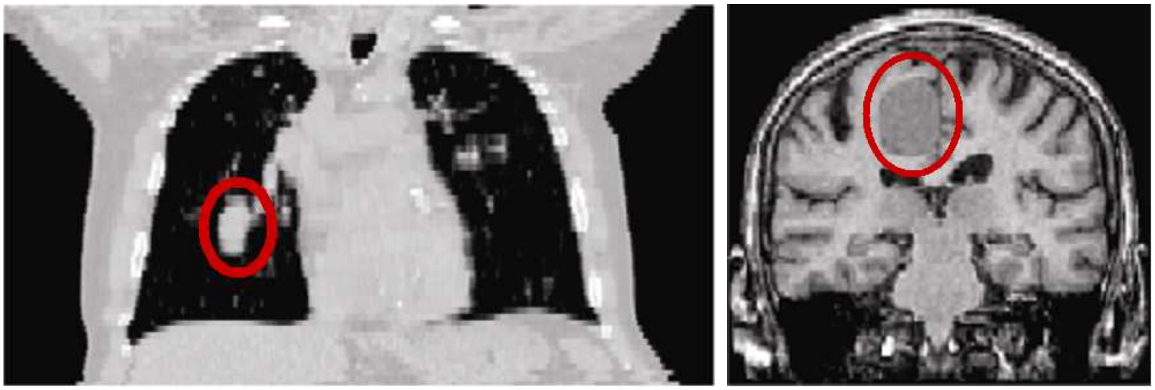

Figure 1.1: Left: tumoral thoracic image obtained with CT acquisition. Right: pathological brain image obtained with T1-MRI acquisition. A circle defines corresponding tumoral regions.

Although CT is effective in disease detection and localization, it does not provide sufficient knowledge about the lesion malignancy, since many have similar attenuation characteristics. Size criteria limits CT ability to characterize masses reliably as malignant or benign. Necrotic, scar (and other post-surgery alterations) or inflammatory tissue often cannot be differentiated from malignancy based on anatomic imaging alone. This implies that CT generally has a high sensitivity [2] for the detection of struc-

---

[2] Sensitivity represents the proportion of truly diseased persons in a screened population who are identified as being diseased by the test; it is a measure of the probability of correctly diagnosing a condition.

tural alterations, but a low specificity [3] for further characterizing these abnormalities and response to therapy. For example, it may not be possible to distinguish fibrotic masses from benign or malignant neoplasms [4] on the basis of their CT appearance alone. Another problem associated to this imaging modality is that it does not easily provide whole-body images, thus, impeding complete metastasis detection.

1.2.2 Positron Emission Tomography (PET)

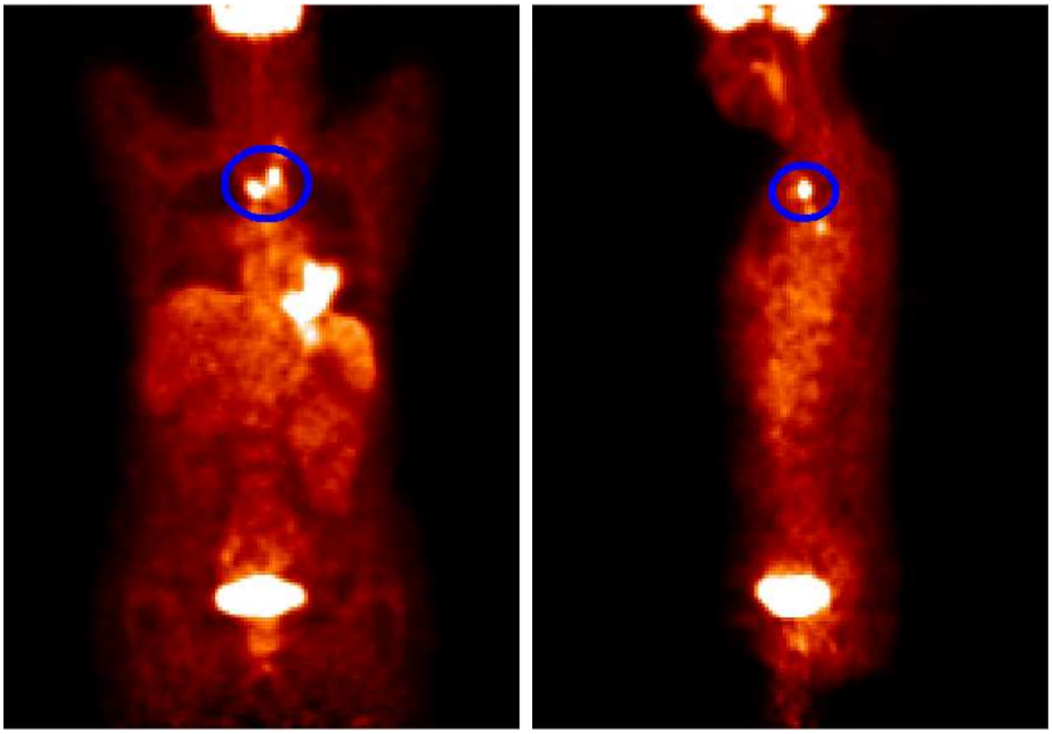

Figure 1.2: Coronal and sagittal slices from a PET volume with an uptake in the tumoral regions (a blue ellipse defines them).

PET imaging modality uses a tracer to image biochemical basis of normal and abnormal functions within the body. This is very important because [5]:

- the basis of all tissue function is chemical;
- diseases result from errors introduced into its chemical systems by different factors (viruses, bacteria, genetic abnormalities, ...);

---

[3] Specificity is the proportion of truly non-diseased persons who are so identified by the screening test. It is a measure of the probability of correctly identifying a non-diseased person.

[4] A neoplasm is an abnormal new growth of tissue.

[5] From the tutorial called Let's play PET of the Crump Institute for Molecular Imaging, UCLA School of Medicine. `http://www.crump.ucla.edu/software/lpp/`.

- the most selective, specific, and appropriate therapy is one chosen from a diagnostic measure of the basic chemical abnormality;
- detection of chemical abnormalities provides the earliest identification of disease;
- assessment of restoration of chemical function provides an objective means for determining the efficacy of therapeutic interventions in the individual patient;
- the best way to judge whether tissue is normal is by determining its biochemical function.

A tracer is an analogue of a biologically active compound in which one of the atoms has been replaced by a radioactive atom. When the tracer is introduced into the body, its site-specific uptake can be traced by means of the labeled atom. PET tracers are labeled with positron emitting isotopes, such as Fluorine-18 (F-18) and Carbon-11 (C-11), having in general a relatively short half-life (about 110 minutes for Fluorine-18 and 20 minutes for Carbon-11), then putting a practical upper limit on the activity of the manufactured isotope. Nevertheless, the F-18 isotope half-life allows a certain independence from the cyclotron required to produce it.

When the labeled atom disintegrates in the body, the emitted positron comes to rest and annihilates with an electron. This event produces two 511 keV photons which fly off at almost 180 degrees to one another. The PET detector is set up in such a way as to accept events in which both annihilation photons are detected in coincidence.

Attenuation correction of the *emission* [6] PET image is necessary because deep-seated tissues appear to contain less activity because the annihilation photons stand a higher chance of being absorbed before leaving the body. This correction enhances emission PET image quality and it is in general achieved by means of radioactive sources (Germanium^{68} and Cesium^{137} are frequently used) integrated in the PET scan, producing *transmission* PET images. This transmission image is often acquired immediately before acquisition of the emission image, thus, it may be a non-negligible misalignment between the emission and transmission scans. In PET-CT combined machines (see Section 1.3.3) attenuation correction can be performed by means of the X-ray source of the CT scan [142], which has proved to be a faster and more precise strategy in several cases [198], even if several artifacts may appear [104].

PET tracers include *18-fluorodeoxyglucose* (FDG), a marked analogue of glucose that contains the radionuclide Fluorine F-18. FDG is employed to image general metabolic rate and can be used to image tumors. As a matter of fact, FDG utilizes the markedly increased glucose metabolic activity of tumor cells and provides images of the whole-body distribution of phosphorylated FDG, in which benign from malignant lesions can be accurately discriminated. This is based on the fact that malignant tissue exhibits markedly increased rates of glucose consumption. Even if FDG is the most used tracer in oncologic applications, there is an active research on new and more specific molecules such as *fluorothymidine*, *fluorotyrosine* or *fluorocholine*, that permit cancer detection by means of the evaluation of other metabolisms. For instance,

---

[6] PET images displaying functional activity (emitted photons) are then called *emission* ones

FDG has some disadvantageous properties such as the accumulation in inflammatory tissue. The 18-fluorodeoxy-L-thymidine (FLT), a new radiopharmaceutical reflects DNA-synthesis and shows promising clinical potential since it is expected that FLT accumulates more specifically in tumor tissue than FDG. In fact, imaging of the DNA-synthesis rate with FLT is a direct measure of cell proliferation and tumor growth whereas glucose consumption (FDG-PET) is a derivative of tumor growth.

In our work, only PET images based on the FDG tracer were available. These images are very useful because of its sensitivity and specificity in identifying the biological behavior of tumors (see Figure 1.2), thus diagnosing, staging and re-staging cancer with a substantially higher accuracy than CT. Furthermore, whole-body FDG-PET images permit the detection of unsuspected distant metastasis unlike CT ones.

Several clinical studies have proved these improvements in a wide variety of oncologic applications. For instance, Dwamena [86] concluded that PET demonstrated both higher sensitivity (79% versus 60%) and specificity (91% versus 77%) than CT for correctly classifying mediastinal lymph nodes. Similar observations have been made in patients with lymphoma [134], colo-rectal cancer [290], breast cancer [293], and many other malignancies. FDG-PET has also been established as a powerful prognostic and treatment evaluation tool in cancer patients [293]. Gambhir et al. [97] have recently summarized the power of FDG-PET based on tabulated research data obtained in more than 26,000 patients with a variety of cancers. PET was 10% to 20% more accurate than conventional imaging for diagnosing staging and re-staging most cancers. Based on these studies, PET acquisition with FDG has become a very extended technique in oncologic applications involving lung and colo-rectal cancer, lymphoma, melanoma, head and neck cancer pancreatic, hepatocellular carcinoma or esophageal cancer [73].

While PET imaging furnishes a valuable functional information about cancer, it provides little information on the anatomy around the increased uptake due to the non-specific uptake in several organs (muscles, brain, heart, liver, colon, ...), the low spatial resolution, the low Signal-to-Noise Ratio (SNR) and the strong presence of noise and artifacts. Thus, making a precise lesion localization is quite difficult, and additional anatomical information is required in some oncologic applications, as shown in Section 1.3).

1.3 Combination of CT-PET images in oncologic applications

1.3.1 Contribution

As mentioned above, PET and CT techniques each have limitations that can lead to diagnostic uncertainty in certain cases. Their combination is especially complementary: PET is a highly accurate method for detecting cancer and other metabolic abnormalities, but it does not provide the anatomical landmarks needed to precisely locate lesions. On the other hand, CT scans are not as sensitive but offer excellent anatomic detail, pinpointing the exact size, shape, and location of diseased tissue.

The combination of the mutual advantages of both techniques can have a significant impact on improving medical decisions [294] for diagnosis, staging, re-staging, selection of treatment modalities, biopsy guiding, recurrence detection, planning of radiation therapy (definition of clinical target volume), or the monitoring of surgical, chemotherapy and radiation treatments. In the particular case of thoracic and abdominal regions, some more specific tasks can be: diagnosis of isolated lung cell; staging of primitive lung cancer and metastasis; definition of radiotherapy target volumes in non-small cell lung cancer; follow-up of the response to therapy in primitive lung cancer; detection of mediastinal or parietal lesions; staging of recidives of colo-rectal cancer; differentiation of urinary artifacts; location of the pelvis and biopsy guiding in hepatic metastasis.

Figure 1.3 shows two examples in which the combination of information provided by the CT and PET images could improve the knowledge about the disease. On the CT image (left in Figure 1.3) corresponding to the first case (top images in Figure 1.3), tumors are not distinguishable from surrounding structures, making risky several decisions such as the definition of radiotherapy target volumes. On the other hand, the tumors are well contrasted in the PET image (right in Figure 1.3), but there is a lack of anatomical references. The superimposition of both images will be very useful in this case. In the second case (bottom images in Figure 1.3), the tumor can be easily recognized in both scans, but the PET image (right Figure 1.3) provides a valuable additional information consisting in the definition of the necrotic part of the tumor (the inner dark region of the tumor). Nevertheless, for diagnostic or radiotherapy purposes, the CT scan must be used as an anatomical reference, then again, the combination of information provided by both images could be quite useful.

Several clinical studies have proved the benefits of the PET-CT combination in some of the applications mentioned above.

Charron et al. [46] compare combined whole-body PET and CT imaging of malignancies with the results from PET imaging alone. Thirty patients with a variety of malignancies were examined. In 8 patients, images from the combined scanner allowed differentiation of areas with variable amount of physiologic FDG uptake from juxtaposed contiguous neoplastic process. Martinelli et al. [187] reviewed more than 100 oncology studies acquired with a PET/CT scanner. From their observations in patients with a variety of malignancies, they concluded that PET/CT offered significant advantages including more accurate localization of FDG-uptake, distinction of pathological from physiologic uptake, and improvements in monitoring treatment. In another study [10], PET/CT improved the accuracy of PET in 48% of the patients mainly by improving lesion localization, and led to retrospective detection of CT abnormalities in a considerable number of patients. Gupta et al. [110] studied the staging and diagnostic accuracy increase combining CT-PET images in a database composed of 23 patients. The combination confirmed PET staging in 6 patients, changed cancer staging in 4, led to cancellation of surgery in 3, directed successful biopsy in 4 and changed diagnosis in 2. PET lesions were also evaluated with PET/CT by Yeung et al. [311]. Analyzing the findings in the first 100 patients studied with PET/CT, they reported that 57% of the equivocal PET findings could be classified correctly

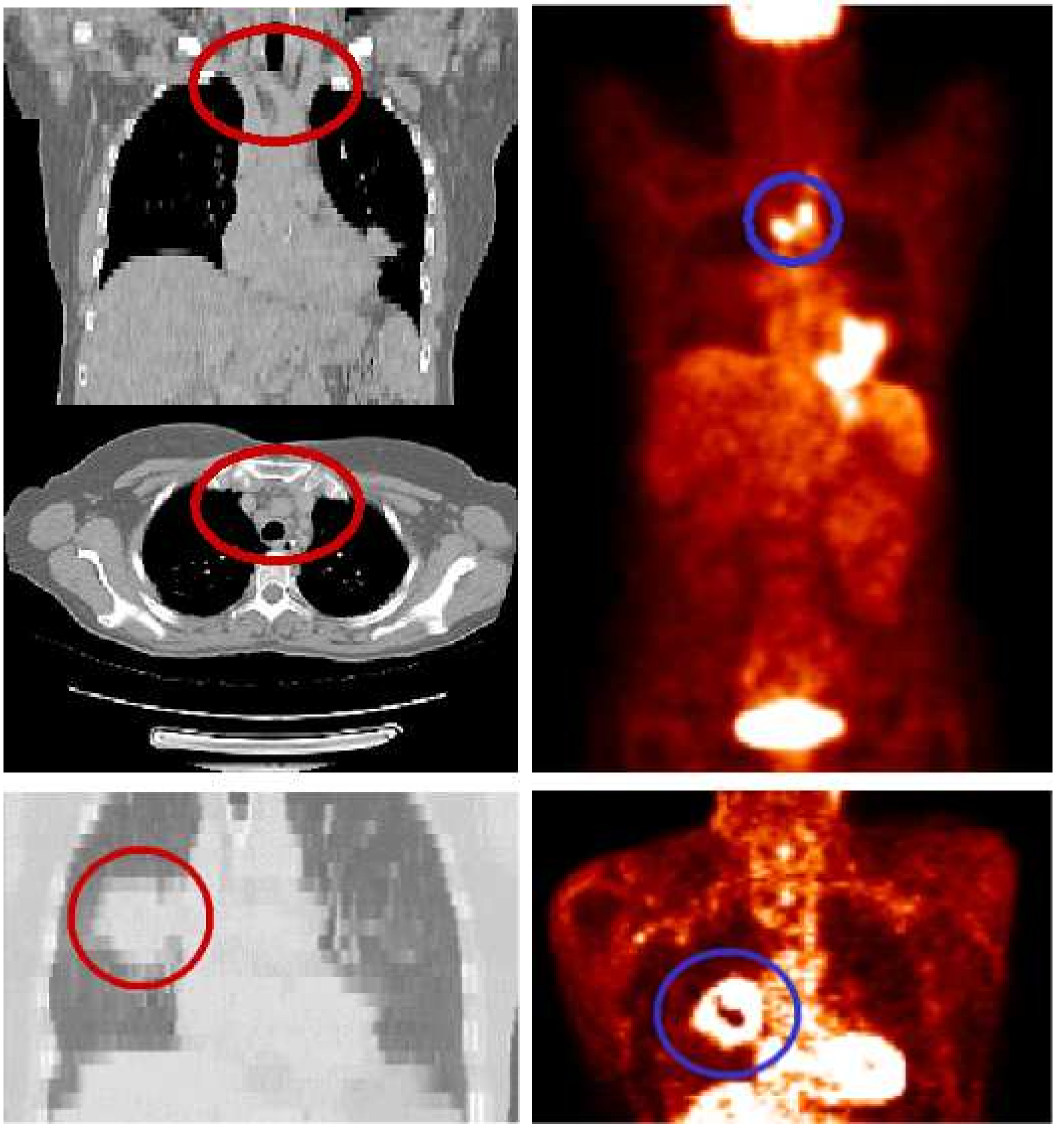

Figure 1.3: Two examples in which a combination of anatomical and functional information provided by CT (left) and PET (right) images could be useful. A circle defines tumoral regions in each image. Top images: patient 1. Bottom images: patient 2.

into normal or abnormal categories, differentiating benign or artifactual lesions from malignant disease.

The role of PET/CT for evaluating patients for lung cancer recurrence was assessed by Keidar et al. [140]. This study of 26 patients revealed that PET/CT provided important additional information in 56% of the patients. Importantly, lesions missed by CT initially were visualized by PET/CT and were identified subsequently on CT images. Similarly, Weng et al. [297] also reported a higher diagnostic accuracy for PET and CT than for PET or CT alone for lung cancer staging. The impact of PET/CT imaging on the pre-operative staging of lung cancer patients was evaluated by Steinert et al. [265]. These authors reported an incremental impact of PET/CT imaging with increasing patient stage, concluding that PET/CT was superior to PET or CT alone in initial staging of lung cancer. Another advantage of PET/CT in the staging/re-staging of lung cancer patients was provided by Osman et al. [202] in 34 patients.

Chin et al. [50] reported a series of 30 patients studied with PET and CT to determine mediastinal lymph node involvement. They concluded that the combined information of PET and CT yielded the highest diagnostic accuracy (90%). Kamel et al. [137] reported focal FDG uptake in the lower anterior neck in 6 of 184 patients who underwent lung cancer staging. The PET/CT assessment avoided the false positive findings of PET alone. Makhija et al. [179] used PET/CT to evaluate patients with suspected recurrent ovarian cancer. PET/CT identified the site of recurrence in 5 (62%) of 8 patients who had negative CT findings.

One important emerging clinical contribution of PET/CT is its role in the field of radiation oncology, specifically radiation planning. This is because CT alone can only delineate mass lesions, but frequently fails to determine reliably the amount and extent of viable tumor. PET merged with CT makes it possible a structural and functional approach to optimize biological target volumes in radiation therapy planning. Dizendorf et al. [81] evaluated prospectively the impact of PET/CT on radiation planning in 30 consecutive patients scheduled to undergo external beam radiation. Combined PET/CT changed the radiation treatment strategy from curative to palliative in 20% of the patients. In 30% of the patients, the radiation dose was changed and changes of the target volume were reported in 40% of the patients.

Finally, an interesting use of the PET-CT combination concerns the validation of new tracers for PET imaging and the combination of complementary information they provide. As mentioned in Section 1.2.2, even if the FDG is the most employed tracer due to its good properties in terms of half-life, new tracers are emerging. These new tracers use different metabolism procedures for cancer detection and they allow a new role of PET images in radiotherapy (tumoral hypoxic tracers, 18-fluoromisonidazole), chemotherapy (marked chemotherapeutic products) or hormonotheraphy (marked hormones, 18-fluoroestradiol) planning definition. One characteristic of the images acquired with these new tracers is that they have even less anatomical references than FDG-PET images. Thus, the combination of the information provided by these functional images must be based on a CT associated to each one of these PET scans.

1.3.2 Difficulties

Integrating data from different imaging modalities requires a prior geometric alignment or *registration* phase to be able to compare both images and superimpose the homologous structures they contain. The aim of our work is to develop a registration procedure of CT and PET images to be applied to thoracic and abdominal regions. This is a challenging task due to several difficulties associated to this application that are mainly due to:

- the elastic and local nature of the organs located in these regions;
- the large inter-individual range of structure movements and metabolic activity;

- the different physical nature underlying both acquisition techniques;
- the different acquisition protocols and the time passed between them;

The first problem concerns the elastic nature of the deformations to cope with in thoracic and abdominal structures, being much more complex than in other more rigid regions such as the brain. For instance, the lung volume and morphology vary considerably during the respiratory cycle, as shown in Figure 1.4. In these coronal slices, we can observe these differences between breath-hold and normal breathing acquisitions. Top images show CT scans acquired when the patient is breathing normally and bottom images show CT ones performed in a single breath-hold at full inspiration (maximum expansion of the thorax). Moreover, these deformations have a very local nature, as observed in the lung example in which the diaphragmatic wall suffers a severe displacement while the upper part of the lungs remains quite stable.

A second problem associated to our application is the large inter-individual variability concerning structure morphology, nature of their movements and metabolic activity, as illustrated in Figure 1.4 (each column of Figure 1.4 corresponds to one patient). This image illustrates the large inter-patient variability in terms of severity of the deformations and structure morphology.

Figure 1.4: Examples of deformations suffered by the lungs through the respiratory cycle. Top images show CT scans acquired at normal respiration while bottom images show those ones performed in a single breath-hold. Left: patient 1; right: patient 2.

CT and PET techniques are based on different physical properties that lead to images displaying the same scene in a different way. A critical consequence is the lack of linear correspondences between some anatomic and functional set of grey-levels. For instance, the intensity values corresponding to the heart can vary up to a factor of ten in PET images, while in CT ones they are almost constant. Furthermore, there are structures that do not appear at all in PET scans because they do not accumulate the tracer (thus, no uptake in the image), producing an incomplete representation of the anatomy. This problem is aggravated by the strong presence of noise and artifacts in PET images.

Finally, the different clinical acquisition protocols and the time passed between them produce differences in the presentation of the data scans that the registration procedure must recover. Therefore, it allows us barely no prior knowledge on resolution, displayed region, patient position, ..., beyond the most basic, such as the general orientation of the patient, as illustrated in Figure 1.5. For instance, in thoracic CT, the scan is sometimes performed in a single breath-hold and the patient is requested to maintain maximum inspiration if possible during the acquisition (15 seconds in a helicoidal scanner). Also, to avoid attenuation of the arms in the X-ray beam, the patient holds them above his head. In PET, the scan time is longer (30-60 minutes) and the patient breathes normally. Due to the long duration of this scan, reconstruction algorithms provide an averaged image over the respiratory and cardiac cycles. A respiratory gating of the PET acquisition would be helpful [30], but at the moment it is not a promising approach due to the substantial resulting increase in imaging time [103]. Furthermore, the arms are in general placed at the side of the body because some patients cannot endure an arms-up posture during a full PET acquisition. The fact that the time between both image acquisitions can be very long (weeks or even months) involves even more differences between CT and PET scans due to long-term changes in the patient's anatomy. Deformations induced by different patient positioning, scan formats or time passed between both acquisitions are considerably reduced in hybrid PET/CT systems (see Section 1.3.3) with respect to stand-alone devices.

The differences mentioned above leave among the images little more than a statistical, *conceptual* similarity, in the way that organs generally correspond to uniform regions (except in some structures such as the heart), and spatial relationships among these organs are very stable in the two image volumes. Thus, a combination of information provided by anatomical and functional imaging modalities can only be performed by experts trained on this task.

Until few years ago, image registration was achieved by the physicians in a visual way, meaning that the physician had the 2D slice series from each modality mounted on a traditional light box. Then, the physician should combine the information from several imaging modalities in his mind to produce a mapping of the 3D homologous points between the images. This mapping depends on the physician's knowledge and expertise but it is influenced by different structure orientation, field of view and resolution of the images, making it difficult to determine the correspondence between anatomical structures. This procedure, even performed by expert physicians, remains very rough and time-consuming, and uncertainty in the mental mapping from one

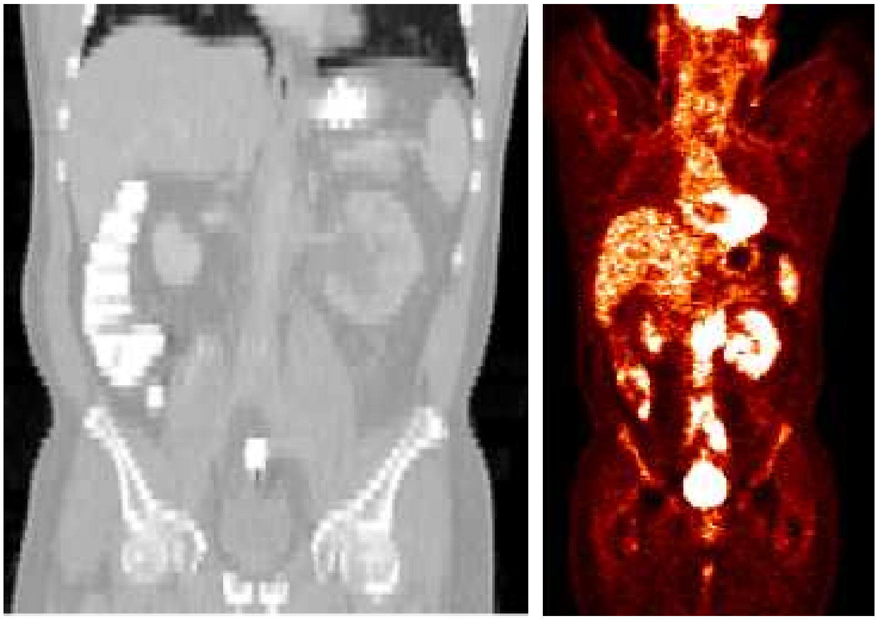

Figure 1.5: Example of CT (left) and PET (right) images of an abdominal study illustrating the differences in the presentation of the data. The CT image is focused on the abdominal region while the PET one displays the whole body. Size and resolution of the images are also quite different.
CT size: 512 x 512 x 59 pixels; CT resolution: 0.84 x 0.84 x $7.5mm^3$
PET size: 128 x 128 x 205 pixels; PET resolution: 4.297 x 4.297 x $4.297mm^3$.

image to another may lead to uncertainty in the diagnosis or planning. Therefore, solutions providing a fully or semi-automatic and more objective way to produce this mapping could considerably help the physicians to improve their decisions.

1.3.3 Current techniques to combine anatomical and functional information

Nowadays, four different techniques could be used to combine anatomical and functional information provided by CT and PET scans.

The simplest of these techniques is manual registration, in which an operator matches recognizable objects in each of the images. In our application, manual registration is not considered because it has most of the weaknesses of the mental mapping mentioned above.

Another technique involves the use of temporary markers on the patient to help register images. Nevertheless, external landmarks will not give crucial information about the nature of the elastic and local deformations to cope with in thoracic and abdominal structures. This is therefore not a well-suited approach for our application. Furthermore, one of the main requirements for our registration procedure is to not modify the acquisition protocols employed in the clinical sites associated to the project, but working with images acquired in clinical routine.

Another possibility concerns the use of the recently introduced hybrid PET-CT systems that produce images that are intrinsically registered because both scans are obtained one immediately after another with the patient in the same position (except for an axial translation of the bed).

Finally, computer algorithms also allow to register images, looking for the geometrical transformation which best superimposes CT and PET images.

Combined machines and computer algorithms, being the most used techniques in the registration of CT and PET images, are further discussed below.

Combined PET-CT systems

Combined PET-CT systems (see Figure 1.6) have been introduced by scanner constructors (General Electric, Philips and Siemens) a few years ago [18]. These machines allow the acquisition of anatomical and functional information in the same examination, thus furnishing a hardware (or mechanical) rigid registration. The fact that the CT and PET images are acquired one immediately after another with the patient in the same position avoids strong deformations appearing in images obtained by separated machines. For instance, a slight variation in the patient trunk position will produce strong image differences in terms of rotation. Other advantages of this technique include organizational facilities (images almost at the same time in the same room), a better attenuation correction of the emission PET image (it is achieved using the CT scan) and the possibility of comparing PET images acquired with different tracers (using the CT scan as an anatomical reference).

The importance of these hybrid systems is illustrated by the fact that the majority of the PET devices installed in 2004 will be combined PET-CT machines. A very interesting review of this technique can be found in [283].

Figure 1.6: Combined PET-CT machines. Left: General Electric; Center: Philips; Right: Siemens.

Even if this technology is a huge step towards an automatic and objective mapping of CT and PET images, there are some unanswered questions. As a matter of fact, there are remaining potential registration errors in these systems due to the physiological motion in the patient. In the chest, these errors are predominantly caused by breathing, except in the vicinity of the heart, where cardiac movement is the major reason, or with insufficient patient cooperation [103]. This motion consists of anisotropic movements of the thoracic wall and the diaphragm, moving tumors and organs in a non-linear way in all three directions, thus leading to distortions and asymmetrical position changes.

Several studies [24 ; 204] have proved the presence of artifacts in images acquired with combined PET-CT machines due to respiration. The anatomic regions most affected by breathing artifacts include the diaphragm, the base of the lung, and the upper pole of the liver [283]. Blodgett et al. [24] found non-systematic displacements of the diaphragm by as much as 25mm in the axial direction. Osman et al. [204] have quantified the Respiration Motion Artifact (RMA) in a database of 50 patients, being noted in most (84%) of the studied patients. RMA was $16.4 \pm 10.5mm$ at anterior, $14.3 \pm 7.6mm$ at middle, and $13.6 \pm 8.6mm$ at posterior aspects of the right lung base and $17.8 \pm 10.8mm$ in the posterior aspect of the left lung base. In a more recent study [203], these authors noted that, in 300 patients with proven liver lesions, approximately 2% appeared to have the lesion localized in the lung due to respiratory motion. Therefore, even in images provided by hybrid systems, a non-linear registration phase is necessary in order to cope with these physiological deformations.

Computer-based registration algorithms

The current processing ability of computers allows the development of software algorithms that solve complex image processing and computer vision problems. In registration applications, it offers another way to compensate for the differences between two images to register, computing the transformation which best aligns them. A computer-based registration algorithm, together with an interactive and user-friendly visualization interface can be a very helpful tool to the physician.

Software-based registration techniques have been developed and successfully used in several medical applications such as computed-assisted surgery [150], radiation therapy planning [49], brain database studies [60] and others (the interested reader is referred to the classical medical image registration reviews [177 ; 119 ; 217] for more examples). The majority of these registration algorithms provide a cheap, attractive and suitable tool for clinical routine in brain imaging applications, but they do not fulfill the requirements of robustness, speed and minimum interaction when applied to more elastic regions. In Section 2.6, an exhaustive state-of-the-art of software-based registration methods applied to CT and PET images is presented.

In the context of thoracic and abdominal CT-PET registration, software-based registration techniques can be seen as an alternative or a complement to hybrid systems. In fact, some scanner constructors actually offer semi-interactive options in their visualization workstations to compensate remaining errors between PET and CT images acquired with hybrid machines [7].

Regardless of the CT and PET image provenance (hybrid system or stand-alone scanners), a software-based registration algorithm must deal with several difficulties (see Section 1.3.2) linked to the particularities of our application (severe deformations, incomplete and noisy anatomy representation in PET images, anatomy variability, ...). Furthermore, if the algorithm is planned to be used in clinical routine, other

---

[7] `http://www.gemedicalsystems.com/rad/nm_pet/products/workstation/aw_fusionsw.html`

constraints are imposed on the methodology:

- robustness and precision: clinical routine asks for a robust enough algorithm in order to assure a good solution in most of cases. This is an essential requirement because an error may have serious consequences to the patient. The large inter-patient anatomy variability in thoracic and abdominal structures and the severe deformations they suffer make this constraint a challenging one;
- speed: clinical routine asks for a fast enough algorithm in order to be embedded in it without altering clinical schedules. In practice, with current acquisition times, the registration phase should be obtained in less than an hour;
- maximum automatisation and minimum interaction: these constraints are important in order to avoid to avoid subjective and time consuming manual adjustments. Anyway, the algorithm must offer the possibility of manual modifications and easy user-interaction and introduction of prior information after each processing intermediary phase.

Therefore, the main goal of our work has been the development of a software-based algorithm capable of fulfilling these requirements in order to achieve a robust, fast enough and good quality registration of thoracic and abdominal CT and emission [8] PET images.

It must be pointed out that a particular requirement (coming from the industrial partner associated to the project) for our methodology was to work on the images acquired with already defined acquisition protocols, without altering them. Therefore, we should focus on the image processing and analysis and forgive techniques involving changes in the image reconstruction stage [26] or the acquisition protocol (for instance using fiducial markers), that could be considerably helpful to find better registration methodologies. In the future, our work should be completed with research on these crucial aspects.

---

[8] It is important to specify that the aim is to register the emission PET image and not only the transmission one. It means that we will not use the assumption of no deformation between both emission and transmission PET scans. This subject is further discussed in Section 2.6.

CHAPTER 2

Registration theory

Contents

This chapter presents the theorical framework of a classical registration system. First, in Section 2.1, a general scheme of a registration is described, followed by an introduction of the peculiarities of a registration procedure working with thoracic and abdominal CT and emission PET images. Afterwards, the choices for the different stages of an image registration method are briefly enumerated: image representation (Section 2.2); transformation model (Section 2.3); similarity criterion (Section 2.4); and optimization method (Section 2.5). In Section 2.6, an exhaustive state-of-the-art of registration methods applied to CT and PET images is presented. Finally, Section 2.7 justifies the particular choices for each of these registration components in the context of CT/PET registration of the thorax and abdomen.

2.1 Introduction

2.1.1 Registration of medical images

Registration or spatial alignment of images is not a recent topic in the literature. D'Arcy Thompson [279] has treated this subject in 1917, concerning a morphometry application [12]. Several decades later, Talairach et al. [274] presented a registration system for brain imaging. It was in the 1980's when the registration was introduced as a computer based procedure with the works of Bacjsy et al. [8 ; 7], Broit [36], Bookstein [27] and others.

Nowadays, the literature in the field of image registration is extraordinary large. As an estimation, according to the database of the Institute of Scientific Information (ISI), in the last 10 years, more than 1000 papers were published on this topic [316]. Another recent study [215] illustrates the growth of the medical image registration field over the past decades, in particular elastic registration, as can be seen in Figure 2.1.

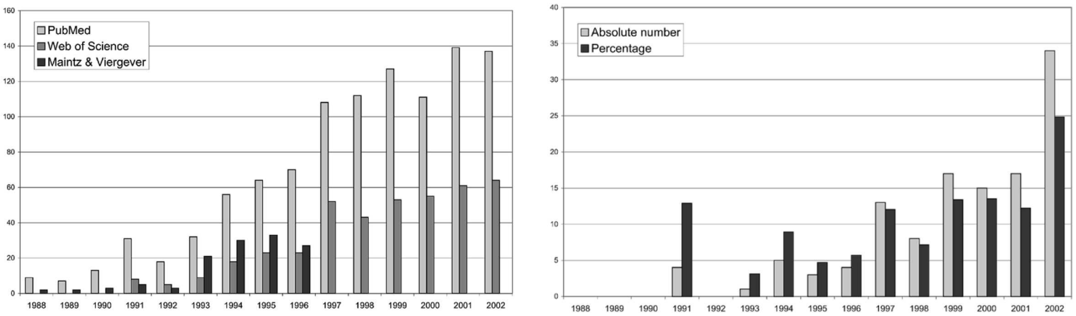

Figure 2.1: Publications on image registration (left) and on elastic image registration (right). From [215].

Because of this importance, several complete reviews have appeared providing classifications of the registration methods proposed by the research community. The first surveys were proposed in [102] and [101] presenting correlation-based and medical registration methods respectively. Later, Brown et al. [37] published a key review paper, including registration techniques in several application domains and a complete classification according to the different phases composing a registration system. After that, the overviews-expert research group of the University of Utrecht has published the most complete surveys on medical image registration [291 ; 177]. Other interesting reviews on this subject can be found in [119 ; 159 ; 316 ; 5].

A registration procedure is needed in very different computer vision and image processing medical and non-medical applications. Within former ones, we can mention pathology detection, localization and follow-up or computer-assisted surgery. With respect to non-medical applications, some examples include segmentation improvement, object or template recognition, stereovision, shape reconstruction or tracking. In all these applications, medical or not, a registration phase is required to combine information provided by two or more digital images of the same scene taken from dif-

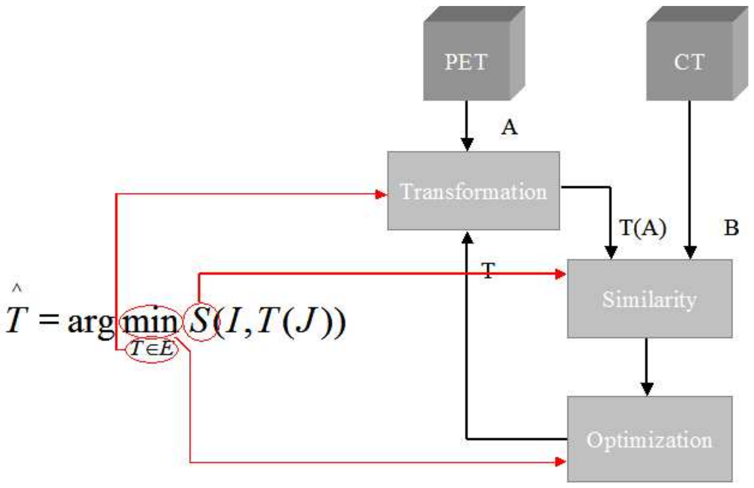

Figure 2.2: Classical scheme of a registration system.

ferent sensors, different viewpoints, or at different times. But, what does *registration* [1] means? In this document we shall use the term *registration* for the process of determining a spatial transformation $\hat{T}$ that relates the position and its associated intensity of features appearing in one image with the position and its associated intensity of their corresponding features in a different image. In this way, we include in the registration process *sampling* and *interpolation* phases that are required after computing the spatial transformation. The goal of an image registration procedure is then to determine the parameters of the transformation that spatially aligns the images to register in order to superimpose voxels representing the same reality, therefore having complementary information in each one of these voxels.

Brown [37] provides the following mathematical definition of a registration system:

$$\hat{T} = \arg\max_{T \in E} S(I, T(J)) \tag{2.1}$$

where I is the fixed image (*reference* or *target* image), J is the image to transform (*source* or *floating* image), and $\hat{T}$ is the spatial transformation (in a defined transformation space E) which maximizes, by means of an optimization phase, an appropriately chosen similarity measure S between images to register. Figure 2.2 shows a classical scheme of a registration system with the steps involved in the procedure. Another possible mathematical formulation of a registration process is proposed by Gee et al. [53 ; 98] expressing this task in a Bayesian framework.

Several authors have proposed different classifications of registration methods, defining the different steps constituting a classical registration procedure. It is not a straightforward task due to the large variability of applications and the different points of view to face the problem. Brown [37] and Maintz [177] have proposed exhaustive classifications which decompose a registration algorithm into several steps.

---

[1] words like *matching*, *fusion*, *warping*, *fitting*, *co-registration*, *correlation*, are also employed to refer to the same procedure

Maintz use nine basic criteria, augmenting and detailing the classification proposed by Van den Elsen et al. [291]: dimensionality; nature of registration basis; nature of transformation; domain of transformation; interaction; optimization procedure; modalities involved; subject; and object.

The goal of this chapter is not to provide an alternative classification of registration methods. We only enumerate the different choices for the different aspects of a registration process in order to evaluate each possible option according to the particular requirements of our application. The majority of registration systems can be roughly divided into four main phases, as it can be seen in Figure 2.2:

- image representation,
- transformation,
- similarity measure,
- optimization.

The first step, **image representation**, deals with the extraction of significant features from the images to register, that will guide the registration procedure. The next issue concerns the modeling of the **transformation** between recognized features in both images. The **similarity measure** is the criterion that evaluates the goodness of the registration using the estimated transformation. Finally, the **optimization** phase must find the set of transformation parameters that provides best registration results. These four phases are strongly linked between them and the particular choices for each of these registration components cannot be made independently from each other.

2.1.2 Peculiarities of a thoracic and abdominal CT-PET registration application

CT-PET image registration of thoracic and abdominal regions is a recent medical image processing topic. This statement is confirmed by studying the few number of published works on this subject with respect to brain or other modality registration applications. For instance, one of the most complete and cited registration surveys, published by Maintz et al. [177] in 1998, does not include any reference on this particular registration application. In our opinion, this lack of registration bibliography about this particular application is mainly due to the following reasons.

The first cause concerns PET images. Actually, this nuclear medicine imaging modality is widely used in clinical routine but few years ago the acquisition of PET images was a real challenge for the image processing community. Several problems emerged for the acquisition of a PET machine in a clinical institution: economical aspects; the availability of a close cyclotron in order to furnish isotopes to inject in the patient; and in some countries (for example, France), the unwillingness of the governments to bet on an imaging modality involving the *nuclear* word. Fortunately, several factors have made the tables turned, PET images being, at the present time, easily available for image processing researchers. Some of these factors are: the development of new and cheaper PET machines; the availability of new radiotracers with longer life times, allowing a certain spatial independence of the cyclotron; law adaptation due to evidences demonstrating the impact of PET images on medical decisions; progressive digitalization of clinical services.

The second cause concerns the historical research evolution in medical image registration. As a relatively recent topic, researchers have naturally adopted a simple-to-complex strategy, beginning with anatomical brain images, in which deformations to cope with are less severe than in other regions. Therefore, brain image registration has induced the development of rigid or linear transformation models that provide efficient and robust solutions in mono-modal and multi-modal brain registration applications. Once this challenge has been overcome, researchers turn to registration applications involving body regions in which structure movements are more complex than in the brain. Another factor that makes it possible to work these days with 3D thoracic and abdominal images is the improvement of the processing capacity of computers. Until a few years ago, as they are considerably bigger than brain images, their analysis and processing was discouraged. In our opinion, other possible obstacle was the quality of emission PET images (low SNR, high presence of artifacts) that hindered the development of accurate and in particular robust (most important quality in a medical image processing procedure) algorithms. Fortunately, new PET acquisition devices furnish high quality images (see Figure 2.3). We have observed the evolution of the quality of PET images during the last three years. In Figure 2.3, this evolution is illustrated, by showing snapshots of the first and the last PET images we have worked with.

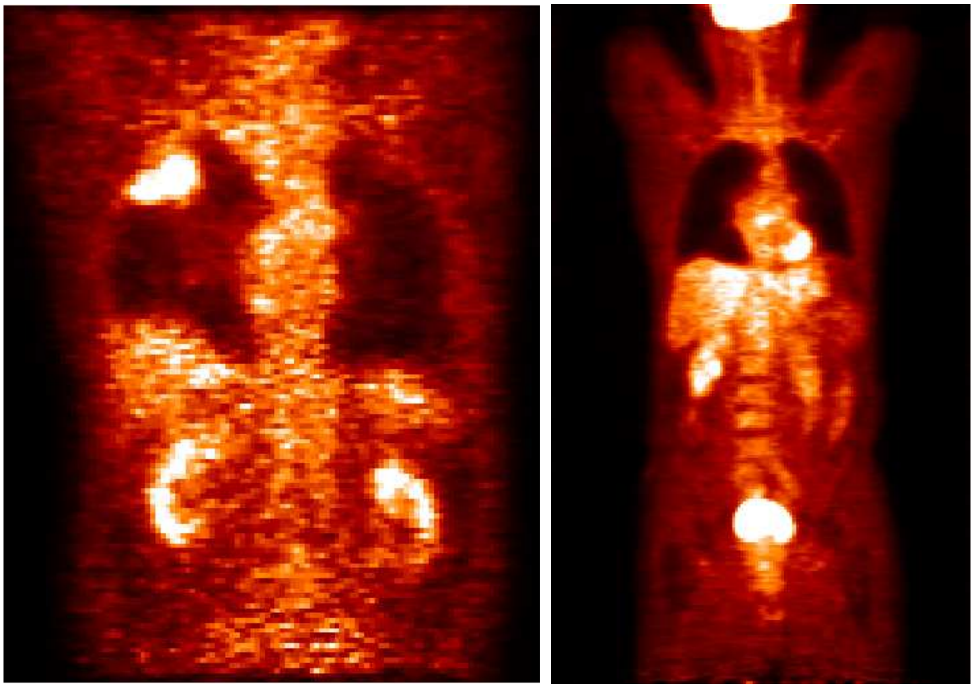

Figure 2.3: Examples of emission PET images having different spatial resolution, SNR and presence of artifacts. Left: three years ago (2000); right: nowadays (2003).

The choice of each phase of the registration procedure will be made according to some conditions or requirements (see also Section 1.3.3) imposed by the application:

- image representation: this phase must take into account the high difference of quality (and voxel resolutions) between CT and PET images and the high presence of noise and artifacts in the latter, in order to fulfil the crucial requirement of robustness of the developed algorithm. Another impeding point concerns the impossibility of using external markers because clinical protocols should not be modified. Furthermore, the need of some kind of user interaction will also influence the chosen image representation;

- transformation: a high number of degrees of freedom is required in order to cope with large and local deformations involved in inter-patient thoracic and abdominal applications. On the other hand, computational cost of the algorithm must remain reasonable in order to be possible to use it in clinical routine;

- similarity criterion: it must be able to guide a registration procedure between images having a non-functional relation between their intensities;

- optimization: in this registration aspect, the main requirement is also the computational cost of the algorithm. Nevertheless, the optimization method will fully depend on the transformation model and the similarity criterion chosen in the registration system.

As mentioned above, the need of a high number of degrees of freedom is confronted with the requirement of a limited computational cost, thus a trade-off between these conflicting requirements must be made that will influence the choice in each aspect of the registration algorithm. Another critical aspect is the robustness of the procedure, which is especially critical when working with medical images that will influence physician decisions.

The registration literature review in the following sections is discussed with respect to these requirements. Section 2.6 groups registration methods that have been applied to CT and PET images.

2.2 Image representation

Image representation involves the decision about which features are going to be used to guide the registration procedure. It must search homologous and significant features between the images to register, assuring that they represent information contained on these images with an enough accuracy. The criteria to select a particular image representation are application-specific, depending on the characteristics of the anatomy, the nature of the transformation to be computed and the imaging modalities used in the registration procedure.

Registration methods can be classified into two categories with respect to the image representation aspect: *feature-based* methods; and *whole-content* based methods.

Former methods attempt to express image content as a set of features extracted by means of a recognition phase to provide a compact and sparser description of the image. These features must constitute homologous reference structures that could guide the transformation computation between the images to register. In general, a feature-based registration method comprises three steps: feature extraction; computation of the transformation between features; and computation of the entire volume deformation. The first step extracts meaningful features that can be categorized according to their intrinsic dimension, the dimension of their evolution space and their intrinsic nature [11], as can be seen in Table 2.1. The second step must provide the transformation which better aligns segmented corresponding features. Finally, this transformation must be extended to the entire volume. A regular interpolation is usually employed to this purpose. Feature-based methods have been successfully used in a large number of different medical registration applications [27 ; 236 ; 194 ; 176 ; 79 ; 93 ; 151 ; 208]. Complete reviews on these registration techniques can be found in [5 ; 11 ; 316 ; 177].

Table 2.1: Different classes of features

Intrinsic dimension	- OD:	Point:	$\Omega = constant$
	- 1D:	Contour:	$\Omega = f(u)$
	- 2D:	Surface:	$\Omega = f(u, v)$
	- 3D:	Volume:	$\Omega = f(u, v, w)$
	- nD:	Hypersurface:	$\Omega = f(u_1, u_2, \ldots, u_n)$
Dimension of the evolution space	- 2D: Discrete or continuous	(image, surface, projection,...);	$\Omega \in \Re^2$
	- 3D: Discrete or continuous	(volume, hypersurface),	space-time (2D+t): $\Omega \in \Re^3$
	- nD:	Hypersurface	space-time(3D+t): $\Omega \in \Re^n$
Nature	Explicit	Implicit	
	-External markers	-anatomical references	scalar or vectors of statistical characteristics
	-stereotastic frameworks	-image characteristics: intensities and its partial derivatives (gradients, curvatures, ...)	-moments
		-regions of segmented images	-principal axes

Whole-content based methods operate on the image grey-levels without prior reduction of image information, so they consider pixel or voxel intensity values as image features. Therefore, all information available in the images is used to determine the registration transformation. The registration is usually achieved by transforming one image and measuring the similarities of all spatially corresponding voxel pairs of the two images. The optimization of the transformation parameters is performed by means of an energy or cost function representing similarity between the images and some kind of regularization. Whole-content based registration methods have been extensively used in a vast number of different medical image applications. The interested reader is referred to the exhaustive registration reviews available in the literature [177 ; 119 ; 159 ; 316 ; 217 ; 11 ; 301 ; 159].

The main advantage of feature-based methods concerns the reduction of the data involved in the registration procedure, leading to less expensive computational cost algorithms. On the other hand, the registration accuracy is frequently limited to the accuracy of the segmentation step. Furthermore, the selection of homologous, distinctive, reliable and stable features in both images to register remains a hard task to achieve, in particular in thoracic and abdominal (due to the large inter-patient variability) PET images (due to their low SNR quality). The main advantage of intensity-based methods over feature-based ones is the absence of the feature recognition step. Another advantage of these techniques is their robustness to the variations of input image nature, resulting in more flexible and application-independent registration methods than feature-based ones. On the other hand, the considerable computational cost associated to these methods has impeded their use in clinical routine, in particular in applications involving 3D images. Furthermore, these methods do not seem to be well-suited for multi-modal applications. In fact, whole-content based methods tend to get trapped in local minima of the chosen similarity criterion if they are not initialized within a relatively narrow range near the desired solution or if the imposed relation between grey-values of the images to register is slightly violated.

An interesting idea is to merge features with intensity-based methods in order to combine their associated advantages while cancelling their drawbacks. For instance, this strategy is proposed by Pluim et al. [216] in order to introduce spatial information obtained from image gradients in a whole-content based registration approach guided by the Mutual Information criterion.

2.3 Transformation

2.3.1 Classes of transformations

A spatial transformation model must be chosen in order to compensate differences between the features that represent images to register. The transformation will be applied to the *floating* image in order to map its information into the *reference* one. This spatial transformation model must be completed with an interpolation step in order to obtain an intensity mapping as well (see Section 2.3.3).

Several confronting factors influence the critical decision about the transformation model in a registration procedure. Some of them include: nature of the deformations to cope with; availability of robust prior information about the targeted transformation; desired result accuracy; and importance of the algorithm computational cost. The two former factors control the flexibility of the transformation model, while a trade-off must be taken between the accuracy of the desired solution and the computational cost of the algorithm. As a matter of fact, a high level of accuracy needs an elevated number of degrees of freedom in the transformation model that necessarily involves computational costing registration methods. The decision of the transformation model in medical image registration applications is also critical due to the non-unicity of the solution. As a matter of fact, different transformations can provide very similar results, as confirmed in the RIRE project [298].

The type of transformation can be classified according to three different criteria: influence area, nature of the model and geometry preservation.

The influence area criterion divides spatial transformations into two categories: *local* and *global*. A transformation is called *global* if it is applied to the entire image. On the other hand, when transformation parameters depend on the spatial location, this transformation is called *local*.

Concerning the nature of the transformation model, we distinguish *parametric* from *non-parametric* models. Non-parametric models consist in the direct computation of a displacement vector field applied to the entire image that transforms each point

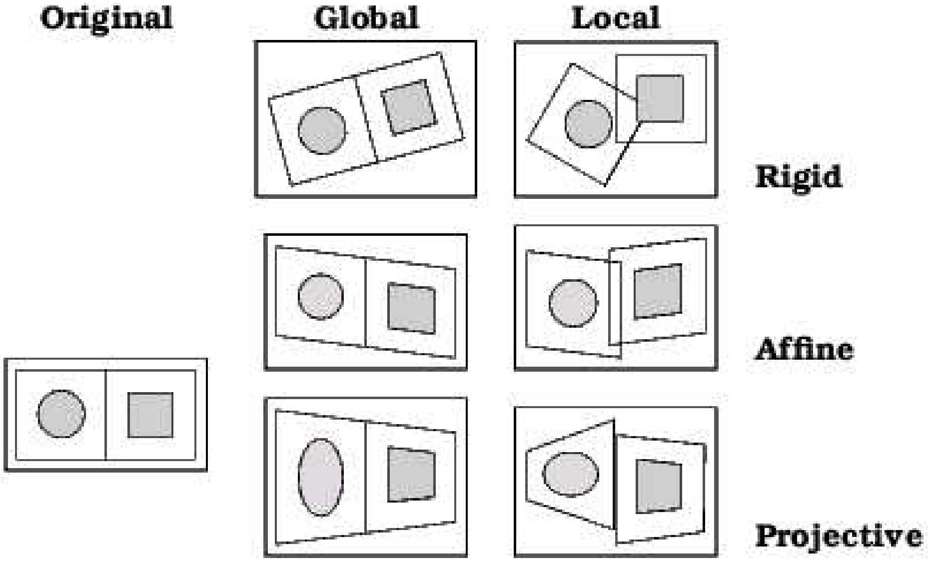

Figure 2.4: Synthetic example of linear transformations, from [175].

of the floating volume. On the other hand, a parametric transformation implies the optimization of a limited number of parameters of a given transformation model that furnishes the displacement for each voxel of the image.

Concerning geometry preservation, transformations can be categorized into *linear* and *non-linear*. A linear transformation maintains geometrical relationships between the structures. This category includes *rigid* (composed of translations and rotations), *affine* (rigid plus isotropic or anisotropic scale and skew, mapping parallel lines onto parallel lines) and *projective* (maps lines onto lines) transformations. The interested reader is referred to [89] in order to find a complete description of projective geometry. Figure 2.4 shows a synthetic example of linear transformations, including local and global behavior. Non-linear transformations possess more degrees of freedom, allowing to cope with more complex deformations associated to some body structures. They can transform a straight line into a curve, thus structures transformed in a non-linear way may not necessarily retain their shape. Registration methods employing these transformations include polynomials, Radial Basis Functions (RBF), Free-Form Deformations (FFD), Elastic Body Splines (EBS) and viscous models (some of these techniques are further detailed in Section 2.3.2). A recent survey of registration approaches focused on non-rigid approaches is proposed by Lester and Arridge [159].

Traditional registration methods apply rigid or affine transformations, which are useful in cases where rigid body assumptions are likely to hold and structures retain their shape during the registration procedure. Some examples include bone or brain alignment applications. Furthermore, linear registration methods have a small number of parameters to estimate, thus being fast convergence algorithms. However, for most body organs, many more degrees of freedom are necessary to accurately represent the anatomical movements due to their deformable nature. Moreover, linear transformations cannot account for morphological variability between different subjects, which is crucial in pre-operative, post-operative or atlas-patient registration applications. Deformations involved in our particular application has a non-linear nature. Therefore, the next section details some non-linear transformations frequently used in registration applications.

2.3.2 Non-linear transformations

In general, non-linear transformations are represented by means of a dense deformation field and a displacement vector δ is associated to each point of the feature or volume to transform:

$$x' = x + \delta(x) \tag{2.2}$$

In order to compute the displacement $\delta(x)$ for each point of the volume, the majority of methods optimize a cost function composed of a data fitting term and a regularization term to ensure the local continuity of the transformation [11]:

$$\hat{T} = \arg\max_{T \in E}(E[S(x + \delta_T(x), x')] + E[\delta_T]); \tag{2.3}$$

where $E[S(x+\delta_T(x), x')]$ is the data fitting energy associated to the similarity function S, and $E[\delta_T]$ is the regularization energy over the class of transformations ($\delta \in T$).

Non-linear transformations may differ by several aspects, such as the degree of elasticity and constraints of the deformation model. In order to model severe non-linear deformations, the transformation model needs a high number of degrees of freedom. If this transformation is computed only from information provided by the images to register, this problem is ill-posed in in Hadamard's sense. The introduction of additional constraints is required in order to assure the uniqueness of the solution and have a well-posed problem. The regularization of the transformation can be either constrained by underlying physical models of material properties (*realistic* models) or by free-form constraints (*free-form* models), were any deformation is allowed, even if this deformation can be based on a physical model which may not necessarily conform to any known behavior. Some classical non-linear transformations that have been extensively used in registration applications are detailed below.

Radial Basis Functions (RBF)

Radial basis functions [3 ; 243] (or particle models in computer graphics), formulate the transformation as a linear combination of basis functions. In general, registration methods based on RBF use control-points derived from corresponding anatomical features (*landmarks*). Then, the RBF map each control point in one image to its homologous in the other one and provides an interpolation of this mapping at intermediate points. Each basis function can be expressed as a combination of a polynomial that provides the global component of the transformation and a sum of a weighted elastic or non-linear basis function RBF are then a linear combination of radially symmetric basis functions, each centered on a control point.

Different basis functions can be used in this technique to guide a registration algorithm and some examples are Multiquadrics [112], Gaussians [3], Wendland's functions [95], and Thin-Plate Splines [111 ; 27]. Nevertheless, several studies [107 ; 300], aiming at comparing the performances of different Radial Basis Functions, conclude that Thin-Plate Splines have favorable properties for image registration.

Thin-Plate Splines (TPS), is a particular case of RBF that employs splines as basis functions. The use of TPS for medical image registration has been introduced by Bookstein [27]. An exhaustive review of medical image registration methods based on TPS can be found in [235]. The transformation produced by these basis functions is expressed differently in all three dimensions by means of linear combinations of mono-dimensional splines. Knowing the position of the corresponding pairs landmarks in both images, the TPS forces the transformation to superimpose them by means of either an exact interpolation [107] or an approximation computed with a mean square algorithm [237].

An interesting characteristic of these techniques is that the geometry of the control point grid has no restrictions, i.e., it can be sparse and irregular. On the other hand, a high number of control points and well-distributed in the image are required in order to assure acceptable registration results. The selection of these control points in a simple and robust way remains a difficult problem in some images such as PET ones. Furthermore, if the number of control points is elevated, this technique is very expensive in computational terms. Another problem associated to TPS concerns their infinite support because it impedes a local control of the deformation, thus limiting its use in certain applications.

Free-Form Deformations

Free-Form deformations (FFD), introduced by Sederberg et al. [253], also models the transformation by means of a linear combination of spline basis functions. In this technique, deformations of the object volume are achieved by tuning an underlying mesh of control points, but unlike the case of TPS, FFD employs a grid of control points distributed in a regular way on the image. Control point displacements are interpolated to obtain a smooth and continuous C^2 transformation. There are two major advantages of FFD with respect to TPS: the absence of a control point detection phase; and a local control of the deformation due to their limited support. Nevertheless, this local control depends on the nature of the chosen basis function. For instance, if cubic B-spline basis functions are used, we will obtain a more local control, at the expense of a higher number of control points in the FFD grid. On the other hand, if Bernstein basis functions are employed, a lower number of control points is required, but we will obtain less local deformations as well. In medical applications involving elastic deformations in which a high local control is desired, B-splines is the most frequently used basis function [76 ; 123 ; 190 ; 250 ; 234 ; 241]. Further details of this technique are discussed in Section 5.4.1.

Elastic models

Elastic registration methods, introduced by Bajcsy et al. [7], are based on physical models of the behavior of elastic materials under the influence of external forces. The behavior of the deformation is composed of two terms: the set of external forces applied to the image, aiming at superimposing the homologous structures; and a set of internal forces of elasticity, induced by the characteristics of the material in answer to the external forces. The non-linear transformation will describe the equilibrium state between these two forces, and can be obtained in an iterative way, as the deformation field that solves the linear partial differential equations (PDE) of Navier [280]. In a registration algorithm, the external forces are defined as a function of a given similarity criterion, and the feature matching and mapping are performed simultaneously. Elastic registration methods have mostly been used in brain image-to-atlas registration applications [8 ; 71].

The main drawback of this technique is that it cannot deal with severe deformations because it is constrained by the internal energies. Nevertheless, multi-resolution approaches or prior global registration techniques can be used in order to solve this problem.

Fluid models

Fluid techniques can deal with severe local deformations, unlike elastic methods. This non-linear transformation model is based on physical laws that provide an unconstrained model which allows free deformations similar to the behavior of viscous fluids [158]. The floating image is modeled as a viscous fluid which gradually deforms over time to match the reference image. Fluid models are frequently used in medical image registration [34 ; 51 ; 70]. A comparison between different fluid-based techniques can be found in [302].

Several drawbacks are associated to this transformation model. Since a high non-linear equation has to be solved, the solution must be approximated, thus involving excessive convergence times. Furthermore, global behaviors are not taken into account by using this transformation, but this problem can also be overcome by using multi-resolution approaches or prior global registration algorithms.

The combination of fluid models with other transformation techniques has been largely proposed in order to overpass their limits. For instance, several authors [157 ; 52] have mixed elastic or radial basis functions with fluid models, producing *viscoelastic* approaches in order to compensate drawbacks associated to each method.

Physical models

Physical or behavior-based deformable models, unlike elastic and fluid techniques, use actual physical models of change, describing behaviors by means of partial differential equations. They mimic the actual behavior of a specific region of the body, thus being very application-depended. For instance, Bro-Nielsen [35] employs this technique in order to model bone growth between time sequences of human mandibles.

A drawback of this technique concerns the difficulty of modeling and dealing with temporal or inter-subject registration due to the high variability of deformations involved in these applications.

Other methods

Two examples of other interesting non-linear registration methods are the optical flow [127] and the *Demons* [277 ; 278] techniques, that have been widely used in medical applications.

The optical flow technique uses an intensity conservation hypothesis in order to compute the displacement field between the images to register. A good review of these techniques can be found in [152]. Some improvements of this technique has been proposed in order to bypass its problems associated to the hypothesis of intensity conservation. Hellier [115] replaces the quadratic cost term of the function with robust estimators in order to make the algorithm more robust with respect to outliers.

The *Demons* algorithm, introduced by Thirion et al. [277 ; 278], is based on the search of attraction or repulsion forces between points belonging to the contour of the structures to register. A Gaussian regularization embedded in a multi-resolution procedure is used, equivalent to a dense field regularization by means of a linear elasticity [34]. Roche [227] has adapted this technique in order to deal with registration of multi-modal images.

2.3.3 Interpolation and resampling

An interpolation step is required in order to complement the chosen spatial transformation model. The interpolation technique must provide the value of the reference image at the position where the transformed voxel has arrived. This interpolation phase will have an important impact in terms of computational time and result accuracy of the registration system, thus a trade-off between both aspects must be taken. This impact is due to the high number of times that the interpolation step is employed during the registration process. At the end of the system, a final interpolation is required to yield the final registered image, but this task is only performed once, thus a more complex interpolation method can be adopted.

Several interpolation algorithms, based on different approximations of the sinc kernel (ideal one) with bounded support, has been proposed in registration applications such as nearest-neighbor [230 ; 171], bilinear and cubic functions [206 ; 304], quadratic [124], cubic [276 ; 189] and higher-order splines [155], Gaussians [2], truncated sinc functions [275] and others. Nearest Neighbor (NN) and linear (TRI) interpolation methods are the simplest and quickest between these interpolation techniques. They represent a good choice when the computational time is the most important requirement, at the expense of increasing interpolation artifacts that can introduce mismatches in the registration procedure. Partial Volume (PV) interpolation was proposed by Collignon [59] in order to overcome these drawbacks when constructing the joint histogram in registration methods using statistical similarity measures. Several interpolation comparative studies can be found in the literature [108 ; 154].

2.4 Similarity criterion

The similarity criterion evaluates the quality of the registration result accuracy of a given transformation comparing the reference image with the transformed floating one. If the similarity between these images is not accurate enough, the registration procedure must produce an alternative transformation in order to obtain a better similarity between both images to register. Consequently, the transformation will be optimal when the similarity measure reaches a global maximum (or minimum depending on the optimization implementation).

A distinction must be made between similarity criteria used in feature-based and full-content based approaches, because of their different nature.

2.4.1 Feature-based algorithms

Similarity criteria associated to feature-based algorithms can be divided into two categories [175]: *rigid* and *deformable.*

Rigid criteria have in general a Euclidean nature [11]. Distances, areas and volumes are included between the similarity measures that are applied to segmented features obtained from the images to register. Some of the most popular registration methods using rigid similarity criteria include nearest-neighbor based approaches (Procrustean-based [84 ; 93 ; 105] or ICP [16 ; 314 ; 151]), probabilistic models [296 ; 69 ; 54], the head-hat algorithm [208 ; 48] and Chamfer distance-based [29 ; 19 ; 184] techniques.

Feature-based registration methods using deformable criteria typically employ *active contours* or *snakes* in order to make contours of the structures in the floating image evolve towards contours of their corresponding structures in the reference image. Further information about deformable models can be found in Section 4.2.3. A drawback of deformable models is the requirement of a good initialization in order to assure a good convergence towards desired contours in the reference image, having difficulties to cope with severe deformations. On the other hand, deformable models are well suited for registration applications involving local curved transformations, such as in inter-subject and patient-atlas applications.

2.4.2 Whole content-based algorithms

In whole-content based registration methods, the similarity criterion is based on the assumption that some kind of dependency exists between the set of intensities of both images. As a matter of fact, it supposes that a given anatomical structure falls into a certain range of grey-values in both imaging modalities, and that it is possible to model the relation between these sets of grey-values. This relation obviously depends on the imaging modalities involved in the registration procedure and it is more complex to model it in multi-modal applications.

The choice of the similarity measure is a critical decision in registration algorithms because of the difficulties to model this relation and the high impact of this step in final results. Furthermore, a trade-off must be taken between the accuracy of the results and the computational complexity and robustness. Some similarity measures are very general and complex but are difficult to optimize, leading to high convergence times. On the other hand, general similarity criteria can be used in different applications without algorithm redefinition.

The assumed dependency between the intensities of the images to register can be *functional* or *non-functional*, according to how much constrained is this relation.

Functional relation

These similarity criteria measure the functional (linear or non-linear) dependency by comparing the intensities of corresponding voxels in the images to register. Several of these similarity measures have been proposed to guide registration procedures, differing by the constraints imposed on the functional relation between the intensities.

The simplest similarity measures consist in directly analyzing the difference between the corresponding voxel intensities. The Sum of Squared Differences, the Mean Square Error, the Mean Square Differences, the Sum of Absolute Differences [122 ; 153] or the Stochastic Sign Change [122 ; 153] are examples of these measures.

The second important group of functional-relation similarity criteria is composed by correlation-based measures. If the images to register only differ by a linear relation between the intensities and an additive Gaussian noise, these measures can efficiently estimate their similarity. The normalized cross-correlation (NCC) coefficient [153 ; 221] is the most popular version of these measures. A weakness of this technique is that it is not robust enough with respect to the presence of local distortions or outliers in the image. Furthermore, the search for the optimal registration is difficult due to its narrow peak in the correlation space. Despite these drawbacks, these measures are frequently used, in particular in mono-modal applications, due to their easy implementation.

Several improvements of this technique can be found in the literature. Roche et al. [228 ; 229 ; 109] have introduced the correlation ratio that deals with the intensity differences between multi-modal images, by assuming a non-linear function between them. They claim better performance of this criterion over other statistical measures in certain registration applications because the correlation ratio takes into account proximity in the intensity space, resulting in higher robustness at relatively low resolution and in attractive computing time.

An interesting option to explore, if fast-to-compute measures are required or if the images are influenced by a frequency-depended noise, is the use of Fourier methods [316], which represent the images in the Fourier space. The Fourier Shift Theorem [33] is used to guide a phase correlation method and it computes the cross-power spectrum of both images to register and search the peak corresponding to the correct registration on its inverse.

Non-functional relation

In multi-modal registration applications, the assumption of a functional relation between the intensities of the images to register is not further valid or at least very difficult to model. Furthermore, some mono-modal applications may also require non-functional dependency because of intensity changes between both image acquisitions (for instance, after administration of a contrast agent).

Even if image intensities corresponding to the same structure may be very different depending on the imaging modality, they are not completely independent because they represent the same underlying physical reality. In fact, a statistical relation between the two sets of intensities can be assumed because the availability of information about a given region in one of the images will necessarily reduce the uncertainty about the same region in the other image. Based on this principle, several statistical similarity criteria have been proposed to evaluate registration result accuracy.

Woods et al. [304 ; 305] were the first to introduce a similarity measure adapted to multi-modal images, which is based on the following hypothesis: a given anatomical region having a more or less homogeneous set of intensities in one image corresponds, after a registration procedure, to a regular region in the other image, also having a limited variation in its voxel intensities (but probably in a different grey-level range from those of the first image). Then, the ratio of the intensities for all homologous points in a given region in each image will vary little and the average distance of this ratio for all regions may be minimized to achieve registration [217]. Woods obtains good registration results on a PET-MRI brain application with an accuracy of 2mm.

Based on the work of Woods, Hill et al. [121] propose an adaptation of the algorithm using the *joint histogram* of the images. Hill and colleagues have observed that the behavior of the joint representation of the intensities reflects the mismatching between the images. In fact, they postulate that when a joint histogram of two images is more dispersed, the misalignment between them is high. Starting from this idea, Hill et al. [120] employ the third-order moment of the joint histogram of two images, which represents the skewness of the distribution, in order to guide the registration procedure.

The use of the n-th order moment of the joint histogram as a measure of dispersion is equivalent to a generalized version of the joint entropy [171]. Collignon [59] and Studholme [270] were the first to propose the *entropy* as a similarity measure of the correspondence of two images due to the capacity of the entropy of adequately measuring the dispersion of the joint histogram. In fact, a dispersed histogram (and consequently, a misregistration) produces a high entropy while an histogram with a few number of sharp peaks (and then, well-defined correspondences between intensities) provides a low entropy. Shannon entropy [259] is the most widely used in entropy-based registration algorithms. Nevertheless, alternative entropy formulations have been also proposed such as Jumarie entropy [230 ; 135], Renyi entropy [130 ; 168] or f-entropies [239 ; 212 ; 200], to overcome some drawbacks associated to Shannon's expression of the entropy.

Mutual Information (MI), simultaneously proposed by Viola [292] and Collignon [59], has represented a step forward in the use of entropy-based measures on image registration. It expresses the quantity of information remaining in one of the images to register knowing the other one, which is maximal when equivalent data sets are correctly registered. A good property of this similarity criterion is its flexibility to deal with a high variety of applications and images. As a consequence, Mutual Information has been used in a large number of different registration applications, as illustrated in an exhaustive review performed by Pluim et al. [217] about these techniques. Further details about Mutual Information can be found in Section 6.3.

The main advantage of entropy-based similarity measures is that the weight accorded to each voxel is independent of its intensity. This allows these measures to be only influenced by the statistical properties of the joint probability density function of the intensities. This makes these approaches very appropriate for multi-modal applications where the relation between intensities is not functional.

A good review including other similarity criteria used in image registration can be found in [244], where a high number of different measures coming from different fields are presented. Some of these measures include: matched filters, optical flow computation, grey-level variance in segments, gradient differences, normalized standard deviation, cosinus criterion, divergences, distance to the independence, pattern intensity, convolution,... Another comparison study between different similarity measures can be found in [209].

2.5 Optimization

The optimal parameters of the chosen transformation model must be determined. This can be seen as a multi-dimensional optimization problem in which the degrees of freedom of the transformation will define the dimensionality of the situation. These optimal parameters are assumed to produce the transformation that best aligns the images to register. In the case of registration applications, the cost function to optimize is usually composed of a dissimilarity term based on the selected similarity criterion, and a regularization term that constrains the search in the parameter space.

Two possible approaches can be considered to obtain the optimal transformation parameters, either by means of an *exhaustive* search or by means of an *iterative* search of the optimum of the cost function in the parameter space. The former technique determines the parameters in a direct way and it assures the obtention of a global optimum but it is very expensive in terms of computational cost. Due to the high complexity of non-linear transformation models and similarity measures, the second approach is the most common one.

It would be desirable that the cost function to optimize is convex, continuous and of class C^1, in order to guarantee a good behavior of the optimization step. In general, the similarity function is quasi-convex [175] and most of the classical optimization methods can be used. Nevertheless, it normally lacks of smoothness and several local minima that could disturb registration results frequently appear. These local minima can occur for several reasons [217] such as a local good match, errors due to the choice of interpolation, distortions induced by noise and artifacts or overlap change. Some solutions have been proposed in order to minimize the number of local minima: pre-processing; noise and artifact elimination; the employment of higher-order interpolation methods; the normalization of the similarity criterion by the overlap region; or the use of a constrained search space for transformation parameters.

Among the vast literature of optimization methods, the most popular in medical registration applications are the *quadratic* or *semi-quadratic* approaches. These methods assume the quasi-convexity of the cost function around the optimal solution. The popularity of these approaches is due to their good performance in a well constrained situation, such as in a registration case [11]: high similarity between homologous features, adapted cost functions, quasi-unicity of the solution (if the search space is limited), initialization close to the final solution, ...

A simple classification divides quadratic optimization methods in those that require function derivatives, and those which do not require them. The exact or approximate computation of the cost function gradient implies higher computational costs than a simple evaluation of the function. Optimization methods based on the Hessian matrix are even more expensive in computational terms. On the other hand, these methods compensate this drawback with a fast and robust convergence towards the desired solution once the gradient or the Hessian are already computed. Furthermore, they are less sensitive to local minima than optimization methods that do not require function derivatives. The choice between these two types of optimization methods will depend on the application requirements in terms of accuracy and computational cost, and in the availability or not of the cost function gradient. Some examples of optimization methods that do not require function derivatives include the Downhill Simplex [223] and the Powell [220] techniques. With respect to optimization methods using derivate functions, some of the most popular in registration algorithms include the steepest and conjugate gradient-descent, Newton-based, the Gauss-Newton and the Levenberg-Marquardt [276 ; 173] techniques. The majority of cited optimization methods are well detailed in [223]. A comparison of the performance of some of these optimization methods can be found in [125 ; 170 ; 244].

Other optimization methods have been occasionally used in certain image registration applications. Simulated annealing [201 ; 226 ; 264], genetic methods [40 ; 120 ; 131], stochastic search [292 ; 195] or heuristic methods [88 ; 156 ; 180] are some examples of these alternative optimization techniques.

Several improvements on these optimization techniques can be found in the literature in order to improve their performance in terms of accuracy, robustness and computational cost. Some of the most frequently used in registration applications are multi-resolution (*pyramids*) approaches, multi-scale schemes or the combination of different optimization methods.

Pyramid schemes start by performing the optimization of the transformation parameters at a coarse resolution, which initialize the optimization at a finer resolution stage of the pyramid, then refining the previous estimation, until reaching the sampling of the original image. Different techniques have been proposed in order to construct the pyramids. Gaussian pyramids [176 ; 162 ; 39], local averaging [29 ; 304], wavelets [224 ; 182 ; 78] or spline pyramids [288 ; 287] are the most commonly used. A good review of these hierarchical methods can be found in [159]. Multi-scale schemes consist in increasing the transformation complexity instead of modifying the image resolution. In fact, the majority of registration methods use this strategy when they first compute a linear transformation followed by a non-linear one. But some authors have also introduced a hierarchy scheme in the non-linear phase [268 ; 45 ; 234 ; 166]. Finally, another possible improvement is based on the succession of several optimization methods using fast and rough methods to obtain a first estimation of the initial position, followed by more accurate and slower optimization techniques to refine the result. Several combinations of methods are possible but Powell's method is frequently used in the first stage [136 ; 231 ; 133].

2.6 CT-PET registration bibliography

Brain regions

Even if the main subject of the presented work is focused on thoracic and abdominal registration applications, some references of CT-PET registration methods applied to brain images are given as complementary information.

In brain image registration involving PET imaging modality, anatomical information is usually provided by MR images due to their better quality with respect to CT ones in these regions. Nevertheless, some works have been published in the CT-PET brain registration context [48 ; 295 ; 38 ; 58 ; 175]. The registration literature in brain MR-PET imaging is very large. Several of the most popular registration methods have been evaluated in the Retrospective Registration Evaluation Project (RREP) [298]. Registration techniques involved in this project only provide linear transformations. Other useful and non-linear registration methods for brain MR-PET images can be found in the classical reviews on image registration [177 ; 159 ; 316 ; 217].

Thoracic and abdominal regions

A registration method applied to thoracic and abdominal regions is more complex than methods for brain regions due to the higher severity of the deformations in these zones. Additional problems appear when working in multi-modal applications, in particular involving functional images. Some registration methods have been proposed in order to overcome these difficulties.

Some of these registration techniques employ linear transformations in these regions. Wahl et al. [295], aiming at registering PET with either CT or MR thoracic images, use a 2D rigid, point-based method. Yu et al. [312] match PET and CT images using a 2D rigid surface-based algorithm. A registration surface technique based on the Chamfer distance is the choice of Cai et al. [42] in order to achieve a thoracic CT-PET matching. Parsai et al. [207], in another surface-based approach, use the ICP algorithm in a CT-SPECT thoracic and abdominal application. Maes et al. [172] proposed a fully automatic affine geometric registration method based on Mutual Information. It is applied to thoracic CT and PET images and on other multi-modal applications. As mentioned in Section 2.3, linear transformations are not as well adapted to registration of thoracic and abdominal images as non-linear ones.

Sato et al. [246] propose a point-to-point based matching methodology that uses the Cauchy-Navier spline transformation to model the deformable anatomical behavior associated with non-rigid thoracic medical image registration. This transformation is applied to landmarks extracted from both images. The main drawback of this method is the high computational cost associated to the optimization of the cost function.

Meyer et al. [194] apply a Mutual Information-based registration algorithm in thoracic CT-PET images. They employ a full affine mapping and a five-point Thin-Plate Spline (TPS) warped registration technique. Furthermore, this technique is also used in a CT-SPECT abdomen application. The major drawback of this method is the manual selection of the control points required for the TPS model.

In a similar method, Slomka et al. [263] propose a registration strategy divided into four steps: a first step consisting of a 9-parameter linear multi-resolution registration based on Mutual Information between the CT image and a combination of the emission and transmission PET scans; the next step concerns the automatic lung contour detection in CT and transmission PET images; afterwards, a large number of corresponding control points are computed on the detected lung contours by means of a ray-tracing technique from the centroid of the lungs and outside the body; finally a TPS interpolation algorithm from the corresponding control points is used in order to furnish a dense non-linear transformation. The main drawback of this approach concerns the selection of the control points, which in our opinion, is not optimal. Furthermore, there is a lack of information in the regions far away from lungs and body contours (even the information of the inside of the structure is not taken into account). Finally, the use of TPS transformation model does not assure a local control of the deformation, which is required in thoracic regions.

Tai et al. [273] have developed and evaluated a non-rigid CT and whole-body PET registration method. Registration is performed following a multi-stage procedure: mask on transmission images; compensation of linear attenuation coefficients of different energy spectrums; and linear and elastic transformations.

Erdi et al. [87] also employ the transmission PET image to guide the registration with the CT image in a thoracic application, based on the Mutual Information measure.

One elegant solution to the registration of chest CT and transmission PET images was proposed by Mattes [188 ; 190]. They model deformations with cubic B-splines defined by placing a regular grid of control points over the transmission PET volume and then modified by moving the control points. Mutual Information is used to measure image similarity, computed by means of a Parzen window technique. The optimization procedure is based on a hierarchical multi-resolution approach. The authors point out that obtained results are not completely satisfactory on more deformable regions such as the diaphragm or the abdomen. Based on Mattes' work, Delzescaux et al. [76] studied the influence of the CT respiration phase and the Free-Form Deformation (FFD) model ability to cope with non-linear deformations due to respiration movements. They propose to transform the CT image instead of the PET one in order to preserve the metabolic information provided by PET images, this approach being well-suited for radiotherapy applications. Carlsen and Wischmann [43] also proposed a FFD-based procedure using a CT-derived pseudo-transmission image to compute a non-linear transformation based on tri-cubic B-splines

All previous non-linear techniques (except that one proposed by Sato [246]) assumes a linear relation or even no deformations between emission and transmission PET scans. This hypothesis is not always accomplished because emission and transmission images are not acquired in a simultaneous way. Apart from little differences that can appear in cardiac regions, the main danger of this assumption concerns pathologies or tumors that are only visible in emission PET images. Using only the transmission PET scan to guide the registration process, tumors shall not take into account. Furthermore, the liver can not be distinguishable from the surrounding structures in transmission PET scans, therefore, these methods cannot be used in abdominal registration applications. Figure 2.5 illustrates uptake differences between emission and transmission PET scans that can influence considerably in the registration with the CT image.

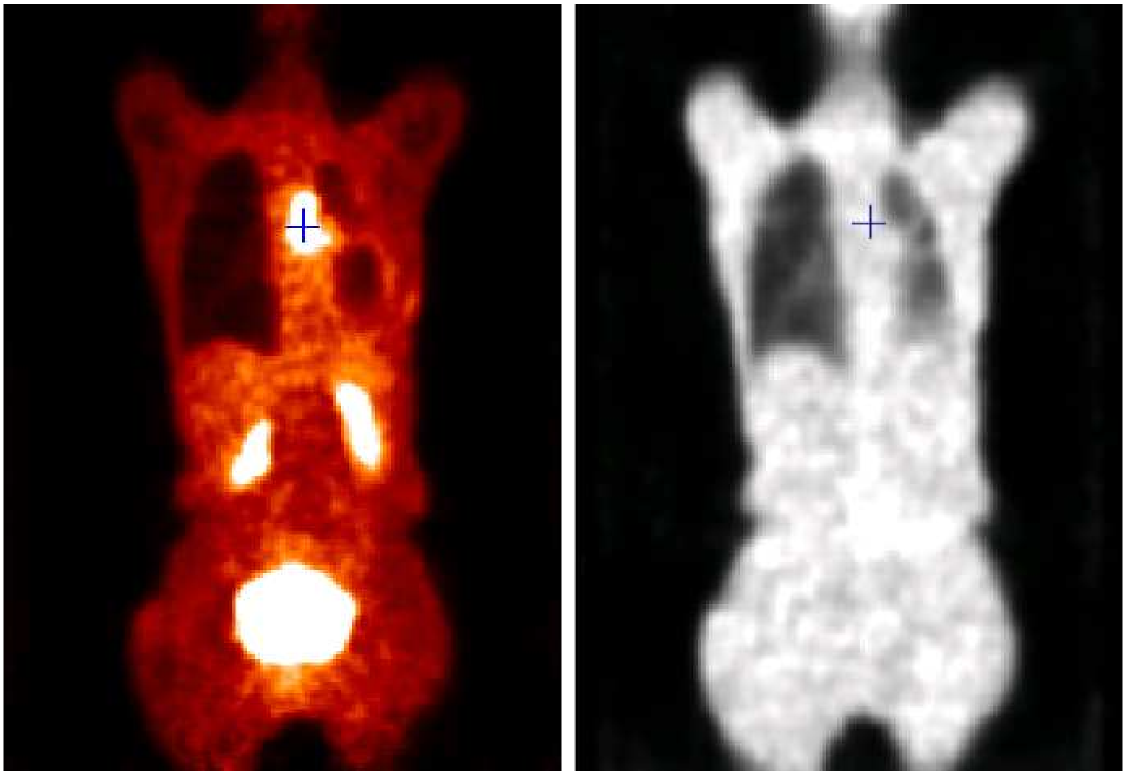

Figure 2.5: Coronal slices showing uptake differences between emission and transmission PET scans. Left: emission PET scan. Right: transmission PET scan. The blue marker is placed in a tumoral region. In the transmission PET image, tumor, kidneys and liver are not as well contrasted as in the emission PET scan.

With respect to precedent FFD-based registration techniques, none of them directly work on emission PET scans due to their low SNR quality and the lack of constraints on the FFD transformation model. As a matter of fact, when working with emission PET images, these approaches tend to get trapped in local minima of the chosen similarity criterion if they are not initialized within a relatively narrow range near to the final solution. This point is further discussed in Chapter 3.

In the particular case of abdominal images, SPECT images are sometimes used instead of PET images. An affine point-based transformation is used by Kaplan et al. [138]. Kramer et al. [146] propose a 2D polynomial-based technique in a CT and MR-PET thoracic and abdominal image registration application. A similar low-degree polynomial-based technique is introduced by Maguire et al. [174] to match CT and SPECT images of the abdomen. Concerning the same application, Koral et al. [145] propose a Mutual Information-based registration approach. Scott et al. [251] use a rigid surface-based technique combined with manually segmented contours of the CT image to achieve a MR or CT-SPECT image registration application focused on the lower abdomen. Studholme et al. [271] apply a rigid transformation computed by means of a Mutual Information-based approach to match MR and PET images of the pelvis. Pérault et al. [222] compute an affine point-based transformation to register CT and SPECT pelvic images. Sjögreen et al. [262] use a rigid method based on the principal-axes technique and optimized by means of the cross-correlation similarity measure in a CT-SPECT kidney registration application.

In another context, General Electric provides a semi-interactive non-linear registration method, called *Advantage Workstation Fusion software*, in the stations furnished in conjunction with the PET-CT combined systems. The goal is to correct the possible differences that still exist in the images provided by combined CT/PET machines. The algorithm is not well explained in its corresponding site [2], but it seems to create a model for the CT and PET transmission images using a six degrees of freedom transformation.

2.7 Conclusions

The different possible choices for each aspect of a registration system have been briefly presented. The first conclusion that can be drawn is that no registration methodology is universal or well-suited for the broad range of registration applications which exist due to their different requirements in terms of accuracy, robustness or computational cost. Furthermore, some studies such as the RREP project [298] have proved that different registration strategies applied to the same images can lead to very similar results. Therefore, the choices for each aspect of the registration technique shall be taken according to the particular characteristics of the images involved in the process and the constraints imposed by the application (see Section 2.1.2 and 1.3.1). A discussion about each phase of a registration system with respect to our application is presented below.

Image representation We recall that registration methods can be classified into two categories with respect to the image representation aspect: *feature-based* methods; and *whole-content* based methods. Due to the low SNR quality of emission PET scans, the presence of severe deformations in thorax and abdomen and the lack of linear correspondences between the intensities of homologous regions, a whole-content based approach could rarely provide satisfactory enough registration results without additional prior information. In our application, some thoracic and abdominal structures can be more or less easily recognized in CT and PET images, and these anatomical features could be used to guide the registration procedure. Nevertheless, the number

---

[2] `http://www.gemedicalsystems.com/rad/nm_pet/products/workstation/aw_fusionsw.html`

of these structures is limited and using only this feature-based strategy we will not take into account local deformations far away from the recognized structures or even those in the inner parts of the structures, leading to misregistrations. In consequence, we propose to merge the advantages associated to each one of these strategies, using a feature-based phase to incorporate prior information in a whole-content based registration method, as detailed in Section 3.2.

Transformation In Section 2.3.1, we have divided the type of transformation according to three different criteria: influence area, nature of the model and geometry preservation.

Concerning the influence area criterion, a combination of local and global transformations becomes necessary in order to model the different deformations of the thoracic and abdominal structures between CT and PET images. For instance, differences in scan formats such as size, resolution or field of view influence the whole scans while movements due to cardiac cycle are only suffered in a local zone around the heart. As a matter of fact, since macroscopic features are generally more stable than microscopic ones (for human anatomy), it is always better to recover first global deformations and in a later stage, local ones.

The geometry preservation criteria divides transformations into linear and non-linear. As mentioned in Section 2.3.1, linear transformations are appropriate in registration applications where rigid structures are involved such as the head. A limited number of parameters have to be estimated and thus, low time-cost procedures, well-suited for clinical routine use, are obtained. Thoracic and abdominal structures undergo complex deformations due to respiratory and cardiac cycles and other physiological processes that cannot be classified as rigid or linear ones. Moreover, the time passed between both scan acquisitions induces long-term differences in the structures that cannot be either modeled in a linear way. On the other hand, computation times of non-linear transformations are usually too high (due to the high number of parameters to estimate) in order to be used in clinical routine.

The particularities of our application force us to use local and non-linear techniques, but it do not impose any constraint on the use of parametric and non-parametric transformation models. In theory, non-parametric techniques are better suited than parametric ones in some situations where the studied organs are very deformable [152 ; 197]. Moreover, they allow a high control of the regularization term, thus permitting the the presence of discontinuities in the deformation field. This characteristic could induce problems (it may violate the local continuity and bijectivity of the transformation) in the interfaces between organs but it will represent the complex nature of body structure movements in a more accurate way. On the other hand, these approaches are in general more expensive in terms of computation time than parametric techniques. Furthermore, a parametric transformation model with an enough number of parameters and local control of the deformation can also provide accurate results while assuring smooth transformations.

Due to the non-unicity of the solution in medical image registration applications, the decision of the transformation model will be taken according to the particular requirements of our application: a high number of degrees of freedom to cope with large and local deformations; and a reasonable computational cost.

Elastic, fluid, visco-elastic and physical models are limited by their time consuming nature due to the regularization phase and therefore they are not well-suited in our application. Moreover, this regularization stage does not guarantee that the deformations are correct, even if they are constrained to be realistic (based on the particular characteristics of a given material). Radial Basis Functions methods are less accurate than realistic approaches mentioned above, but they perform better in terms of computational cost, being able to be used in clinical routine. The principal drawback of these methods is the selection of control points that guide the transformation computation, in particular in our application due to the lack of stable and reliable anatomical landmarks in PET images. Free-Form Deformations (FFD) bypass this problem by using a regular grid of control points superimposed on the floating image, without a previous segmentation step. Furthermore, this model is very flexible because no assumptions on the underlying anatomy are made, thus allowing to deal with the great variability of the anatomical structures in the thoracic and abdominal regions. Another good property of this deformation model is that it has a limited support, i.e. it furnishes a local control of the deformation, which contributes to reduce significantly the amount of computation needed during the optimization process. Registration algorithms based on a FFD model with B-spline functions have been proposed in a wide variety of medical applications [76 ; 123 ; 190 ; 250 ; 234 ; 242] in which structures suffer local and non-linear deformations between the images to register. Even if FFD have been mostly used in *almost* mono-modality applications [3], our methodology will be based on this transformation model, as is further detailed in Section. 3.2. Nevertheless, we will need to adapt this model in order to overcome problems associated to this transformation model when used in multi-modal applications.

Similarity measure In Section 2.4, the two main approaches with respect to the similarity measure have been presented: methods assuming a functional relation between the set of intensities of the images to register; and statistics-based similarity criteria. In CT and PET applications involving thoracic and abdominal regions, no prior information about the relation between the intensities is available, thus statistics-based approaches seem to be better suited than functional-based ones. Among the statistics-based methods, the ones based on Mutual Information (MI) are the most advanced and generally applicable. Therefore, in multi-modal medical image registration applications, these approaches have become a standard reference. Nevertheless, MI-based methods have proved to fail in certain situations due to the presence of local or spurious global maxima of the cost function to optimize. The use of multi-resolution techniques or the combination of MI-based methods with feature-based ones can limit these failures.

---

[3] It means that FFD have not been tested to register anatomical and functional images. To our knowledge, they have only been used in anatomical registration applications (CT-CT, MR-CT, CT-transmission PET scan).

Optimization This registration stage is completely dependent on the choice made in the precedent three phases. The optimization method must be chosen according to the cost function nature, the availability or not of its gradient and the time constraints of the targeted application.

Part II

Proposed methodology

CHAPTER 3

Initial tests and proposed methodology

Contents

This chapter presents the methodology we propose to register CT and emission PET images of thoracic and abdominal regions. First, in Section 3.1, some results applying linear and Free-Form Deformation registration techniques to our images are shown. The poor quality of the results obtained by these methods justifies the development of a new registration approach dedicated to our application. The proposed methodology is detailed in Section 3.2.

3.1 Initial tests

In Section 2.7, we have reached several conclusions about several parts of the registration methodology we need to develop, but some questions remain unanswered.

Things are clear concerning the need of a non-linear transformation and the use of Mutual Information (MI) as similarity criterion. The choice of a Free-Form Deformation model over other techniques as non-linear transformation has been justified in Section 2.7. Nevertheless, we need to verify if a whole-content based approach may provide satisfactory enough registration results or if it needs additional prior information in our application. In theory, this approach has difficulties to deal with the low SNR quality of emission PET scans, the presence of severe deformations in thorax and abdomen and the lack of linear correspondences between the intensities of homologous regions. In the following sections, we show some initial tests we have performed in order to answer this question and to better identify the challenges of our registration application.

3.1.1 Linear registration

Even in registration applications requiring non-linear deformations, linear transformations are very helpful and they are mostly used to initialize posterior non-linear stages. They can cope with larger and global deformations, leaving more local ones to more accurate transformation models. Therefore, in these initial tests, we have used an affine (12 parameters) registration algorithm, based on MI, in order to better identify regions that undergo large non-linear deformations and to observe the difficulties of a linear model to cope with them. The Powell optimization method [220] is employed to obtain the transformation parameters. Similar strategies have been successfully used for the registration of rigid structures (bone, brain). The interested reader is referred to the survey on MI registration methods proposed by Pluim et al. [217] for a complete list of these works.

Figure 3.1 shows results obtained by this linear registration algorithm in a thoracic case. We can observe huge differences between the CT and the linearly registered PET images, in particular around the diaphragmatic wall, i.e. the lower part of the lungs or the upper part of the liver. This zone suffers severe non-linear movements due to the respiratory cycle (in this case, CT was acquired in a single breath-hold at full inspiration), mostly in the z axis, as seen in Figure 3.1. Nevertheless, in more rigid regions such as the upper part of the lungs, the skeleton or the kidneys, the linear registration algorithm provides correct correspondences.

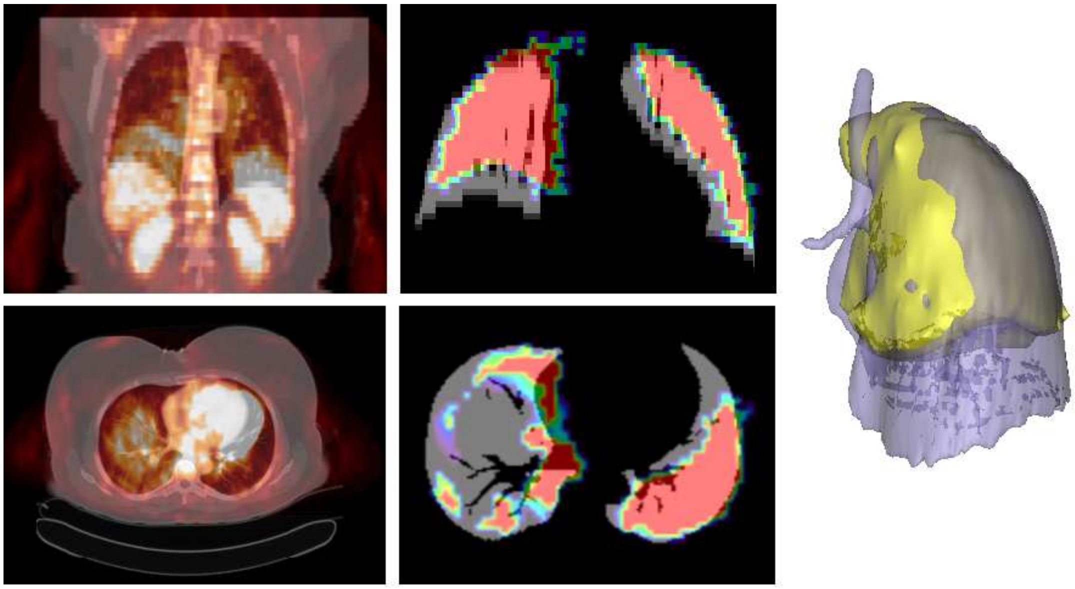

Figure 3.1: Linear registration results in a thoracic case. Left: coronal (top) and axial (bottom) slices of the superimposition of CT (grey) and registered PET (red temperature) images. Center: coronal (top) and axial (bottom) slices of the superimposition of CT (grey) and registered PET (red) segmented lungs Right: 3D superimposition of CT (blue) and registered PET (yellow) rendered lungs. The three different displays prove that a linear transformation cannot cope with deformations suffered by some thoracic structures such as the lungs.

3.1.2 Free-Form Deformation based registration algorithms

Once more deformable regions have been identified, we wanted to test the performance of the FFD-based techniques in our registration application. Rueckert et al. [242] were pioneers in using B-Spline FFD as the non-linear transformation modeling deformations between two images to register. As mentioned in Section 2.7, this technique has been mostly used in *almost* mono-modality applications in which correspondences between the images to register are better defined than in multi-modal cases. In theory, the lack of constraints on the FFD model combined with the lack of uptake of several structures and the low SNR quality in the emission PET scans, does not lead to good registration results with this strategy.

CT and emission PET registration

Therefore, we have applied this registration methodology to CT and emission PET scans of thoracic and abdominal regions [1] in order to identify its limits in our application.

Rueckert's registration method is divided into two phases: an affine registration phase; and a non-linear registration phase based on a B-spline FFD model. The affine transformation (some results are shown in Figure 3.1) initializes the non-linear stage in which local deformations are recovered. Both stages use the Mutual Information criterion to guide the optimization of the set of transformation parameters by means of a gradient-descent technique. The optimization stage is embedded in a multi-resolution framework, speeding up the convergence of the algorithm and providing more accurate results. This registration technique is further detailed in Chapter 6.

Several parameters must be specifically tuned in a FFD-based registration technique, mostly the number of control points of the grid (the number of multi-resolution levels, bins or target blurring are common parameters of any registration procedure) that will define its resolution and in consequence the degree of local deformations the transformation could cope. Another aspect to be taken into account with respect to this choice is the computational cost of the algorithm because a higher number of control points involves a higher quantity of parameters to optimize. In our example, we have found a good trade-off between these two aspects with a grid of 10 control points per dimension, i.e. one control point each 60mm. The number of multi-resolution levels has been set to 3 and the incremental step decreases from 8 to 0.5 through the optimization procedure (these parameters have been tuned in an experimental way).

Figure 3.2 shows results obtained by applying this strategy to CT and emission PET images of thoracic and abdominal regions. We can observe in the non-linearly registered emission PET image (bottom right in Figure 3.2) that the FFD-based registration technique fails to provide good results, even if it is initialized with an affine registration phase (bottom left in Figure 3.2 and Figure 3.1). For instance, we can observe that several critical structures are fully misregistered such as the liver or the kidneys and that the lung registration is neither accurate enough. The set of intensities in emission PET scans corresponding to the boundaries of these structures are

---

[1] Open-source codes of this method are available at `www.imageregistration.com`

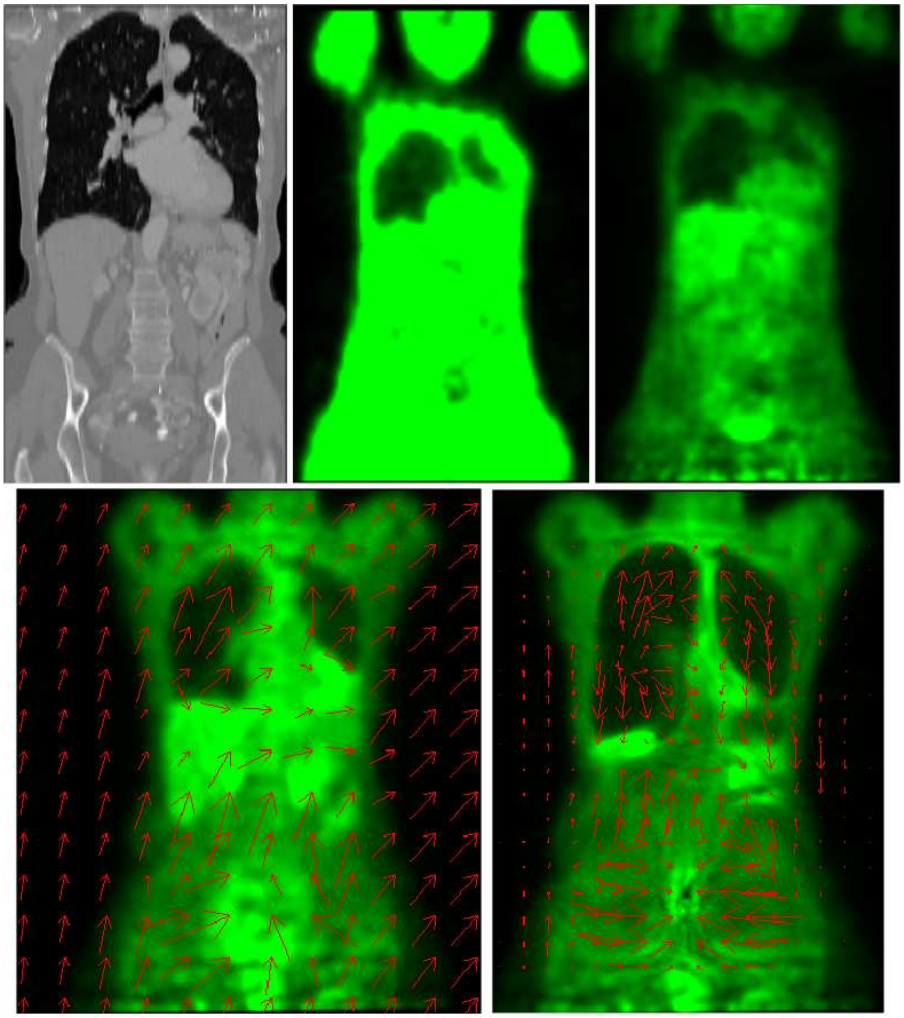

Figure 3.2: Results obtained by computing an affine + FFD transformation between CT and emission PET images. Top: CT (left) transmission (center) and emission PET (right) original images. Bottom: registered emission PET images obtained by applying affine (left) and affine+FFD (right) transformations. The displacement field (red arrows) associated to each one of these transformations (affine on the left and FFD on the right) is superimposed on the images. These results prove the difficulties of this approach to deal with the particular characteristics of our application.

not well distinguished and, depending on the incremental step in the parameter optimization stage, some incorrect transformations can provide good similarity measure values. As a matter of fact, the optimization step must be large enough to cope with severe deformations involved in these elastic regions, but the lack of constraints in the FFD model allowing any possible correspondence between the images produces these misregistrations. The tuning of the registration parameters coul improve these results as well as the use of multi-grid techniques, but we consider that, even if this MI-FFD registration technique is very useful in some applications, we need to change the strategy in order to deal with CT and emission PET images.

CT and transmission PET registration

In addition, we have also tested the strategy proposed by Mattes et al. [242] in order to register CT and PET images of the thorax. They use a similar registration approach as Rueckert et al. [242], but in order to deal with problems associated to emission PET images, they employ the transmission PET scan to compute the transformation which best aligns it with the CT scan. Therefore, they assume that there are no deformations between emission and transmission PET images. This strategy seems to provide good results when this assumption is fulfilled, but in some pathological images, the strong differences existing between emission and transmission PET scans in tumoral regions make this assumption too risky. Moreover, Mattes' approach cannot be used in abdominal images because structures located on this region cannot be seen in transmission PET images. Some results obtained by applying this strategy to CT and emission PET images of thoracic and abdominal regions are illustrated in Figure 3.3. This figure shows the transmission (bottom row) and emission (second row) PET scans registered with the affine (left) and affine + FFD (right) transformations obtained between the CT and transmission PET images. The displacement field (red arrows) associated to each one of these transformations is also superimposed on the images.

We can observe in Figure 3.3 that this registration strategy provide accurate results for the lungs, due to the high contrast of these structures with respect of neighboring regions in transmission PET scans. Nevertheless, the algorithm furnishes misregistrations of the liver and the kidneys, and in general, in the abdominal region, due to the lack of uptake of these structures in the transmission PET scans. As a matter of fact, we can see that the FFD displacement field (red in middle and bottom righ images of Figure 3.3) forces the lower part of the liver to go up, while in order to obtain a better matching with the CT liver, the PET one should be deformed in the opposite direction.

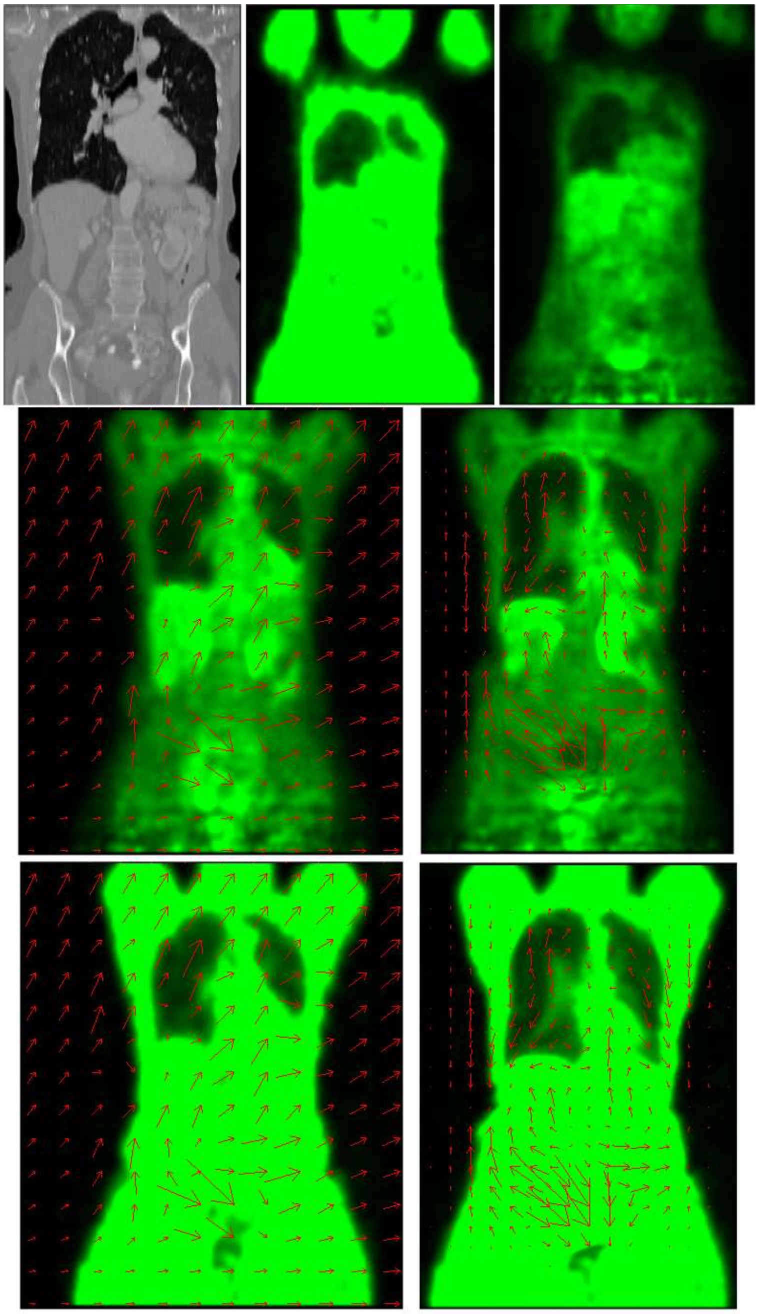

Figure 3.3: Results obtained by computing an affine + FFD transformation between CT and transmission PET images. Top: CT (left) transmission (center) and emission PET (right) original images. Middle: emission PET image registered by applying the transformation computed between the CT and transmission PET scans. Bottom: transmission PET image registered by applying the transformation computed between the CT and transmission PET scans. The displacement field (red arrows) associated to each one of these transformations (affine on the left and FFD on the right) is superimposed on the images. These results prove the difficulties of this approach in several regions, in particular in the abdomen.

3.2 Proposed methodology

In the previous section, we have highlighted the problems associated with whole-content based non-linear registration approaches when working with emission PET images in thoracic and abdominal cases and without prior information or constraints introduced in the procedure. These techniques must cope with large and elastic deformations but they are usually trapped in local minima of the cost function due to the strong presence of noise and artifacts, slowing down the convergence of the algorithm, but even worse, providing incorrect registration results.

In order to avoid these problems, prior information about the anatomical structures involved in the application must be introduced in the registration procedure. The incorporation of prior anatomical information in registration processes is at the core of current state-of-the-art research in non-linear registration.

In the majority of cases, prior anatomical information is introduced in an *implicit* way. This approach forces the registration procedure to furnish plausible deformations that have been found by modeling the expected structure variability between the images to register and the spatial relationships between these structures. Biomechanical Finite Element Models (FEM) such as NCAT phantom [254 ; 255] and statistical model methods such as Active Appearance Modeling (AAM) [67] or Statistical Deformation Modeling (SDM) [241] can be used to obtain prior information about plausible deformations. Two major drawbacks are associated to this approach in the context of our application. First, relying in anatomical atlas or expected structure morphology and movements obtained by means of an average of different images seems too risky when working with pathological images (as in the case of oncology) due to the large inter-patient variability. As a matter of fact, tumors may appear anywhere in the image, being able to modify considerably shape and volume of structures, as well as spatial relationships between them. Secondly, implicit approaches ask for additional registration processes in order to align prior anatomical models to the image data. The main consequence is an increase of the computational overhead of the whole procedure, which is a critical point in our application, as justified in Section 1.3.3.

Due to the particular requirements of our application, we propose an alternative approach based on an *explicit* incorporation of anatomical prior information into the registration procedure. This approach consists in obtaining anatomical knowledge directly from the images to register by means of segmentation techniques. This information is used to initialize deformations as close as possible to the final solution before applying whole-content registration techniques. With this initialization, the search of the global solution will be constrained and the algorithm will converge in a more robust and faster way. This approach does not make assumptions on the structures or their deformations but only rely on available information in the images, permitting to work with any kind of unexpected situations. Moreover, the extraction of anatomical knowledge from the images is in general less expensive in terms of computational cost than registration procedures.

A general scheme of the registration approach we propose is shown in Figure 3.4. It is divided into two stages: a **structure registration** phase (see left part of Figure 3.4) in which homologous structures are segmented (A' and B') in both CT and emission

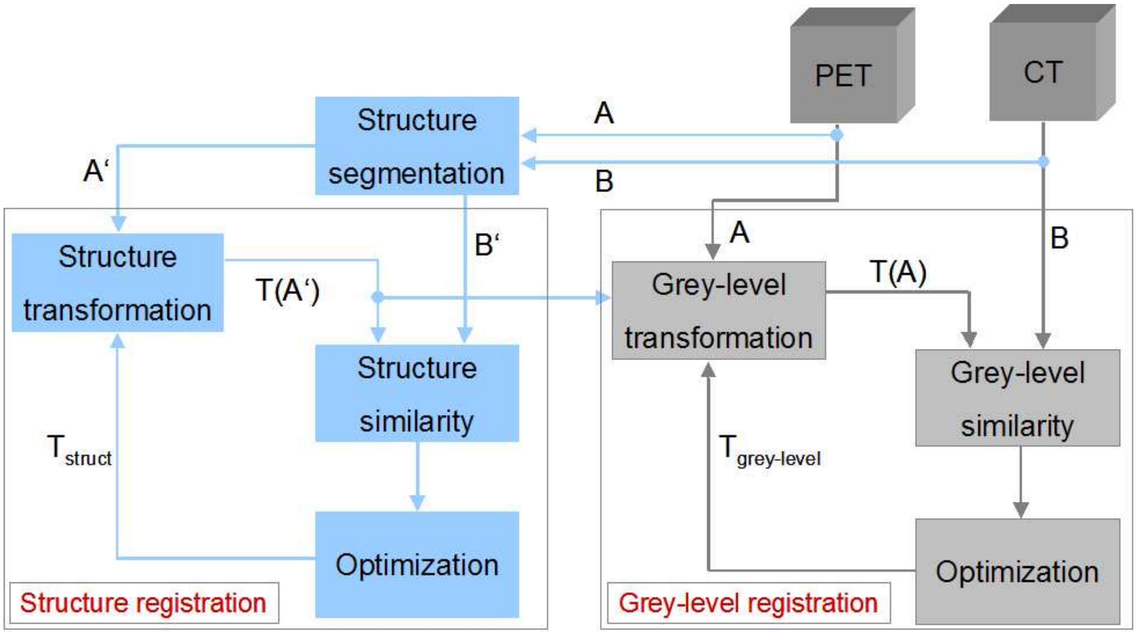

Figure 3.4: General scheme of the proposed approach. The left part corresponds to the structure registration stage and the right part to the grey-level registration stage. The transformation obtained between the segmented structures initializes the registration phase that works with the whole set of intensities.

PET grey-level images (A and B) and registered; and a **grey-level registration** phase in which a non-linear registration technique is applied to the whole set of image intensities of the images. The second stage is initialized with the transformation (T_{struct}) provided by the structure registration stage and it furnishes the final non-linear transformation ($T_{grey-level}$).

As a matter of fact, the structure registration phase (see Chapter 5) can be seen as an anatomical multi-resolution step, filtering out from the data the main anatomical structures, then transferring the result as an initial estimate to a higher level where finer anatomical detail will be considered. The grey-level registration phase (see Chapter 6) can be considered as a refinement step of the structure registration results, capable of correcting any errors the segmentation might have induced and improving the registration of those regions distant from the segmented structures.

Transformations in both steps are modeled by means of Free-Form Deformations (FFD), governed by a three-dimensional grid of control points. This choice facilitates the interaction between initialization and refinement stages, as it will be shown in Section 6.2. Nevertheless, different similarity criteria will be used in each registration phase to compute the transformation parameters due to the difference of working with the segmented and labelled anatomical structures (structure registration phase) or the whole set of intensities (grey-level registration phase).

The use of this strategy also implies a less expensive registration procedure in terms of computational cost. The reasons are the robustness improvement of the registration algorithm in the presence of local minima, and the reduction of the number of iterations required for the grey-level registration phase due to the proximity of the initial transformation to the final solution. On the other hand, the inclusion of the anatomical feature extraction stage (see Chapter 4), makes the registration methodology dependent on the amount of anatomical information obtained from both data volumes. Furthermore, this segmentation stage is a challenging task in emission PET images, in particular if a high accuracy is required. Nevertheless, as further detailed in Chapter 4, the proposed registration methodology only asks for an approximative segmentation of the structures in both scans in order to obtain an initial transformation between them, that will be refined in the grey-level registration stage.

CHAPTER 4

Structure segmentation

Contents

This chapter is devoted to the structure segmentation stage, which is the first phase of the structure registration stage. First, in Section 4.1, the choice of the common structures to be extracted in CT and emission PET images is justified and an explanation of the segmentation procedure is given. This procedure is based on a hierarchical strategy (Section 4.2), divided into an initial segmentation and a refinement phase based on a deformable model. In Section 4.3 some results of the structure segmentation in CT and PET images are shown and discussed, and finally, in Section 4.4 conclusions about this segmentation stage are presented. This chapter is complemented with Appendix D, in which preliminary results on a semi-interactive tumor segmentation procedure are shown.

4.1 Introduction

It should be evident at this point that the effectiveness of the proposed registration method is strongly related to the actual amount of anatomical information that we are capable to extract from both data volumes. This anatomical information will be explicitly incorporated in the registration procedure in order to complement information provided by the images and to constrain and initialize the subsequent whole-content based registration phase.

Segmentation or recognition of anatomical structures in medical images is at the core of current state-of-the-art research in image processing and computer vision fields. The constant improvement of the quality of these images and the availability of powerful computers allow to develop medical segmentation-based procedures (atlas construction, medical training) helping physician's critical decisions. Nevertheless, medical image segmentation remains a challenging task due to either inter-patient variability or imperfections linked to image acquisition devices.

Given the noisy and complex nature of functional images employed in our application, it could be a serious problem if an accurate segmentation were needed, as would be the case if the final result would only rely on the registration of extracted anatomical structures. Even if it is possible to localize several common structures in both imaging modalities and if their segmentation in CT volumes can be achieved in an efficient and robust way (depending on the desired accuracy), their recognition in emission PET scans, in an automatic, robust and accurate way, is not a trivial task. This is due to the poor emission PET image quality (noise, weak contours, artifacts) and the large variability of the metabolic activity (uptake in the scans) in a given structure in different patients or even within the structure [1], as detailed in Section 1.3.2. These characteristics make difficult the finding of structure contours in emission PET scans, even visually in some cases.

However, in the proposed registration procedure, segmentation errors will not necessarily be propagated to the final result, as the second intensity-based registration stage will be able to correct them. Thus, we just need to get a reasonably good approximation of the anatomical features visible in both volumes, or, if this is not possible, as many references about them as can be detected. So, instead of accuracy, our main concerns here are the speed and the reliability of the system. Speed prerequisite comes from the desire of using the registration methodology in clinical routine, which forces us to develop robust and fast image processing algorithms. As registration techniques are already high computational cost procedures, structure segmentation must be performed in almost real-time in order to dedicate most of the time to the alignment computation. Furthermore, if a minimum interaction is desirable in order to improve result robustness, a fast segmentation method is required.

Our registration methodology requires a list of homologous structures that can be found and recognized in thoracic/abdominal emission PET and CT images in a robust way. Furthermore, it is important that the representation of the selected structures

---

[1] As a matter of fact, emission PET segmentation procedures must deal with the same difficulties as registration algorithms working with these images. This is not surprising because registration and segmentation techniques are strongly linked, even if they are often seen as separated processes.

would be as equivalent as possible in both scans (i.e. we visualize the same object in both images), in order to deal with deformations caused only by physiological structure movements and not by the acquisition characteristics. As mentioned in Section 1.3.2, when using certain image modalities such as PET one, only a part of the structure (the tracer is not accumulated in the same way through the whole structure) can be seen and the registration procedure will try to compensate these differences produced by the acquisition device, introducing wrong and sometimes severe deformations. For instance, in the case of the lungs, the bronchia are seen in the CT acquisition while in the PET image they do not appear, and these differences must be taken into account before the computation of the transformation between the structures is performed. Another example concerns the accumulation of the 18-FDG tracer in the heart, that can vary up to a factor of ten in PET scans while it remains constant in CT images.

Based on discussions with medical experts, we finally chose to segment the following structures: skin, skeleton, lungs, kidneys and liver. Since the skeleton is difficult to extract with enough robustness in emission PET scans, it is only used for the CT image segmentation as a support structure constraining the construction of some ROIs, but does not play any role in the registration procedure.

Segmentation of the targeted anatomical structures is a challenging task, in particular in functional images due to the problems discussed above. Several authors have proposed different segmentation algorithms for each targeted structure, in particular in CT images, including the segmentation of lungs [17 ; 286 ; 4 ; 148], skeleton [315], liver [196 ; 256 ; 163 ; 14 ; 161] or kidneys [266]. We do not present a complete review of these methods in this manuscript because it is not the scope of our work. Due to the proposed registration methodology, the segmentation accuracy is not the end-goal validation criterion, unlike published segmentation techniques. Therefore, we decided to develop a segmentation procedure according to the special requirements of our application.

For the segmentation of the targeted structures, relying only on their image grey-level intensities is not a robust and stable enough strategy, as they depend too much on the acquisition characteristics and suffer from a high intra-patient variability. Consequently, other types of information must be used to complement or constrain information provided by the image. A classical way to introduce this *prior* information is to use atlases or anatomical models. Apart from the high degree of shape variability of thoracic and abdominal structures (e.g. over 40 different liver morphologies can be found in the human being [68]), the use of atlases or anatomical models is always open to criticism when working with pathological images, in particular in oncology applications where tumors or surgical operations may modify considerably the morphology of a given structure. Furthermore, the large structure deformations involved in the targeted regions would require a previous registration phase between the atlas and the images to segment, thus considerably increasing the computational cost of the algorithm.

Instead, we decided to exploit the spatial relationships between the organs, which are less sensitive to the deformations than the characteristics of the organs themselves (shape or grey-level values). For instance, we can assure, without any doubt, that the liver is always localized below the lungs. This knowledge will provide a constraint allowing to locate the liver which would not be segmentable relying only on intensities. Therefore, we propose an original hierarchical segmentation procedure based on the mathematical modeling of robust spatial relationships between the targeted structures that shall provide *prior* constraints to be combined with information from the images. Furthermore, using this strategy, we imitate the reasoning of a physician when interpreting a medical image and it allows an easy introduction of user or additional prior information into the procedure. The segmentation of each structure is performed in two steps: a first stage composed of automatic thresholding and other low-level processing operations in a ROI defined by previously segmented objects; and a second stage consisting in refining the result using a 3D deformable model.

4.2 Hierarchical procedure

Spatial relationships have been rarely used in medical image segmentation algorithms. Some exceptions can be found in [22 ; 214 ; 64], where they are employed in brain imaging applications. They take benefit of considering human body as a structured scene, in which some relations between organs possess a high degree of robustness and have a low inter-subject variability. In our application, we must also take into account that in some pathological cases, some of these relations may be altered. Many examples of stable spatial relations can also be found in thoracic and abdominal regions only using basic knowledge on human anatomy: "stomach is placed above kidneys", "lungs are included inside the thoracic cage", "liver is placed under the lungs", "kidneys are closer to liver than to lungs", ... Although these spatial relationships may seem trivial, their addition to an image processing algorithm can considerably help in constraining or rejecting possible solutions.

Therefore, the proposed hierarchical procedure classifies the different anatomical structures in a progressive fashion. The extraction of a given structure will be constrained by the information derived from those which are simpler to recognize. An anatomical structure is considered as *simple* to segment if its associated intensities are fairly homogeneous, if it is well contrasted with respect to neighboring structures and if its morphology, spatial location and relationships are robust and not very variable among different patients.

In general, spatial relations are categorized into three classes: topological, distance and orientation relations [149]. Morphological and symmetry relations are sometimes added as new classes. In our work, topological, orientation and symmetry spatial relations are used as *prior* constraints. This information is employed to construct Regions Of Interest (ROI) (see Section 4.2.1) in which the search for new structures will take place. As mentioned above, the segmentation of each structure [2] is performed in two steps in the corresponding ROI: a first stage where a structure-specific combination of low-level image processing techniques provide an initial segmentation; and a second stage in which a 3D simplex mesh deformable model refines the previous results. As

---

[2] Skin and skeleton are segmented only using the first stage because they are only support structures in the segmentation procedure.

shown in Sections 4.2.2 and 4.2.3, spatial relationships are also used to select structures in the ROI corresponding to a given criterion and to constrain the subsequent deformable model phase.

The proposed hierarchical method requires a specific order for the segmentation of the structures. This order, which has been chosen based on structure recognition simplicity and relationship robustness, is (see Figure 4.1):

1. skin,
2. skeleton (only for CT scan),
3. lungs,
4. kidneys,
5. and liver.

Using this hierarchical procedure, a good trade-off between speed of the algorithm and quality of segmentation results can be achieved. Nevertheless, it must be pointed out that an important drawback of this strategy might be the error propagation between different stages, i.e., errors obtained in the segmentation of simpler structures will highly influence the segmentation of subsequent ones. In order to avoid this problem, consistency checks are included after each structure recognition, as it is further detailed in Section 4.2.2.

4.2.1 Construction of the Regions Of Interest (ROI) by means of spatial relationships

As described above, the search of a given structure is limited to a ROI defined using robust and stable (even in pathological cases) spatial relationships with respect to previously segmented structures. Relationships used in the proposed procedure include direction, symmetry and exclusion relations.

The ROI for each structure is defined as follows.

Skin and skeleton

The skin constitutes the first step of the segmentation procedure in CT and PET images and therefore no ROI is used. Concerning skeleton segmentation in CT scan, it is only constrained to be placed inside the skin volume.

Lungs

In CT images, the lung ROI is derived from the skin, i.e., lungs must be included in the area delimited by the skin.

As discussed in Section 2.6, several CT-PET registration methods [190 ; 263 ; 273 ; 87] proposed in the literature consider strictly no movement between emission and transmission PET acquisitions. This assumption is not valid in all cases, as illustrated

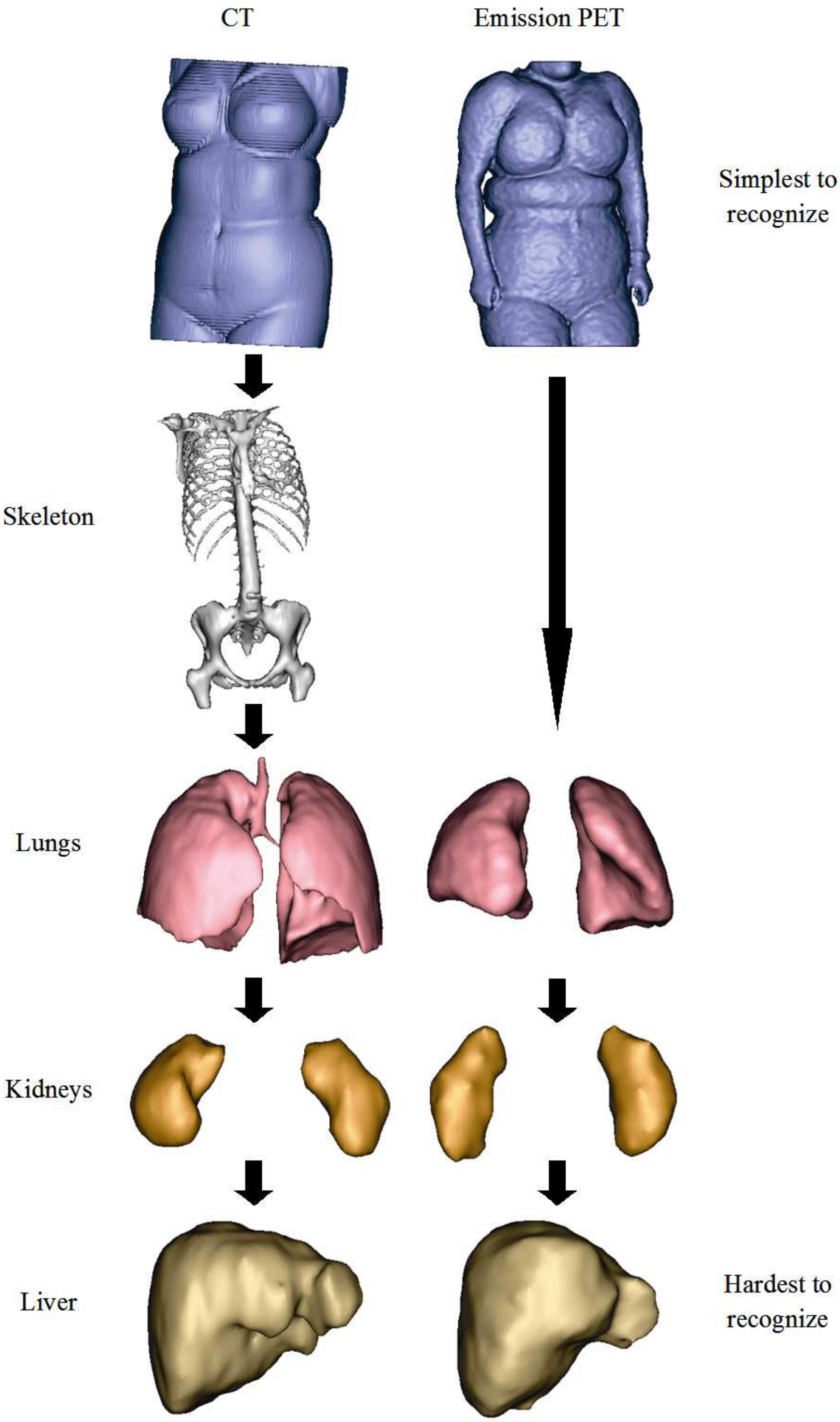

Figure 4.1: CT (left) and PET (right) structures and order of the hierarchical segmentation procedure.

in Figure 2.5 and 4.2. For instance, in some clinical protocols the patient is moved from the scanner bed after the transmission scan for tracer injection. Furthermore, transmission PET scans do not give any metabolic information about tumor nature, then there is not any uptake for the malignant tumors. On the other hand, as illustrated in Figure 4.2, lung contours are usually better defined in transmission PET images than in emission ones, in which lungs are difficult to recognize [3].

Therefore, we use the transmission PET image, in which lungs are easier to segment in order to obtain the lung ROI for the emission PET image, making the assumption that there are no large lung deformations between emission and transmission scans. This strategy will allow us to cope with little differences between both scans that frequently appear in the cardiac region and to include information from tumoral regions. The segmentation procedure detailed in Section 4.2.2 is used to recognize the lungs in the transmission image. Then, we dilate (mathematical morphology dilation) them in order to construct a ROI for the lungs in the emission image. Figure 4.2 shows the contours of the segmented transmission PET lungs (red) superimposed on the transmission (left) and the emission (center) scans, and the ROI (right) for the segmentation of the PET lungs.

Figure 4.2: ROI construction for the segmentation of emission PET lungs. The contours (red) of the segmented tranmission PET lungs are superimposed on the transmission (left) and the emission (center) PET scans. A dilation of the transmission lungs is performed in order to obtain the ROI (right) for the emission lungs.

As mentioned in Section 1.3.3, in PET-CT hybrid systems, the attenuation correction is perfomed by means of the CT image, therefore the transmission PET scan is not always available. Nevertheless, our strategy is still valid because in these cases, the ROI for the emission PET lungs is built from the CT ones because they are already rigidly registered, and there are not strong lung deformations between both scans.

Kidneys and liver

In CT images, an upper bound in the z axis is derived from previously segmented lungs based on the following spatial relationship: "liver and kidneys are under the lungs".

---

[3] Nevertheless, emission PET images acquired with recent high-quality scanners allow to segment lungs without using transmission scans due to their well-defined contours.

This upper limit, computed on each 2D coronal slice, is composed of the lower lung contours and a line linking two automatically extracted landmarks: the lower-left [4] limit of the right lung (point B in Figure 4.3) and the lower-right limit of the left lung (point C in Figure 4.3). These landmarks have proved to be robust and stable enough in all studied cases to define an upper bound for the kidneys and liver ROIs.

The automatic detection of these landmarks is achieved by the following procedure. For each 2D coronal slice, the first lung contour point, starting from left columns of the 2D slice, is selected (point A in Figure 4.3). Starting from this point, the next landmark is defined as the one which has $max(x+z)$, x and z being spatial coordinates of the image (point B). In order to compute the corresponding points in the left lung, the same procedure is used in a symmetrical way, this time the second landmark point corresponding to $max(z-x)$ (point C in Figure 4.3). Once points B and C are found, a line linking them is automatically drawn, defining, together with the lower lung contours, the upper limit of kidneys and liver ROIs for each 2D coronal slice. This upper bound has proved to be very helpful for separating the liver from the heart, in particular in CT images, in which these structures have similar grey-level intensities.

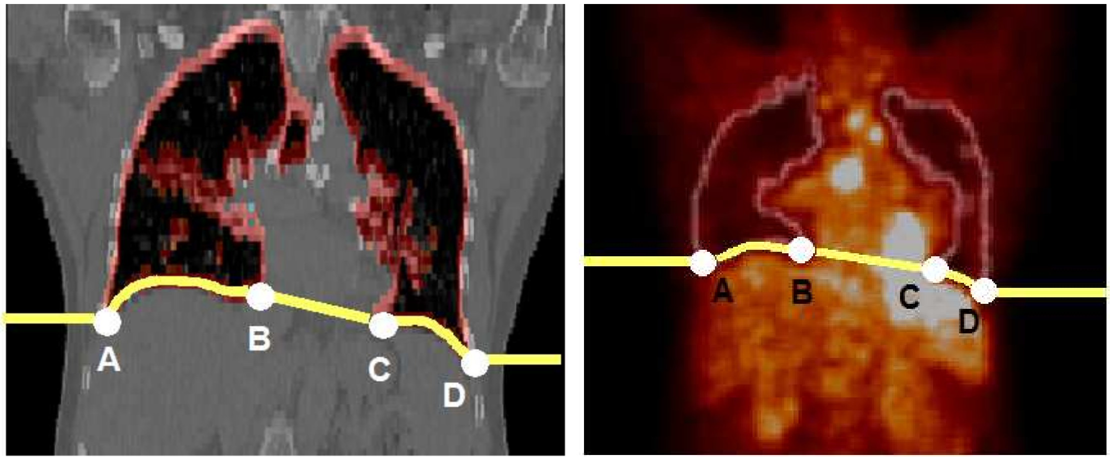

Figure 4.3: Landmarks (points A, B, C and D) and upper bound obtained from the lungs in CT (left) and emission PET (right) images in order to built liver and kidneys ROI.

If the skeleton has been segmented, as in the case of CT images, additional limits can be obtained for the kidneys and liver ROIs, by detecting the top of the pelvis and the ribs. The following spatial relationships are then employed: “liver and kidneys are above the top of the pelvis”; and “liver and kidneys are laterally limited by the ribs ”.

A lower bound is also computed using the top of the pelvis, which is extracted from the skeleton. The top of the pelvis is found by the following procedure. The area of the skeleton surface is computed for each 2D axial slice. This area can be used to detect the first 2D axial slice in which the spine is visible, coming from the pelvic region in a foot-to-head scanning: the top of the pelvis is then obtained when the 2D axial skeleton area is below a given threshold which is chosen in an experimental way.

---

[4] In medical imaging the “left is right”convention is used.

Finally, ribs are also used to laterally limit the ROI corresponding to kidneys and liver. First, we remove z slices under the top of the pelvis that has been computed just before. The next step separates the ribs from the rest of the skeleton by computing symmetrical pairs of objects distant from the image symmetry plane in each 2D coronal slice. Image symmetry plane and selection of symmetrical pairs of objects algorithms are detailed in Section 4.2.2. Once ribs are found for each 2D coronal slice, a line linking each rib with its two neighbor ribs is drawn, defining other limits of the CT liver ROI, as can be seen in Figure 4.4.

In PET images, as skeleton is not available, we only use the upper bound derived from segmented lungs.

Concerning the ROI for the liver, in addition the previously segmented kidneys are suppressed from the ROI in order to avoid overlap between these structures, as illustrated in Figure 4.4.

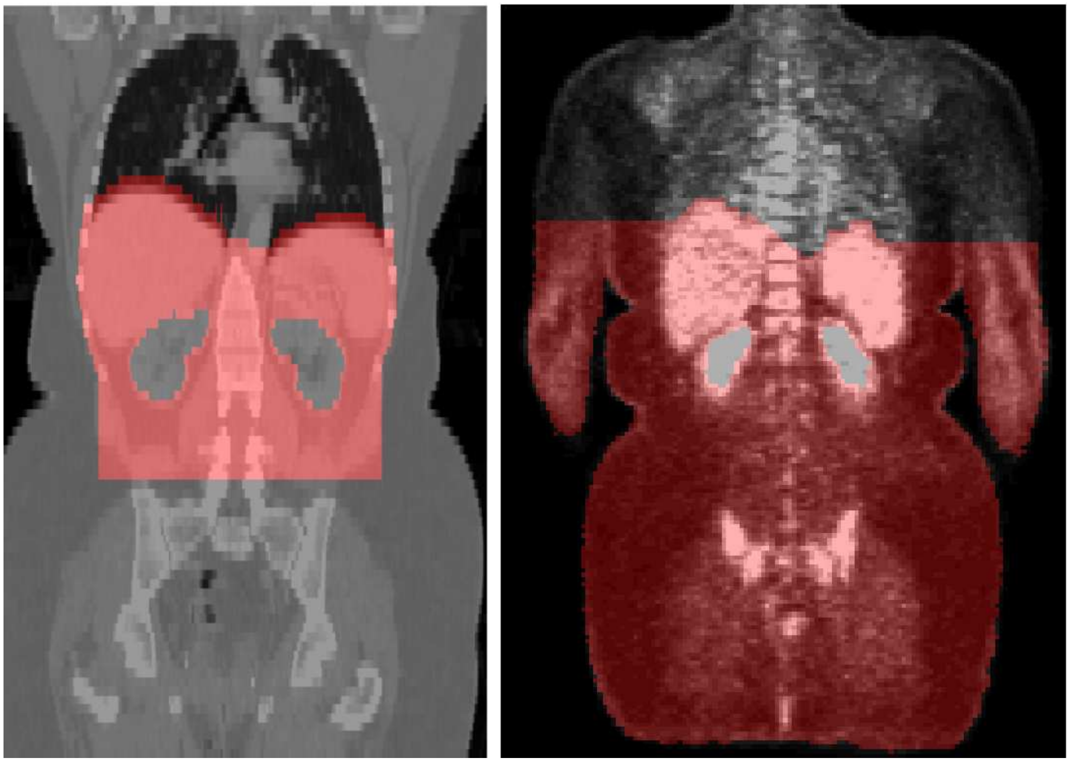

Figure 4.4: Examples of liver ROIs (in red) superimposed on grey-level images. Left: CT image; Right: PET image.

The proposed procedures to obtain the limits of the ROI are very structure-specific and have been derived from stable and robust relationships between the targeted structures. Nevertheless, in largely pathological cases, some of these spatial relations can be slightly disturbed. For instance, in post-operative images, one of the lungs may be removed. In the proposed ROI construction methodology, lung recognition is only critical to obtain the upper bound for liver and kidneys ROIs, but a lung removal does not affect it because we could always use a more flexible upper bound computed from information provided by the remaining lung. The presence of large tumors in the images do not have altered the performance of the ROI construction either. As a matter of fact, the use of direction, symmetry and exclusion relations allows to impose soft constraints on the algorithm, unlike other less flexible spatial relationships such as distances.

The structure segmentation phase depends on the accuracy of the ROI construction, therefore each phase involving critical parameter tuning is followed by consistency checks of the results, as detailed in the next section. Furthermore, the proposed methodology permits an easy introduction of additional information about general spatial relationship perturbations in some particular cases, thus improving the robustness of the algorithm as well.

4.2.2 Initial segmentation

The initial segmentation of each structure is obtained by means of the following sequence of operations (in this order) that are applied to the corresponding ROI:

1. K-means and automatic thresholding;
2. binary erosion;
3. selection of connected components;
4. binary dilation;
5. consistency check.

K-means: The well-known K-means clustering method [169 ; 85] is the first step of the initial segmentation procedure. The goal of the K-means algorithm is to minimize dissimilarity in the elements within each cluster (K denotes the number of clusters) while maximizing this value between elements in different clusters. This method is able to provide satisfactory classification results only if it is applied to a restricted ROI, in which not too many structures (and thus, not too many different grey-level values) appear. Otherwise this method will produce several segmentation errors. This will be typically the case for the liver because it will be classified into the same class as the heart due to the high similarity between their intensities. The use of spatial relationships to construct the ROI solves this problem and allows us to apply automatic thresholding. Nevertheless, an initial phase of parameter tuning (number of classes and their centers) must be performed for each structure. In our case, after this training phase, parameters have proved to be robust enough in order to fix them (for a given anatomical structure) for the whole set of processed images.

Mathematical morphology: The two basic binary mathematical morphology operations, erosion and dilation, are used in the initial segmentation procedure. The former, applied after the K-means stage, aims at separating undesirable components from relevant structures and dilation, applied after the selection of connected components stage, recovers some of the data lost in the erosion step. The interested reader is referred to some of the classical books on mathematical morphology [247 ; 257] to find further details about these operations.

A combination of mathematical morphological operations can be used as a *3D hole filling* procedure. The presence of holes in some segmentation results is induced by either segmentation errors or the existence of small structures with highly different grey-level values within a larger structure. For instance, in the case of lung structures, in CT images, the bronchia are easily distinguished in the lungs in CT images, producing the apparition of holes in the segmented volume, whereas in the PET scans, the bronchia do not appear. This difference between CT and PET segmented volumes will be wrongly interpreted by the registration procedure as a deformation to cope with, thus producing wrong transformations. Therefore, the 3D hole filling stage is employed to limit these differences.

Selection of connected components: This stage consists in selecting the correct connected components among those classified by the automatic thresholding phase as having similar intensities as the targeted structure.

In the case of liver and lung segmentation, the chosen criterion is to select the largest connected components. A particularity of the lung segmentation concerns the removal of the trachea in CT scans. This anatomical structure appears attached to the segmented lungs in this imaging modality while it does not always appear in PET acquisitions. In order to avoid the possible misregistrations induced by this situation, the part of the trachea above (in the z axis, i.e. closer to the head) the lungs is removed from the images. It is achieved by looking for the first axial slice (in a head-to-foot scanning), in which only two connected components are found. As a matter of fact, when the trachea is present, three connected components can be seen in the axial slices. Therefore, these upper slices (with three connected components) are removed from the segmentation. The subsequent segmentation stage based on a deformable model prevents any problem due to the trachea removal by regularizing the solution. Therefore, this special situation does not further lead to misregistration of the lung structures.

A noteworthy exception in the selection of connected components is the case of kidneys because they are not the largest connected components in the ROI. The two most symmetrical components with respect to the body symmetry plane are selected, as illustrated in Figure 4.5. The symmetry plane computation is based on an algorithm originally developed for brain images [285] and the selection of symmetrical regions is made using a symmetry measure proposed in [65].

For a 3D grey-level image f, a symmetry mesure of f with respect to a given plane Π can be defined as a similarity measure between f and its reflection with respect to Π, denoted $e_\Pi(f)$:

$$\sigma_f(\Pi) = S(f, e_\Pi(f)), \tag{4.1}$$

The search of a symmetry plane can be seen as a monomodal registration problem, thus a standard l_2 metric or normalized correlation measure can be chosen. The corresponding symmetry measure $\sigma_f(\Pi)$ is computed as follows:

$$\sigma_f(\Pi) = 1 - \frac{\|f - e_\Pi(f)\|_2^2}{2\|f\|_2^2} \tag{4.2}$$

where $\|f\|_2$ denotes the l_2 metric of f.

The problem of finding the best symmetry plane is then expressed as the maximization of the symmetry measure which is an optimization problem in the parametric space $]-\pi/2, \pi/2] \times [0, \pi[\times \mathbb{R}$ representing all possible plane orientations and directions. The optimization procedure needs an initialization and the ellipsoid of inertia is usually used to define candidates for this starting point, in the case of brain images. In our application, the vertical plane passing by the center of mass already provides a good initialization. Afterwards, the symmetry plane initialization must be refined, improving the position and the orientation of this plane. The *Nelder-Mead downhill simplex* method [223] is used to this purpose. This method is accurate and robust under a good starting point and it produces good results in our application, as can be seen in Figure 4.5.

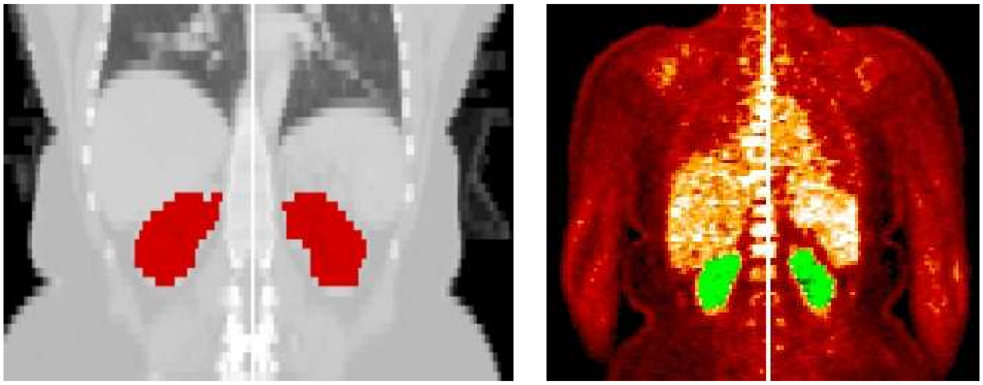

Figure 4.5: Symmetry plane (white vertical line) in a whole-body image and kidneys symmetry. Left: CT image; right: PET image

Once the best reflection symmetry plane for the images is computed, the selection of the most symmetrical components must be done. The symmetry measure of a pair of binary objects (A, B) is defined as :

$$S(A, e_\Pi(B)) = \frac{|A \cap e_\Pi(B)|}{|A \cup e_\Pi(B)|}$$

Then, for each pair (A, B) of connected components in the image, this symmetry measure is computed. The pair of connected components furnishing the highest measure will be chosen as the most symmetrical one.

Consistency verification: Robustness is a major concern for any medical image processing algorithm. In order to improve the robustness of the initial segmentation procedure (in particular of the steps involving parameter tuning), we automatically verify result consistency after each critical phase. To this purpose a set of routines have been developed that systematically check for certain parameters of the extracted organ, like dimensions, volume or compactness, to be within the expected range. As a matter of fact, physicians usually ask for an interactive control of structure segmentation procedures, therefore, these check routines will help the development of an user-friendly segmentation interface. From the robustness point of view, the most critical operations include automatic thresholding and selection of connected component. Nevertheless, due to the limited size of ROIs where structures are searched, errors produced by these stages have been well identified and taken into account in the procedure. Some situations involving repetitions of the procedure are:

- Skin: the K-means algorithm is systematically repeated with a range of different number of classes because a circle around the visualized region appears in some of the available CT images, as shown in Figure 4.6;
- Lungs: after the K-means stage, the lungs are classified either as a unique connected component or as separated structures in CT images. This fact is due to the thin part that separates both lungs in the anterior region and the low resolution of some CT images, producing partial volume errors in the images, as shown in Figure 4.6. By computing the centroid location of the recognized structure, it can be known whether segmented lungs are joined or not (if the centroid is placed far away from the symmetry plane of the image or not). If only one of the lungs is found (lungs are separated), the selection of connected components is repeated by selecting the two largest connected components of the image instead of only the largest one.
- Liver: the separation of the liver from surrounding small structures having similar grey-level values is a complex task that even the use of a ROI has not solved. Nevertheless, as we only require an approximation of the structure, possible liver segmentation errors will be corrected in subsequent stages of the methodology.

In each image processing step, when consistency measures are finally within the expected range, the detected region is the input of the following regularization phase.

If an inconsistency in the final segmented structure were ever detected, the proposed methodology will force the whole procedure to be repeated with a different set of parameters.

Even if the proposed segmentation procedure is a simple combination of low-level image processing techniques, it is the introduction of robust spatial relationships and the automatical construction of the ROIs that allows the system to provide an approximative segmentation of the structures. This approximation is accurate enough for our application, keeping in mind that a regularization phase by means of a 3D deformable model will be further applied. Nevertheless, the proposed methodology allows an easy integration of more sophisticated segmentation techniques that could be applied in the ROI corresponding to a given structure.

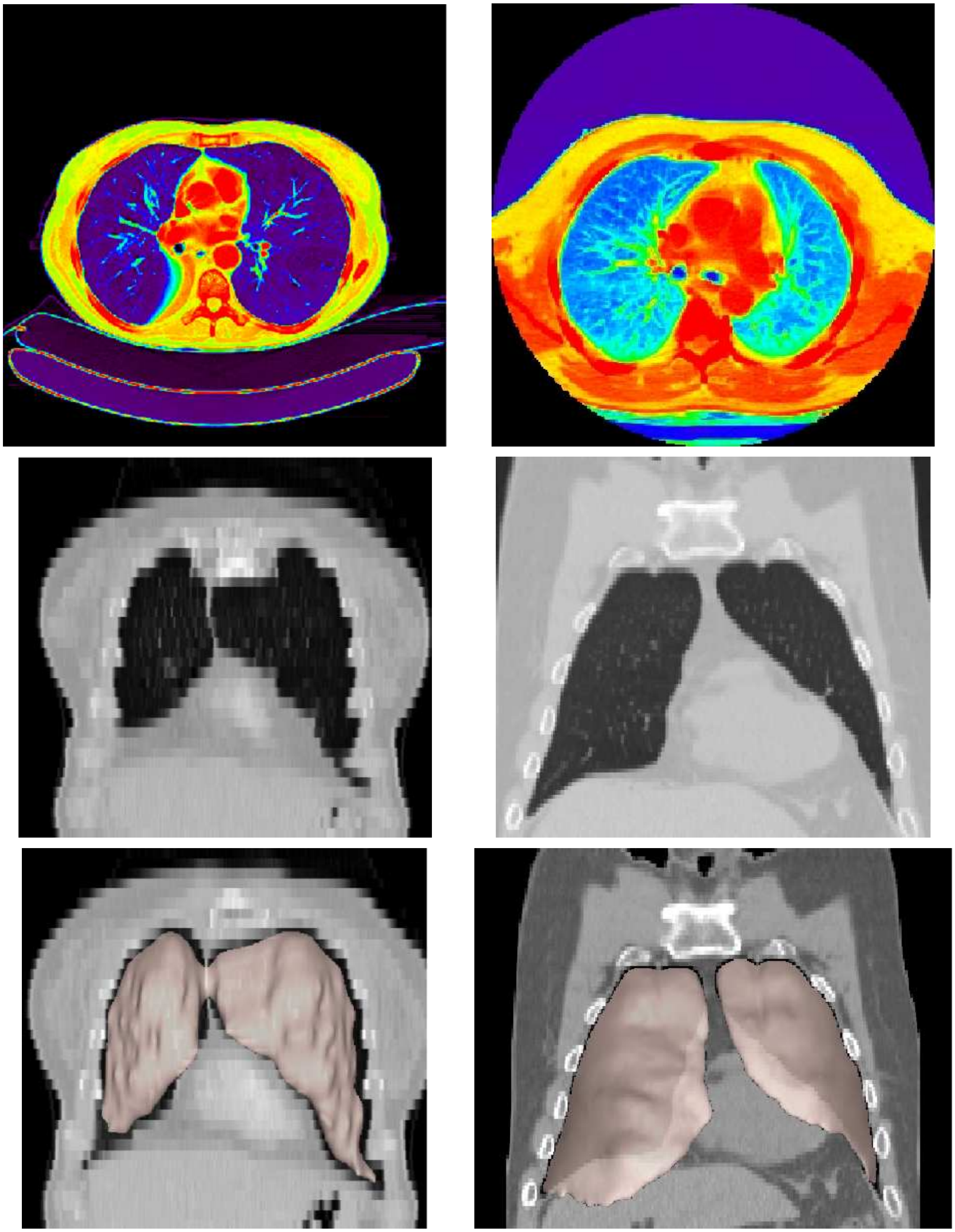

Figure 4.6: Ambiguities solved by consistency verification checks. Top: Presence or absence of a circle limiting the FOV of the CT image. Middle and bottom: low (left) and high (right) resolution CT images with joint (left) or separated (right) lungs, leading to the selection of one or two connected components in the segmentation procedure. The 3D rendered segmented lungs are shown in the bottom images.

4.2.3 Refinement with a deformable model

The previous initial segmentation phase provides a good approximation of the structures, indicating their location in an accurate way. However, this result cannot be considered as an accurate final segmentation result, even in our context of initial registration. The main problem is the lack of regularization. This has proven to be an inconvenience in the case of subtle structures such as the bronchia (even after applying hole-filling techniques), which can be detected in the CT scan but not in the PET one, thus introducing a difference that the registration process will wrongly interpret as a deformation and try to compensate. Furthermore, a regularization stage can be very helpful to define the boundaries where, due to an insufficient image resolution or to patient motion, no significant edges are found, such as in the liver.

These problems are overcome using a 3D simplex mesh deformable model [75], applied to the binary images containing structures segmented in the initial segmentation phase.

Deformable models [139] are curves or surfaces defined in a given image domain which evolve under the influence of constraints computed from image data (usually an edge map) and regularity constraints. They have been largely used in several image processing and computer vision applications, such as image segmentation, animation, contour or motion tracking or shape and geometric modeling.

Basically, there are two main types of deformable models: *parametric* [139] and *geometric* [181 ; 44] ones.

The former needs a parametric or discrete representation and it is based on an elastic curve (or surface) that can dynamically evolve towards object shapes in response to internal forces and external forces. Geometric deformable models, based on the theory of curve evolution and the *level sets* method, employ an implicit representation of the model and allow topology changes. They consider the snake as the zero level set of a higher dimensional function, solving the corresponding equation of motion. This approach is well-suited for the recovery of objects with complex shapes and unknown topologies. Parametric deformable models are more intuitive for shape analysis and visualization or for user interaction, and less expensive in terms of computational cost. As a matter of fact, their mathematical formulation makes easier to integrate image data, initial estimations, desired contour properties and *prior* constraints. Furthermore, they are robust enough to noise and possible contour discontinuities, obtaining theoretically a sub-voxel segmentation of the image.

Due to the particular requirements of our application, a parametric technique has been chosen. Geometric deformable models allow the structure topology to change but in our specific problem, this is not needed and is even undesirable, according to the physician's point of view. Furthermore, when parametric deformable models are implemented using a discrete representation, a fast convergence can be obtained. As mentioned above, parametric techniques have also the advantage of naturally allowing the use of initial results, which is very suitable in the proposed segmentation strategy.

Otherwise, parametric deformable models also present several problems. The most critical one concerns the sensitivity of these models to their initial conditions, and they have therefore to be initialized as close as possible to the true contour to avoid the convergence to an erroneous result. Nevertheless, segmentation results provided by the initial segmentation stage are close enough to the final solution to assure a good performance of the deformable model.

In the following paragraphs, basic guidelines on 3D deformable models are given. Further details about 2D active contours, its numerical implementation and the extension to 3D can be found in Appendix C.1.

Evolution of the deformation model

The evolution of a deformable surface is usually described either using an energy minimizing formulation or a dynamic force formulation. We present here the latter which allows the use of more general data terms. The evolution of the deformable surface $\mathbf{X}$ can be written as follows:

$$\gamma \frac{\partial \mathbf{X}}{\partial t} = \mathbf{F}_{int}(\mathbf{X}) + \mathbf{F}_{ext}(\mathbf{X}) \tag{4.3}$$

where $\mathbf{F}_{int}$ is the *internal* force related to the physical properties or constraints of the model that specifies the regularity (elasticity and stiffness) of the surface and $\mathbf{F}_{ext}$ is the *external* force that drives the surface towards the desired features in the image (in general image edges), and sometimes includes forces interactively introduced by the user. The solution is the steady state of the previous equation. The chosen internal force is:

$$\mathbf{F}_{int} = \alpha \nabla^2 \mathbf{X} - \beta \nabla^2 (\nabla^2 \mathbf{X}) \tag{4.4}$$

where α and β respectively control the surface tension (prevent it from stretching) and rigidity (prevent it from bending) and ∇^2 is the Laplacian operator. It is then discretized on the simplex mesh using the finite difference method [306].

Gradient Vector Flow The choice of the external force is crucial in order to make the deformable model evolve towards the contours of the object to segment. Initially, Kass et al. [139] have proposed a force computed from the image gradient to achieve this. Some drawbacks of this technique include a reduced attraction region and the need of an initial deformable model surface very close to the targeted contour.

To solve these problems, in particular the capture range (or attraction domain), Xu et al. [307] have introduced an external force based on the diffusion of the gradient vector associated to a given contour map, called *Gradient Vector Flow* (GVF). A generalization of this technique was also proposed, the GGVF [309], that improves the convergence towards thin concavities and that converges towards the middle of thick contours. On the other hand, this is a relatively high computational cost algorithm, sometimes more expensive than the model evolution in computational terms.

The GVF technique produces dense vector fields derived from the images, by solving the equation of vectorial diffusion that distributes gradient vectors of a binary or grey-level contour map computed from the image. Then, deformable models using GVF as external force cannot be formulated as the negative gradient of a potential force, unlike those using other forces, and the approach is expressed by means of a dynamical equation of forces. The GVF field $u(x)$ of the function $f(x)$ is defined as the equilibrium solution of the following vector diffusion equation:

$$\begin{cases} \mathbf{u}_t = g(|\nabla f|)\nabla^2 \mathbf{u} - h(|\nabla f|)(\mathbf{u} - \nabla f) \\ \mathbf{u}(x, 0) = \nabla f(x) \end{cases} \tag{4.5}$$

where $u_t = \frac{du}{dt}$ and t is the time parameter. The first term of the first equation is called *smoothing* term, and tends to smooth the resulting vector field. The second term is the *data* term, and drives the vector field u towards the $\bigtriangledown f$ computed from the data. The function $f(x)$ can be any edge map and a classical Canny-Deriche [77] edge detector followed by a hysteresis thresholding was initially used. However, this technique often fails due to its Gaussian smoothing phase which looses weak contours. A gradient computed after applying an anisotropic diffusion algorithm [100] has proved to provide better results in some cases, because this technique removes noise in homogeneous regions while keeping and even enhancing contours in the image. This has been very useful for PET images due to their noisy nature.

The functions $g(\cdot)$ and $h(\cdot)$ are weighting functions that apply respectively to the smoothing and data terms. They depend on the gradient of the contour map, which is spatially variable, thus, these functions will also vary through the space domain. As it is desirable that the vector field will vary in a slow and smooth fashion far away from the contours (where the gradient is weak), but at the same time acts as ∇f near them, $g(\cdot)$ and $h(\cdot)$ must be decreasing and increasing functions of $|\bigtriangledown f|$, respectively. Thus, a small smoothing is performed near strong contours (where h dominates), producing a vector field similar to the one obtained only with the edge map gradient. The following weighting functions, proposed in [309], accomplish these conditions:

$$g(|\nabla f|) = e^{-\left(\frac{|\bigtriangledown f|}{K}\right)^2} \tag{4.6}$$

$$h(|\nabla f|) = 1 - g(|\nabla f|), \tag{4.7}$$

where K determines the trade-off between the field smoothness and the fidelity to the contour gradients of the image. This formulation allows gradient vector diffusion only where there are no strong edges, thus preventing the smoothing effect from averaging close opposing gradients, which could lead to a gap in the contour through which our model could leak. An example of a GVF field computed for an emission PET lungs is shown in Figure 4.7.

Regions of Interest constraining the deformable model A large number of works [66 ; 260 ; 196] have introduced shape constraints in the deformable models. However, as we previously mentioned, relying on shape information would be hazardous in our application and we rely instead on knowledge derived from spatial relations. The Regions of Interest (ROI) computed from the spatial relations are used in order to limit the evolution of the *snake*. An approach for integrating spatial relations into deformable models has been proposed in [64]. This approach deals with relations represented by fuzzy sets which can be seen as fuzzy ROIs. In our case, the ROIs are binary and are therefore considered as a particular case of the previous

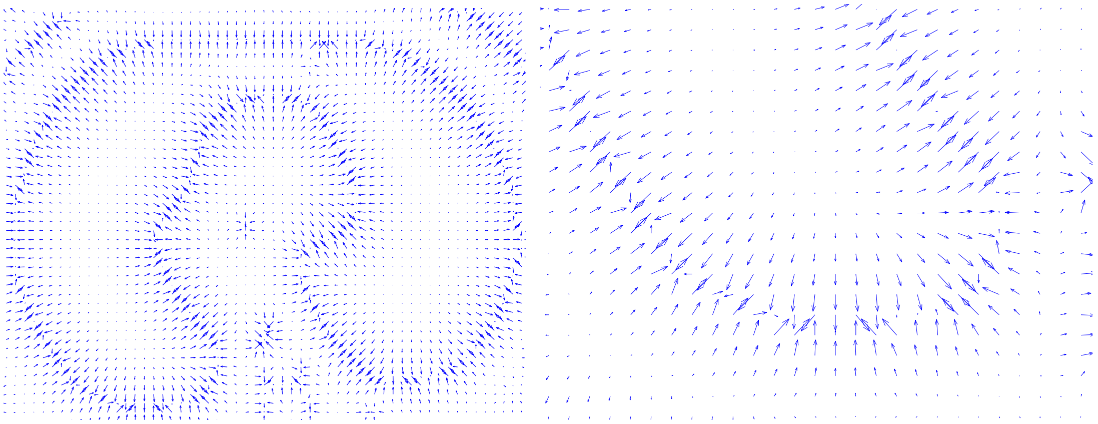

Figure 4.7: Axial slice of GVF computed on an emission PET image (left) and detail (right).

approach. The integration is accomplished by means of an additional term inserted in the external force formulation. This term, called a *limiting* force, must be combined with one derived from the image data and must constrain the model to keep it from going outside the ROI. But inside the ROI, the model must be only limited by the data term (the limiting force must be zero inside the ROI). Thus, the modulus of this force must be inversely proportional to the satisfaction of the condition. Finally, this force is preferable to have a certain spatial regularity and its computation should remain reasonable.

Therefore, the external force is not only derived from image edges but also constrains the deformable model to stay in the ROI. It can be written as a linear combination:

$$\mathbf{F}_{ext} = \lambda \mathbf{v} + \mu \mathbf{F}_{ROI} \tag{4.8}$$

where $\mathbf{v}$ is a Gradient Vector Flow (GVF) field and $\mathbf{F}_{ROI}$ is the force attached to the ROI and λ and μ are weighting parameters.

The second term of the external force is used to prevent the deformable model from going outside the ROI. This can be useful, for example, for separating the liver from the ribs, the heart or the kidneys. $\mathbf{F}_{ROI}$ is a distance potential force [56] and it can be written as follows:

$$\mathbf{F}_{ROI}(x) = -\chi_{ROI}(x) \frac{\nabla d(x)}{\|\nabla d(x)\|} \tag{4.9}$$

where d is a distance map to the ROI and χ_{ROI} is the characteristic function of the ROI (this means that this force is switched-off inside the ROI). It should be noted that we also use the ROI as a mask on the GVF and thus the GVF is equal to zero outside the ROI. Finally, we also use the ROI as a mask on the obtained segmentation to ensure that no objects are overlapping.

Simplex mesh deformable model

A discrete representation has to be chosen in order to implement the parametric deformable model to achieve the refinement stage. Most common discrete representations are *triangulations* and *simplex meshes*. Even if triangulations are easier to construct, simplex meshes, introduced in [75], are the selected discrete representation. This decision avoids problems due to surface parameterization associated to triangulations, while remaining a reasonable computational cost algorithm. In addition, local shape constraints can be easily added to the model, and there are also simple discretization methods for the evolution equations and topologic and geometric adaptation algorithms. Other good properties of this approach include that they are are topologically dual to triangulations and have a constant vertex connectivity. Complete details on simplex meshes can be found in [74 ; 75 ; 196].

The following procedure is used to obtain simplex meshes:

1. Erosion of initial segmentation;
2. generation of triangulations with the isosurface algorithm;
3. decimation of triangulations;
4. conversion from triangular to simplex meshes.

First, initial structure segmentations are systematically eroded in order to ensure that this initialization is inside the targeted object. The next step consists in transforming them into a triangulation. This transformation is performed by means of an isosurface algorithm [213] based on tetrahedra. Once the triangulation is computed, the mesh must be decimated in order to reduce the number of triangles to a manageable quantity. The last step converts the triangular mesh into a simplex mesh [75], using the dual operation.

Definitions A simplex mesh is a polygonal mesh where each node (vertex) has a constant number of connections to its neighbors (a k-simplex of $\mathbb{R}^n$ is then a mesh with every vertex having $k+1$ neighbors, k being equal to n). This neighbor relationship defines the edges of the mesh. In addition, a face is defined as a series of vertices, successively linked in pairs by the edges, and in a way that no edge divides by two this face. Then, faces in a simplex mesh are not necessary flat. Mathematically, a k-simplex mesh $\mathcal{M}$ of $\mathbf{R}^n$ is defined as the pair $(V(\mathcal{M}), N(\mathcal{M}))$ where $V(\mathcal{M})$ is the vertex set of $\mathcal{M}$ given by

$$V(\mathcal{M}) = \{P_i, i \in \{1,\ldots,n\}, P_i \in \mathbf{R}^n\} \tag{4.10}$$

and $N(\mathcal{M})$ is its associated connectivity function, defined as follows:

$$N(\mathcal{M}) : \{1,\ldots,n\} \longrightarrow \{1,\ldots,n\}^{k+1} \tag{4.11}$$

in such a way that

$$\forall i \in \{1,\ldots,n\}, i \longmapsto (N_1(i), N_2(i), \ldots, N_{k+1}(i)) \tag{4.12}$$

and

$$\forall i \in \{1,\ldots,n\}, \forall j \in \{1,\ldots,k+1\}, \forall l \in \{1,\ldots,k+1\}, l \neq j \tag{4.13}$$

$$\begin{array}{ll}(1) & N_j(i) \neq i \\ (2) & N_l(i) \neq N_j(i).\end{array}$$

Constraints (1) and (2) assure that the mesh will not present loops or double edges. A connectivity constraint is also added in order to guarantee that for every pair of vertices, there exists a path between them. A simplex mesh can be defined in any dimension, but in our work, only the case of 2-simplex meshes of $\mathbb{R}^3$ are considered (every 3D surface can be represented by means of a 2-simplex mesh). Thus, these meshes are 3-connected. Examples of 2-simplex meshes are shown in Figure 4.8.

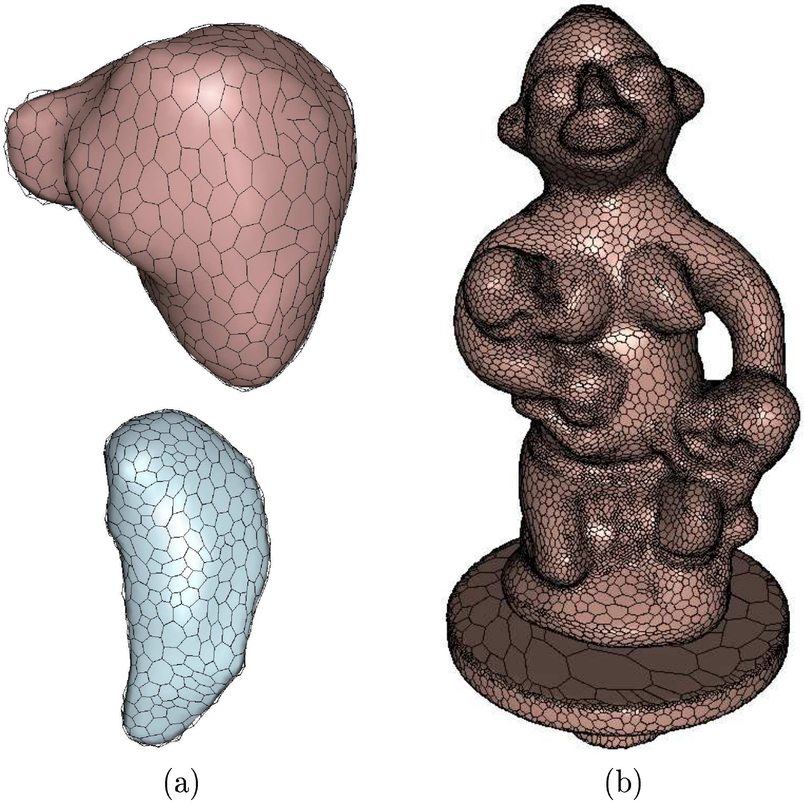

Figure 4.8: Examples of simplex meshes. (a): liver (top) and caudate nucleus (bottom) simplex meshes; (b) simplex mesh of an art object (by courtesy of Carlos Hernandez [118]).

Dual operation Triangular meshes have been largely studied in recent years for several computer vision applications and they are obtained in a simple fashion. The topological duality of these meshes with simplex ones offers us the possibility of generating, in a simple fashion, a simplex mesh from a triangular one. The dual operation is based on the following correspondences from a triangular to a simplex mesh: a vertex becomes a face; and a triangle becomes a vertex.

It must be pointed out that this duality is only exact in a topological sense, but not in geometrical terms. Therefore, if a triangular mesh is transformed into a simplex one, and then, reconverted to a triangulation, it would be topologically similar, but geometrically different due to the position changes of the vertices. The center of each face must be joint to its vertex, obtaining a triangulation with more vertices, but geometrically correct, as can be seen in Figure 4.9.

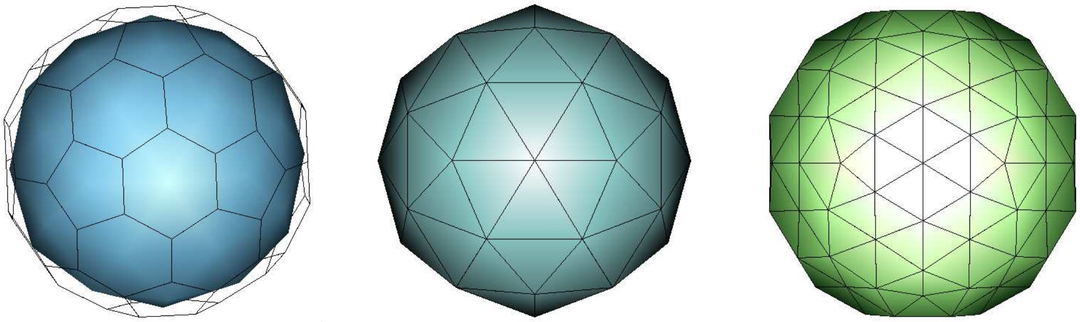

Figure 4.9: Left: simplex mesh; Center: dual triangulation; Right: triangulation geometrically corresponding to the simplex mesh.

Construction of the triangular mesh A triangular mesh is constructed from each segmented structure by means of isosurface techniques. An isosurface is a surface that goes through the whole set of space points that have values equal to a specified isovalue, resulting in a tesselated surface. The *marching cubes* algorithm, proposed in [165], has been largely used in recent years in visualization and other computer vision applications. In spite of being an efficient and simple algorithm, it has been proved that it possesses some inconsistencies and ambiguous cases [213], producing rendering errors in the resulting surface. Thus, another isosurface algorithm [213], based on tetrahedra instead of cubes, is employed because it produces an Eulerian surface, while being simpler and more general.

Evolution of the simplex mesh The dynamical equation 4.3 is discretized by means of a finite differences method [306], resulting in the following formulation of the evolution for each vertex $\mathbf{p}$ of the mesh:

$$\mathbf{p}^t = \mathbf{p}^{t-1} + \tau(\alpha\tilde{\Delta}\mathbf{p}^{t-1} - \beta\tilde{\Delta}(\tilde{\Delta}\mathbf{p}^{t-1}) + F_{ext}(\mathbf{p}^{t-1})) \tag{4.14}$$

where τ is the time step and $\tilde{\Delta}$ is the discrete Laplacian operator computed on the simplex mesh ($\tilde{\Delta}^2$ is the discrete biharmonic operator).This operator is computed as follows:

$$\tilde{\Delta}\mathbf{p} = \frac{1}{3}(\mathbf{p}_1 + \mathbf{p}_2 + \mathbf{p}_3) - \mathbf{p} \tag{4.15}$$

$$\tilde{\Delta}(\tilde{\Delta}\mathbf{p}) = \frac{1}{9}(\sum_{i=4}^{9}\mathbf{p}_i + 6\sum_{i=1}^{3}\mathbf{p}_i + 12\mathbf{p}) \tag{4.16}$$

points $\mathbf{p}_1 \ldots \mathbf{p}_9$ corresponging to the neighbors of first and second order of $\mathbf{p}$.

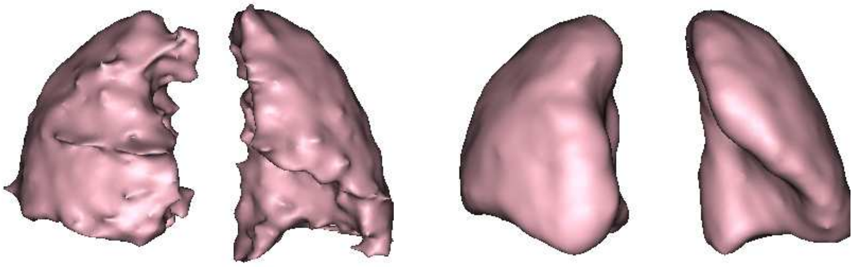

Figure 4.10: Example of an initial segmentation (left) and its refinement (right) with the deformable model of emission PET lungs.

As in the case of 2D deformable contours (see Appendix C), the external energy term F_{ext} can be obtained for each vertex $\mathbf{p}$ of the mesh by means of an interpolation of its values in the discrete contiguous positions to the vertex. Then, an efficient numerical implementation of the deformable surface will depend on the regularity and the simplicity on the obtained mesh.

Topology and geometric refinement Several techniques have been proposed in [196] and [74] in order to improve the quality of the resulting simplex mesh in topological and geometrical terms, using mesh characteristics such as the normal of a vertex, the simplex angle or the mean curvature. The topological quality is defined as the regularity of the number of edges which make up a face, since it is desirable to have a similar number of vertices for each face. Our meshes have been refined in order to fulfill these topological quality requirements by means of a succession of edge exchanges. Geometric refinement is useful to simplify the representation and to reduce computational costs, but it is not necessary for our application due to the relative small size of our objects and the closeness to the final solution of the initialization provided by the first initial segmentation step.

Influence of the regularization phase An example of the influence of this regularization phase is shown in Figure 4.10. In this figure, we can observe the effect of the deformable model refinement in the segmentation of PET lungs. The initial segmentation result (left in Figure 4.10) is not a smooth surface due to the nature of the PET scan. This is corrected in the deformable model stage, producing a regular surface better suited for subsequent algorithm stages. Care must be taken concerning the trade-off between the data and the smoothing terms in the deformable model evolution . In our application, a different set of parameters have been chosen for CT and PET images due to the different level of confidence on their contour gradients For instance, in PET scans, the smoothing term has more influence in order to define the boundaries where no significant edges are found in the image. This is done at the expense of loosing some local data provided directly from the image, such as in the upper part of the right lung in Figure 4.10. Nevertheless, the grey-level registration stage will recover this loss of information.

4.3 Results

In our work, 20 data sets composed of CT and PET (emission and transmission) scans of thoracic and/or abdominal regions provided by three different hospitals have been used. An example of structure segmentation results in both CT and emission PET images is shown in Figures 4.11, 4.12 and 4.13. In the first figure, 3D simplex meshes of final segmented structures, including skeleton (white), lungs (red), kidneys (yellow) and liver (blue), are superimposed on 2D coronal slices of CT and PET grey-level images. In the second (CT) and third (PET) figures, 2D axial slices of original grey-level volumes are superimposed with contours of final segmentation results corresponding to lung (red), kidney (green) and liver (blue) structures.

There has been no quantitative validation of these results because it would require too much additional time, since it involves the acquisition of manual ground-truth segmentations (in emission PET images, manual structure segmentations will not be reliable enough to assess a segmentation procedure). Furthermore, the end-goal validation criterion is not the segmentation accuracy, but the final mapping of the anatomy in both data sets.

Nevertheless, we have assessed segmentation results in two different ways: a visual inspection of these results by expert observers; and a retrospective segmentation evaluation from the assessment of final registration results.

Visual inspection of segmentation results has been done by superimposing them on original grey-level images and comparing corresponding structure contours. The visual accuracy criterion has taken into account our context of initial registration and it should be more severe if these segmented structures would be used as final results. Segmentation results have been positively evaluated by medical experts, in all CT and PET structures. Lung segmentation results are very accurate in CT images (in practice, we obtain global sub-voxel segmentation accuracy) while in emission PET ones, some insignificant errors (these errors do not induce further misregistrations) appear due to the low SNR of these images. Furthermore, the strategy of using the emission PET scan to refine lung segmentations obtained in the transmission PET images has proved to provide more accurate results, in particular in pathological cases. Concerning kidney segmentation, the symmetry plane procedure has proved to be very efficient and the only problem has been the classification of the inner part of these structures, that sometimes has different grey-level values. A 3D hole filling processing stage has solved this situation. The liver is the most difficult structure to segment both in CT and PET images due to the presence of several neighboring structures with similar grey-level values. A reasonable approximation of the liver is obtained, notably separating it from kidneys and heart. Nevertheless, we have sometimes found unidentified small structures close to the liver (i.e. the rate) that our procedure does not separate. In our application, this situation is not a major concern but in other medical segmentation applications it must be classified as a bad segmentation result.

The second way of evaluating segmentation result accuracy is based on the assessment of final registration results obtained by the proposed methodology. As a matter of fact, the transformation computation between CT and PET images strongly depends on the anatomical information that we are capable to extract from both data volumes, i.e., it depends on the segmentation result accuracy. Therefore, the evaluation of final registration results can also be seen as a retrospective assessment of the segmentation stage. This point is discussed in Section 8.4.

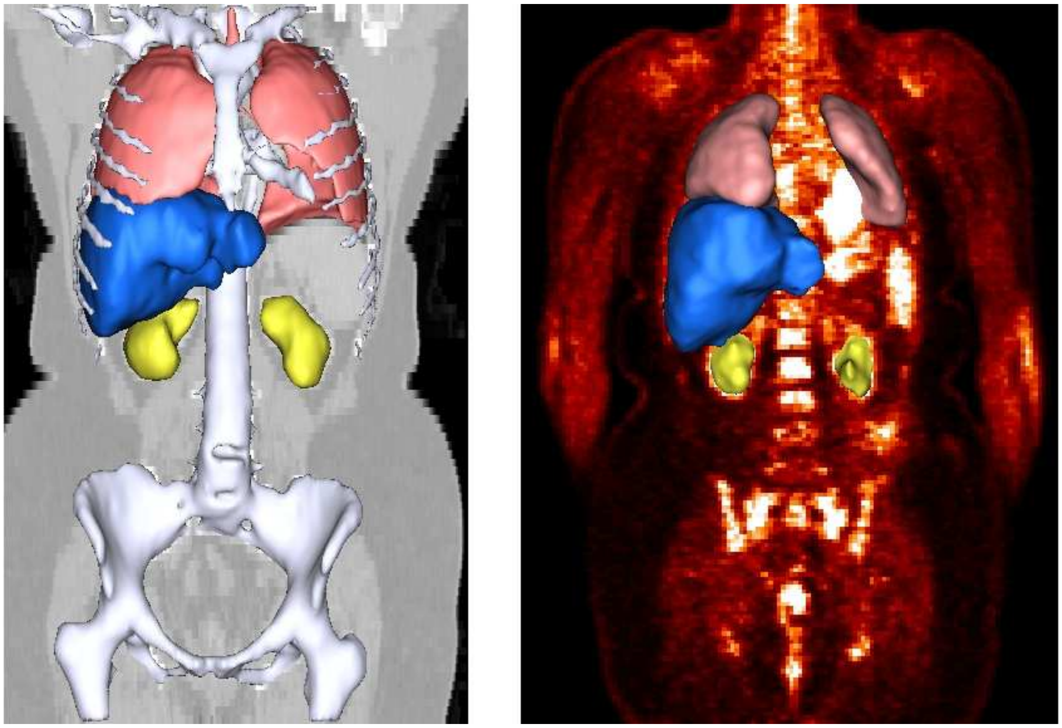

Figure 4.11: Simplex meshes of final segmented structures, including skeleton (white), lungs (red), kidneys (yellow) and liver (blue). Left: 3D rendering of CT segmented structures superimposed on a 2D coronal grey-level slice. Right: 3D rendering of PET segmented structures superimposed on a 2D coronal grey-level slice.

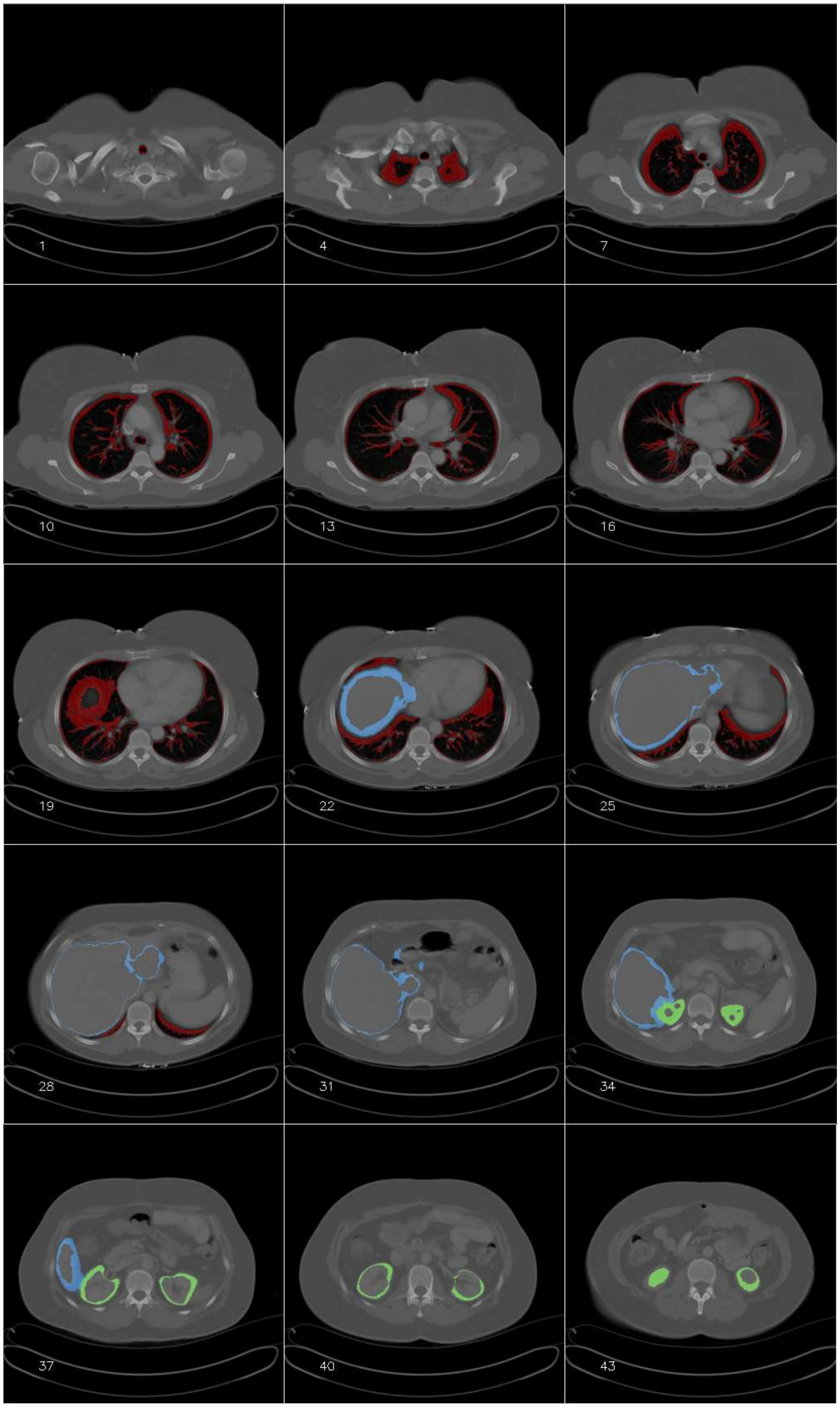

Figure 4.12: Contours of the CT segmented lungs (red), liver (blue) and kidneys (green), superimposed on 2D axial slices of the CT grey-level image.

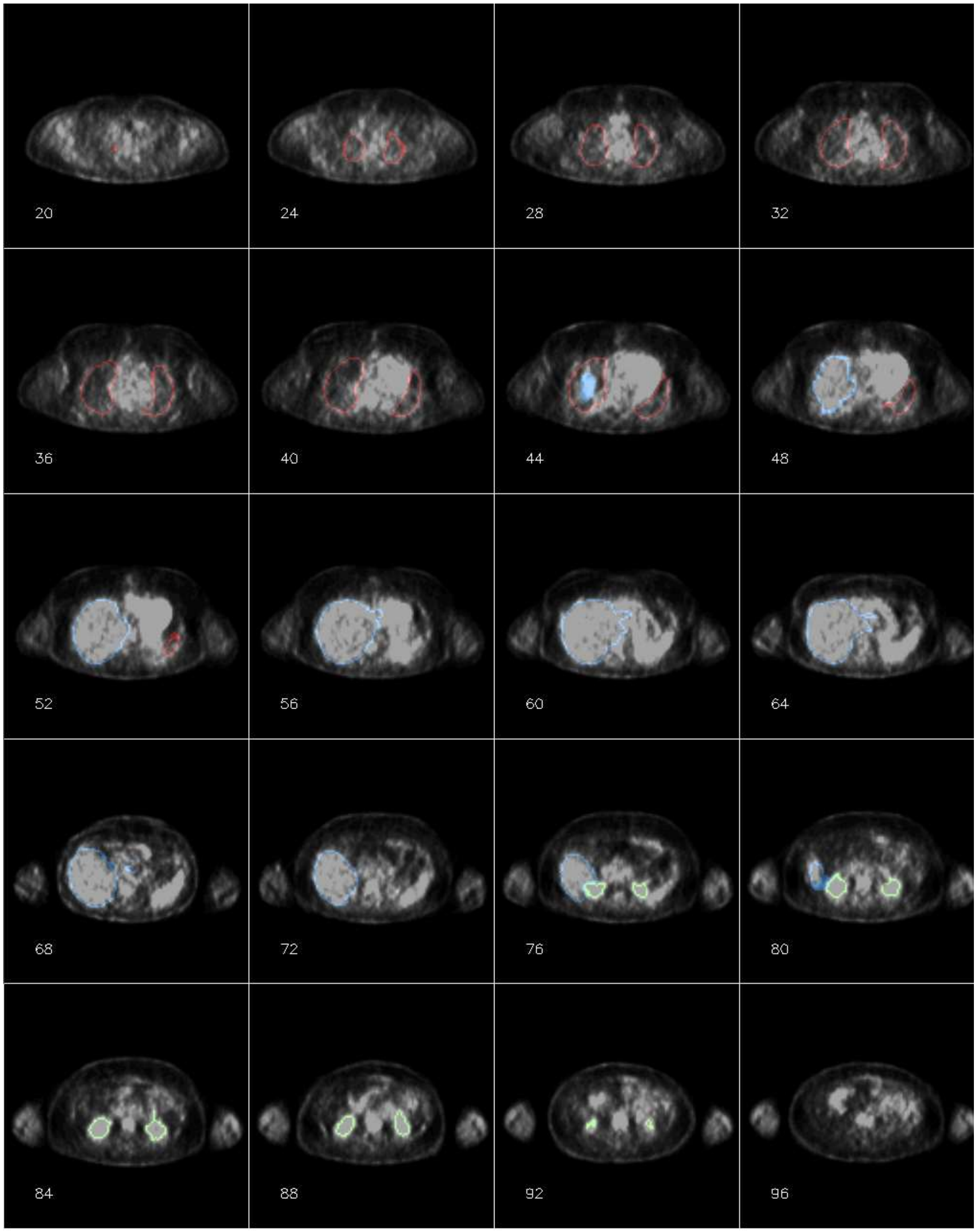

Figure 4.13: Contours of the emission PET segmented lungs (red), liver (blue) and kidneys (green), superimposed on 2D axial slices of the emission PET grey-level image.

4.4 Conclusions

In this chapter, we have presented an original hierarchical segmentation procedure aiming at segmenting several significant anatomical structures (lungs, kidneys, liver) in CT and emission PET images. The segmentation strategy has been implemented according to the special characteristics of the structures, the imaging modalities involved in the application and our context of initial registration.

The use of a hierarchical procedure takes advantage of stable spatial relationships between structures to construct the ROIs where the search of a given structure takes place. In this way, segmentation of the most difficult structures, such as liver in emission PET scans, has been achieved by using classical image processing techniques that could not been used without spatial constraints provided by simpler and previously segmented structures.

The ROI construction is very structure-specific because it is based on spatial relationships that can not be generalized to other structures or even to the same structures imaged with other modalities. For instance, in PET images acquired with new tracers (see Section 1.2.2), there are even less anatomical references than in FDG-PET scans and the segmentation of some structures in these images is, at the moment, quite impossible. Nevertheless, the general proposed segmentation procedure can be used in other recognition applications. As a matter of fact, we have employed a similar strategy in a brain internal segmentation application [64], obtaining very good results (see Appendix E for further details about this work). The developed strategy could be also used in non-medical applications, in structured scenes in which spatial relationships present high robustness. It is only required to identify and model them, and construct their corresponding ROIs.

The main concerns in this stage have been the robustness and the convergence speed of the procedure, therefore the segmentation methodology has been designed according to these requirements. Concerning robustness, consistency check routines have been added after segmentation steps involving less robust parameter tuning. An important drawback of the proposed strategy could be the error propagation between different segmentation stages, i.e., errors obtained in the segmentation of simpler structures will highly influence the segmentation of subsequent structures. Here again, the consistency checks included after each structure recognition appear to be very important and allow us to avoid these problems. The robustness of the segmentation procedure cannot be satisfactory enough in largely pathological cases when spatial relationships or structure morphology are considerably altered. For instance, if our segmentation procedure is applied to a case in which a kidney has been removed, the selection of the two most symmetrical components for kidney segmentation will provide incorrect results. On the other hand, a lung removal will not influence the final segmentation results, as discussed in Section 4.2.1. However, the proposed segmentation strategy allows an easy introduction of prior information and user interaction, that could solve these problems.

With respect to convergence speed, the procedure employs low computational cost algorithms in the initial segmentation phase, while the regularization phase has been implemented to assure a fast convergence as well. For a pair of images with standard dimensions [5], the initial segmentation phase takes about 60 seconds and the regularization phase about 90 seconds for each structure. These computation times fulfill time constraints of our algorithm, thus having a larger time margin for registration algorithms of the proposed methodology.

Therefore, using the proposed hierarchical procedure, a good trade-off between speed and segmentation accuracy has been achieved. A visual inspection of the results has been done because a quantitative validation would ask for a manual segmentation of several structures in CT and emission PET images. Furthermore, these manual segmentations will not be reliable enough for segmented structures in emission PET images due to their low SNR. The second way of evaluating segmentation result accuracy is based on the assessment of final registration results obtained by the proposed methodology, as discussed in Chapter 8.

---

[5] CT image with a size of 512 x 512 x 60 voxels and a PET image with 144 x 144 x 200 voxels.

CHAPTER 5

Structure registration

Contents

This chapter is devoted to the registration between the CT and PET homologous segmented structures. After a brief introduction (Section 5.1), the initial linear transformation computed between the segmented structures is detailed in Section 5.2. Thereafter, in Section 5.3, the Iterative Closest Point (ICP) algorithm and its use in order to initialize the grey-level registration stage is discussed. The following section presents two additional non-linear registration methods, called RMS-FFD and GVF-FFD, both based on the optimization of a Free-Form Deformation model. Finally, we evaluate and compare the results obtained with the three different surface non-linear registration methods in Section 5.5.

5.1 Introduction

The main goal of this stage is to find a transformation between homologous CT and PET anatomical features that have been recognized in the previous segmentation phase. The segmented structures employed in this stage include lungs, kidneys and liver. Skin and skeleton (in CT images) are also obtained in the segmentation procedure (see Chapter 4). Nevertheless, the skin is not used for registration purposes due to the excessive variability of this structure among the images without providing a reliable reference for guiding the registration of other internal structures. The skeleton is not used due to the difficulty of its extraction from PET scans, thus, it is only a complementary step in the segmentation of CT images but without playing a role in the registration procedure.

The transformation between segmented structures can be seen as an initialization of the final registration stage working with the whole set of grey-level values. The non-linear transformation chosen for the last registration stage is a FFD model, therefore, the structure registration procedure must, in some way, initialize the control points of the FFD grid close to their final displacement value, in order to make their optimization easier in the last step. Then, an important issue will be the interaction between both registration phases, as discussed in Section 6.2.

The registration method in this phase works with labeled images (a different label is affected to each 3D surface) and it must compute the deformation between corresponding 3D surfaces representing segmented thoracic and abdominal structures. Registration of 3D surfaces has been extensively treated in various fields of image processing and computer vision. Interesting reviews of these techniques can be found in [5 ; 177]. In our application, the registration procedure must deal with structures having different characteristics in terms of geometry, local irregularities and topology (even if they have in general spherical topology). For instance, the algorithm must deal with the concavities produced by the bronchia in lung surfaces while assuring an appropriate regularization in the most sphere-shaped structures such as the kidneys.

First, a linear registration is applied to the extracted homologous structures, as detailed in Section 5.2. Then, three different methods to compute the non-linear transformation between CT and PET anatomical features are implemented: a first one based on the ICP algorithm (see Section 5.3); and two methods derived from the FFD deformation framework, called RMS-FFD (see Section 5.4.2) and GVF-FFD (see Section 5.4.3), each of them with a different optimization method. A scheme of this stage, including the different phases of each structure registration method, is displayed in Figure 5.1.

5.2 Linear registration

In general, non-linear registration methods proposed in the literature compute an initial *rigid* or *affine* transformation in order to cope with global deformations between the images to register. In the developed procedure, before moving to the non-linear registration of the labeled images, the segmented structures can be easily used to au-

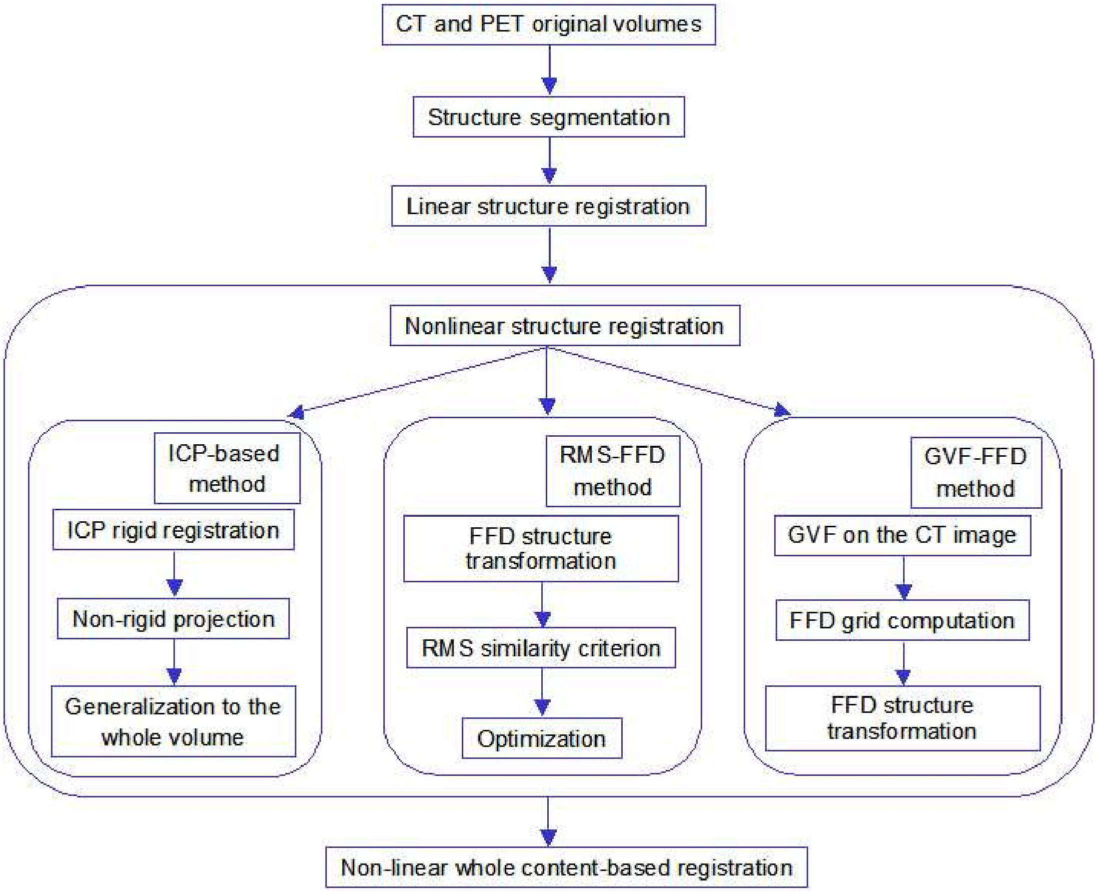

Figure 5.1: Scheme of the non-linear structure registration stage. Different phases corresponding to each developed method are shown. Left: ICP-based method. Center: RMS-FFD method. Right: GVF-FFD method.

tomatically establish a first approximation of the alignment. This includes translation and independent scaling in the three axes and cropping out the parts of the volumes without a correspondence or that have no interest for our application. This is achieved using a computed bounding box surrounding the structures to register in both modalities [1], as illustrated in Figure 5.2. Trivial as it may seem, this simple step allows the whole system to be independent of the actual field of view (FOV) of the original images, unlike the classical registration methods which need a manual adjustment (mainly in the z direction, as in [170]) before being able to apply them to CT and whole-body PET images. The difference in field of view of the images to register can cause difficulties, as anatomical structures identified in one image may not be present in the second. By using the proposed strategy, our image database may include volumes as dissimilar as torso CT and whole-body PET scans. The combination of the hierarchical segmentation strategy and this initial cropping stage allows us to register

---

[1] When there are several segmented structures (lungs, liver, kidneys) in one image, we use a unique global bounding box for all structures.

these images without the need of any user interaction, concerning their differences in FOV.

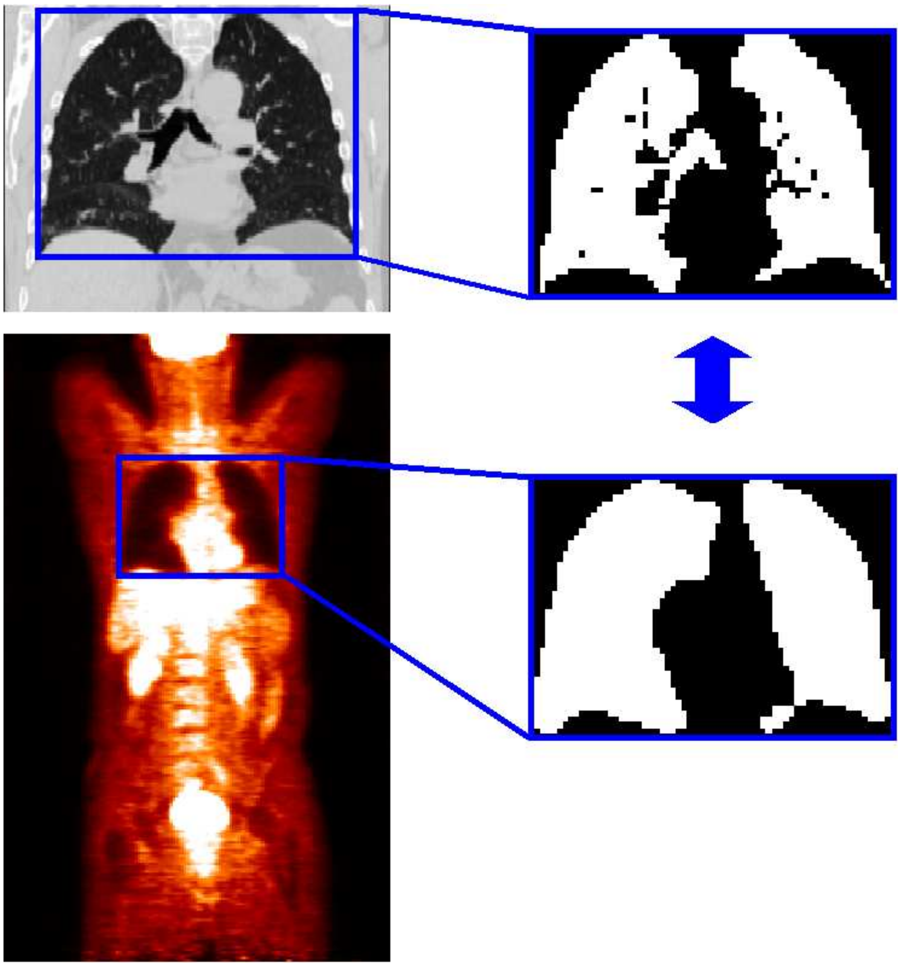

Figure 5.2: Example of different fields of view and bounding boxes computed around the structures. Left: original CT (top) and PET (bottom) images superimposed on the bounding box computed from lung segmentation. Right: input of the lung structure registration stage.

In addition, this approach simplifies and speeds up the registration procedure, by reducing the spatial resolution and size of the images. To this purpose, we assume that the anatomical regions visualized in both bounding boxes are in general equivalent in terms of real spatial dimensions. For instance, even if PET lungs are smaller than CT ones, they represent the same structure, and then, the CT and PET bounding boxes surrounding them must have approximately same dimensions in millimeters. Even if this hypothesis is not completely true, due to the deformations suffered by the organs between both image acquisitions (respiratory and cardiac movements, different part of the structure visualized in CT and PET images, ...), errors produced by this assumption are not important enough and will be compensated in the final grey-level registration phase. In the particular case of the lungs, one of the most deformable structures, this hypothesis is still valid due to the small movements suffered by the upper part of the lungs and the lower point of the lung (usually placed at the lower-left part of the right lung) between CT and PET images. Concerning liver and kidney segmented structures, our assumption does not affect the performance of the registration procedure.

Therefore, the sampling spatial resolution of each axis corresponding to the volume with higher resolution is modified in a way that the number of voxels match with that one of the lower resolution. In our application, the registration accuracy is limited by the resolution of the PET image, then the CT volume is downsampled, removing large quantity of data that do not provide significant information for registration. Once bounding boxes are built and downsampled, translational and scale degrees of freedom are already roughly recovered. Then, we apply a classical affine registration technique [171] between CT and PET bounding boxes, using the Powell's multi-dimensional direction set method [220] in order to find remaining parameters of the linear transformation (rotation and skews).

5.3 Iterative Closest Point (ICP) algorithm

One of the most successful linear registration feature-based methods is the Iterative Closest Point (ICP), proposed by Besl et al. [16], and it has been widely used with good results in several applications [207 ; 314 ; 151 ; 191]. A non-linear transformation is more approppriate in our application for initializing the subsequent grey-level registration phase, therefore, an adaptation of the rigid ICP transformation must be done. To this purpose, we employ the distance map provided by the ICP, as detailed in Section 5.3.2.

5.3.1 Linear transformation

The ICP algorithm iteratively tunes a rigid transformation to minimize the Euclidean distance between two element (point, line, triangle, ...) sets, the correspondences of which have been determined by proximity, as shown in Figure 5.3. Even if any kind of element sets can be used, the ICP algorithm establishes point-to-point correspondences using a given distance, so the data may need decomposition into point sets. Its popularity is mainly due to the fact that it always converges in a monotonous way towards the closest local minima, having a fast convergence rate in the first iterations.

S and S' being two surfaces, there exist two ways of performing the registration: either by determining for each point P' of S' its corresponding point P in the surface S, by means of a search under some constraints in a specific region of S; or by using an iterative estimation of these correspondences. The latter option is the approximation used by the ICP. Two steps are iterated in this algorithm until a given stop criterion is satisfied:

- let S be the surface of the reference image (the fixed one) and S' the surface of the target one (that one to transform). To each element $P'_i \in S'$, we assign the

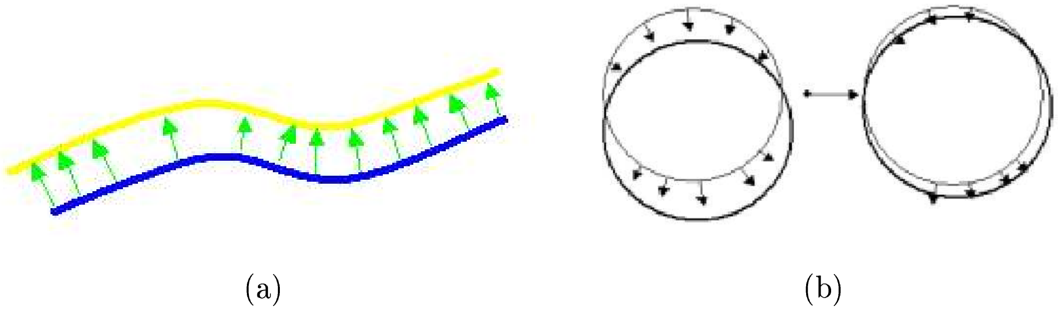
(a) (b)

Figure 5.3: ICP correspondences in a line (a) and a circle (b) registration case.

homologous element $P_j \in S$ which minimizes the following distance:

$$d^2(P'_i - P_j) \tag{5.1}$$

In order to speed up the procedure, a precomputed distance transformation of the volume containing S can be used. To achieve this, a Chamfer Distance Transform (CDT) technique is employed, avoiding the high computational cost associated to the exact Euclidean distance. The CDT, proposed by Rosenfeld et al. [238] and generalized in [28], is a fast algorithm that only uses two scans of the volume in order to compute an approximation of the distance transform.

- the computation of the parameters corresponding to the rigid transformation T which minimizes the following distance is performed:

$$D = \sum_i d^2(T(P'_i) - P_j), \tag{5.2}$$

The transformation is calculated by a quaternion-based method [126] in each iteration and the optimal transformation is applied to the surface S'.

As mentioned above, this scheme converges in a monotonous way towards the closest registration position.

5.3.2 Non-rigid adaptation

The rigid (translations and rotations) transformation provided by the ICP algorithm does not provide too much additional information with respect to the result given by the linear registration phase (Section 5.2).

Some non-rigid extensions of the ICP algorithm can be found in the literature. Feldmar et al [90 ; 91] define a 3D Euclidean point in 8D with normal and principal curvatures in addition to the spatial coordinates component, implementing global and local affine, volume spline and radial basis functions transformations.

However, we propose a simpler non-linear adaptation of the ICP algorithm, based on the distance map computed for this method, in order to cope with more local deformations and thus better initialize the subsequent grey-level registration phase. The procedure is composed of three stages: an estimation of the non-linear transformation between surfaces already registered by the rigid ICP method; a generalization of this estimation to the whole volume; and the initialization of the positions of the FFD control points that will drive the grey-level registration stage.

Non-rigid projection of the surface

The distance map computed for the ICP method by means of the CDT technique is employed to estimate an efficient, if primitive, non-rigid transformation. This distance map is used in order to project the elements P' of the surface S' onto their homologous closest points of the reference surface S. In fact, the non-rigid deformation field f is obtained by storing the distance between each pair of corresponding points. In order to compensate for the lack of regularization, each vector is averaged with the mean of its neighborhood. One example of the non-rigid projection is shown in Figure 5.4. It can be observed an evident improvement of the surface matching with respect to the rigid ICP results, in particular in most deformable parts such as in the diaphragmatic wall.

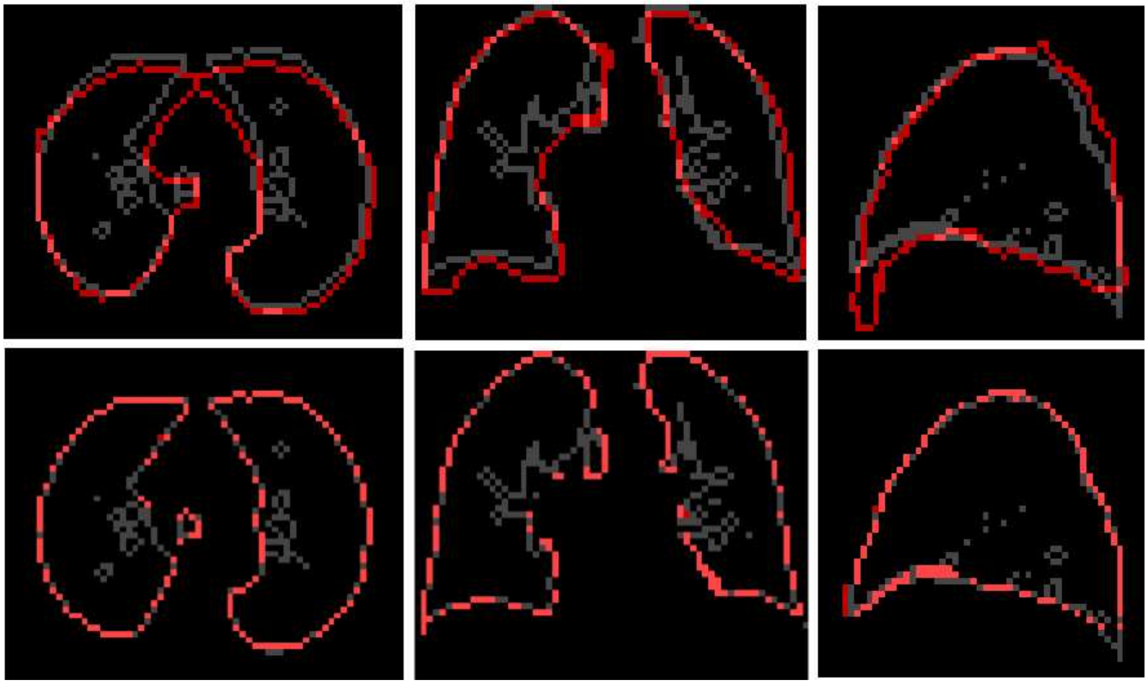

Figure 5.4: PET lung contours (red) registered with the rigid transformation provided by the classical ICP registration method (top) and non-rigid projection (bottom), superimposed on the homologous CT lung contours (grey).

Generalization of the deformation to the whole volume

The previous step provides a transformation only valid for image points placed on the surface of the structures. Therefore, this transformation must be extended to the whole structure volume, for instance by propagating the solution defined on the surface. An iterative diffusion process, proposed in [99], is applied to the deformation vector field f by forcing it to have a zero Laplacian $\nabla f = \vec{0}$. This technique consists in solving the zero Laplacian field, knowing the limit conditions, by changing (in a parallel way) the non-limit values into the mean of its neighbor values, and by iterating these changes until convergence is reached. For each spatial dimension, the procedure is initialized by a linear interpolation of the deformation values on the surface and then their propagation onto the interior of the volume is done.

Initialization of the FFD control points

Once this non-rigid transformation is obtained, we need to transfer it to the FFD grid that will guide the grey-level registration phase, i.e. initialize the FFD control points with the 3D dense vector field provided by the extended ICP algorithm. This is achieved by a classical linear interpolation, assigning to each control point the 3D dense vector field values in its neighborhood, weighted by the distance to the control point. It is clear at this point that the accuracy of this FFD grid initialization will strongly depend on the number of control points, meaning that we will need a enough populated grid to recover information provided by the extended ICP algorithm.

5.3.3 Results and conclusions

Some results obtained by using this registration procedure are shown in Figure 5.5. The evaluation of their registration accuracy is done in Section 5.5. Anyway, by simple visual inspection of the images, it can be appreciated a noticeable improvement on the CT and PET structure matching with respect to linear registration results. This enhancement relies on the better proximity of the PET structure contours to the CT ones, in particular in regions having more global non-linear deformations. As a matter of fact, this method works better when applied to more sphere-shaped structures such as the liver, as illustrated in Figure 5.5, due to a lower number of ambiguities in the projection step.

Nevertheless, some drawbacks associated with this technique must be pointed out. Some erroneous deformations appear around structures without an obvious correspondence. This is due to the projection of the segmented structure contours which is very sensitive to large differences between CT and PET anatomical features. One example concerns the errors found in the lungs, caused by the presence of large local irregularities that the ICP-based structure registration method cannot cope with. In fact, there is a trade-off between the regularization of the results and the capacity of the method to cope with more local deformations, which prevents this technique to provide better transformations in these zones.

Another criticism on this method concerns the simplicity of the generalization of the deformation on to the whole volume, based on a zero Laplacian condition. Furthermore, it is a time consuming step, which is a critical point in our methodology. Some modifications could be done in order to speed up the algorithm convergence such as the use of a multi-resolution approach in the propagation. Further work must be done in order to improve this stage.

Finally, another drawback of this structure registration procedure involves the interaction with the FFD-based registration, that is solved in such a way that some information can be lost and, consequently, some of the precision achieved in the registration of the segmented structures can be lost as well.

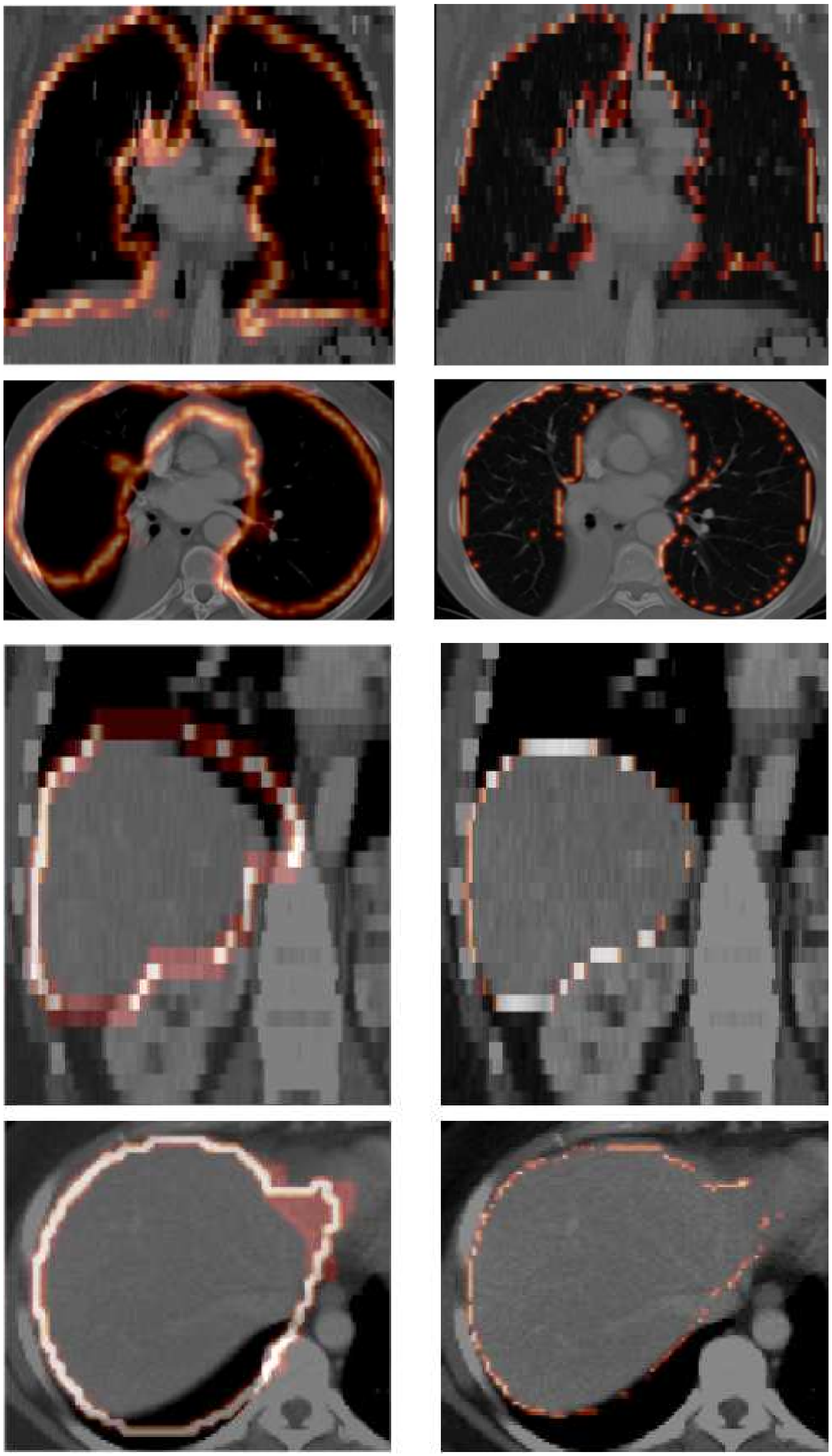

Figure 5.5: Structure registration results obtained with the ICP-based method. Grey-level coronal and axial CT slices are superimposed on contours (red temperature) of registered PET lungs (top rows) and liver (botton rows). Left: PET structures registered with a linear transformation. Right: PET structures registered with the ICP-based method.

5.4 FFD-based non-linear structure registration algorithms

Due to the limits of the ICP-based procedure concerning the interaction with the grey-level registration stage, we have chosen to integrate both structure and grey-level registration phases within the same FFD deformation framework, originally intended only for the grey-level stage. Therefore, thoracic and abdominal PET structures in the labeled PET image will be mapped onto their homologous CT ones in the labeled CT image. The main advantages of this strategy are: the availability of more degrees of freedom in order to model more local deformations; and the simplification of the interaction between both phases. On the other hand, this approach implies an increase of the computational burden of the registration procedure, as shown in Section 5.5.

5.4.1 Free-Form Deformation model

As justified in Section 2.7, a non-linear transformation based on B-spline Free-Form Deformations (FFD) has been chosen to model differences to cope with in our application. FFDs, introduced by Sederberg et al. [253] and first used by Rueckert et al. [242] for registration purposes, are a particular case of non-linear transformations computed by means of a linear combination of spline basis functions.

In this technique, deformations of the floating volume (the PET scan in our application) are achieved by tuning an underlying mesh of control points, but unlike the case of TPS, FFD employs a regular mesh of control points equally distributed on the image, thus avoiding the complex control point selection phase needed in TPS approaches. On the other hand, several control points of the FFD grid will be located in places with no interest for registration purposes, thus increasing computational cost of the procedure without providing additional information.

Once the FFD grid has been optimized, control point displacements are interpolated to obtain a smooth and continuous C^2 deformation field for the whole image, using some spline basis functions. The nature of the chosen basis function will strongly influence the local control of the deformation. For instance, if cubic B-spline basis functions are used, we will obtain a more local control, at the expense of a higher number of control points in the FFD grid. On the other hand, if Bernstein basis functions are employed, a lower number of control points is required, but we will obtain less local deformations as well. In medical applications involving elastic deformations in which a high local control is desired, B-splines is the most frequently used basis function [76 ; 123 ; 190 ; 250 ; 234 ; 241].

A B-spline based FFD can be written as a 3D tensor product of one-dimensional cubic B-splines, producing a transformation separately for each axis. Let Φ denote an uniformly spaced grid of $n_x \times n_y \times n_z$ control points $\phi_{i,j,k}$ with a spacing of δ, where $-1 \leq i < n_x - 1, -1 \leq j < n_y - 1, -1 \leq k < n_z - 1$. Then, the non-linear transformation for each image point x,y,z is computed as:

$$u(x, y, z) = \sum_{l=0}^{3} \sum_{m=0}^{3} \sum_{n=0}^{3} \theta_l(u)\theta_m(v)\theta_n(w)\phi_{i+l,j+m,k+n} \tag{5.3}$$

Here, $i = \lfloor x/n_x \rfloor - 1$, $j = \lfloor y/n_y \rfloor - 1$, and $k = \lfloor z/n_z \rfloor - 1$, denote the index of the control point cell containing *(x,y,z)*, and $u = x/n_x - \lfloor x/n_x \rfloor$, $v = y/n_y - \lfloor y/n_y \rfloor$, and $w = z/n_z - \lfloor z/n_z \rfloor$ are the relative positions of *(x,y,z)* in the three dimensions, θ_0 through θ_3 being 1D cubic B-splines:

$$\begin{aligned} \theta_0 &= (1-u)^3/6 \\ \theta_1 &= (3u^3 - 6u^2 + 4)/6 \\ \theta_2 &= (-3u^3 + 3u^2 + 3u + 1)/6 \\ \theta_3 &= u^3/6. \end{aligned} \tag{5.4}$$

As mentioned above, a very convenient property of B-splines is the fact that they have a limited support, thus providing us a local control of the transformation, which contributes to reduce significantly the amount of computation needed during the optimization process. Furthermore, thanks to this compact support and the separability as a tensor product, the B-spline can be precalculated and stored in an array to accelerate the process. A 2D grid of control points and a 3D teddy bear deformed with a FFD model are shown in Figure 5.6. This figure illustrates the effect of control point displacements on the object deformations.

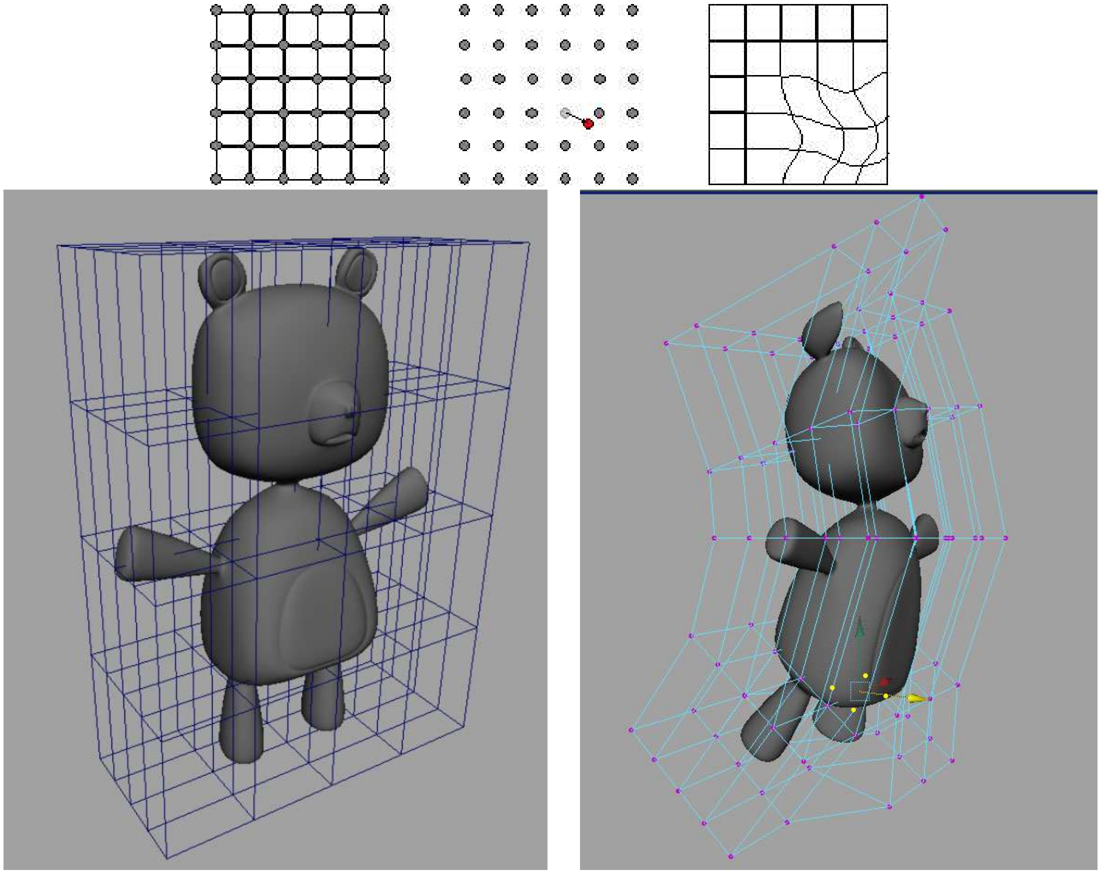

Figure 5.6: A 2D grid of control points and a 3D teddy bear are deformed with a FFD model. The displacement of several control points of the grid induces smooth deformations of the objects.

The number of control points of the grid is chosen according to the magnitude of the local deformations to cope with, the resolution and the size of the images to register. In general, we have experimentally set the distance between control points to 20mm in the bounding box around the structures to register, that has proved to provide accurate enough results.

5.4.2 RMS-FFD

Once the transformation model is chosen, the similarity criterion that will drive the optimization of the control point displacements must be defined. The choice of this metric is, in this case, straightforward as we are working with labeled images with a linear intensity relation. Thus, the Root Mean Square (RMS) difference of corresponding voxel intensities, summed across the whole volume, will be used to determine the optimal deformation parameters [2].

It should be pointed out that employing RMS as similarity criterion allows us to deal with several structures in each image at the same time to perform the registration, by assigning adequate values to the labeled structures. For instance, right lung and liver are spatially close, so we give them values as most separated as possible in the color scale. Moreover, additional weights can be used in order to further penalize deformations overlapping close structures, such as the lungs and the liver.

Optimization

The optimization of the transformation parameters (i.e. control point displacements, $\phi_{i,j,k}$) is achieved by applying iteratively a gradient descent technique to all control points simultaneously, as proposed by Rueckert et al. [242], advancing along the gradient direction until no further improvement of the similarity measure is found:

$$\phi_{i,j,k} = \phi_{i,j,k} + \mu \nabla \phi_{i,j,k}, \tag{5.5}$$

where μ is the optimization step size and $\nabla \phi_{i,j,k}$ is the gradient estimation, that must be re-calculated after each iteration of the procedure.

This gradient estimation is performed by computing local differences over the control point grid: for every control point, one step displacements are tried along each axis, and subsequent differences in the similarity criterion are measured. If one of these displacements provides better similarity measures (i.e. better registration results), the control point displacement is updated.

This procedure is embedded in a multi-step framework, in order to cope with more global deformations at the beginning and more local ones at the end. Furthermore, a local spring force regularization term, pulling each node towards the centroid of its neighboring nodes, has been added to avoid overfitting and to prevent the nodes from intersecting, which could lead to unwanted alterations of the structure topology. The following scheme summarizes the optimization of one control point displacements:

---

[2] from now on, *RMS-FFD* is used to refer this method.

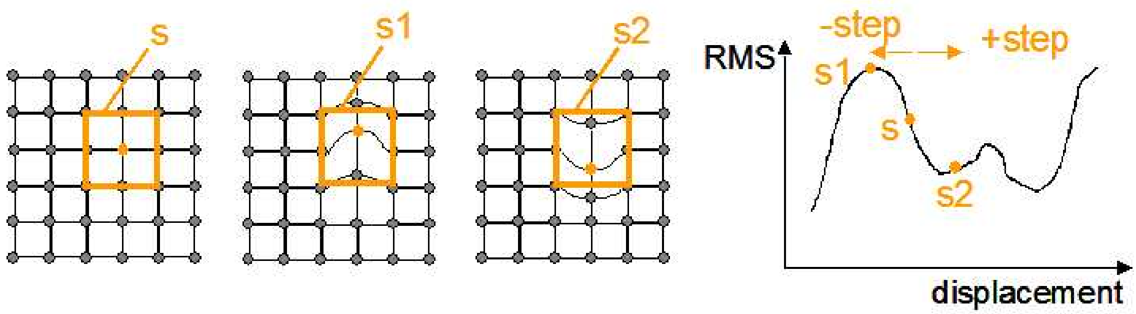

Figure 5.7: Gradient estimation based on local differences over the grid of control points.

Algorithm 1 Optimization of node displacements with a gradient estimation

```
for all 3 degrees of freedom (x,y,z) of each control point (i,j,k) do
    computation of the similarity measure ($s$ in Figure 5.7) in a small window around the control point
    set control point displacement to + step size: $\phi_{i,j,k} = +\mu$
    re-computation of the similarity measure ($s1$ in Figure 5.7)
    set control point displacement to - step size: $\phi_{i,j,k} = -\mu$
    re-computation of the similarity measure ($s2$ in Figure 5.7)
    if $s1$ or $s2$ is better than $s$ then
        update control point displacement: $\phi_{i,j,k} = \phi_{i,j,k} + \mu \nabla \phi_{i,j,k} = \phi_{i,j,k} + \mu(s2 - s1)$
    end if
end for
application of local spring regularization term
```

Results and conclusions

Examples of results obtained by registering PET segmented structures (lungs and liver) with their homologous in CT images using the RMS-FFD and linear registration methods are displayed in Figure 5.8. On the left part of the figure, 2D axial and coronal slices of superimposed CT (grey) and registered PET (red) structures are shown. In a similar way, two different views of the superimposition of the 3D CT (blue for CT lungs and green for CT liver) and registered PET (brown for registered PET lungs and red for registered PET liver) rendered structures are also shown. We can visually appreciate the good performance of the RMS-FFD algorithm in both lung and liver cases, even with largest and most local deformations. A complete evaluation of these results is achieved in Section 5.5.

It is worth noting that using this scheme to register the segmented images raises convergence and computational cost issues that could be avoided if a simpler registration method, like the ICP-based method of Section 5.3, were applied instead. However, this implementation melts elegantly with the next registration stage, integrating as just an extra step of the multi-resolution chain used in most voxel-based techniques. Moreover, as seen in Figure 5.8, the obtained transformation provides a high quality and valuable initialization that will make easier and notably accelerate the final grey-level registration step.

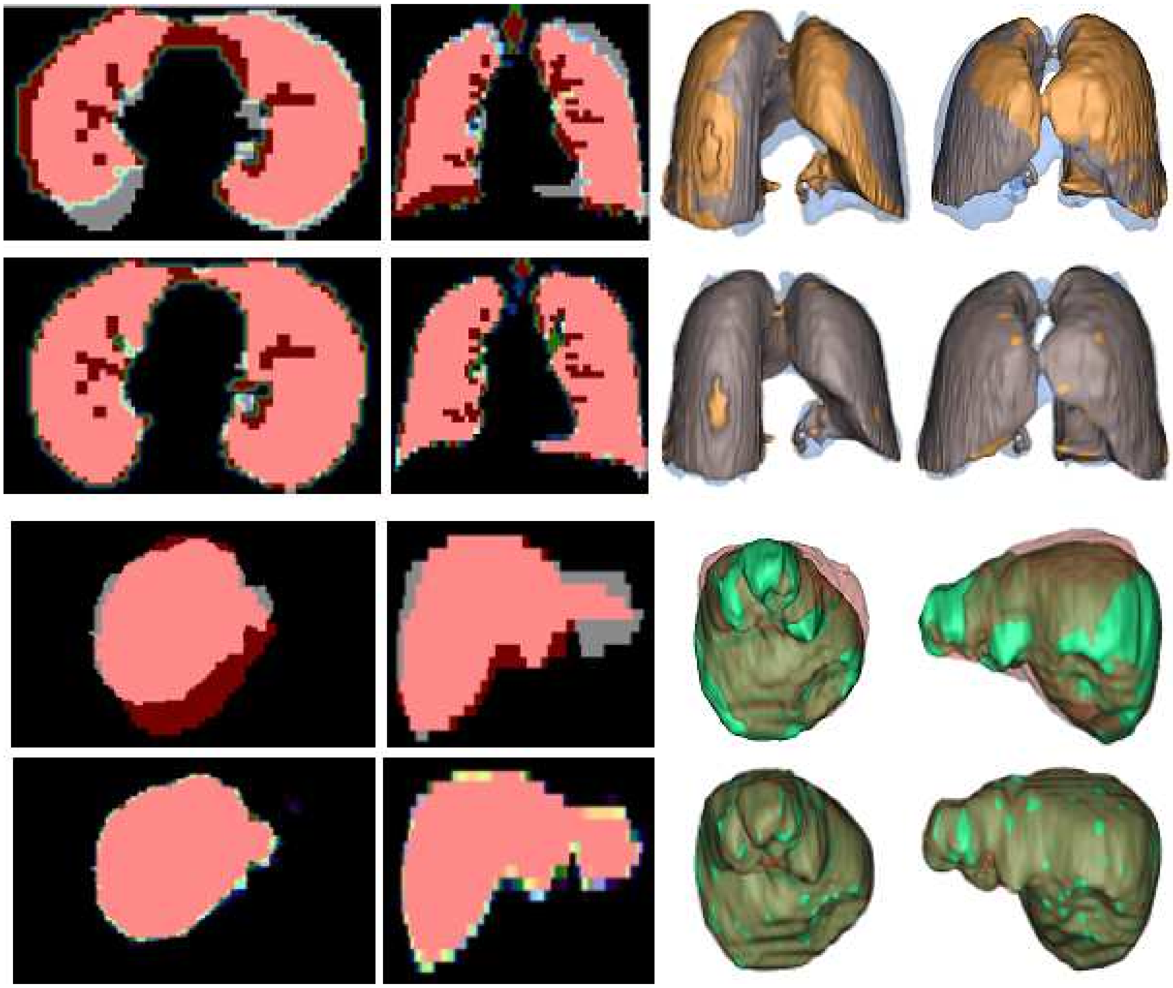

Figure 5.8: Structure registration results obtained with the RMS-FFD method. Left part of the figure: 2D coronal and axial slices of CT (grey) segmented lungs (top rows) and liver (bottow rows) are superimposed on their homologous PET structures (red), registered with a linear transformation (first and third row) and with the RMS-FFD method (second and fourth row). Right part of the figure: a 3D representation of the same structures is shown (CT lungs in blue, registered PET lungs in brown, CT liver in green and registered PET liver in red).

5.4.3 GVF-FFD

An important drawback of the RMS-FFD method in our application, that is quite limited in terms of convergence times, is precisely its associated high computational burden. This is due to the nature of the optimization procedure, in which a local gradient estimation is needed at each iteration to update the control point displacements of the whole grid. For instance, in a typical grid of 10 nodes per dimension, the algorithm must compute at each iteration the gradient for 3000 parameters. Multi-resolution and multi-grid approaches accelerate the convergence of the algorithm, but the gradient estimation remains a problem in terms of computation time.

Optimization

We propose an original way to speed-up the optimization of the control point displacements, using a 3D dense vector field v computed over the contours of segmented target structures (in our case, CT structures) instead of the gradient-based procedure employed in the RMS-FFD algorithm. This vector field provides a displacement vector at each image voxel pointing the direction towards CT structure contours, thus giving us information about how a surface must evolve to assure a good matching. Therefore, we update control point displacements of the FFD grid at each iteration with the information provided by displacement vectors located in the neighborhood of each control point:

$$\phi_{i,j,k} = \phi_{i,j,k} + \mu \frac{1}{R} \sum_{r=0}^{R} p(r,i,j,k) v_r, \tag{5.6}$$

where R denotes the number of floating structure contour points under the influence of a given control point and $p(r,i,j,k)$ is a weight depending on the distance between the contour and the control points.

The main advantage of this approach is that the vector field must be computed only once, unlike the gradient estimation that must be updated at each iteration. Moreover, as we work with structure contours, voxel scannings will take lower times as if whole volumes were considered, thus reducing even more the computational burden of the algorithm. The following algorithm summarizes this optimization procedure:

There are several options to obtain v. The simplest one could be the use of some kind of vector distance transform technique such as the CDT (already used in the ICP-based registration algorithm, see Section 5.3), computed on CT structure contours. Another possibility concerns the use of the Gradient Vector Flow (GVF) technique, described in Section 4.2.3, that is usually employed to guide deformable models in segmentation applications, but to our knowledge, it has not been used before to guide a FFD model in registration algorithms. The advantage of the GVF with respect to the CDT approach is the presence of a regularization term controlling the trade-off between the smoothness of the vector field and the fidelity to the contour gradients of the image. As a matter of fact, a smooth vector field is better suited for optimizing FFD control points, at the expense of slightly increasing the computational cost of the algorithm due to the regularization term. However, a trade-off must be taken between

Algorithm 2 Optimization of node displacements with a 3D dense vector field

```
for all segmented structures to register do
  contour detection of the structures to match {already registered in a linear way}
  computation of $v$ over target structure contours
  while $\mu \neq \mu_{end}$ do
    while distance(n) $\leq$ distance(n-1) do
      for all control points do
        computation of $r$
        store $v$ values of $r$ (i.e., $v_r$) and weight them with the distance with respect to the control point ($p(r, i, j, k)$)
        update control point displacement with Equation 5.6
      end for
      application of local spring regularization term
      apply FFD grid to floating structure contours
      computation of the distance between target and floating contours
    end while
    divide $\mu$ by 2
  end while
end for
```

outlier rejection and the nature of the local deformations to cope with in the vector field computation.

Therefore, the GVF technique is chosen to furnish the 3D dense vector field [3]. The left part of Figure 5.9 shows a 2D axial slice of the superimposition of CT lung contours on the GVF field computed over them. It can be observed that despite of the regularization term, the local irregularities of the lungs are well coped with.

Once v is obtained, we need to update the control point displacements of the FFD grid according to the GVF vector field. As we are working with structure contours, we only take into account the v values of the set of floating structure contour points r under the influence of each control point. These v_r values are weighted according to their distance to the control point under consideration $p(r, i, j, k)$, and the mean of the resulting vectors are taken as the optimal control point displacement direction. The magnitude of the displacement also depends on the step (μ) of the optimization procedure. At the end of each iteration, a local spring regularization term is applied in a similar way as in the RMS-FFD algorithm (see Section 5.4.2).

The convergence of the algorithm depends on the quality of the computed vector field. As a matter of fact, in some cases, the evolution tends to oscillate in the vicinity of CT structure boundaries. In order to avoid that, the distance between target and registered floating contours is computed at the end of each iteration and is used as a stop criterion when the contour evolution starts to oscillate. Furthermore, we have introduced the procedure in a multi-step framework in order to cope with large deformations in the first iterations and with more local ones at the end.

---

[3] from now on, *GVF-FFD* is used to refer this method.

An example of the evolution of PET lung contours towards their corresponding CT contours is shown in Figure 5.9. It can be appreciated the remarkable improvement of the contour match after applying the GVF-FFD registration method (right in Figure 5.9) with respect to results obtained by a linear registration procedure (center in Figure 5.9). Nevertheless, some problems appear in regions undergoing more local deformations.

It must be pointed out that in our registration context, in which we need to register several thoracic and abdominal structures at the same time, some problems could arise if structures overlap with non-corresponding structures since the labels are not taken into account in the contour evolution. We deal with this situation by computing the GVF field and making the floating contours for each structure evolve independently. In fact, possible errors produced by that will be corrected in the subsequent grey-level registration phase.

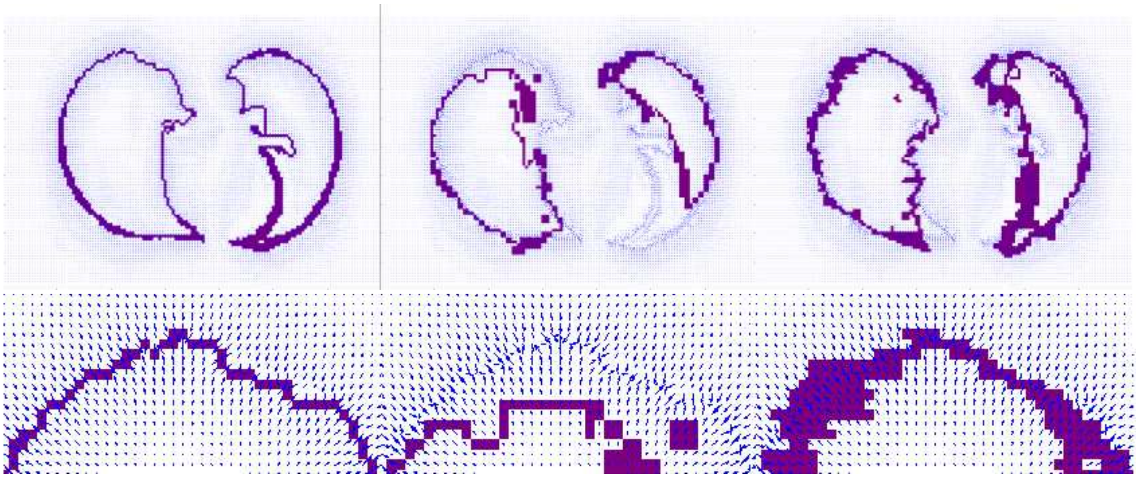

Figure 5.9: Contour evolution of PET lung contours towards their corresponding CT ones using the GVF-FFD method. A 2D axial slice of the GVF field computed over the CT contours is superimposed on them (left), and on PET contours before (center) and after (right) applying the GVF-FFD method. Top: 2D axial slice. Bottom: detail.

Results and conclusions

Examples of results obtained by registering PET segmented structures (lungs and liver) with their homologous in CT images using the GVF-FFD and linear registration methods are displayed in Figure 5.10. On the left part of the figure, 2D axial and coronal slices of superimposed CT (grey) and registered PET (red) structures are shown. In a similar way, two different views of the superimposition of the 3D CT (blue for CT lungs and green for CT liver) and registered PET (brown for registered PET lungs and red for registered PET liver) rendered structures are also shown. By means of a simple visual inspection of the results, we can appreciate that we obtain better registration accuracy using the GVF-FFD method with respect to the linear registration algorithm, but it does not reach that one derived from the use of the RMS-

FFD registration procedure. On the other hand, the GVF-FFD technique converges much faster towards acceptable (in our application) transformations, as detailed in Section 5.5, in which a complete evaluation of these results is also presented.

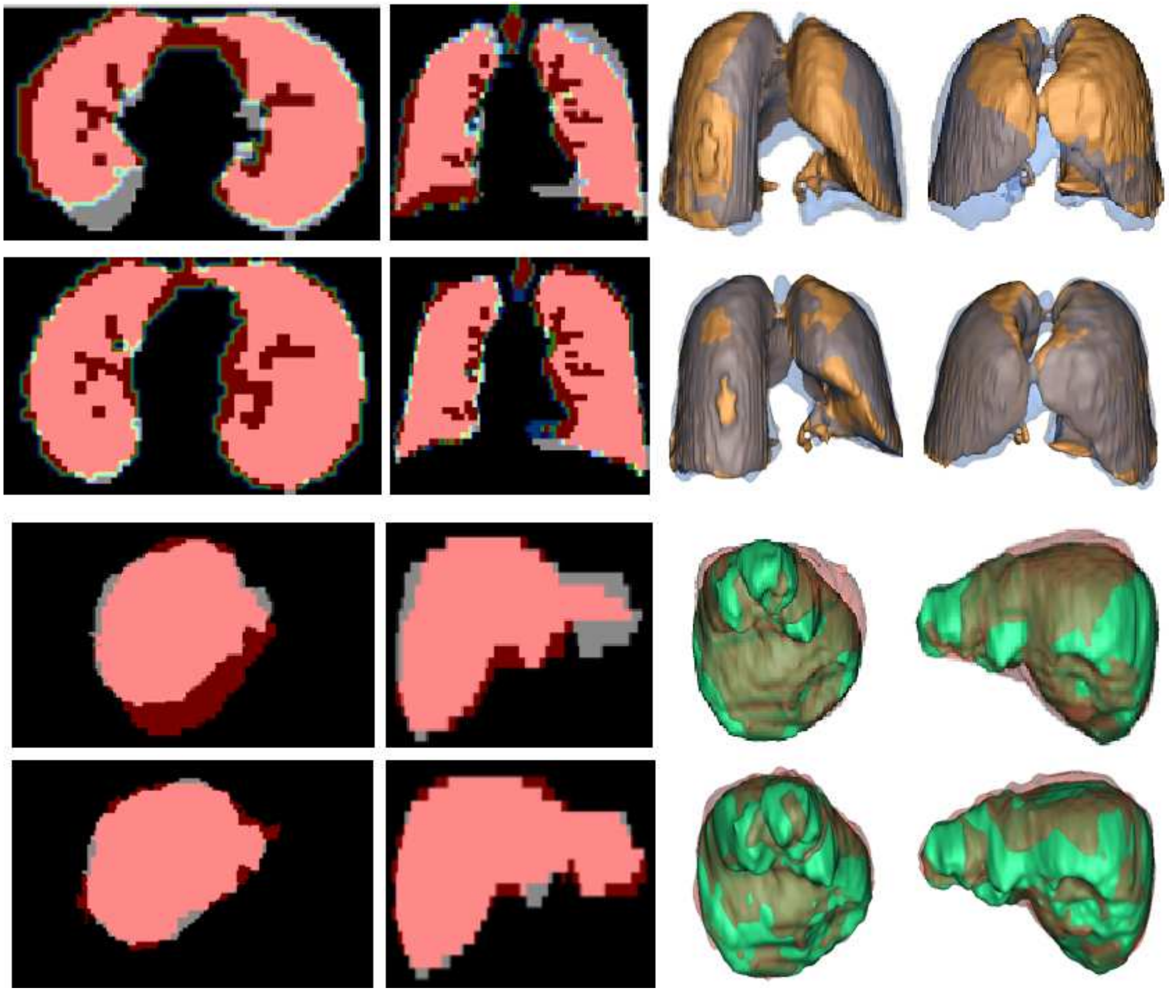

Figure 5.10: Structure registration results obtained with the GVF-FFD method. Left part of the figure: 2D coronal and axial slices of CT (grey) segmented lungs (top rows) and liver (bottow rows) are superimposed on their homologous PET structures (red), registered with a linear transformation (first and third row) and with the GVF-FFD method (second and fourth row). Right part of the figure: a 3D representation of the same structures is shown (CT lungs in blue, registered PET lungs in brown, CT liver in green and registered PET liver in red).

5.5 Evaluation of structure registration methods

5.5.1 Quantitative measures

The visual inspection of results provided by the three structure registration methods described in this chapter is not enough for evaluating in a proper way their registration accuracy. Therefore, we have computed four different measures on target and registered floating structures aiming at assessing, in a quantitative way, the performance of each one of the proposed structure registration techniques.

Let T and F be the set of voxels corresponding to the target and the registered floating structures respectively and the operator $|A|$ be the cardinality of the set of voxels A. The four criteria [196] used for estimating registration accuracy are the following:

- overlap Measure
$$OM = \frac{\mid T \cap F \mid}{\mid T \cup F \mid}; \tag{5.7}$$
- similarity
$$SIMI = 2\frac{\mid T \cap F \mid}{\mid T \mid + \mid F \mid}; \tag{5.8}$$
- sensitivity
$$SENS = \frac{\mid T \cap F \mid}{\mid T \mid}; \tag{5.9}$$
- specificity
$$SPEC = \frac{\mid T \cap F \mid}{\mid F \mid}. \tag{5.10}$$

The overlap measure (OM) is a classical criterion to evaluate the matching between two structures and consists of the quotient between intersection and union of structures to evaluate, which is equal to 1 if total overlap is achieved (best registration). The similarity criterion (SIMI) provides an estimation of the reliability of the superimposition of both structures, which is also equal to 1 for the ideal case. The sensitivity (SENS) and specificity (SPEC) measures give us additional information about how the overlap of both structures is achieved. For instance, if two structures provide a low sensitivity value but a high specificity one, it means that the registered floating structure is too small and is included on the target structure. Both criteria are also equal to 1 if total overlap is achieved.

Table 5.1: Evaluation of structure registration methods. OM: overlap measure. SIMI: similarity. SENS: sensitivity. SPEC: specificity. Values corresponding to these measures represent the mean and the standard deviation of these measures computed on the structure database.

		Lungs	Liver
ICP	OM	0.731 ± 0.129	0.820 ± 0.034
	SIMI	0.838 ± 0.094	0.901 ± 0.021
	SENS	0.831 ± 0.171	0.893 ± 0.026
	SPEC	0.869 ± 0.039	0.909 ± 0.033
RMS-FFD	OM	0.857 ± 0.037	0.902 ± 0.006
	SIMI	0.923 ± 0.022	0.949 ± 0.003
	SENS	0.996 ± 0.003	0.998 ± 0.001
	SPEC	0.860 ± 0.035	0.904 ± 0.006
GVF-FFD	OM	0.821 ± 0.065	0.876 ± 0.016
	SIMI	0.901 ± 0.040	0.934 ± 0.009
	SENS	0.956 ± 0.048	0.987 ± 0.014
	SPEC	0.852 ± 0.038	0.886 ± 0.006

5.5.2 Results

We have applied the three structure registration methods detailed in this chapter to a database composed of 20 pairs of deformable structures (13 lungs and 7 livers). These structures have been obtained by either applying the segmentation procedure described in Chapter 4 to CT and PET images of the same patient (8 cases) or using the NCAT phantom [254 ; 255] for generating structures at different stages of the respiratory and cardiac cycles (12 pairs of structures). It must be pointed out that differences between segmented structures coming from real CT and PET data are larger than those from the NCAT phantom and, in a similar way, lung registration is more challenging than liver one due to the presence of large surface irregularities to deal with.

Table 5.1 summarizes statistics (mean value ± standard deviation) furnished by the quantitative assessment measures computed on the whole set of target and registered floating structures. Figures 5.11, 5.12, 5.13 and 5.14 show registration accuracy measures obtained for each pair of structures of the database. We have separated results of lung and liver structures in order to analyze the behavior of the registration techniques with respect to different structures.

The four studied evaluation criteria furnish consistent results on both set of images (patients and NCAT) and confirm visual inspection conclusions with respect to the comparison between the three structure registration methods. That is, the RMS-FFD technique provides the most accurate registration results, while the GVF-FFD method still clearly surpasses the ICP-based registration technique. The three evaluated methods provide more accurate results when working with liver than lung structures, and in a similar way, they perform slightly better with data coming from the NCAT phantom than from CT and PET patients. This is due to the difference nature of the deforma-

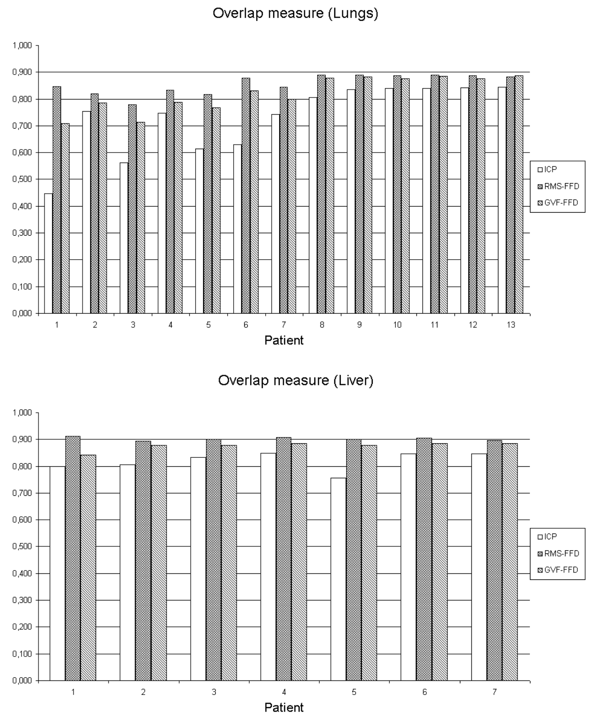

Figure 5.11: Overlap measure graph of structure registration methods applied on 13 lung (top) and 7 liver cases (bottom).

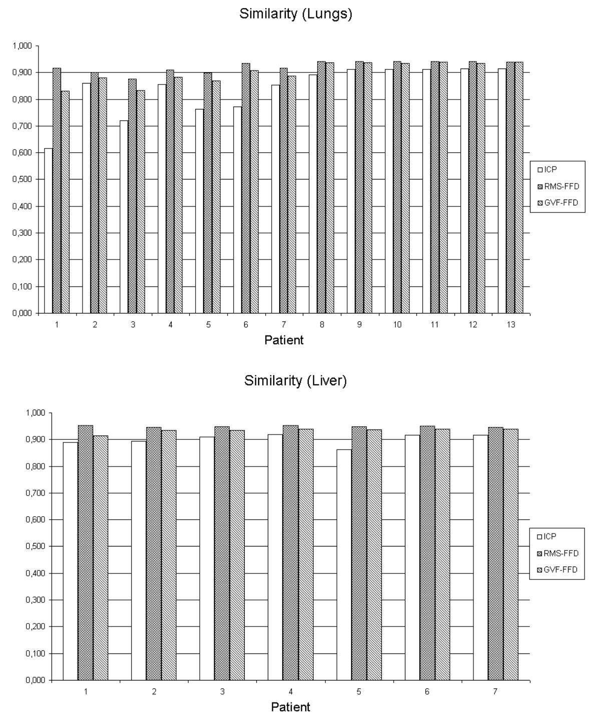

Figure 5.12: Similarity measure graph of structure registration methods applied on 13 lung (top) and 7 liver cases (bottom).

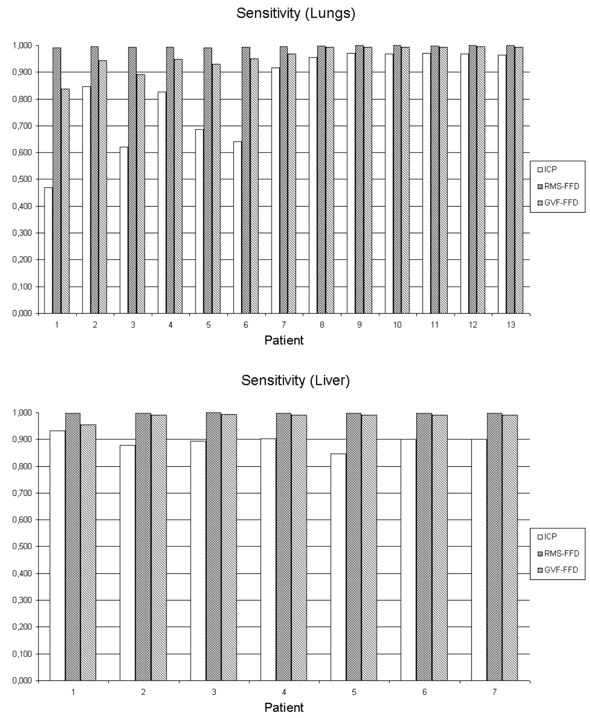

Figure 5.13: Sensitivity graph of structure registration methods applied on 13 lung (top) and 7 liver cases (bottom).

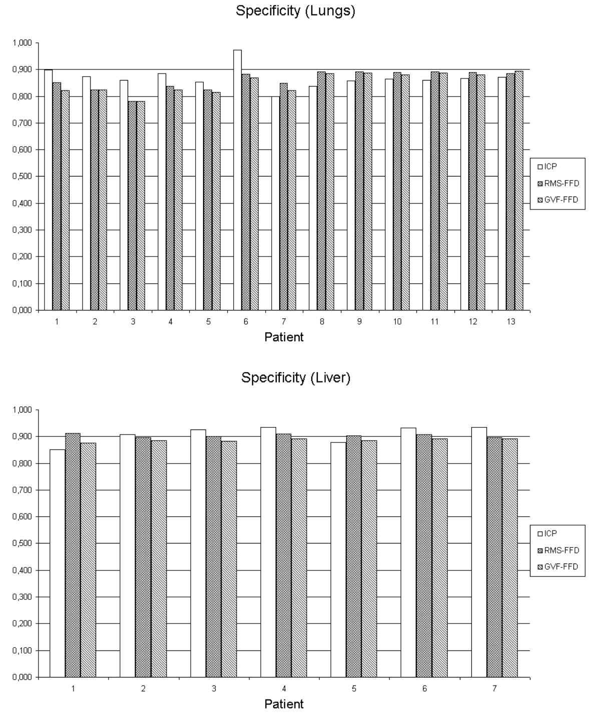

Figure 5.14: Specificity graph of structure registration methods applied on 13 lung (top) and 7 liver cases (bottom).

tions to cope with in each case. It is evident that the lungs suffer more deformations than the liver because of the effect of the respiratory cycle on these structures. In a similar way, the registration of structures provided by applying the segmentation step to CT and emission PET images is more challenging than that one working on the NCAT images, since in the former application the algorithm must also recover large deformations such as those ones concerning differences on arm's position in both acquisitions (arms along body in PET scans and above head in CT acquisitions).

Sensitivity and specificity measures are close to 1 for both FFD-based methods, with specificity values slightly lower, proving that in general, the registered floating structure remains smaller than the target one. On the contrary, the ICP-based method produces surfaces overpassing target structure sizes.

Moreover, we observe that differences of registration accuracy between results provided by the RMS-FFD and GVF-FFD are larger in structures undergoing more local deformations such as the lungs. These effects are due to the trade-off taken in the computation of the GVF vector field between the rejection of outliers and the capacity to cope with local deformations.

In addition to the registration accuracy measures, we have analyzed the convergence times of each structure registration method due to its major significance in our application. We have normalized them by the dimensions of each image, to be able to compare directly method performances, independently of image sizes. The GVF-FFD method shows better performances (52.610 $\mu s./voxel$) than the RMS-FFD technique (699.365 $\mu s./voxel$), which remains a high-computational cost algorithm. This is due to the gradient computation associated to the RMS-FFD technique, that must be updated at each iteration, while the GVF-FFD technique uses a vector field computed only once at the beginning of the procedure to optimize the control point displacement of the FFD grid. The ICP-based registration approach provides very low convergence times (6.607 $\mu s./voxel$) but the registration accuracy provided by this method is not enough for our application.

5.6 Conclusions

In this chapter, we have proposed three different structure registration methods in order to provide an initial transformation between the CT and PET structures segmented in the precedent stage of the proposed registration methodology. This structure transformation will initialize the subsequent grey-level registration stage of the proposed methodology.

First, we have adapted a well-known surface registration method, the ICP technique, in order to furnish non-rigid deformations between the structures to register. While the non-rigid projection of the surface stage provides good visual results, as shown in Figure 5.4, the poor final performance of the ICP-based method in the evaluation stage shows that the transfer of the non-rigid field generated by this technique to the FFD grid is not correctly achieved, loosing valuable information.

Thereafter, we have decided to employ directly the same FFD registration framework in the structure registration stage as well. At the beginning, the optimization of the control point displacements of the FFD grid is done in a classical way (we called it RMS-FFD), using a gradient descent technique guided by the RMS similarity measure, that needs the computation of a gradient estimation in each iteration. This gradient estimation makes this structure registration algorithm very expensive in terms of computational cost.

Then, we propose an alternative and original way to optimize control point displacements of the FFD grid, the GVF-FFD technique, that uses a 3D dense vector field computed on the target structure contours to guide the evolution of the floating structure ones.

We have evaluated and compared these three structure registration methods in a database of 20 pairs of deformable objects coming from real patients and the NCAT phantom. We have computed four measures in order to assess the registration accuracy provided by each method. In addition, we have also analyzed the computational burden associated to each structure registration algorithm. RMS-FFD has proved to be the method providing best results in terms of registration accuracy, at the expense of a high computational cost. On the other hand, GVF-FFD, furnishing slightly less accurate registration results, converges towards the solution in a much shorter time (10 times). The ICP-based technique fails to provide accurate enough results due to the loss of information in the transfer between the non-rigid projection surface and the FFD grid initialization stages.

The choice between the RMS-FFD and GVF-FFD techniques will depend on the priorities for a given application, concerning registration accuracy or low computational costs. In our context, the subsequent grey-level registration phase will complement the structure registration stage, thus at this point we only need an approximation of the transformation between the structures to register. Therefore, we prefer to use the GVF-FFD technique due to the good trade-off between its convergence times and the registration accuracy it provides. Nevertheless, if we would need better registration accuracy for a given application, we could use the GVF-FFD technique as a starting point and employ the RMS-FFD to refine the results.

CHAPTER 6

Grey-level Registration

Contents

This chapter describes the last stage of the proposed registration methodology, i.e. the registration phase working with the whole set of image intensities. After an introduction about the objectives of this stage in Section 6.1, we detail in Section 6.2 how the transfer between the structure registration phase and the grey-level one is done. This registration phase is based on a FFD model, that has been described in Section 5.4.1, using Mutual Information as the similarity criteria to guide the optimization of the control point displacements. Therefore, Section 6.3 is devoted to the theory of Mutual Information and its use in our application. The optimization procedure of the grey-level registration stage is detailed in Section 6.4 and finally some conclusions are given in Section 6.5. Some registration results obtained after the grey-level registration phase are shown in Section 8.3. In addition, in Chapter 7, we have developed a visual assessment protocol (see Section 7.4) aiming at evaluating in a semi-quantitative way registration accuracy furnished by the proposed methodology, and it is applied to the registered images after this grey-level registration stage.

6.1 Introduction

The grey-level based registration phase is the last stage of the proposed registration methodology. As already mentioned, this stage aims at refining registration results provided by the initial structure registration phase computed on segmented thoracic and abdominal structures. Furthermore, it must furnish a displacement field for regions far away from the segmented structures because at this point, reliable registration information is not yet available for them. For instance, the region located under the left lung and above the left kidney, where the stomach is usually found, only benefits from the registration information interpolated from deformations corresponding to the lungs and the kidneys. Finally, another objective of this stage is the correction of misregistrations that may have been introduced by structure segmentation errors, taking advantage of the entire image grey-level information with which we are now working.

This grey-level registration stage is based on the method proposed by Rueckert et al. [242] in a non-rigid registration of contrast-enhanced breast MRI application. The elastic transformation is modeled by a FFD based on B-splines (see Section5.4.1 for details on this model) using Normalized Mutual Information (NMI) as a similarity measure [1]. This approach has been successfully used in several registration applications [190 ; 250 ; 211]. Nevertheless, as shown in Section 3.1.2, a drawback of this method when it is directly applied to CT and emission PET images of thoracic and abdominal regions concerns the lack of constraints on the FFD model, the lack of uptake of several structures and the low SNR quality in the emission PET scans. Therefore, the transformation tends to converge towards local minima of the similarity criterion unless a very accurate initialization was provided.

For this reason, we have proposed our registration methodology, in which the initialization is provided by the initial structure registration stage, furnishing to the NMI-FFD approach an initial transformation very close to the final solution, at least in the neighborhood of segmented structures. Moreover, as shown in Section 5.5, structure registration methods providing more accurate results were those based on a FFD framework, thus allowing a better interaction between the two registration phases, as described in Section 6.2.

The NMI-FFD registration approach employed in this stage is basically the same as we have called RMS-FFD in Section 5.4.2, but the fact of working with the whole set of grey-level values forces us to change the similarity criterion that will guide the optimization of the control points of the FFD grid. This similarity criterion must model the relation between the intensities of the CT and emission PET images we are working with, that is extremely more complex than in the structure registration stage dealing with labeled images. Mutual Information and its variations have proved to be able to guide this type of multi-modal registration applications, as further detailed in Section 6.3.

---

[1] Rueckert's codes and other softwares from the CISG group of King's College can be downloaded on `http://www.imageregistration.com`.

6.2 Interaction between structure and grey-level registration phases

As a consequence of the proposed methodology, we need to transfer information provided by the structure registration phase to the FFD grid we are going to use in the grey-level based registration stage.

As seen in Section 5.3.2, the interaction between the initialization provided by the ICP-based algorithm and the grey-level registration stage was not optimal, in the sense that some information about the deformation may be lost during this transfer. This is not the case with the initial transformation furnished by both FFD-based methods, RMS-FFD and GVF-FFD (see Section 5.4), since the interaction between both stages is solved using a common grid of control points. Therefore, those control points located near segmented structures will already be a very good approximation of their final displacement before the grey-level registration stage that will be mostly devoted to the optimization of the control points which are far away from the relevant structures.

If we use a common FFD grid of control points through the whole registration methodology, grid dimensions should be the same in both registration steps, i.e., have the same number of control points per dimension. One solution to that is the use of a multi-grid framework. Some authors [242 ; 248 ; 234] have proposed registration algorithms where the number of control points increases during the optimization procedure, starting to cope with more global deformations and finishing with more local ones. The main drawback of this kind of refinement is the significant increase of the computational burden of the algorithm since the refinement is usually applied on the whole FFD grid, thus limiting its use in applications with strong time constraints, as in our case.

An alternative is to identify the regions in which the refinement is more necessary. In the proposed registration methodology, we can take benefit of information derived from segmented structures in order to only refine or subdivide the grid in a bounding box around these structures. The algorithm starts with a large grid (white stripes in Figure 6.1) of control points superimposed on the emission PET image, reasonably populated (taking into account that a linear registration step has been previously done). After the structure segmentation stage, we can adjust the bounding box in order to match its vertices with control points of the large grid. Then, we increase the resolution of the grid within this bounding box (green stripes in Figure 6.1), coping with more local deformations in these crucial zones of the image, as shown in Figure 6.1 in a thoracic case (the CT is a thoracic scan while the emission PET images is a whole-body scan). Once we have built the FFD grid, the optimization of the control point displacements is performed following the proposed registration methodology. Furthermore, the grey-level registration stage can be implemented in order to devote most of its time to the optimization of control points not located within the segmented structures.

Unluckily, this refinement strategy is still in testing phase, but some promising results in terms of computational cost and registration accuracy have been already obtained for a few cases.

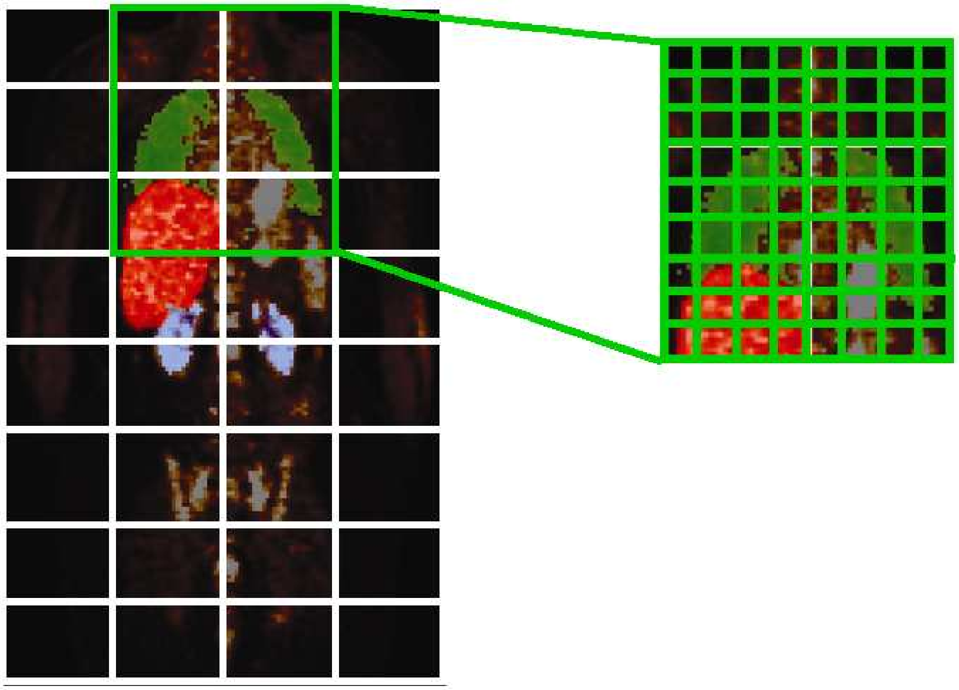

Figure 6.1: Example of multi-grid registration strategy. Left: large original FFD grid. Right: region in which the FFD grid is refined using information provided by lung segmentation (red).

6.3 Similarity criterion: Mutual Information

Mutual Information (MI), simultaneously proposed by Viola [292] and Collignon [59], has represented a step forward in the use of statistical measures in image registration, in particular in multi-modal applications, as illustrated in an exhaustive review performed by Pluim et al. [217] about these techniques. The main advantage of this similarity criterion is its flexibility to deal with a high variety of applications and images since it is only influenced by the statistical properties of the joint probability density function (PDF) of the image intensities, as shown in Section 6.3.1. As a matter of fact, in our application, the relation between the sets of intensities corresponding to CT and emission PET images of thoracic and abdominal regions can only be assumed statistical, due to the large differences between both images to register (see Section 1.3.2 for a list of factors inducing these differences).

Several variations of the original MI formulation can be found in the literature and some of them, including the Normalized Mutual Information (NMI), are detailed in Section 6.3.2. One common problem of all these measures concerns the histogram computation phase, that will influence registration accuracy and convergence times of the algorithm, as described in Section 6.3.3.

6.3.1 Mutual Information theory

Mutual Information (MI), simultaneously proposed by Viola [292] and Collignon [59], has represented a step forward in the use of statistical measures in image registration, in particular in multi-modal applications, as illustrated in an exhaustive review performed by Pluim et al. [217] about these techniques. The main advantage of this similarity criterion is its flexibility to deal with a high variety of applications and images since it is only influenced by the statistical properties of the joint probability density function (PDF) of the image intensities.

This similarity criterion expresses the quantity of information remaining in one image I_A knowing another image I_B, which is maximal when equivalent data sets are correctly registered. Another interpretation of this similarity criterion is that it measures the degree of dependence of two images, I_A and I_B, as the distance between the joint probability distribution $p_{i,j}$ and the distribution functions p_i and p_j obtained in case of total independence, by means of the Kullback-Leibler measure [289]:

$$\mathrm{MI}(I_A, I_B) = \sum_{i \in I_A} \sum_{j \in I_B} p_{i,j} \log_2 \frac{p_{i,j}}{p_i p_j} \tag{6.1}$$

The hypothesis leading to this interpretation states that when both images are well registered, a maximal dependence between them will be found and misregistration will cause a decrease of the MI, as shown in Figure 6.2. The left part of this figure shows two sets that are completely independent, without any overlap region between them and therefore misregistered. On the right part of the figure, we can observe the effect of improving the registration of both sets, leading to the apparition of an overlap region and increasing the dependence between them. If this overlap region, that represents the MI (or some of its variations such as the NMI) increases, the registration between both sets will be better done, meaning that information remaining in one set once the other is known has been reduced.

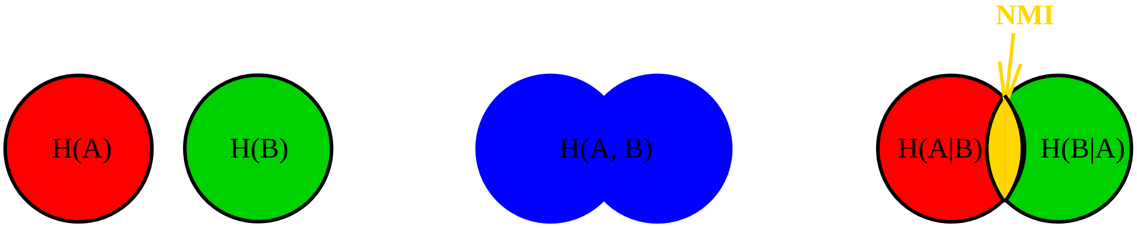

Figure 6.2: Diagram representing the Mutual Information concept. Left: Two sets fully independent without overlap region, thus misregistered. Center and right: if one of the sets is slightly translated, an overlap region between them appears, that symbolizes the MI (or the NMI) similarity criterion. The increase of MI or the overlap region means a better registration.

Mutual Information is related with the entropy theory by the following expressions:

$$\begin{aligned} \mathrm{MI}(I_A, I_B) &= H(I_A) + H(I_B) - H(I_A, I_B) = \\ &= H(I_A) - H(I_A \mid I_B) = \\ &= H(I_B) - H(I_B \mid I_A), \end{aligned} \tag{6.2}$$

where $H(I_A)$ and $H(I_B)$ are the marginal entropies of the images, $H(I_A, I_B)$ their joint entropy and $H(I_A \mid I_B)$ and $H(I_B \mid I_A)$ are the conditional entropy of I_A given I_B and of I_B given I_A respectively.

These entropies (according to Shannon's [259] definition of entropy) are defined as:

$$H(X) = -\sum_{x \in X} p_x \log_2 p_x \tag{6.3}$$

$$H(I_A, I_B) = -\sum_{i \in I_A} \sum_{j \in I_B} p_{i,j} \log_2 p_{i,j}, \tag{6.4}$$

$$H(I_A \mid I_B) = -\sum_{i \in I_A} \sum_{j \in I_B} p_{i,j} \log_2 p_{i|j} \tag{6.5}$$

where p_x is the PDF of the random variable x. In the case of images, p_x corresponds to the joint PDF of the intensities of the images.

Some properties of Mutual information [170 ; 289] are given in Table 6.1 (where T is the transformation applied to image B).

Table 6.1: Mutual Information properties

Non-negativity:	$MI(I_A, I_B)$	≥ 0
Independence:	$MI(I_A, I_B)$	$= 0 \iff p_{i,j} = p_i p_j$
Symmetry:	$MI(I_A, I_B)$	$= MI(I_B, I_A)$
Self information:	$MI(I_A, I_A)$	$= H(I_A)$
Boundedness:	$MI(I_A, I_B)$	$\leq min(H(I_A), H(I_B))$
		$\leq (H(I_A) + H(I_B))/2$
		$\leq max(H(I_A), H(I_B))$
		$\leq H(I_A, I_B)$
		$\leq H(I_A) H(I_B)$
Data processing:	$MI(I_A, I_B)$	$\geq MI(I_A, T(I_B))$

Finally, we can also interpret the Mutual Information criterion as a measure of the dispersion of the *joint histogram* of two images. As mentioned in Section 2.4.2, the behavior of the joint representation of the intensities of two images reflects the mismatching between them, being more dispersed as the misalignement is high. The entropy can be used to measure this dispersion since a dispersed histogram produces a high entropy value [270]. The MI can be also used to measure joint histogram dispersion, but an important difference appears with respect to the only use of the joint entropy. It also takes into account the marginal entropies of the images because it reduces the dependence to the size and contents of the overlap zone between the images (marginal entropies penalize transformations that decrease the amount of information in the separate images [217]). An example of joint histograms corresponding to different matchings of two images and their MI values is shown in Figure 6.3. It can be appreciated the relation between the dispersion of the joint histograms, i.e. the accuracy of the registration, and the Mutual Information similarity measure (decreasing as misregistration increases).

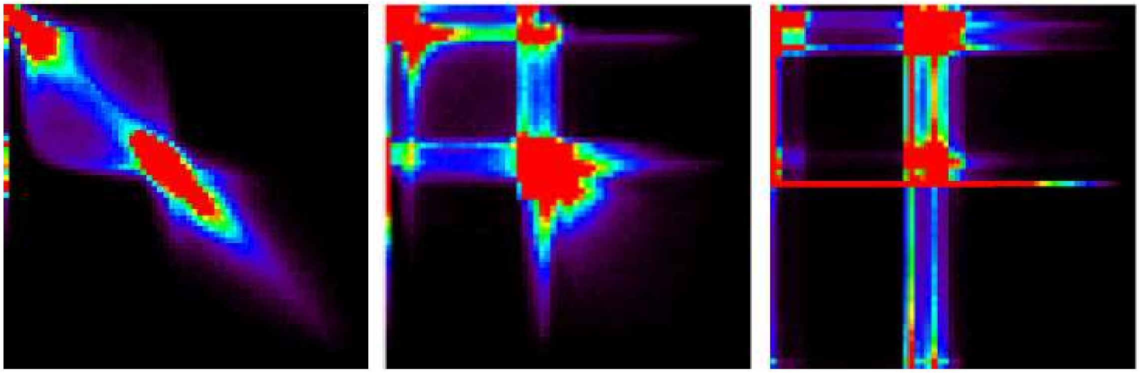

Figure 6.3: Joint histograms corresponding to different matchings of two images. Left: good matching and thus little dispersion of the histogram, MI is equal to 1.47748. Center: regular matching and thus medium dispersion of the histogram, MI is equal to 0.852934. Right: bad matching and thus medium dispersion of the histogram, MI is equal to 0.681276.

It must be pointed out that MI requires some conditions in order to be useful as similarity measure. The first one is related to the fact that it is a measure based on the estimation of intensity probability distributions. Due to this dependence, the Mutual Information criterion is more reliable when the quantity of available data for histogram computation is large enough to assure a good PDF estimation. The second requirement is that this criterion must vary smoothly when changing transformation parameters in order to assure a good behavior of the optimization procedure. This requirement directly concerns the smoothness of the estimated joint and marginal probability distributions, $p_{i,j}$, p_i and p_j with respect to parameter variations and it depends on the spatial correlation between the voxels of the image [170]. If the image intensities are spatially correlated, the search space will be better behaved (less local maxima, big attraction basin of the global maximum) and the optimization phase will be more robust.

6.3.2 Variations of Mutual Information

Although MI has proved to be a very efficient technique in a vast number of different registration applications, sometimes it does not lead to correct results. For this reason, several improvements have been proposed in the literature.

Normalized Mutual Information (NMI) was proposed by Studholme [269] in order to avoid the dependence of the MI on the size of overlap between the images. It can be expressed as:

$$\mathrm{NMI}(I_A, I_B) = \frac{H(I_A) + H(I_B)}{H(I_A, I_B)} \tag{6.6}$$

This modification was proved to provide better results than the classical MI formulation in some applications such as the rigid registration of brain MR-CT and MR-PET images [269]. Another normalization of the MI was also proposed in [171], called Entropy Correlation Coefficient (ECC). Recently, Butz et al. [41] has demonstrated mathematically that this equation is equivalent to the *efficiency coefficient* of order n with $n = 1/2$ which they obtain by interpreting image registration as a particular case of feature selection, modeled by means of Markov chains:

$$e_n(X, Y) = \frac{MI(X, Y)^n}{H(X, Y)^{1-n}}, n \in [0, 1] \tag{6.7}$$

The inclusion of spatial information in a MI-based technique has been also studied [216 ; 240]. Rueckert et al. [240] propose to include the spatial correlation between neighboring voxels by computing a higher order joint histogram. A different approach to add spatial information is proposed by Pluim et al. [216], adding a multiplicative term based on the image gradients into the cost function to constraint the MI term.

On the other hand, in [216] a multiplicative term based on the image gradients is added to the cost function of the registration algorithm to constraint the MI term.

In Section 2.4.2, it has been recalled that some authors use alternative entropies to Shannon's one in order to bypass some of the drawbacks associated to this information measure. From these different entropies, alternative expressions of Mutual Information are obtained with a different behavior from that one derived from Shannon's entropy. For instance, *f-informations* are obtained by using *f-entropies*, that provide fast and robust convergences while dealing with complex joint statistics [212].

An interesting idea is to adapt the Mutual Information measure to work in registration applications involving more than two images. It is defined as higher-dimensional MI [25 ; 1 ; 267]. Other variations that must be mentioned include the computation of this criterion in a local way [160 ; 232] that notably reduces computational time and, the original use of the MI in feature-based registration algorithms [225 ; 40].

In our work, we have only tested the Normalized Mutual Information, proposed by Studholme [269]. It has proved to be slightly more efficient than the classical MI formulation in some cases (for instance, when differences between the FOVs of the images are large), and for this reason this similarity criterion has been adopted in the proposed approach to guide the refinement registration phase.

6.3.3 Histogram computation

Histogram computation plays a key role in an entropy-based registration algorithm because it directly influences result accuracy and computational complexity of the method. Two important points in the histogram construction are discussed in this section: the estimation of the joint probability distribution and the *binning* stage.

Estimation of the joint probability distribution

The interest of the joint histogram of two images in a registration context has been already highlighted in Section 6.3.1. This property is used by several similarity measures, in order to measure registration accuracy provided by a certain set of transformation parameters. Each time these parameters are changed in the optimization procedure, the joint histogram must be recomputed to know if the new transformation produces less misregistrations than the preceding one. This histogram computation clearly influences the registration system in terms of accuracy and computational burden.

Once we have the joint histogram built, it is used to estimate the joint probability distribution. This estimation can be obtained by different techniques, but two approaches have been mainly used in image registration: *empirical* (or frequential) approximation and *Parzen window.*

- Empirical approximation: it is the most straightforward method to obtain an estimation of the joint probability distribution and it consists in a normalization of the joint histogram. Therefore, having a joint histogram $Hist(z)$, the probability distribution is approximated as:

  $$p(z) = \frac{Hist(z)}{N} \tag{6.8}$$

  where $z = (z_A, z_B)$ is a pair of voxel intensity values from both images (A and B) to register and N is the sample number in the overlap region between the images to register.

- Parzen window: this non-parametric technique is based on the overlap of centered kernels in each element of the sample sets of the histogram. It may be formulated as follows:

  $$p(z) \approx P^*(z) = \frac{1}{N_A} \sum_{z_j \in A} R(z - z_j), \tag{6.9}$$

  where N_A is the number of elements of a sample A and R is the windowing function. The most frequently used windows include Gaussian and cubic splines due to their derivation simplicity.

  The difference of this approach with respect to the empirical approximation is that the Parzen technique updates the bin where the kernel is placed, but also the neighboring bins weighted by the kernel function. At the expense of a higher computational cost, this approach has proven to be more robust.

Some authors have proposed different techniques aiming at reducing the computational cost of the histogram, for instance by means of lookup tables replacing the most expensive calculations [245 ; 193].

In our case, the simplicity and the low-cost nature of the empirical approximation have turned the balance towards this approach instead of Parzen windowing.

Binning

Another crucial implementation aspect in the PDF estimation is the *binning.* This task concerns the division in classes or *bins* of the histogram and its main goal is to reduce histogram complexity by classifing the combinations of intensity pairs into a determined number of classes. For instance, for a joint histogram of two images coded in 8 bits, each with 256 different grey-levels, 65536 combinations are possible and in order to obtain a significant statistical representation for each intensity pair, images should have bigger dimensions to provide enough samples. Thus, the binning step solves this problem by fixing the number of possible combinations, depending on the specific needs of each registration application.

A critical aspect of the binning step is the choice of the number of bins for each axis in order to avoid intensity pairs corresponding to different regions falling into the same bin whereas assuring a certain quantity of samples for each bin. Although several criteria have been proposed in the literature to solve this uncertainty in the case of 1-D histograms, such as the Sturges [272], the Scott [252] or the Freedman-Diaconis [96] norms, this choice remains empirical in bi-dimensional applications. Furthermore, a regular division of the histogram is in general achieved, meaning that the size of a given bin is fixed. Recently, Knops et al. [144] have demonstrated that a wiser idea is to adapt the bin size according to the anatomical structures being visualized. In [313], a computation of different histograms, each with different bin widths is used.

In our work, it has been verified that the use of 32 bins (regular division approach) for each axis of the histogram provides a good trade-off between computation times and the separation of intensities associated to different structures in different bins.

6.4 Optimization phase

This stage must compute the optimal displacement for each control point of the FFD grid that provides the best similarity measure, hence, theorically, the best superimposition between both images to register. Therefore, the parameters to optimize are these 3D displacements of each control point, like in the RMS-FFD structure registration technique described in Section 5.4.2. Free-Form Deformation optimizations are intrinsically critical due to the high number of parameters to estimate. For instance, for grid of $10 \times 10 \times 10$ control points, the optimization procedure must estimate 3000 transformation parameters or degrees of freedom. For this reason, several tricks are applied in order to reduce the computational cost of these estimations such as not taking into account the control points placed on the background of the image.

As seen in Section 2.5, the optimization stage completely depends on the nature of the cost function to optimize and if its gradient is available or not. In full content-based registration methods, the cost function is usually composed of a similarity criterion term and a regularization term. Therefore, the possibility of having a gradient will depend on the way the similarity criterion is computed and on the nature of the chosen regularization. In the case of MI-based algorithms, probability distribution computations and interpolation methods notably influence the cost function nature. For example, algorithms employing Parzen windowing technique to estimate the probability distribution, due to its formulation, obtain an analytic expression of the gradient. Maes et al. [171] have proved that the use of Partial Volume interpolation involves that the MI criterion varies smoothly with the parameters of an affine transformation and then, the gradient of the MI can be exactly computed, using analytic expressions for the partial derivatives of MI with respect to the registration parameters.

In the presented work, the optimization procedure is based on a gradient estimation computed by local differences over the control point grid (see Algorithm 1), as Rueckert et al. have proposed in [242]. It is basically the same optimization algorithm we have employed in the RMS-FFD structure registration technique detailed in Section 5.4.2, but using the NMI as a similarity criterion instead of the RMS measure.

It must be pointed out that the inclusion of the precedent initial structure registration phase allows us to skip some of the lower multi-resolution steps of the time-consuming fine registration, thus significantly speeding up the overall process. For instance, if a multi-resolution pyramid of 4 levels is chosen for the grey-level registration stage, we reduce it to 2 levels because large deformations are already recovered. Furthermore, displacements of a large number of control points do not start from zero, but from the initialization furnished by the previous structure-based phase, and in the majority of displacement optimizations, only a few number of iterations is needed to reach the optimal displacement.

6.5 Conclusions

This stage is basically based on the elastic registration method proposed by Rueckert et al. [242]. Most part of our work has been the adaptation and parameter tuning of these techniques in order to insert them into the proposed registration methodology and to apply them to CT and emission PET images of thoracic and abdominal regions.

In Section 3.1.2, we have proved that this technique fails to provide accurate enough results when it is directly applied on the grey-level images. The proposed registration methodology furnishes to this grey-level based stage an initial transformation very close to the final solution that solves problems of the NMI-FFD registration approach when dealing with our images. The Free-Form Deformation model has proved to be a flexible technique allowing us to construct an original registration methodology based on it and providing us a simple way of interaction between feature-based and full content-based registration phases. This interaction between these two theorically confronted methods, derived from the chosen strategy, has allowed us to combine their associated advantages while canceling their drawbacks.

The Normalized Mutual Information similarity criterion has allowed to measure the statistical relation between the CT and emission PET sets of intensities and thus to guide the refinement of the control point displacements of the FFD grid. Nevertheless, this similarity measure can easily lead to incorrect registration results in regions without any prior anatomical information derived from the structure-based stage, due to the strong presence of noise and artifacts in the PET image. Furthermore, as mentioned in Section 1.3.2, CT and emission PET images represent the same scene in different ways. The fact that some structures such as the heart or the stomach can appear with different intensities (or even not be present) in the PET image while in the CT scan they are almost constant will mislead the NMI and consequently, the optimization of the FFD grid of control points. As shown in Chapter 8, in which final registration results obtained after this grey-level stage are shown, this has not been a major problem for the heart since it is already very well initialized and constrained by the segmentation and registration of the lungs. On the other hand, the NMI-FFD has not provide accurate enough registrations of the stomach. Further details and comments of these results are described in Chapter 8, as well as conclusions of the visual assessment protocol (see Section 7.4) we have developed to evaluate in a qualitative way the registration accuracy provided by the proposed registration methodology.

As mentioned above, implementation choices of the histogram computation have been mostly chosen according to the computational burden of each technique, rather than on their resulting accuracy. Finally, the optimization phase has been designed having in mind that the initialization of control point displacements is very close to their final position, hence, a simple optimization technique can be used.

CHAPTER 7

Validation of the registration methodology

Contents

This chapter is dedicated to the evaluation of the registration accuracy obtained by the proposed methodology. First, in Section 7.1, we enumerate some classical definitions of the criteria related to this validation stage. Then, in Section 7.2, we review the techniques usually employed to assess registration results in medical imaging applications. In Section 7.3, we specify the constraints for this task in our application. In Section 7.4 we describe the visual assessment protocol we have developed in collaboration with several physicians involved in the project to validate accuracy of the registration results provided by the proposed methodology. Finally, in Section 7.5, some conclusions about this validation stage are given.

7.1 Validation in medical imaging

Numerous image processing methods have been developed for medical data applications, such as segmentation, registration, or calibration methods, but most of them have remained research tools without being incorporated into clinical routine. This surprising fact is sometimes due to the lack of an exhaustive validation phase, an imperative prerequisite before they can be used in a medical environment. Validation of medical image processing methods is not a trivial task, in particular for non-linear registration algorithms in which, in general, there is no available ground truth for comparison. Thus, it is a key topic of several multi-disciplinary meetings and workshops [164 ; 261 ; 258 ; 132], aiming at bridging the gap between theory, experimentation and practice. Furthermore, in order to launch onto the market a medical image processing software, it must receive the approval of health institutions such as the Food and Drug Administration for the American market, the CE certification for the European market or the Japanese health ministry. These approvals are obtained after a huge inspection/validation on different aspects of the software algorithm to prove its robustness and effectiveness.

But, what does *validation* means? Goodman [106] defines the health care technology assessment (HCTA) as the *process of examining and reporting properties of a medical technology* and as the *systematic evaluation of properties, effects and/or impact.* The most important thing about the validation stage is which questions it must answer about the method to evaluate. It must characterize the method behavior with respect to variations of parameter values and input data (image modalities, spatial resolutions, dimensions), as well as analyze computational cost and output quality of the results. It should include both individual evaluation of each stage and validation of the overall system, defining their performances and limitations. Moreover, this phase must define the targeted clinical context or application and prove its clinical benefit. Finally, an estimation of the social or economic impact may be performed as well. These issues depend on image characteristics and the specificities of the clinical context, thus, validation and its requirements are in general application-dependent. For instance, the required precision for a registration method involving cerebral pathologies is high, while in abdominal exploration it is lower due to the motion that affects each region.

Some conventional criteria or measures are defined in the literature to standardize and verify the objectives of an evaluation stage:

- accuracy: Goodman [106] defines accuracy as the *degree to which a measurement is true or correct.* For each sample of experimental data *local* accuracy is defined as the difference between computed values and theoretical values, i.e., known from a ground truth. This difference is generally referred to as local error. The major constraint of this measure is the need of a ground truth or gold standard, which in several applications such as non-rigid registration is not possible to establish. If, in some way, we could obtain this reference for a registration application, we can measure accuracy as the difference in each point between the known transformation and the one furnished by the method to evaluate. This difference provides the result of the validation, i.e. to accept or to reject the computed transformation. Accuracy can be *qualitative* or *quantitative*. The former relies on simple visual inspection of the results to assess global performance of the method. As mentioned before, quantitative accuracy needs a gold standard, unavailable for several applications, thus the following measures are employed.

- precision: it is the resolution at which the results provided by a given method are repeatable, i.e., the value of the random fluctuation in the measurement made by the process. Precision measures can be obtained concerning the entire system, or applying to specific components.
- reproducibility or reliability: Goodman defines this measure as *the extent to which an observation that is repeated in the same, stable population yields the same result.*
- robustness: the robustness of a method refers to its performance in the presence of disruptive factors such as intrinsic data variability, pathology, inter-individual anatomic or physiological variability.
- consistency: it is mainly studied in image rigid registration validation [123], by studying the capability of a registration method to find circular [1] transformations. This measure can be sensitive to bias and may not be applicable to non-invertible transformations generated by many non-rigid registration methods [250].
- fault detection: it is the ability of a method to detect when it succeeds (e.g. result is within a given accuracy) or fails.
- functional complexity and computation time: they are characteristics about the method implementation and should be adapted to the time and resource constraints of the clinical environment.
- other factors: other factors may have to be studied such as cost/effectiveness ratio, patient acceptance, and outcome factors.

7.2 Validation in registration applications

Different validation approaches have been proposed to overcome the lack of ground truth in registration applications such as physical phantom, cadaver studies, the use of invasive markers, simulated data or visual inspection of results by expert observers. These techniques present a basic framework to compare methods developed in different research groups, a task that is more complex than it looks like. These difficulties are due to the large variety of clinical acquisition protocols and pathological cases

---

[1] a circular transformation in registration applications is found when applying a given transformation in one sense (for instance floating to reference images) and its inverse on the other sense (reference to floating images), we obtain the identity transformation

to treat, to the high specific nature of some applications, and to the lack of gold standard generally accepted. For this reason, the creation of shared or public image databases with standard ground truth is a crucial point for the evolution of the validation processes and an important research community resource. These databases must include normal and pathological cases, updates with new imaging protocols and new modalities and data from new applications, real and synthetic data and reliable known truth for each context. These databases will allow the exchange of knowledge between institutions and a fast way to compare methods developed in different sites. Beside public databases, other actions are emerging with the same aim of sharing information, such as the *open source* movement. Projects like ITK [2] or VTK [3], must be taken as references for the future in order to share research results.

7.2.1 Physical phantoms, cadavers and invasive markers

Physical phantoms [9 ; 282 ; 317 ; 284] or cadavers [117] may be employed to compute an approximation of the ground truth, by attaching invasive markers to these phantoms. These markers must be densely distributed over the phantom and its movements are fully controlled, providing a Target Registration Error (TRE) [93] at locations of interest of about 0.5mm [192]. The TRE is defined at each point x in the image as the difference between the calculated transformation (T) and the *gold standard* transformation (T_{gs}):

$$TRE(x) = |T(x) - T_{gs}(x)| \tag{7.1}$$

Nevertheless, the range of applications in which this technique can be applied is limited because of nature differences between cadaver and in vivo data, and the difficulty of constructing a physical phantom representing complicated processes in the human body. A globally accepted alternative that can provide the gold standard for inter-patient rigid registration applications consists of the attachment of invasive markers to the surgical patient at the image acquisition time, furnishing a stereotactic reference rigid transformation. This technique has been successfully used by West et al. [298], within the Retrospective Image Registration Evaluation (RIRE [4]) project, in order to compare different linear registration algorithms in multi-modal head data. They attached bone-implanted fiducial markers and a stereotactic frame to the skull in patients undergoing neurosurgery, then the reference gold standard rigid transformation is the one which minimizes the mean square distance between corresponding marker positions in the two images. The accuracy of this reference was estimated to be 0.4mm for CT to MR and 1.7mm for PET to MR registration, being accurate

---

[2] National Library of Medicine Insight Segmentation and Registration Toolkit (ITK). `http://www.itk.org`.

[3] The Visualization Toolkit. `http://public.kitware.com/VTK/`. Also, VTKCISG [114], from the Computational Imaging Science Group Radiological Sciences, King's College London. `http://www.imageregistration.com`.

[4] Also called RREP, Retrospective Registration Evaluation Project, from the Vanderbilt University. `http://www.vuse.vanderbilt.edu/~image/registration/`.

enough for testing registration algorithms. The frame and the markers were manually removed from the images before using them to evaluate registration algorithms.

This approach, however, is not appropriate for non-rigid or intra-patient registration, where deformations can not be properly modeled as linear transformations.

7.2.2 Simulated data

Another option is to use software-based simulated data [199], where the ground truth is perfectly known. These numerical solutions can be adjusted to certain needs and simulated images or transformations are fully controlled, becoming the gold standard required to compare results furnished by the method to evaluate. Concerning registration methods, a known transformation is applied to one image or to some segmented anatomical features, then the registration accuracy can be calculated by comparing the transformation provided by the algorithm with the known, *gold standard* solution. Rohr et al. [236] have employed this technique in a brain non-rigid registration application, displacing a set of landmarks and interpolating a dense displacement map using Thin-Plate Splines.

Nevertheless, simulated data are not usually realistic enough, because they do not take underlying tissue properties into account, so that different tissues can undergo non-plausible deformations [250]. In some applications, this technique can not even be considered, because of the impossibility to model some clinical contexts, as in the physical phantom case. Moreover, any evaluation based on synthetic data must be careful about the possible introduction of bias, in which the algorithm may systematically favor the class of simulated deformations chosen for the study [233]. Anyway, it remains appropriate for comparison of methods that are not related to the spatial deformation model as well as for testing overall registration capabilities.

One improvement of this technique is the addition of realistic modeling of anatomical motion and deformation, including as much biomechanical information as feasible. Schnabel et al. [250] have proposed an original evaluation method, using Finite Element Models (FEM) to develop a biomechanical deformation simulator. They apply a range of physically plausible, biomechanical tissue deformations to FEMs of different patient anatomies, generating model solutions that simulate gold standard deformations. From these biomechanical simulated deformations, deformed images are generated and the registration accuracy of a given algorithm is obtained by using it to register these deformed images with the original ones and comparing the resulting deformation field with the biomechanical simulated deformations. The authors have applied this approach to assess non-rigid registration results for an intra-subject contrast-enhanced MR mammography application, as can be seen in Figure 7.1, but the same method can be used to other organs (heart, liver [205]) as long as plausible finite element models could be generated.

Segars et al. [254] developed the 4D (3D + time) NCAT phantom, which models thoracic and abdominal structure motions due to both respiratory and cardiac cycles. The organ shapes are formed using Non-Uniform Rational B-Splines (NURBS), and

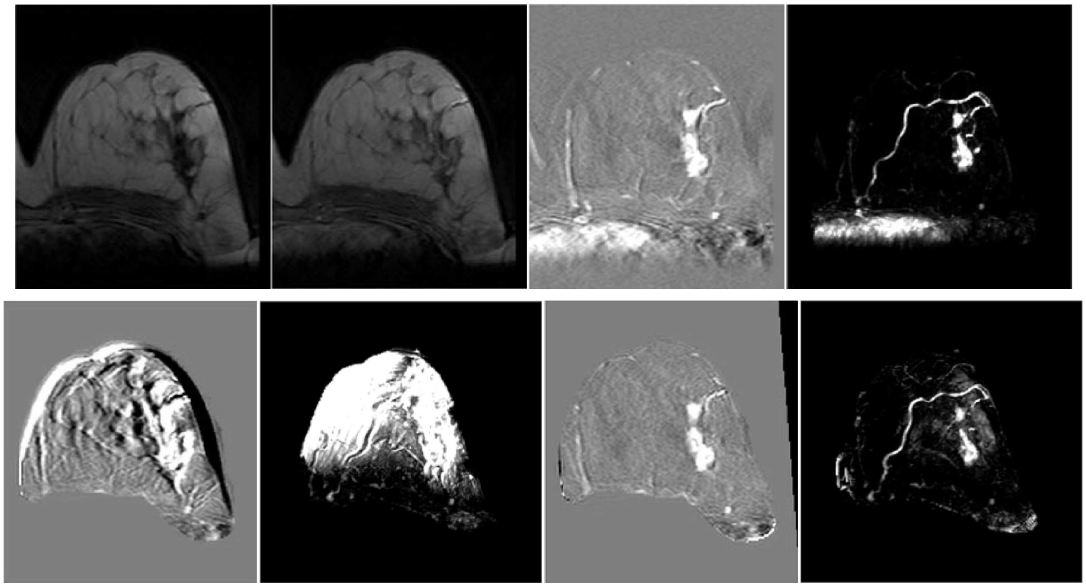

Figure 7.1: Use of FEM techniques to simulate biomechanical tissue deformations in an intra-subject contrast-enhanced MR mammography application, from [250]. Top: (from left to right) pre-contrast image, post-contrast image, subtraction image, and MIP (Maximum Intensity Projection). Bottom: subtraction slices and MIPs through subtraction volumes of original pre-contrast images from example FEM deformation simulations before (left images) and after (right images) registration.

are based on data from the Visible Human image dataset [5]. Three different views of the NCAT phantom can be seen in Figure 7.2. It has been used in different applications such as the study of the respiratory gating in myocardial SPECT [255], but to our knowledge, the NCAT phantom has not been used yet in the assessment of registration algorithms.

7.2.3 Inspection of correspondences between anatomical features

The gold standard for evaluating registration methods is the inspection of correspondences between anatomical features in the registered images [233]. This technique is frequently used when ground truth is not at all available, thus expert observers, some prior clinical knowledge or assumptions may give the reference for comparison [132].

First of all, a segmentation, either manual or automatic, must be performed in order to localize homologous structures in the images. These features can be point landmarks [61 ; 98 ; 270], segmented structures, regions of interest or others. Therefore, some quantitative measures are computed on these homologous structures after the registration stage in order to have an approximation of the result accuracy. For example, Hellier et al. [115 ; 116] proposed an evaluation of several linear and non-linear registration methods in a brain registration application. They compute global

---

[5] `http://www.nlm.nih.gov/research/visible/visible_human.html`.

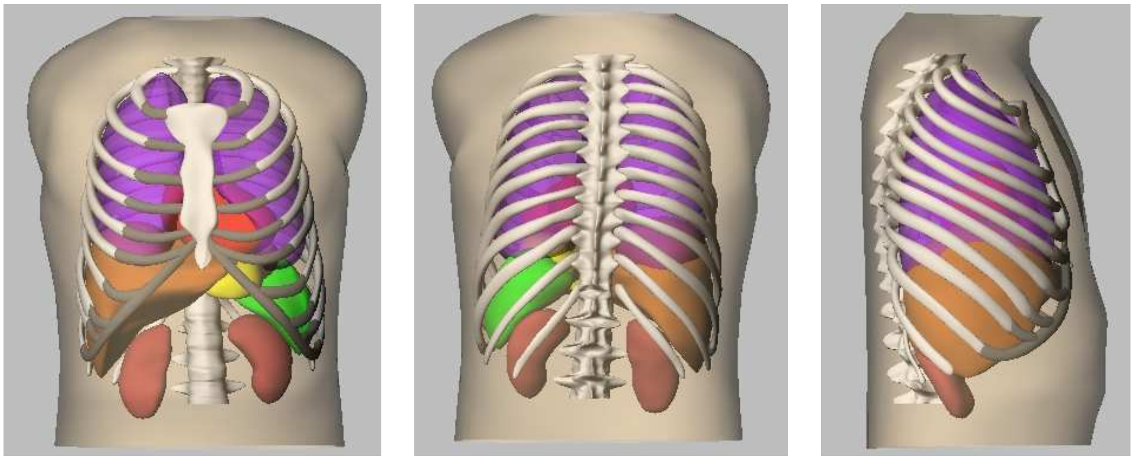

Figure 7.2: NCAT phantom. Left: anterior view; Center: posterior view; Right: right lateral view. Images come from P.W. Segars' site (`http://www.bme.unc.edu/~wsegars/`)

and local measures of the quality of the registration, such as grey/white matter segmentation map overlap, correlation ratio of the mean L_{vv} [6] intensities (i.e. 3D measure of the curvature of the cortex from the MRI volumes), distance and shape variation of cortical sulcal landmarks.

Several problems are associated to this technique. For instance, segmentation-based evaluations do not provide volumetric information, thus they do not detect registration errors within the segmented objects. Concerning landmark identification, the drawback is that, in some applications, the selection of corresponding points is difficult (low contour gradient and inter-patient variability of structures, lack of anatomical references). For example, as Goerres et al. [103] pointed out (and we have largely verified it in our application), it is rather difficult to find stable and reliable landmarks in emission PET scans, due to the poor image quality of these acquisitions. This technique, as in the case of manual segmentation, will always have some degree of error, bias and inconsistencies because it involves human intervention, which is subjective and is not easily reproducible, limiting the precision of the evaluation method. Another drawback of this strategy is the lack of recognized features over the whole data, resulting in the fact that we can find an approximation of the registration accuracy only for certain parts of the image. Nevertheless, expert defined anatomical landmarks or regions of interest remain the gold standard for evaluation of registration accuracy [233].

As an alternative, registration results can be qualitatively evaluated by visual inspection of the images by medical expert observers, classifying the result as success or failure, depending on whether they judge the registration accuracy to be above or below the required application accuracy [119]. In fact, in some clinical applications it is the only reliable method to estimate the quality of the results. This method consists

---

[6] this operator is related to the principal curvatures of the iso-intensity surface and the sign of the mean curvature is used in order to distinguish between sulci and gyri

in presenting the registration results in a user-friendly display to the evaluators who will then rank them according to their quality. This presentation can be composed of both image superimposition, subtraction images, *chessboard* images, or displays of only certain anatomical features or landmarks.

Interesting works have been done to study the accuracy of a visual assessment in a registration framework. Wong et al. [303] studied this issue in a MR-PET rigid registration context. They found that observers could always detect a translational misregistration larger than 2 mm in the x and y directions, and larger than 3 mm in the z direction. Similarly, observers could always detect a rotation larger than 4° and could detect a rotation error of 3° about any axis at least 80% of the time. In a CT-MRI brain image application, Fitzpatrick et al. [94] have shown that observer assessments performed well with registration errors equal or higher than 2mm. These results are influenced by the image modalities and the database involved in the study, the observer experience and the interface used to display images. Moreover, the lack of a result display allowing to highlight 3D complex deformations limits its direct use in non-rigid validation contexts.

Anyway, even if visual assessment remains a subjective observer-dependent validation method, it is an important step towards clinical and routine use of a registration method [249] and can still provide a useful insight on the registration process. As a matter of fact, we must not underestimate the capacity of the human eye to determine registration result accuracy. If two images are presented in a proper way, experienced physicians can rapidly assess the quality of the results in a short amount of time, using their prior knowledge of where in the anatomy the quality of the registration should be high and where these requirements can be relaxed [190].

7.3 Validation in whole-body PET-CT non-linear registration

We divide the evaluation process into three phases:

1. evaluation of algorithm performances based on simulated data;
2. assessment of the registration result accuracy;
3. validation performed in a clinical environment to evaluate its added value in diagnosis tasks.

The first phase is a quantitative or semi-quantitative validation stage where implementation aspects such as automaticity, computational time or robustness with respect to the input data variability have been studied throughout the development of our work. We have also employed some simulated simple data (spheres, cubes, . . .) to validate the non-linear FFD-based registration as well as other phases of the proposed methodology, but they have not any medical interest, and therefore, the proposed registration methodology must be directly assessed on pairs of CT and emission PET images.

The second assessment stage is a qualitative evaluation of the registration result accuracy. It depends on the desired accuracy for the targeted application and it is based on the coherence of anatomical structures displacement, their localization and of the relationships between normal and pathological structures after registration.

The last evaluation stage must be achieved in the clinical sites participating in the project, once the visualization interface will be finished (work in progress). The proposed registration methodology will be tested on a database composed of patients undergoing surgical operations (biopsies) which will furnish us a valuable approximation of a gold standard.

Therefore, in this manuscript, we are going to focus on the second evaluation phase, involving the assessment of the registration accuracy furnished by the proposed methodology. The desired accuracy depends on several factors such as image modalities, spatial resolution or anatomical regions (and nature of its deformations) involved in the process. In our case, the required accuracy will be higher in cervical and thoracic regions than in abdominal ones due to the lack of identifiable structures in this zone and its larger deformations. The chosen accuracy must also assure a correct classification with respect to visualized tumors. In practice, the threshold of the desired accuracy must have the same order of magnitude as the acquisition system owing the poorest spatial resolution, in our case, PET images. This point will be further explained in Section 7.4.

As mentioned above, the evaluation of a method depends on its specific application and its clinical context. In our case, besides the mentioned difficulties caused by the non-linear nature of the application, we must deal with emission PET images, which are very noisy and contain a high number of artifacts, as well as low contrast boundaries in certain regions and low spatial resolution. In addition, to our knowledge, no ground truth is available to assess an emission PET-CT non-linear thoracic and abdominal registration application. Even combined PET-CT scanners are unable to furnish a perfectly registered image that could be used as a reference for testing non-linear registration methods (for linear methods, it could be useful).

For these reasons, most of the techniques previously exposed cannot be used in our context. For instance, the use of extrinsic markers was strongly discouraged by the oncology specialists involved in the project due to its invasive nature. As mentioned in Section 7.2.2, FEM techniques and biomechanical models have a great potential for validation purposes and it would be an interesting evaluation method for our application. This approach requires the generation of a plausible Finite Element Model, which at the time being, is not available. Internal reference landmarks have been used by Goerres et al. [103] to evaluate the optimum breath-holding position of patients during CT imaging that provides the best match with PET imaging of the thorax, by acquiring CT scans during different respiratory phases. They chose a reference point based on the assumption that its position would be stable during the acquisition process. Thereafter, they measure distances between this reference point and other anatomical features, such as the lateral thoracic wall or between the apex of the lung and the top of the diaphragm. The authors pointed out that it is rather difficult to adequately measure distances in emission PET scans, since it is not easy to identify edges of organs, producing large variability in inter-observer agreement. In our context, using physician-defined internal reference landmarks is very inaccurate due to the lack of common anatomical references in both images. This is due to the different physical nature of CT and PET imaging modalities that lead to images representing anatomy in a different way. For example, despite bone structures are easily identified in the CT volume, the corresponding visible structures in the PET one are in fact the living tissue inside those bones, and consequently any measure relying on a pairing of those landmarks would be inaccurate.

7.4 Visual assessment protocol

7.4.1 Procedure

As mentioned above, evaluating the result accuracy of a non-linear registration method is a complex problem both conceptually and in practice. Indeed, elastic motions are difficult to perceive in three dimensions, and it must be checked that the registration phase corrects deformations in mobile structures while not introducing new errors in the more stable ones.

Even if it is a semi-objective validation technique, visual inspection by medical experts allows in our application to judge and classify, into a scale of error values, registration results for the most important anatomical structures. Mattes et al. [190] have also employed this approach to evaluate the registration accuracy of a non-linear approach applied on chest CT and transmission PET images. They have developed a split window interface that shows to the observer different corresponding 2D slices of both registered volumes in order to quantify the registration error. Furthermore, they improve the consistency of the evaluation by adding a display normalization stage. The authors claim that an observer takes around 1.5hours to assess 205 slices of two registered volumes.

We propose a similar visual assessment protocol [7]. It has been developed under the supervision of Dr. Hervé Foehrenbach, from the H.I.A. Val de Grâce in Paris. It allows physicians and registration specialists to rapidly generate a semi-objective and qualitative measure of the registration accuracy, being repetitive enough to allow statistical interpretation of the results.

For this purpose, several anatomically significant 2D slices of both the original CT and registered PET volumes, as well as an overlay chessboard image are presented. This representation was preferred to displaying a single overlay image because, in our opinion, this reduces measure subjectivity. Slices have been evenly spaced through the volume in order to display the most significant thoracic and abdominal structures. For example, for a 256 x 256 x 97 volume, 6 coronal and 6 axial slices are employed. This is performed by means of an automatic procedure that uses CT segmented structures in order to decide which 2D slices must be chosen for evaluation purposes. However,

---

[7] We would like to point out that our visual assessment protocol has been developed independently of Mattes' publication, which has appeared in January 2003, when our evaluation methodology was already finished.

the user has also access to all axial slices of the CT and the non-linearly registered emission PET volume if they must be checked in order to confirm any evaluation score.

Each pair of 2D slices has been marked with a ruler with a spatial resolution of 1cm per mark in the x and y axes and 2cm in the z axis. Every fifth mark is slightly bigger for easier reading. Each ruler defines some reference or landmark points as it crosses significant anatomical structures, such as the chest wall (ribcage), the mediastinal wall (heart), the diaphragmatic wall (liver), or the stomach and kidneys walls. These references allow the clinician to estimate differences in the position of the mentioned structures in both 2D slices and then score the registration accuracy of the method. For instance, in the case of the lungs, the user must evaluate the registration result accuracy in the anterior, posterior, inferior and superior part of both, left and right lungs. Figure 7.3 shows one pair of these 2D slices, corresponding to axial (top) and coronal (bottom) slices with rulers, together with their corresponding overlay chessboard images. This procedure is certainly limited in the sense that the evaluation only measures local translational errors in the reference points that are place on the surface of some structures, and no assessment about registration result accuracy in other regions or even within the evaluated structures is provided.

The developed graphical interface allows a fast interaction between the user (evaluator) and the statistical analysis of the evaluation. The graphical interface consists of a *html* web form where, in a user-friendly way, the evaluator must only click on the chosen registration *score* for each landmark point in the slice to assess. Once all slices are assessed, by clicking on a button, the form sends a text file containing evaluation results to people in charge of their statistical analysis. In general, an expert user needs about 20 minutes to complete the validation process, thus considerably faster than Mattes' evaluation interface [190]. On the other hand, we do not deal yet with any kind of display range setting or normalization in the current web form, but a new version of the graphical interface with this capability is already in progress [8].

The scoring (or dissatisfaction) scale has been defined by the medical specialists involved in the project keeping in mind that the goal of the registration method was to attain errors below the resolution of PET images (in general, voxel dimensions of PET images are around 4.0 x 4.0 x 4.0 mm^3 in our database). Table 7.1 shows the scale and its correspondences in mm and in pixels (we recall that the evaluation is performed in 2D slices). We must point out that since PET images are coming from different sites, and consequently have different quality and spatial resolutions, we have added an intermediate (*acceptable*) quality level.

Table 7.1: Evaluation scale.

Scale	mm	Pixels	Quality
0	0-5	0-1	Good
1	5-15	1-3	Acceptable
2	15-	3-	Unacceptable

---

[8] Nevertheless, we always fix display intensity range settings in order to be consistent and do not induce bias in the evaluation due to false boundary positions.

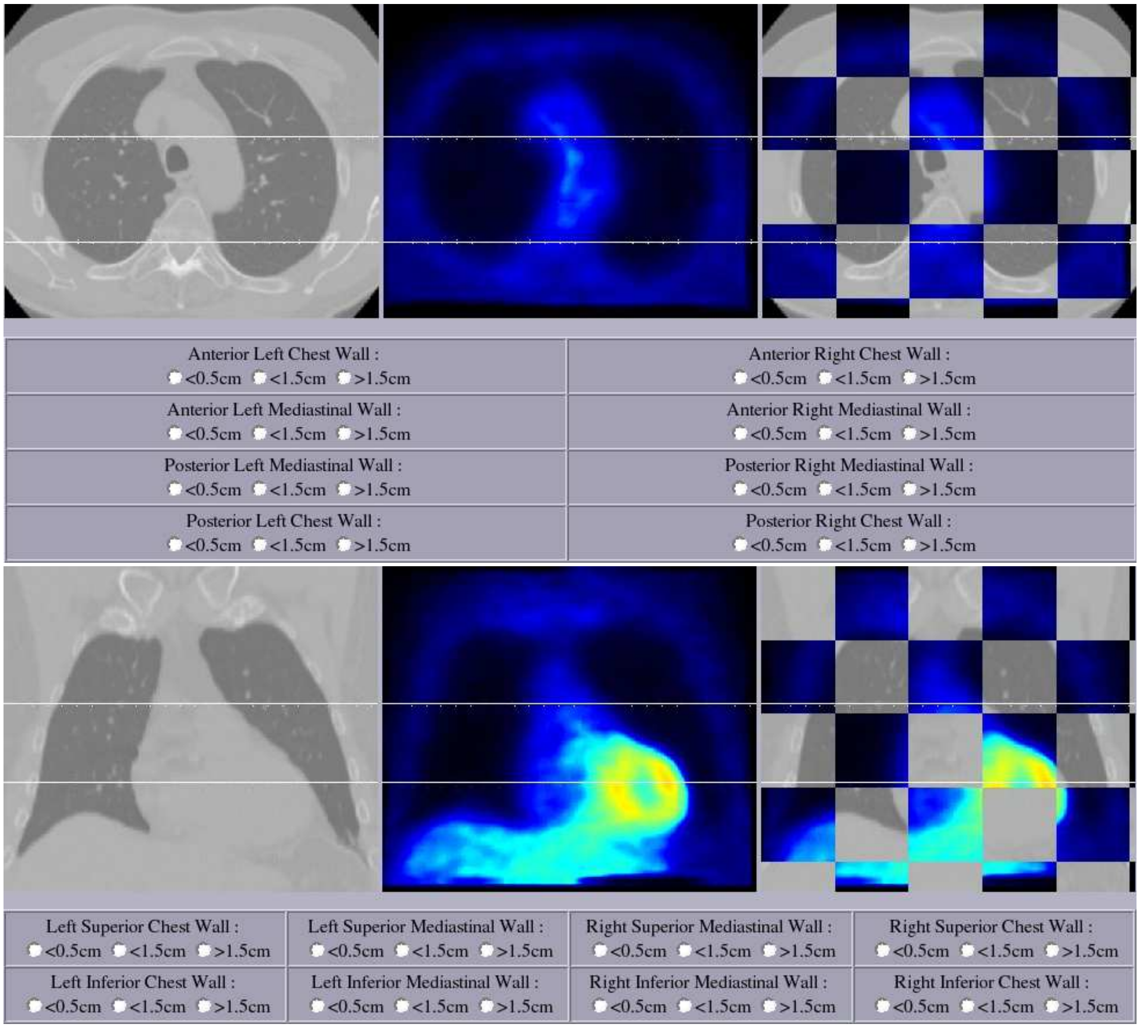

Anterior Left Chest Wall : ○<0.5cm ○<1.5cm ○>1.5cm	Anterior Right Chest Wall : ○<0.5cm ○<1.5cm ○>1.5cm
Anterior Left Mediastinal Wall : ○<0.5cm ○<1.5cm ○>1.5cm	Anterior Right Mediastinal Wall : ○<0.5cm ○<1.5cm ○>1.5cm
Posterior Left Mediastinal Wall : ○<0.5cm ○<1.5cm ○>1.5cm	Posterior Right Mediastinal Wall : ○<0.5cm ○<1.5cm ○>1.5cm
Posterior Left Chest Wall : ○<0.5cm ○<1.5cm ○>1.5cm	Posterior Right Chest Wall : ○<0.5cm ○<1.5cm ○>1.5cm

Left Superior Chest Wall : ○<0.5cm ○<1.5cm ○>1.5cm	Left Superior Mediastinal Wall : ○<0.5cm ○<1.5cm ○>1.5cm	Right Superior Mediastinal Wall : ○<0.5cm ○<1.5cm ○>1.5cm	Right Superior Chest Wall : ○<0.5cm ○<1.5cm ○>1.5cm
Left Inferior Chest Wall : ○<0.5cm ○<1.5cm ○>1.5cm	Left Inferior Mediastinal Wall : ○<0.5cm ○<1.5cm ○>1.5cm	Right Inferior Mediastinal Wall : ○<0.5cm ○<1.5cm ○>1.5cm	Right Inferior Chest Wall : ○<0.5cm ○<1.5cm ○>1.5cm

Figure 7.3: Example of 2D axial (top) and coronal (bottom) slices of the CT (left), registered PET (center) volumes and the chessboard display (left) used in the visual assessment protocol. They are marked with the rulers (white) that define landmark points where registrations must be evaluated.

7.4.2 Evaluation example

We present here a clarifying example of the use of the visual assessment protocol. Figure 7.4 shows CT (top left), emission PET (bottom left) and chessboard overlay (right) 2D axial slices (together with the horizontal rulers used for evaluation purposes) of an abdominal case. The user must evaluate registration in the liver and the stomach, specifically at the landmark points placed in the anterior and the posterior left and right walls of each structure. In this example, we are only going to detail the assessment of two points (yellow point for CT and red one for emission PET in Figure 7.4): the posterior liver wall point (A-A') point) and the anterior stomach wall point (B-B').

First of all, the user must detect in the three 2D slices the landmark points used as references for the evaluation. It means that the user must find where the ruler crosses

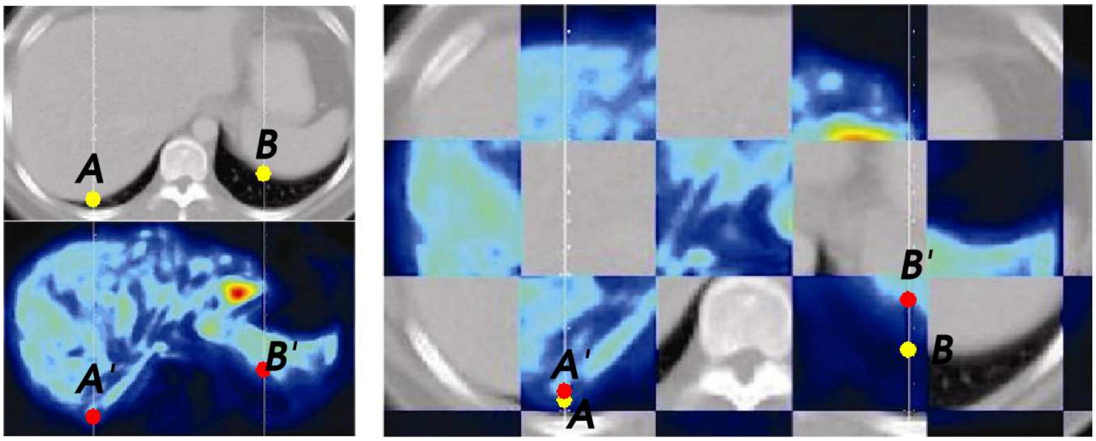

Figure 7.4: Evaluation example using the proposed visual assessment protocol in an abdominal case. Left: 2D axial slices of the original CT (top) and the registered emission PET (bottom) images. The registration accuracy is evaluated in the liver (A-A') and the stomach (B-B') using the landmark points (yellow in the CT and red in the emission PET slices) and the ruler. Right: chessboard image with landmark points from each image modality.
A/A' Posterior Liver Wall; B/B' Anterior Stomach Wall.

the liver and the stomach. Afterwards, helped with the marks of the ruler and the *chessboard* image (eventually, the evaluator can also visualize all 2D axial and coronal slices of the volume for further details), the user must estimate the distance between the pair of corresponding landmark points (for instance the pair A-A') and classify the registration accuracy on it according to the dissatisfaction scale. A given structure or region has several landmark points and thus several registration scores in different 2D slices. Then, an approximation of the registration accuracy on this structure will be obtained by computing the mean of the registration scores in the whole set of their landmark points.

For the particular case shown in Figure 7.4, we observe a good quality of the registration result in the posterior liver wall but, on the other hand, in the anterior stomach wall, the assessment must classify the result as failure (in our scale, *unacceptable*), due to the large distance between CT and emission PET landmark points. Further discussion about these results is given in Chapter 8.

It has to be pointed out that expert observers must use this visual assessment protocol, because, as illustrated in Figure 7.4, emission PET contour structures are very difficult to localize, and it is easy to make a mistake with other tissues different from the structure to validate.

7.4.3 Inter-observer consistency

We have computed the inter-observer consistency of the developed visual assessment protocol in order to verify if it is repetitive and objective enough to be used for the evaluation of registration algorithms. A group of three clinicians of three different clinical centers, all of them with a strong experience in oncology, have used the developed evaluation protocol in order to assess registration result accuracy furnished by the proposed methodology:

- Dr. Hervé Foehrenbach, from *Hôpital d'Instruction des Armées du Val de Grâce (Paris, France)*,
- Dr. Pierre Rigo, from *Centre Hospitalier Princesse Grace (Monaco)*,
- Dr. Xavier Marchandise, from *Centre Hospitalier Régional Universitaire de Lille (Lille, France)*.

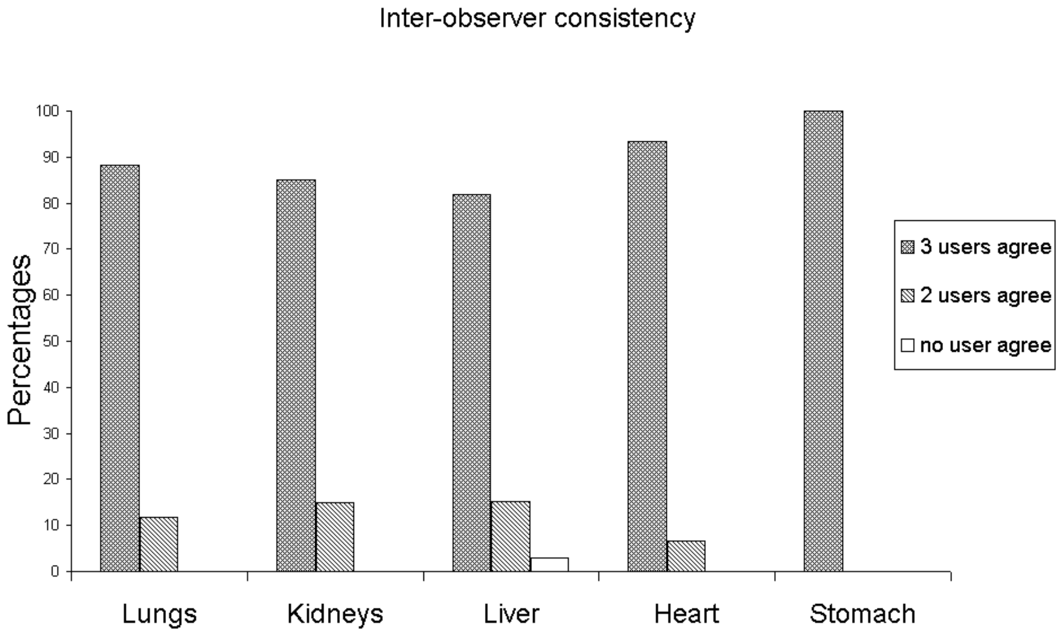

Figure 7.5: Inter-observer consistency measure. Bars illustrate, for each structure, the percentage of landmark points in which: the 3 evaluators have noted the registration accuracy with the same score (left); only two of the evaluators have agreed with the same score (center); and the 3 evaluators do not agree at all (right).

The evaluation procedure detailed in Section 7.4.1 has been used by these physicians in an independent way and assessment results have been sent by means of the developed on-line *html* web form. They have assessed three registration thoracic and/or abdominal cases, each one with different degrees of registration accuracy. The number of landmark points in which the registration has been assessed was: 208 for the lungs; 20 for the kidneys; 36 for the liver; 22 for the heart; and 10 for the stomach.

In order to have an estimation of the inter-observer consistency for each targeted region, we have computed the percentage of landmark points in which: the 3 evaluators have noted the registration accuracy with the same score; only two of the evaluators have agreed with the same score; or when the 3 evaluators do not agree at all.

Obtained results are summarized in Figure 7.5. We can appreciate a good performance of the proposed visual assessment protocol in all the targeted structures in terms of inter-observer consistency. All cases in which one evaluator disagrees with the others involve notes differing only in one step of the scoring scale, i.e. from good to acceptable or from acceptable to unacceptable, but never from good to unacceptable. We also observe that there exists more discrepancies for the liver and kidneys than for the lungs. This is due to the presence of several structures in abdominal CT images having similar intensity values. On the other hand, discrepancies in the lungs are mostly due to the lack of strong contours in emission PET images, in particular after applying the non-linear transformation. An interesting conclusion from the Figure 7.5 is that the protocol can correctly assess the registration accuracy when it is not satisfactory, such as in the stomach. Finally, it must be pointed out that only in one reference point (we recall that 296 of them have been noted), the 3 evaluators have completely disagreed, also proving the goodness of the visual assessment protocol.

7.5 Conclusions

The validation of registration algorithms is at the core current state-of-the-art research in this field, in particular in those applications involving non-linear transformations due to the lack of a reliable gold standard.

We have divided the validation of our registration methodology in three parts: evaluation of algorithm performances based on simulated data; assessment of the registration result accuracy; and validation performed in a clinical environment to evaluate its added value in diagnosis tasks. In this chapter, we have dealt with the second phase of the validation procedure. We have reviewed the different techniques usually employed to assess registration result accuracy in medical imaging applications and enumerated the special requirements in our application. Then, we conclude that, at the time being and due to the lack of time to devote to this stage, a quick way to obtain an estimation of the registration quality furnished by our methodology is the visual assessment of the results by expert observers.

For this purpose, we have developed a visual assessment protocol, based on several significant 2D slices marked with a ruler that defines landmark points (where it crosses with anatomical structures) in which the registration must be evaluated. The registration is scored according to a dissatisfaction scale that depends on the emission PET image resolution. We have computed the inter-observer consistency for three registration results and three different evaluators. Results provided by this study prove that our visual assessment protocol can be used to obtain an objective enough estimation of the registration result accuracy. Nevertheless, this protocol must not be seen as an accurate and definitive validation method and lot of work about this stage must still be made in order to obtain a gold standard for our application.

CHAPTER 8

Results

Contents

This chapter presents final results obtained by the proposed registration methodology, applied on some CT and emission PET images of thoracic and abdominal regions. In Section 8.1 a brief description of the image database we have employed in our work is given. The visual assessment protocol we have detailed in Section 7.4 has been used on some registration results obtained by the proposed registration methodology and some statistics derived from them are summarized in Section 8.2. Several illustrations of three final registration results are shown in Section 8.3 and finally, conclusions on these results and on the proposed registration methodology are discussed in Section 8.4

8.1 Image database

During this work, 20 data sets composed of CT, emission and transmission PET scans of thoracic and/or abdominal regions provided by LifeScan Louisville, Percy Hospital and H.I.A. du Val de Grâce have been used. Furthermore, three additional data sets were available from C.H.P.G. of Monaco, acquired with a combined CT-PET machine. This image database is continually increasing and new cases shall be treated in short term.

A common problem when using images from different sites is the lack of homogeneity in terms of image quality, due to the use of different scanners and clinical protocols employed to acquire the images [1]. We have designed our registration procedure in order to be as much independent as possible of image acquisition characteristics in order to avoid reformatting our image database to a common standard. Therefore, CT images have a size of 256 x 256 or 512 x 512 pixels in the xy plane (axial plane) and between 60 and 125 slices (depending on their FOV, corresponding to a thoracic or an abdominal case), with voxel dimensions approximately 1.0 x 1.0 x 5.0 mm^3. PET images have a size of 144 x 144 pixels in the xy plane (axial plane) with 160 to 230 slices, with voxel dimensions around 4.0 x 4.0 x 4.0 mm^3.

8.2 Visual assessment protocol applied on final registration results

In this Section, we have only employed the visual assessment protocol on the registration results furnished by the proposed methodology and no comparison with other registration approaches such as linear registrations or the MI-FFD technique without a structure-based initialization has been done. We consider that this question is answered in Chapter 3, where some images are shown and clearly illustrate that these methods do not furnish accurate enough registration results. Therefore, we do not see any interest of using the visual assessment protocol to confirm conclusions obtained by visual inspection of images of Chapter 3.

Therefore, the visual assessment protocol we have developed (see Section 7.4) has been used by three expert evaluators to assess five different CT and emission PET image registrations, including thoracic and abdominal cases. These registrations have been obtained by applying the proposed registration methodology (see Section 3.2 for a general system overview), using the GVF-FFD structure registration method detailed in Section 5.4.3 as a starting point to initialize a MI-FFD registration stage (see Chapter 6) working with the original grey-level images. Statistics obtained from the visual assessment protocol are summarized in Figure 8.1 and in Table 8.1. Figure 8.1 shows, for each significant thoracic and abdominal structure, the percentage of landmark points in which the registration error is noted as good, acceptable or unacceptable, according to the scoring scale of Table 7.1. Table 8.1 displays the values of

---

[1] For this reason, we are not going to detail in this manuscript acquisition or scanner characteristics of each site involved in the project.

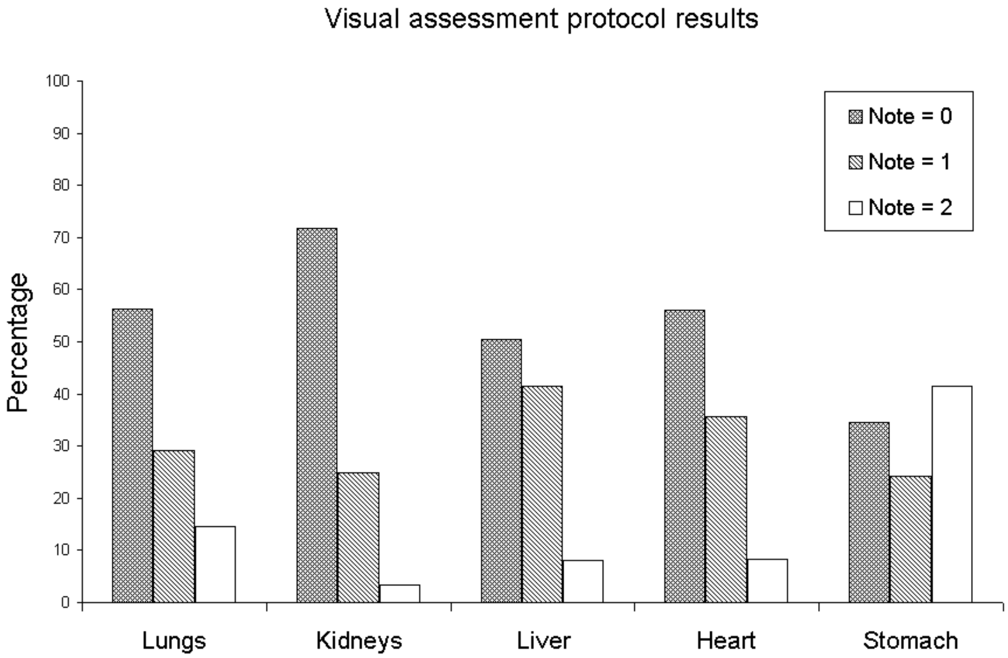

Figure 8.1: Visual assessment protocol applied on final registration results. Bars illustrate, for each structure, the percentage of landmark points in which the registration error is noted as good (left), acceptable (center) or unacceptable (left), according to the scoring scale of Table 7.1.

Table 8.1: Visual assessment protocol results.

Region	Note = 0 (%)	Note = 1 (%)	Note = 2(%)	Mean	Standard Deviation
Lungs	56.32	29.17	14.51	0.58	0.73
Kidneys	71.67	25.00	3.33	0.38	0.61
Liver	50.45	41.44	8.11	0.57	0.64
Heart	56.16	35.62	8.22	0.52	0.65
Stomach	34.48	24.14	41.38	1.07	0.88

these percentages, together with the mean and the standard deviation of the registration scores obtained from the set of landmark points corresponding to each structure. It must be pointed out that these statistics are used only as a qualitative estimation of the registration error, which maximum is equal to 2 (unacceptable registration, error larger than 1.5cm) and the minimum is zero (good registration, error lower than 0.5cm). Therefore, mean and standard deviation values shown in Table 8.1 are in the scoring scale space (not in cm).

Inspection of Figure 8.1 and Table 8.1 illustrates the good performance of the proposed non-linear registration methodology for the majority of the evaluated regions including lungs, kidneys, liver and heart. On the other hand, some significant misregistrations appear near the stomach. This conclusion is based on the percentages of landmark points in which registration is noted as good or acceptable, with respect to those ones having unacceptable registration errors.

In particular, results obtained in the thoracic wall are very satisfactory, even in the diaphragmatic region where the transformation computation was very critical due to the large deformations suffered in this region. The upper part of both lungs have in all cases good registration errors, while some landmark points corresponding to the lower part of the lungs have been noted equal to 1. The unacceptable errors found in the lungs correspond to the posterior mediastinal wall, due to the large differences in this region between CT and emission PET images.

The proposed registration methodology takes advantage of the proximity of the heart to the lungs and the strong constraints imposed on them to furnish good and acceptable registration errors of the heart.

We can observe that the kidneys produce the lowest registration errors, and this is due to the lack of strong deformations on these structures and the good initialization furnished by their segmentation-based registration stage. The landmark points corresponding to the kidneys that have been noted equal to 2 concern those ones of the right kidney close to the stomach, due to the influence of this structure on their registration. On the other hand, most of the landmark points corresponding to the left kidney have been noted to 0 (even if there are some scores equal to 1 in zones close to the liver).

The proposed registration methodology provides good and acceptable registration errors in the liver, despite of the difficulties of this structure. Its landmark points noted as 0 correspond in general to the upper part and the left wall of the liver, while those ones in which registration has been noted to 1 are mostly located on the lower part of the liver. Some unacceptable registration errors are found on the right wall of the liver since, sometimes, there are small abdominal structures close and having similar intensity values to the liver, thus producing good similarity measure values, even if the registration is not well done.

Most important registration errors have been found in the stomach (it is the only targeted structure having a mean of notes larger than 1), due to the severity of its deformations and the lack of strong constraints imposed on this structure. Nevertheless, some good and acceptable notes have been assigned to those landmark points corresponding to the stomach that are relatively close to the kidneys and the lungs because they take advantage of the initialization registration stage applied to these structures.

8.3 Illustrations of final registration results

Three final registration result examples are shown in the following pages. Even if the visual inspection of these examples is biased by the printing quality and the possibility of showing only a limited number of 2D slices, we think that it can provide to the reader an approximation of the good performance of the proposed registration methodology.

The first one contains all segmented thoracic and abdominal structures, i.e., lungs, kidneys and liver, and other regions that have not been introduced in the initialization stage such as heart or stomach. Figure 8.2 includes four axial and two coronal 2D slices of the original CT (left), the registered emission PET (center) image and their superimposition (right). The visualization of these images graphically confirms the conclusions obtained from the visual assessment protocol: registration results are satisfactory in all structures except for the stomach. Nevertheless, some errors appear around the posterior mediastinal region because the grey-level registration stage has displaced this region towards nearby zones with similar heart intensities.

The second case, shown in Figure 8.3, is very interesting due to the presence of a malignant tumor located in the left lung. The challenge of the transformation computation between these images was to compensate their severe differences, illustrated in the top row of coronal slices in Figure 8.3, where it can be easily seen that the tumor is found in distant coronal slices after applying a linear registration transformation to the emission PET image (Figure 8.3, top row, center). The application of the proposed non-linear registration methodology has allowed to obtain a transformation capable of placing the tumor in the correct coronal slice (Figure 8.3, top row, right). The next images shown in this figure correspond to an axial, a coronal and a sagittal 2D slices where the tumor can be seen, corresponding to the CT image (left), the emission PET image after applying our registration methodology (center) and their superimposition (right).

Finally, some axial (Figure 8.4), coronal (Figure 8.5) and sagittal (Figure 8.6) 2D slices of a thoracic case are shown, in order to illustrate the good performance of the registration methodology in the whole 3D volumes.

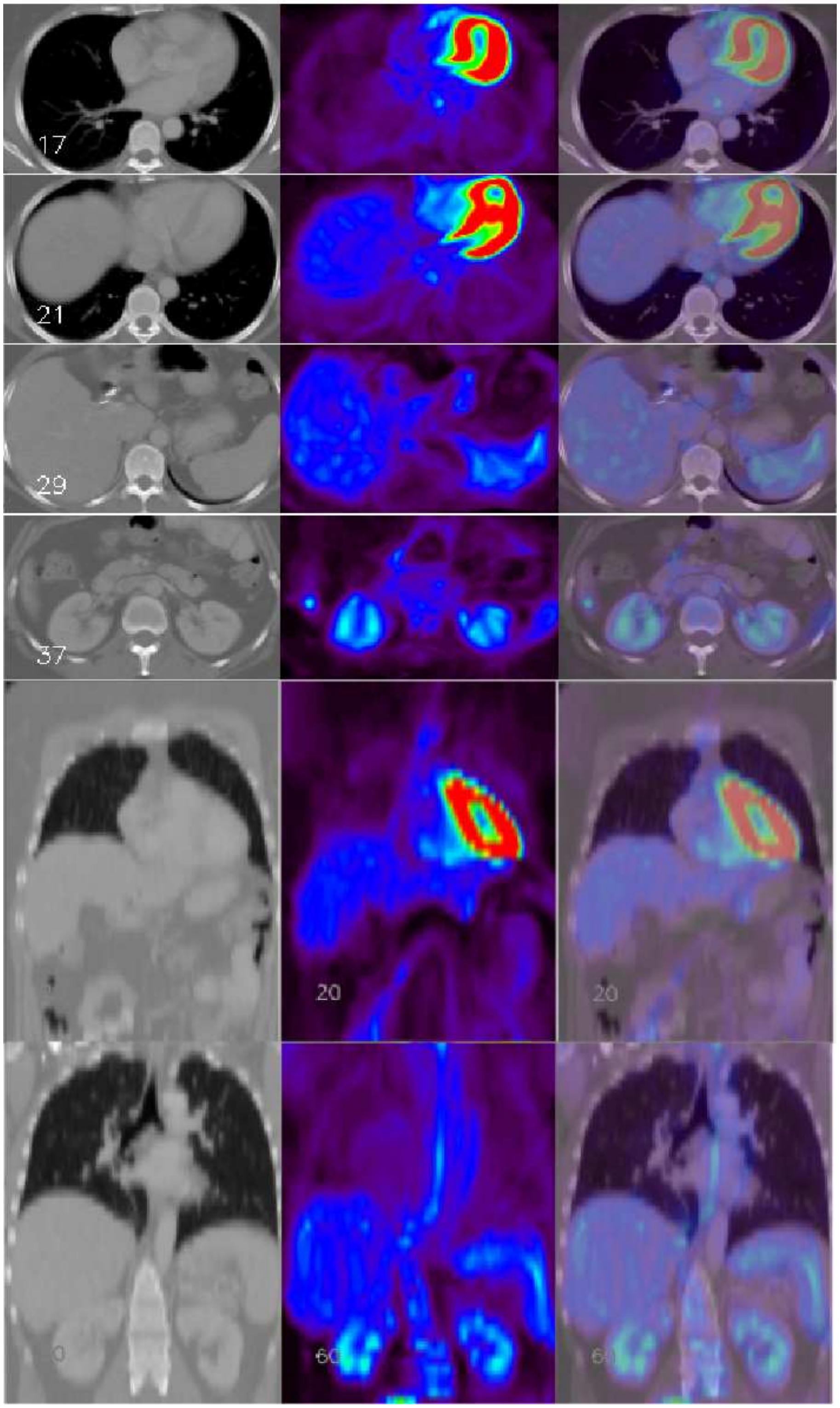

Figure 8.2: Final registration result. Case 1. Axial (four top rows) and coronal (two bottom rows) 2D slices of the CT (left) and registered (with the proposed registration methodology) emission PET (center) images and their superimposition (right).

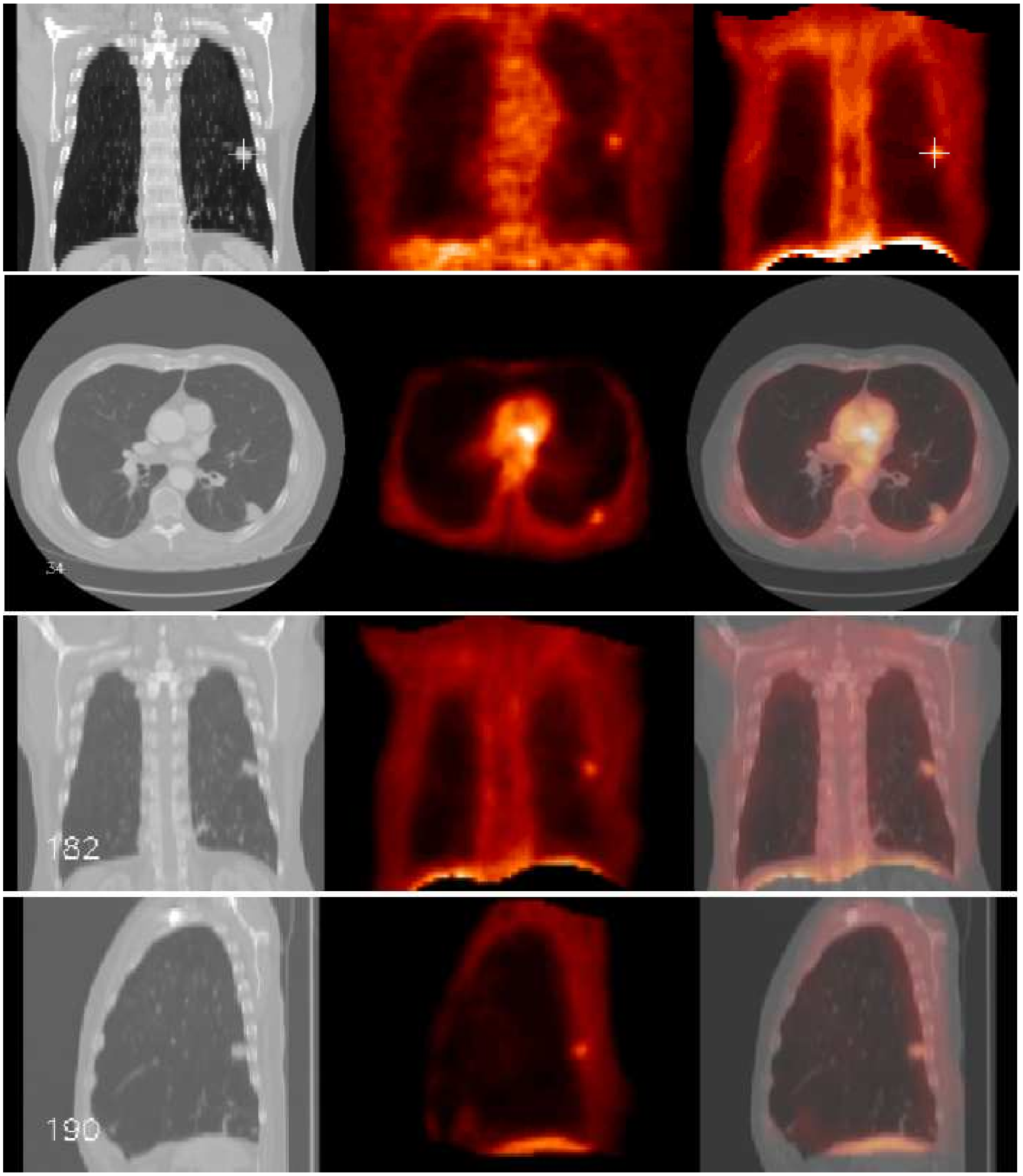

Figure 8.3: Final registration result. Case 2. 2D coronal slices (top row) of the CT image (left), the emission PET image registered with a linear transformation (center) and the emission PET image registered with the proposed non-linear registration methodology (right). The mark on the top row points out where the tumor is located. It can be seen that the tumor is found in different coronal slices after applying a linear transformation (center) and that this problem is solved using the proposed non-linear registration methodology (right).
An axial (second row), a coronal (third row) and a sagittal (bottom row) 2D slices of the CT (left) and the registered (applying the proposed registration methodology) emission PET (center) images, and their superimposition (right).

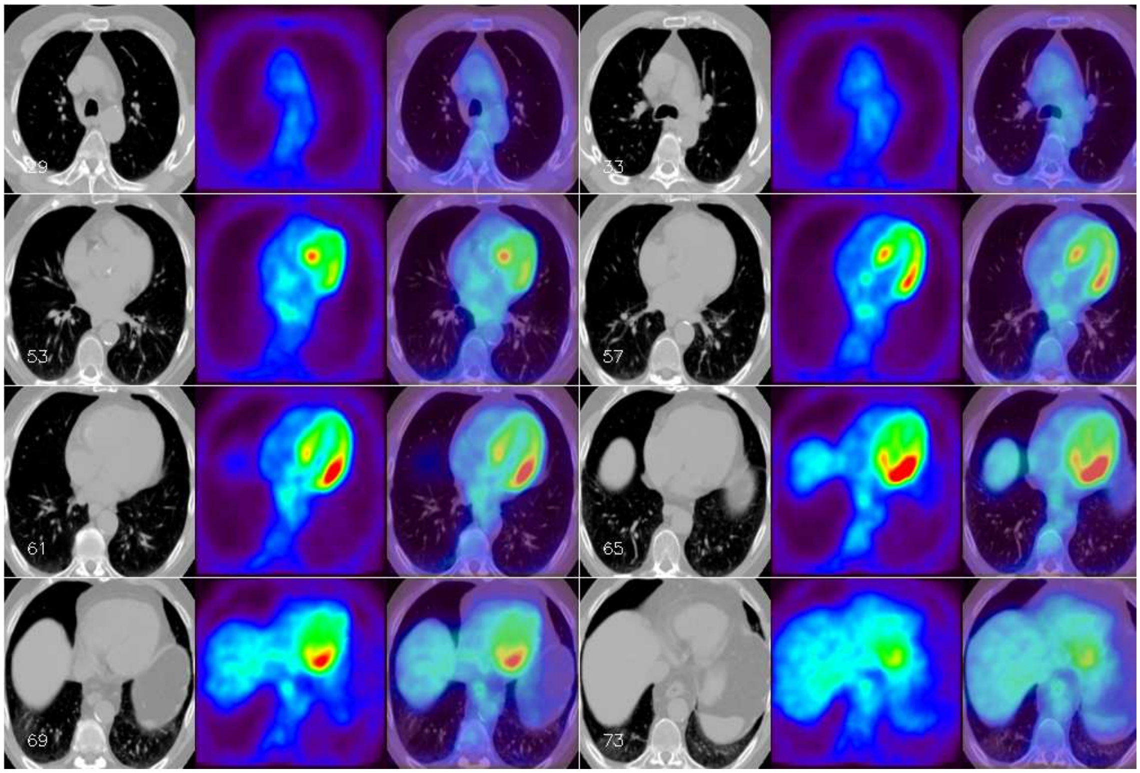

Figure 8.4: Final registration result. Case 3 (axial slices). Some axial 2D slices of the CT (first and fourth columns) and the registered (applying the proposed registration methodology) emission PET (second and fifth columns) images, and their superimposition (third and sixth columns).

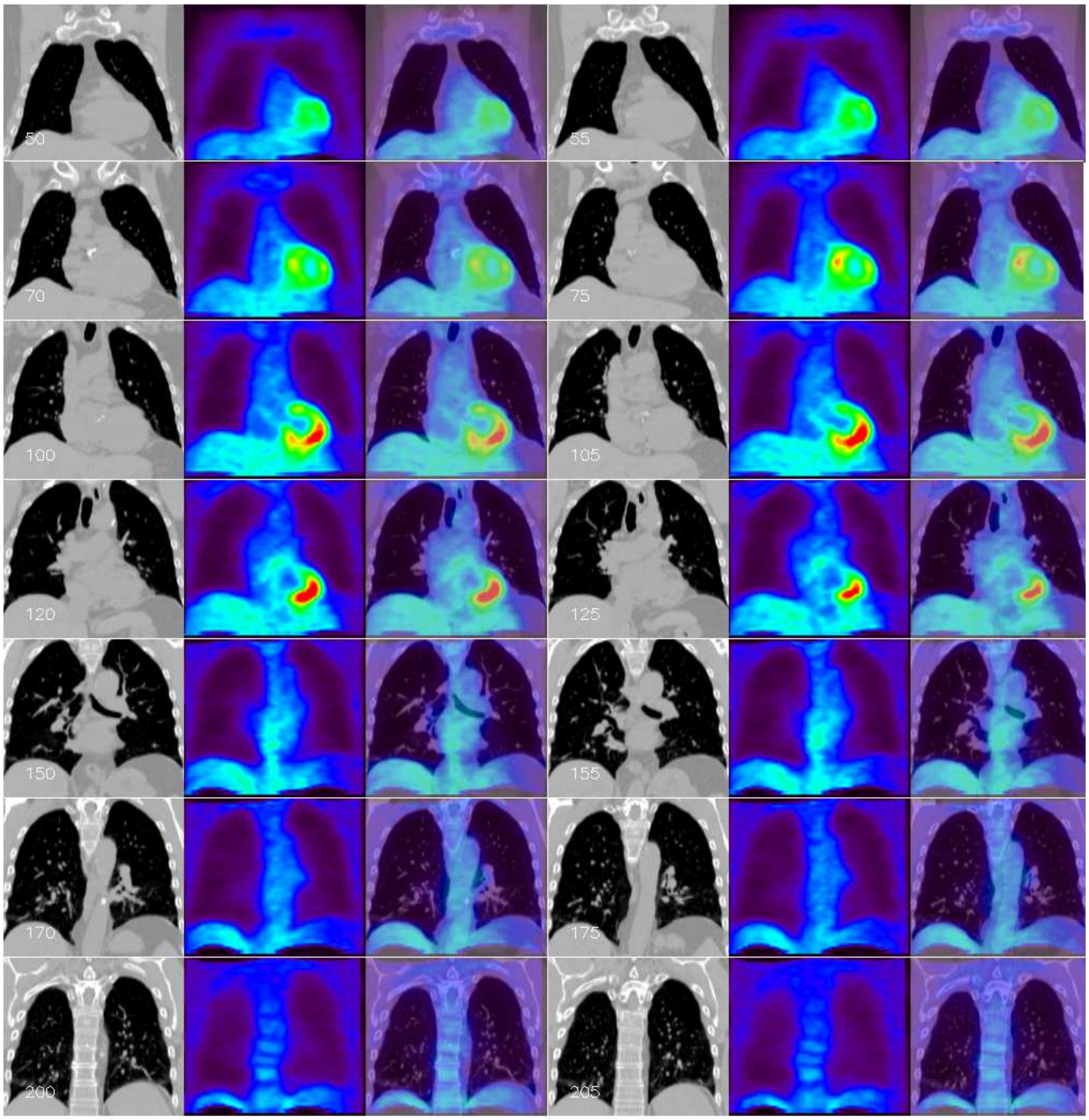

Figure 8.5: Final registration result. Case 3 (coronal slices). Some coronal 2D slices of the CT (first and fourth columns) and the registered (applying the proposed registration methodology) emission PET (second and fifth columns) images, and their superimposition (third and sixth columns).

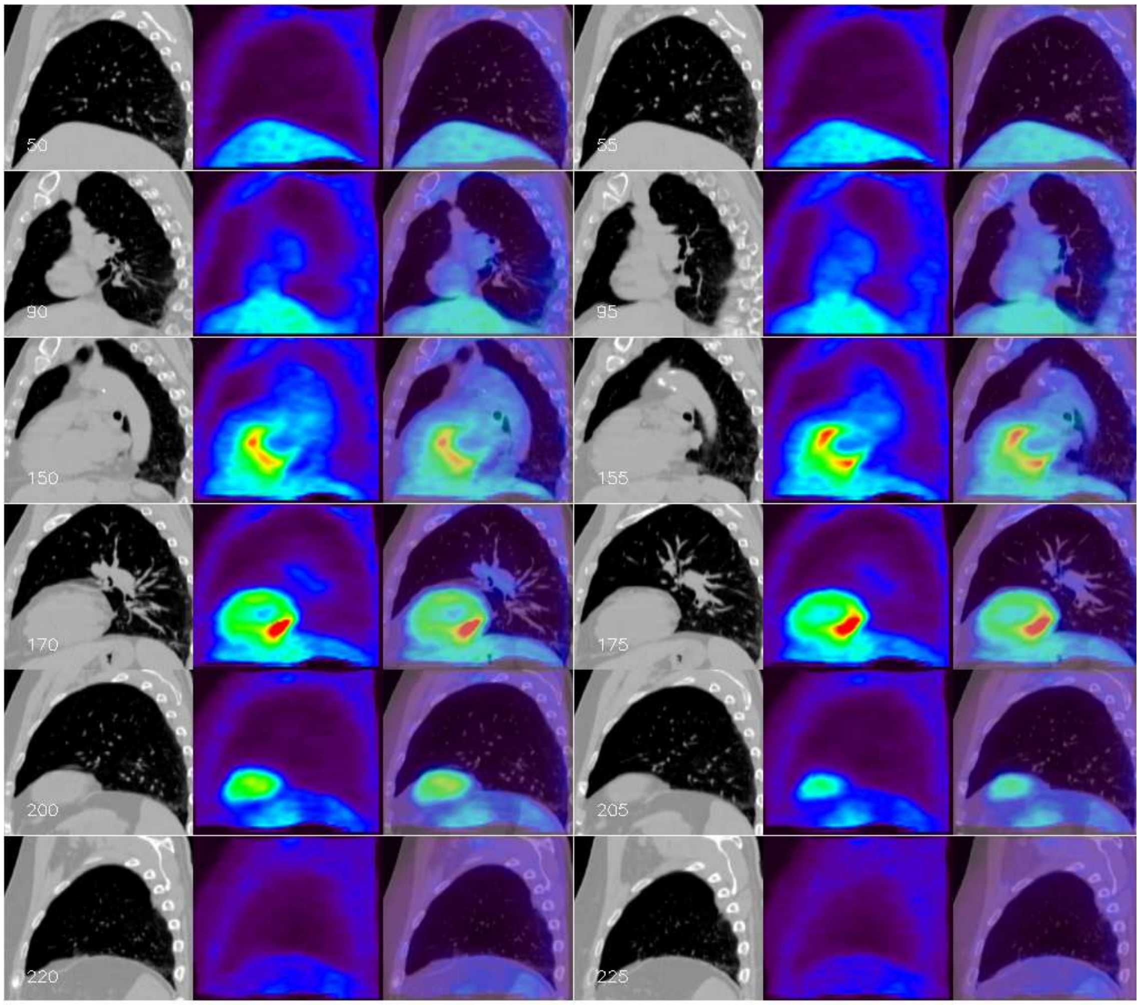

Figure 8.6: Final registration result. Case 3 (sagittal slices). Some sagittal 2D slices of the CT (first and fourth columns) and the registered (applying the proposed registration methodology) emission PET (second and fifth columns) images, and their superimposition (third and sixth columns).

8.4 Conclusions

In this chapter, we have presented some final registration results obtained by applying the proposed registration methodology to thoracic and/or abdominal CT and PET emission images.

Results provided by the application of the visual assessment protocol detailed in Section 7.4 to the pairs of images registered by the proposed methodology prove that we obtain acceptable registration errors for the majority of the targeted thoracic and abdominal structures except for the stomach. This is due to the absence of this structure in the initialization phase, the strong deformations the stomach undergoes and the existence of close small structures with similar intensity values, misleading the fine registration step working with the whole set of image grey-levels.

Therefore, these promising registration results illustrate the fact that registration is better achieved around structures that have been recognized with the segmentation procedure detailed in Chapter 4. We recall that a second way of evaluating segmentation result accuracy was based on the assessment of final registration results obtained by the proposed methodology. As a matter of fact, the transformation computation between CT and emission PET images strongly depends on the anatomical information that we are capable to extract from both data volumes, i.e., it depends on the segmentation result accuracy. Therefore, the evaluation of final registration results can also be seen as a retrospective assessment of the segmentation stage. Final segmentation results have proved to be accurate enough to guide the structure registration procedure that will initialize, close to the final solution near segmented structures, the refinement registration step working with the whole set of intensities.

Several illustrations of three different registration cases are shown. Visual inspection of these images confirms the conclusions provided by the visual assessment protocol.

Some words must be said about registration results obtained by applying the proposed registration methodology to two particular sets of images available in our database: images acquired with a combined CT-PET system; and pathological images with lung tumors.

Insignificant or no improvement has been obtained on the registration of images acquired by a hybrid system. Only in one case, some small differences have been found in the cardiac region. It must be pointed out that only three of these pairs of images were available and they did present neither significant visible artifacts nor visible tumors, it means cases in which a non-linear registration algorithm could give additional information to the mechanical registration furnished by these machines. Therefore, we cannot draw any conclusions about the application of the proposed methodology on this type of images until a more exhaustive database would be available.

As detailed in the manuscript, the proposed registration methodology is based on an initialization phase guided by the segmentation and registration of several thoracic and abdominal structures. In some pathological cases (for instance, when a tumor is located at the middle of a lung), this strategy may produce undesired effects on tumors since their initial registration is guided by larger structures and the fine registration stage cannot recover these misregistrations. In order to avoid that, tumors should be included in the initialization phase as an additional anatomical structure, thus imposing some constraints on their registration. Some initial results of a semi-interactive tumor segmentation procedure we have developed and its effect on tumor registration are detailed in Appendix D.

CHAPTER 9

Conclusions and perspectives

9.1 Conclusions

The main goal of this work has been to provide a satisfactory solution to a complex problem of medical image processing, the registration of CT and emission PET images of thoracic and abdominal regions. This solution should be objective, robust, fast and as automatic as possible in order to be used in clinical routine in a short term. Along this document, the difficulties associated to this application have been described. The main ones include the elastic nature of the organs located in thoracic and abdominal regions, the large inter-individual range of structure movements and metabolic activity, the different physical nature underlying both acquisition techniques, the different acquisition protocols and the time passed between them.

We have reviewed the registration literature and we have justified the use of a Free-Form Deformation model over other non-linear transformation techniques. Furthermore, we have highlighted the problems associated with whole-content based non-linear registration approaches when working with emission PET images in thoracic and abdominal cases and without prior information or constraints introduced in the procedure. As a matter of fact, these approaches have difficulties to deal with the low SNR quality of emission PET scans, the presence of severe deformations in thorax and abdomen and the lack of linear correspondences between the intensities of homologous regions.

Therefore, we have proposed and evaluated a registration methodology in which prior information about the anatomical structures involved in the application is introduced. Conclusions on the proposed registration methodology are given in the following paragraphs.

Proposed registration methodology The proposed registration methodology is based on the incorporation of prior anatomical information in an intensity-based non-linear registration algorithm. The incorporation of this prior information is performed in an explicit way, by initializing the intensity-based registration stage with the solution obtained by a non-linear registration of corresponding anatomical surfaces segmented through a hierarchically ordered set of anatomy-specific rules. Therefore, the general scheme of the registration approach we propose is divided in two stages: a structure registration phase in which homologous structures are segmented in both CT and emission PET grey-level images and registered with a non-linear transformation; and a grey-level registration phase in which a non-linear registration technique is applied to the whole set of image intensities of the images. The second stage is initialized with the transformation provided by the structure registration stage and it furnishes the final non-linear transformation.

As a matter of fact, the structure registration phase can be seen as an anatomical multi-resolution step, filtering out from the data the main anatomical structures, then transferring the result as an initial estimate to a higher level where finer anatomical detail will be considered. The grey-level registration phase can be considered as a refinement step of the structure registration results, capable of correcting any errors the segmentation might have induced and improving the registration of those regions distant from the segmented structures. Therefore, we do not need an accurate structure segmentation of the targeted structures, since only an approximation is required to compute an initial transformation between them.

We have justified the use of this explicit approach instead of an implicit one in our application, in which we work with pathological images and a limited computational burden of the algorithm is very important. This is the main original point of the proposed registration methodology since we only use general anatomical knowledge instead of any kind of geometric or morphologic model of the structures such as atlases of phantoms, permitting to work with any kind of unexpected situations.

Transformations in both steps are modeled by means of Free-Form Deformations (FFD), governed by a three-dimensional grid of control points. The FFD model has proved to be a flexible technique allowing us to construct an original registration methodology based on it and providing us a simple way of interaction between feature-based and full content-based registration phases. This interaction between these two theorically confronted methods, derived from the chosen strategy, has allowed us to combine their associated advantages while canceling their drawbacks. The FFD model uses an uniform grid of knot points superimposed on the target image and that guides its deformation. One could think that this grid of control points is a bit limiting, and certainly, a grid having more control points in regions where more local deformations occurs and a lower number of them in less important regions such as the background could provide better results, in particular in terms of computational cost. Nevertheless, multi-resolution and multi-grid approaches based on uniform FFD grids can successfully cope with large or local deformations, as illustrated in the lung registration stage of the proposed methodology.

A different problem is if the optimization of a given FFD control point is misled by the similarity measure criterion, thus providing wrong registrations. For instance, tumors are usually well contrasted in PET images but in CT ones they may have similar intensities to neighboring structures. The presented registration methodology add some constraints on the registration of some structures, but not on the tumors. Therefore, their registration strongly depends on the deformations undergone by surrounding structures, causing significant tumor misregistrations in some pathological cases such as when the tumor is located in the middle of a lung. In order to avoid these tumor registration errors, we have developed a semi-interactive tumor segmentation approach, aiming at incorporating some tumor-based constraints to the proposed registration methodology. Preliminary results are shown in Appendix D.

We have used the visual assessment protocol we have developed to assess five registrations obtained with the proposed methodology. According to the statistics provided by the visual assessment protocol, the proposed methodology attains the application requirements fixed at the beginning of our work in terms of accuracy of the registration results, furnishing registration errors within clinically acceptable ranges in most relevant structures, unlike other tested non-linear registration methods. Nevertheless, in parts of some structures such as the heart and the stomach, significant errors are sometimes found due to the severity of their differences between two acquisitions and to the lack of strong constraints imposed on them.

We have also applied the proposed registration methodology to three pair of CT and emission PET images acquired with hybrid systems. Insignificant or little registration improvement has been obtained since these images did not include cases in which a software-based non-linear registration algorithm could add some information to the CT-PET combined machines such as in pathological cases. Then, we should wait until a more extensive database of these images will be available in order to evaluate the effect of the proposed methodology on the superimposition of these images.

In terms of computational cost, the proposed methodology has provided the framework for a software that could be used in clinical routine after a phase of code optimization and parallelization (that could reduce computational cost by more or less a factor of 3). At the time being, the proposed registration methodology takes in general less than 2 hours to furnish good quality results (the structure segmentation stages only takes around 2 minutes) for a thoracic and abdominal case. This means a reduction of the computational burden of the algorithm of around 60% (80% if we only take into account convergence times of the grey-level registration stage).

In fact, the firm associated to the project, *SEGAMI S.A.R.L.* is actually developing an interface and adapting our programs in order to provide to the physicians a software solution [1] to this challenging application in their multi-modality workstations (*Mirage* stations), that will be operational at the end of 2004. This option will complete the affine registration (*MIRegister*) solution already available on *Mirage* stations. Due to the large number of hospitals having these workstations, once the non-linear CT-PET thoracic and abdominal option will be added, the clinical evaluation phase could begin. This stage will allow us to test the proposed registration methodology in a clinical environment, providing a useful feedback from the users and a high number of cases to better assess the proposed methodology.

---

[1] Some parts of the presented work have lead to a U.S. patent proposal, that is actually in an evaluation phase. U.S. Provisional Patent Appl., number 60/369, 681, Registration of thoracic and abdominal imaging modalities. I. Bloch, G. Delso and O. Camara.

Recommendations about the acquisition protocol One of the requirement for the proposed registration methodology was to be as independent as possible of the image acquisition protocol. Therefore, we have worked with a database of inhomogeneous CT and PET images with differences including respiratory and arm's position in both scans. We have not observed a different behavior of the proposed registration methodology depending on these factors. Nevertheless, it is clear that the transformation between both images to register will be more complex (strong chest deformations appear) if the arm's position is not the same in both scans, thus making easier to obtain better registration results. As a matter of fact, this is not currently a major problem since acquisition times for PET images are already quite low (around 30 minutes for the most recent scanners), thus, the majority of patients can hold their arms above head during the acquisition.

Concerning the respiratory position of the CT scan, Goerres et al. [103] have shown that in order to make easier a CT-PET registration, the CT scan must be acquired in normal breathing. However, by doing this, the CT scan will have lower image quality due to the apparition of breathing artifacts. Therefore, this choice strongly depends on the targeted application of the registration. Obviously, these problems are considerably reduced in hybrid PET/CT systems with respect to stand-alone devices, thus a software-based registration algorithm can be focused on coping with non-linear deformations still existing between images acquired with these systems.

9.2 Future work

The perspectives of our work are numerous and can be classified into short term, middle and long term and very long term ones.

Short term Future work classified as short term basically concerns implementation details and enhancements of the proposed methodology in each one of its stages:

- Structure segmentation: the main improvement that could be easily added in this phase is the addition of other structures into the hierarchical segmentation procedure such as the heart or the stomach, that would provide additional constraints on image zones where these structures are located. As a matter of fact, the ROI construction corresponding to these structures could be easily derived from already recognized structures by means of robust spatial relations such as the "the stomach is always located under the left lung" or "the heart is always localized on the left of the right lung and close to the left one". Future work concerning this stage could also be the construction of a database of segmented structures in order to study their shape variability and the robustness of their spatial relationships. This *atlas* would allow the study of other type of structure relations such as distances, that could be used to better constrain future structure segmentations.

- Structure registration: results provided by the GVF-FFD method are less accurate than those obtained with the RMS-FFD due to the trade-off between the capacity of coping with local deformations and the rejection of outliers. The use of outlier rejection techniques such as M-estimators or the use of alternative and more robust deformation field computation techniques such as block matching could notably improve the result accuracy of this method. Concerning the RMS-FFD method, the optimization approach implemented was the simplest one, and by using more sophisticated techniques, the algorithm computational cost could be reduced.

- Grey level registration: several ideas that could enhance the performance of this stage have not been implemented because of a lack of time. The first one concerns the use of alternative entropy formulations instead of Shannon's one in order to accelerate the Mutual Information computation and to better take into account the dependence between neighboring voxels. Another idea related to the similarity criterion involves the binning procedure in the histogram computation. Scale space histogram analysis techniques could be used in order to select an optimal number of bins and their size, depending on the image intensities. Finally, from the work of Maes et al. [173] or Hermosillo et al. [47], an analytic expression of the similarity criterion gradient in the case of FFD transformations should be investigated. This will notably improve convergence results with respect to the gradient estimation actually employed.

- Evaluation of the registration result accuracy: an interesting evaluation technique for our application would be the use of biomechanical models, but the lack of time has forced us to leave it for further work. The idea was to employ a labeled whole-body IRM numerical phantom, proposed by Zubal et al. [317] to simulate a PET image by means of Monte Carlo methods, which can describe the geometry and the physical characteristics of a PET camera. Then, a deformation field generated from the NCAT phantom [254 ; 255] could be used to simulate different PET images through the respiratory and cardiac cycles. Another initial idea was the use of a second tracer, 18-fluor under the Na-F shape, employed to mark bone structures, in order to verify the absence of undesired deformations in rigid structures. Unfortunately, these acquisitions are not yet available.

Middle and long term Several possible directions are worth to be evaluated in the future, concerning the proposed methodology. The first one is the use of an irregular grid instead of a FFD one in order to place the control points in image regions where they are needed, such as in the method proposed by Marsland and Twining [186]. This approach will eliminate the unnecessary optimization of several control points that do not significantly contribute to the final results.

Another important aspect that could be interesting to investigate is the number of transformation parameters (control points in a grid-based approach) required for a given technique in order to furnish an acceptable level of registration accuracy. Several methods such as Radial Basis Functions-based or Discrete Cosinus Transform-based can have a lower computational cost than FFD-based because of having a lower quantity of parameters to optimize. On the other hand, fluid and other non-parametric techniques can furnish a very local transformation (three degrees of freedom for each voxel) allowing the existence of irregular transformations at the expense of a higher computational burden of the registration algorithm. A comparison between these techniques and a medical evaluation of the results could furnish useful information in order to state the required accuracy for this registration application.

Other ideas could be investigated that will notably change the proposed registration methodology. One of these suggestions involves the computation of the non-linear transformation using feature and voxel information at the same time, once structures have been segmented. Or even, mixing segmentation and registration procedures in a whole system. Another idea concerns the introduction of prior information by means of biomechanical models, for example modeling structure movements and deformations along respiratory or cardiac cycles. This is a current state-of-the-art research subject [250] and it represents one of the most promising branches in registration because it could furnish valuable information to assure physically correct transformations and it can be a useful tool for the registration result validation. Some existing FEM models available for some structures such as the liver, together with the NCAT phantom [254 ; 255], could be a starting point for this modeling.

The previous idea is linked to the functional tumor registration problem. We have proposed a semi-interactive tumor segmentation (see Appendix D), and preliminary results are very satisfactory. The major problem of a registration technique applied to functional tumors concerns the loss of their significant metabolic information after a non-linear registration is applied. This is a crucial point because it prevents the computation of quantitative information such as Standardized Uptake Value (SUV) measures that are very important for analyzing tumor malignancy, radiotherapy and treatment planning. Some ideas could be studied in order to preserve this metabolic information for some registration applications, such as to compute the registration from the CT image to the PET one.

It could be also useful to take profit of the development of combined CT-PET devices in order to identify the interest of applying the proposed methodology to images acquired with these machines aiming at compensating the deformations that the hardware registration has not been able to cope with. Furthermore, we should study whether the structure registration phase is still required or the mechanical registration provided by these systems is already accurate enough for initializing a whole-content non-linear registration step. As a matter of fact, according to the opinion of the main workstation developers and scanner constructors, the future scheme of an oncology system will be composed of a combined PET/CT machine and a software-based registration algorithm included on the scanner consoles in order to correct possible artifacts and registration errors due to soft tissue and physiological motions. This scheme will allow the apparition of new registration applications involving new emerging PET tracers. The combination of PET images obtained with different tracers will be very useful, but the majority of these tracers produces PET images having even less anatomical references than FDG-PET ones. If these PET scans were acquired with a hybrid system, we could make the assumption that this CT-PET mechanical registration is accurate enough and the proposed registration methodology could be used to obtain a registration between the CT images associated to each one of the PET scans acquired with different tracers.

Finally, future work should be also focused on the adaptation of clinical protocols to be oriented to the image acquisition for registration applications. For instance, a gating PET acquisition could be very useful in order to integrate this complementary information in the registration procedure.

In a non-medical application context, although it has not been described in the manuscript, some parts of the registration system have been successfully used in a face recognition application. This research line must be further studied, as well as the application of our registration system in other registration applications involving other kind of images such as radar ones.

Very long term Future work classified as very long term (10 or 20 years from now) concerns basically our skills as futurologists. In order to clarify this crazy sentence, I shall reproduce the advice given by R. Bajcsy [6] in a workshop devoted to biomedical image registration (WBIR'03) last summer. This adorable woman is one of the pioneers on registration techniques who started to work on this subject in the late 70's. The advice she has given was: "Dream big". When she began her investigations on this subject, and she had problems to read a 2D slice due to the limited capacity of available computers, she could not imagine, even dream, the technology advances that she has lived in medical image applications. In that time, the use of 3D image volumes embedded in a clinical routine protocol or computer-aided surgery applications sounded foolish. Therefore, it is our turn to dream and we can imagine, in a furthest future, the possibility of registering 3D CT and PET whole-body images in real-time, by means of a fast acquisition device (less than one minute), together with powerful, fast and robust image processing techniques. In order to better illustrate this, the interested reader is referred to observe the medical staff and their tools in any episode of Star Trek.

Part III

Appendices

APPENDIX A

Find-Judas registration application

I have taken the liberty of illustrating the context of our work with a metaphoric and non-medical example which could help to better understand the interest of the application. In Figure A.1, a *last supper* picture is shown, where we can appreciate the presence of Jesus and his twelve disciples that are peacefully eating. Poor Jesus knows that one of his friends is a traitor but unluckily he does not know which one. Let me propose the following application to help Jesus: find Judas. If we are not an expert observer, it would be difficult to find him. In fact, this picture has the same characteristics as a CT image: good quality, well localized contours, etc., but it does not provide any information about the malignancy of the disciples.

Figure A.1: Original *last supper* picture.

If we could obtain another version of the picture by means of another acquisition system such as a device that allows to represent in an image the aura of the disciples, or even better the possibility for each disciple of being a traitor, we could know for each disciple if he is benign or malign. This is also the case of the PET image, which like the aura acquisition, is very noisy and has a lot of artifacts, but it provides a necessary functional information. Let the Figure A.2 be the image produced by this miraculous device. The very very bad disciple can be easily recognized (in red, for the not too awaken minds) but the problem is that the nature of both acquisitions is very different, making more difficult the task of finding the traitor.

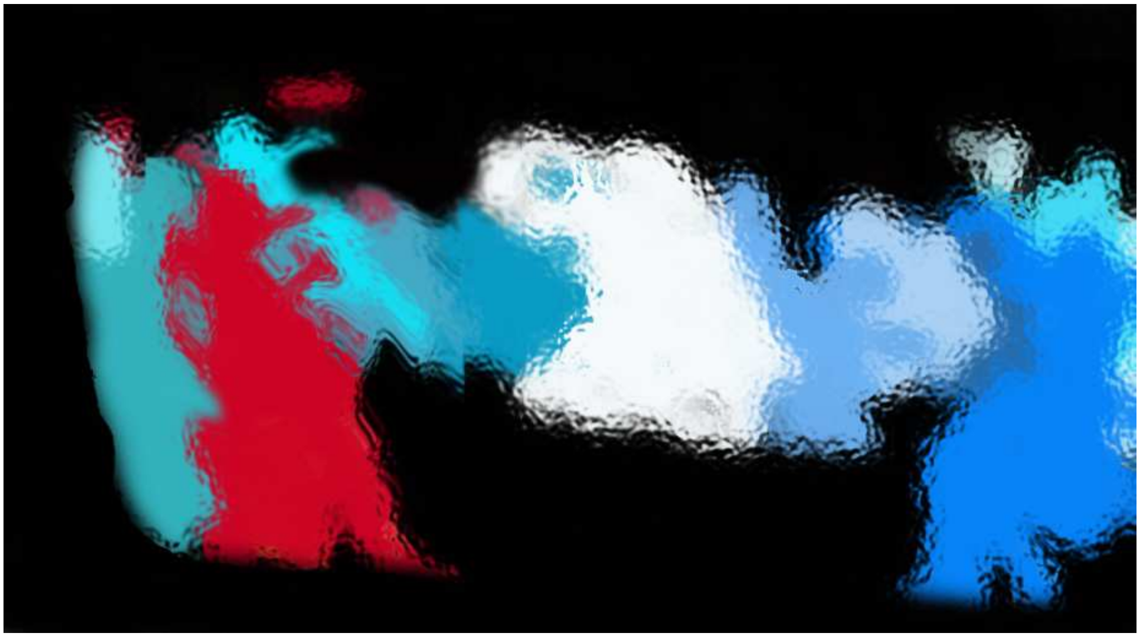

Figure A.2: Aura representation of the *last supper*. The color scale indicates the degree of malignancy of a person, red color corresponding to a very very bad person, blue color to a good person and white color to a saint person.

In order to be able to compare and superimpose both images, one of the images must be transformed (in this case, the aura image) in a non-linear fashion to establish a correspondence between the auras and the disciples of the picture. In Figure A.3, the transformed aura image and the superimposition of both images are shown. The combination of the two images will give us a good localization while preserving the functional information about the disciple or the tumor, as shown in the figure, where Judas is found.

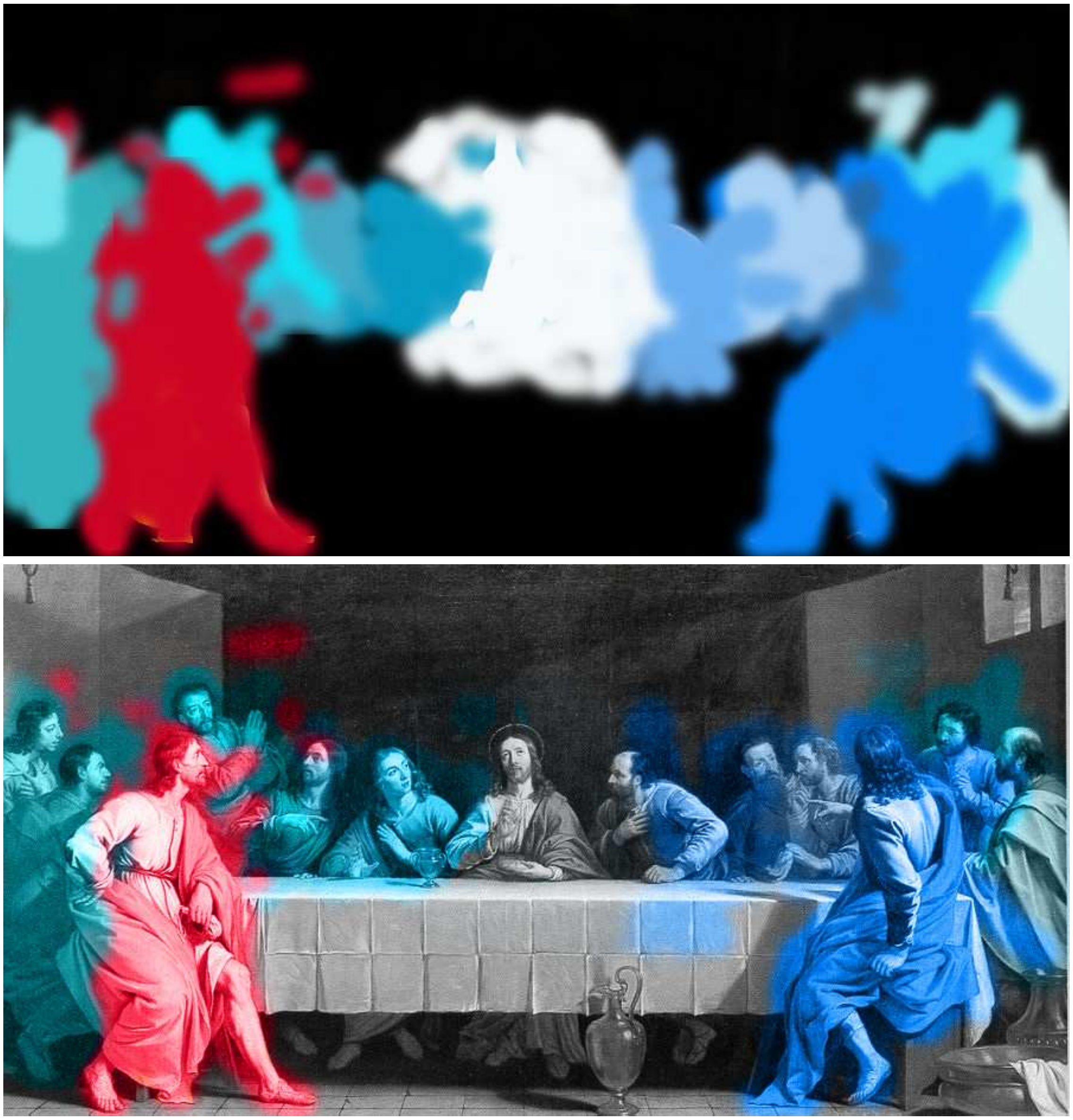

Figure A.3: Results of the find-Judas application. Top: aura transformed image; bottom: superimposition of anatomical and functional images.

APPENDIX B

Medical information about cancer

B.1 What is cancer?

Cancer[1] is a term used to describe a group of illnesses all having in common the lack of regulated cell growth, which results in serious health problems. Cancer has afflicted humans throughout recorded history, the earliest evidence of cancer being fossilized bone tumors, human mummies in ancient Egypt, and ancient manuscripts (see Figure B.1 for an example). The origin of the word cancer is credited to Hippocrates (460-370 B.C.), who used the terms *carcinos* and *carcinoma* to describe non-ulcer forming and ulcer-forming tumors. In Greek these words refer to a crab because of the swollen blood vessels around the area of a tumor, which were thought to resemble a crab limbs.

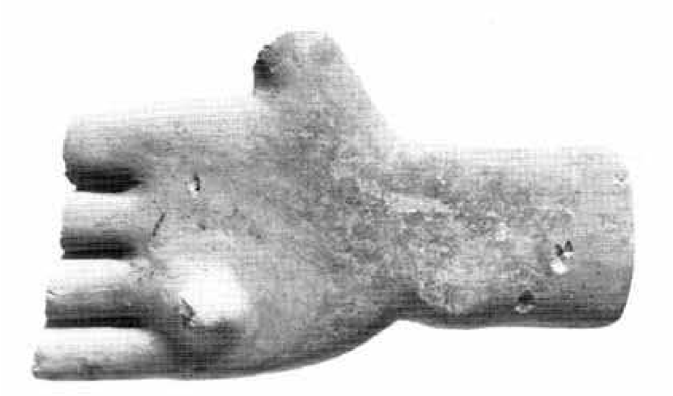

Figure B.1: Mud-fired (terracotta) art object representing a tumor (400 B.C.).

Cancer develops when cells in a part of the body break free of normal constraints and start reproducing out of control. During the early years of a person's life, normal cells divide more rapidly until the person becomes an adult. After that, cells in most parts of the body divide only to replace worn-out or dying cells and to repair injuries. This growth of new cells is a highly complex and tightly regulated process.

---

[1] Apart from Internet resources, interesting tutorials about cancer can be found in [147 ; 143 ; 80]

With cancer, for one reason or another, the growth of new cells has become defective. When a cancer cell begins to grow, rather than just replacing the cells that have been damaged or lost, it multiplies out of control, taking over the organ. Another cause leading to cancerous cells is when a genetic mutation results in a loss of cell ability of self-destructing (called *apoptosis*). All normal cells have surveillance mechanisms that look for damage or for problems with their own control systems. If such problems are found, the cell destroys itself.

Cancer is a disorder that can occur inside any cell in our body and it begins with a damage of the genetic code of the cell (DNA). This substance, presented in every cell, directs all its activities (including the growth task) and most of the time, when DNA becomes damaged, the body is able to repair it. In cancer cells, the damaged DNA is not repaired and this genetic mutation advances when the cell descendants mutate further. There are three groups of genes implicated in the development of cancer:

- oncogenes: they are damaged genes whose presence in certain forms and/or overactivity can stimulate the development of cancer by instructing cells to make proteins that stimulate excessive cell growth and division;

- tumor suppressor genes: they are normal genes whose absence can lead to cancer because their function is to instruct cells to produce proteins that restrain cell growth and division;

- DNA repair genes: they are codes for proteins and their normal function is to correct errors that arise when cells duplicate their DNA prior to cell division.

Cancer often arises because of the accumulation of mutations involving oncogenes, tumor suppressor genes and DNA repair genes.

In some cases the cancer cell grows so much that it forms a mass of abnormal cells called a *tumor*. This tumor can cause health problems by blocking internal ducts or by pressing against other organs, preventing them from working properly. But not all tumors are cancerous and depending on whether they can spread or not, tumors are classified as being either *benign* or *malignant*. Benign cancers cause problems in the organ where they occur, but do not spread. These tumors may be removed surgically or treated with drugs and/or radiation to reduce their size. This action usually cures the disease. However, with a malignant growth, cells from the original tumor have the ability to migrate from the original site and may travel to other sites in the body. This spread happens in two ways: by *invasion*, where the cells directly migrate and penetrate into neighboring tissues; and by *metastasis*, where cells from the original tumor have the ability to penetrate into lymphatic and blood vessels, circulating through the bloodstream. Once this happens, these cancer cells migrate to many other distant sites and organs in the body, as can be seen in Figure B.2. In this way, multiple growths occur, affecting many parts of the body, eventually causing multiple organs to fail. These growths are known as *secondary* cancers or *metastasis*, but they share the name of the original *primary* tumor. Organs or parts of the body that have a rich blood or lymph supply are the most likely sites for these secondary malignant growths to appear (lungs, liver, bone marrow, lymph nodes). By definition, the term *cancer* applies only to *malignant* tumors. A malignant tumor is a more serious health problem than a benign tumor because of this ability to metastasize. Three examples of cell growth leading to skin, lung and prostate cancer are shown in Figures B.2 and B.3, where the progression of the disease can be appreciated.

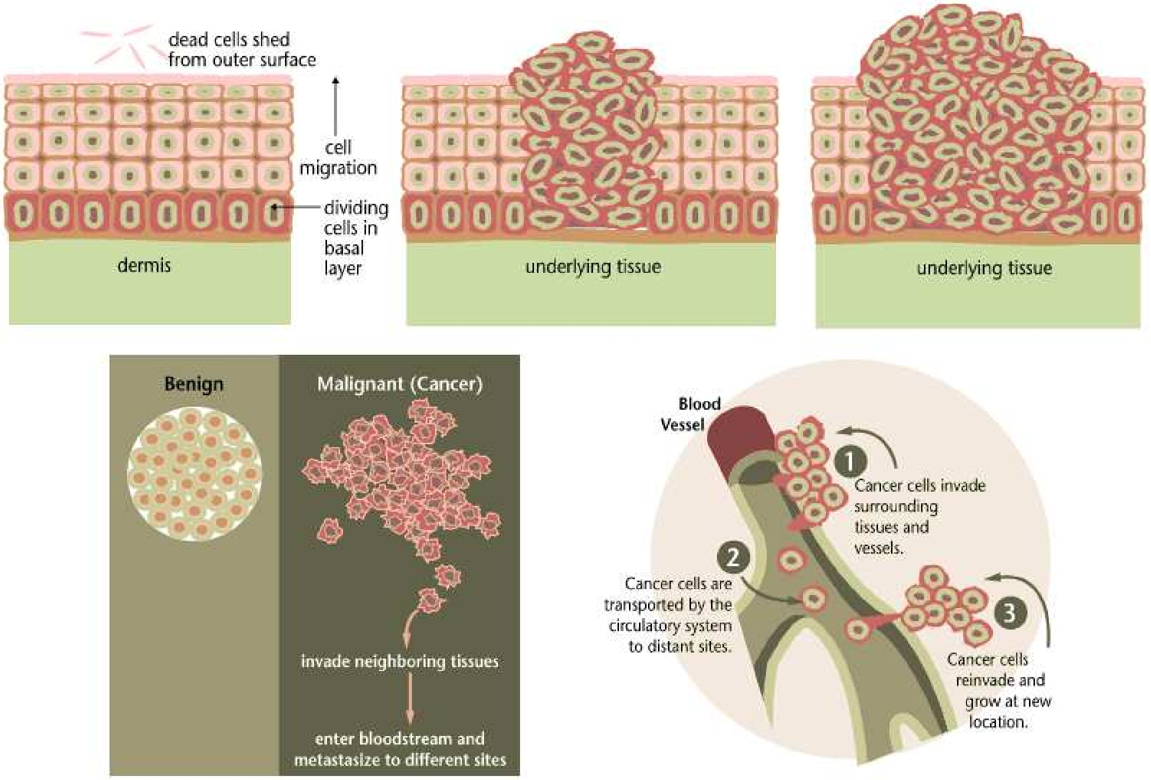

Figure B.2: Top Row. Left: normal growth of skin cells. Cells in the basal layer divide to replenish dead cells shed from outer surface. Center: beginning of cancerous growth. Basal cells divide faster than is needed and there is an increase in the total number of dividing cells. Right: tumor creation. A growing mass of tissue called *tumor* is created by the increase of dividing cells and normal organization of the tissue becomes disrupted.
Bottom row. Left: differences between malignant and benign tumors. Right: example of spreading of cancer by invasion and *metastasis*. Original images come from a National Cancer Institute tutorial (`http://pres2.nci.nih.gov/sciencebehind/cancer/cancer00.htm`).

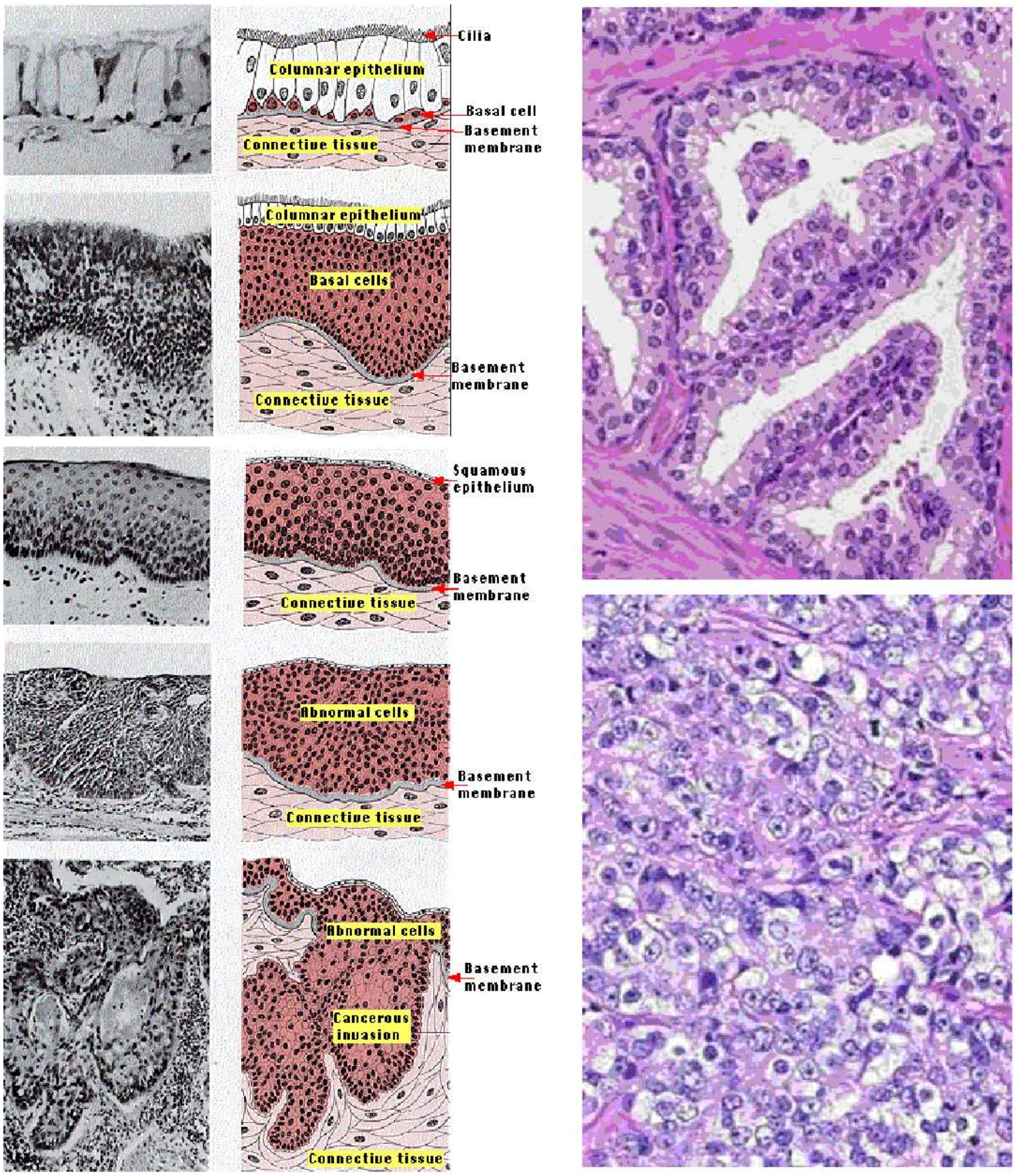

Figure B.3: Examples of lung cancer (two left columns) and prostate cancer (right column). Lung cancer: the top pair of images shows the normal ephitelium of the bronchi. The next pairs of images show successive stages of abnormal changes in the bronchial ephitelium, also showing the cellular organization at each stage. Images come from Kimball's biology pages (`http://users.rcn.com/jkimball.ma.ultranet/BiologyPages/L/LungCancer.html`).
Prostate cancer: the top image shows the organized structure of prostate cells while the bottom image shows the cancerous tissue which is completely disorganized due to the uncontrolled growth of malignant cells. Images come from University of Michigan Health system (`http://www.cancer.med.umich.edu/news/relprostate.htm`).

B.2 Types of cancer

There are over 200 different types of cancer, and each has a specific name, growth rate, treatment and chance of being cured. Anyway, we can distinguish three broad types of cancer:

- carcinomas: the most common types of cancer, they arise from the cells that cover external and internal body surfaces. Lung, breast, and colon are the most frequent cancers of this type;
- sarcomas: they are cancers arising from cells found in the supporting tissues of the body such as bone, cartilage, fat, connective tissue, and muscle;
- hematological cancers: leukemia, lymphoma and myeloma are classified in this category and they are all malignancies that arise from blood cells, from cells that go to make up blood or from the lymph nodes and tissues of the body immune system.

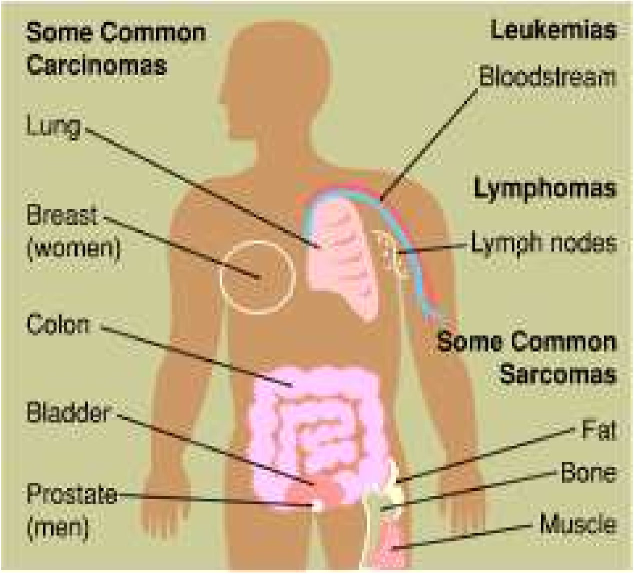

Figure B.4: Most common body organs involved in cancer.

B.3 Cancer causes

From the earliest times, physicians have wondered about the causes of cancer. Between the religious beliefs of the Egyptians (they blamed cancers on the Gods) and the recent genetic theories, there has been a slow process of evolution through the ages. Hipoccrates was the first to propose a theory about cancer, based on his humoral concept of the body. This theory of cancer was passed on by the Romans and was embraced by the influential doctor Galen's (129-200 A.C.) medical teaching, which remained the unchallenged standard through the Middle Ages for over 1300 years. During this period, the study of the body, including autopsies, was prohibited for religious reasons, thus limiting knowledge. Until the middle of the 20th century, several cancer theories were also proposed (lymph, blastema, chronic irritation, trauma, ...), but we only cite two anecdotes concerning the parasite theory to illustrate the misunderstanding level about this disease until recent times. The first one, placed in the 17th and 18th centuries, when some believed that cancer was contagious and one consequence of such thought was the displacement outside the city in 1779 of the first cancer hospital in France (people were afraid of the spread of cancer throughout the city). Another curiosity was the Nobel Prize wrongly awarded in 1926 for scientific research documenting stomach cancer being caused by a certain worm.

Nowadays, more correct causes of cancer have been discovered and documented, mostly due to advances in genetics. While cancer is a mistake at the genetic level of the cell, in up to 90% of cases this genetic mistake is not one that has been inherited; it is mostly the exposure to one or more *carcinogens* during our lifetime that causes cancer to occur. Carcinogens are the factors which cause the DNA inside a cells to become altered or mutated (causing the cell either growing without control or becoming immortal). There can be a delay of several decades between exposure to a carcinogen and the onset of cancer. For example, a group of young people exposed to carcinogens from smoking cigarettes generally do not develop cancer for 20 to 30 years. This period between exposure and onset of disease is the *lag time*. Carcinogens can be physical, chemical or biological mutagens:

- physical mutagens: physical mutation of DNA can be caused by ionizing radiation, ultraviolet radiation and by mineral fibers. These three mutagens act in very different ways. Ionizing radiation literally punches holes in the DNA, breaking the correct genetic sequence. Ionizing radiation can come directly from X-rays, cosmic rays (solar radiation) and indirectly from radon gas. Ultraviolet radiation (from sunlight) by contrast causes mutations by causing certain portions of DNA to remain bound together (even when they should not). This causes mutations by causing misreading of the DNA. Finally, certain natural mineral fibers like *asbestos*, because of their size, can cause damage directly to DNA resulting in carcinogenic mutations;

- chemical mutagens: in the case of chemical mutagens, mutation is caused by foreign molecules binding to a cell DNA, causing it to be misread. Examples or chemical mutagens are *benzopyrene* (found in cigarette smoke) and *vinyl chloride* (found in the plastics industry), *aflatoxin* (found in certain moulds) and *hetrocyclic amines* (found in over-cooked food);

- biological mutagens: biological mutagens may be viral or bacterial. Viral mutagens may use a number of different complex mechanisms to cause a cell to become cancerous (for instance, the insertion of the viral genetic information carried by the nucleic acids of the virus into the chromosomes of the infected cell, causing the cell to become malignant). Viruses that cause cancer include the *human papilloma* virus (implicated in cervical cancer) the *human T-cell lymphyocytic* virus (implicated in lymphoma) and the *hepatitis B* virus (implicated in liver cancer). Known bacterial mutagens are *helicobacter pylori*, implicated in stomach cancer.

The three main daily life causes of cancer are **smoking/alcohol**, **dietary imbalances** (excess of fat and calories; inadequate intake of fruits, vegetables, fiber, and calcium) and **chronic infections** leading to chronic inflammation.

Drinking excessive amounts of alcohol is linked to an increased risk for several kinds of cancer, especially those of the mouth, throat, and esophagus. The combination of alcohol and tobacco appears to be especially dangerous. For example, in heavy smokers or heavy drinkers, the risk of developing cancer of the esophagus is roughly 6 times greater than that for non-smokers/non-drinkers. But in people who both smoke and drink, the cancer risk is more than 40 times greater than that for non-smokers/non-drinkers.

Studies suggest that differences in diet may also play a role in determining cancer risk. But in contrast to the clear-cut identification of tobacco, sunlight, and alcohol, the exact identity of the dietary components that influence cancer risk has been difficult to determine. Recent evidence suggests that the proportion of cancers related to diet is less than 35%, although a definitive value is not yet available. Diet-related factors are now thought to account for about 30% of cancer in developed countries and perhaps 20% of cancers in developing countries. Limiting fat consumption and calorie intake appears to be one possible strategy to decrease risk of some cancers, because people who consume large amounts of meat (which is rich in fat) and large numbers of calories exhibit an increased cancer risk, especially for colon cancer. Epidemiological studies show that the incidence of most types of cancer is double among people who eat few fruits and vegetables as compared to those who eat about five portions per day.

Figure B.5 shows the linear relation between meat consumption and colon cancer rates in different countries.

Hepatitis B and *hepatitis C* viruses, *helicobacter pylori* infection, *schistosomiasis* and others are examples of chronic infections leading to chronic inflammations. This is a major cause of cancer in the world because it releases powerful oxidants which both stimulate cell division and are mutagens.

B.4 Cancer statistics

B.4.1 Measures to assess cancer importance

There are three measures that are commonly used to assess the impact of cancer in the general population: **incidence**, **mortality** and **prevalence** rates.

The **incidence** rate is the number of new cases of a given type of cancer diagnosed per year, usually expressed as the number of cancers per 100,000 population at risk:

$$\text{Incidence rate} \quad = \quad \frac{\text{New cancers}}{\text{Population}} \times 100,000. \qquad \text{(B.1)}$$

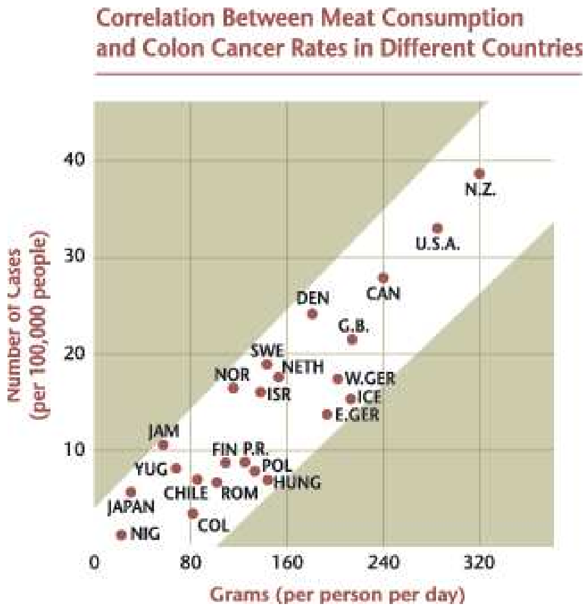

Figure B.5: Correlation between meat consumption and colon cancer rates in different countries. Data come from a National Cancer Institute tutorial (`http://pres2.nci.nih.gov/sciencebehind/cancer/cancer57.htm`)

Usually, incidence rates are age-adjusted to the standard population [2]. Unfortunately, such data can be obtained only from cancer registries or cancer surveys, both of which are relatively recent.

Cancer **mortality** data, on the other hand, have been available for many countries during most of the 20th century, and can be used to study both geographical patterns and temporal changes in the disease. Cancer deaths represent incidence indirectly, since they reflect the failure of treatment as well as the occurrence of the disease. For those forms of cancer for which available treatments are less effective, for example lung and stomach cancer, deaths reflect incidence quite accurately. Mortality is expressed as the number of deaths attributed to a particular type of cancer during the year:

$$\text{Mortality rate} \quad = \quad \frac{\text{Cancer deaths}}{\text{Population}} \times 100,000. \tag{B.2}$$

Included are deaths of patients whose cancer was diagnosed in earlier years, persons with a new diagnosis during the year, and patients for whom a diagnosis of cancer is made only after death. Usually, mortality rates are also age-adjusted to the standard population.

Prevalence is defined as the number or percent of people alive at a certain date in a population who previously had a diagnosis of the disease, including new (incidence) and pre-existing cases.

Other measures used to measure the importance of different types of cancer are:

---

[2] a standard population for a geographic area is a table giving the proportions of the population falling into the age groups 0, 1-4, 5-9, ..., 80-84, and 85+

the deaths to cases ratio, the age-standardized rate or the person-years of life lost (PYLL).

B.4.2 World cancer data

Worldwide, there are over 10 million new cases of cancer and more than 6 million deaths from cancer annually. Two decades ago, these figures were 6 million and 4 million [281]. In approximately 20 years time, the number of deaths annually due to cancer will increase from about 6 million to 10 million.

Of the 10 million new cancer cases each year, 4.7 million are in the more developed countries and nearly 5.5 million are in the less developed countries. Although the disease has often been regarded as a problem principally of the developed world, in fact, more than half of all cancers occur in the developing countries. The reason is that in developing countries, increased development is usually associated with many changes in diet and lifestyle. As a result, patterns of cancer tend to shift towards those of economically developed countries.

In developed countries, cancer generally accounts for about one-fifth of all deaths with mortality figures, second only to those for cardiovascular diseases (see Table B.1). In these countries, of all major conditions that result in death, cancer is one of the very few for which the proportion is rising significantly. In developing countries, cancer is now responsible for about one in 10 deaths (see Table B.1), but incidence of the disease is increasing. As living standards improve and life expectancy is extended, the incidence of communicable diseases declines and non-communicable diseases such as cancer assume greater importance.

Table B.1: Global and regional patterns of annual deaths, by cause, 2000 [299].

	Deaths from all causes (thousands)	Deaths from infectious & parasitic diseases(%)	Deaths from cancer(%)	Deaths from circulatory diseases(%)	Perinatal deaths(%)	Deaths from injury(%)	Deaths from other causes(%)
World total	55694	25.9	12.6	30.0	4.4	9.1	18.0
More developed countries	13594	6.0	21.6	47.9	0.7	7.9	15.9
Less developed countries	42100	32.3	9.8	24.2	5.6	9.5	18.7
Africa	10572	61.7	5.1	9.2	5.5	7.1	11.5
South and Central America	3097	14.6	14.0	28.5	4.3	12.3	26.2
North America	2778	6.3	23.8	41.0	0.6	6.4	21.9
Middle East	4036	32.0	6.1	26.9	7.5	8.4	19.0
South-East Asia	14157	29.9	8.0	28.9	7.1	9.7	16.4
Western Pacific	11390	10.6	18.6	31.2	2.8	10.7	26.0
Europe	9664	5.4	19.8	51.5	0.8	8.5	14.1

Table B.2: Incidence of most common cancers, 2000 [92].

	Males			Females		
	Rank	Cancer	New cases (thousands)	Rank	Cancer	New cases (thousands)
World	1	Lung	902	1	Breast	1050
	2	Stomach	558	2	Cervix	471
	3	Prostate	543	3	Colon/rectum	446
	4	Colon/rectum	499	4	Lung	337
	5	Liver	398	5	Stomach	318
More developed countries	1	Lung	471	1	Breast	579
	2	Prostate	416	2	Colon/rectum	292
	3	Colon/rectum	319	3	Lung	175
	4	Stomach	208	4	Stomach	125
	5	Bladder	164	5	Corpus uteri	114
Less developed countries	1	Lung	431	1	Breast	471
	2	Stomach	350	2	Cervix	379
	3	Liver	325	3	Stomach	193
	4	Oesophagus	224	4	Lung	162
	5	Colon/rectum	180	5	Colon/rectum	154

Among men, lung and stomach cancer are the most common cancers worldwide, while prostate cancer is largely seen in more developed countries (see Table B.2). For women, the most common cancers worldwide are breast and cervical cancer, although cervical cancer is primarily seen in less developed countries. Lung, colorectal and stomach cancer are among the five most common cancers for both men and women, in both more developed and less developed countries.

There are four principal reasons for the increase in cancer mortality: deaths from cardiovascular diseases are declining in developed countries; more people are surviving to old age, when cancer is more likely to occur (for instance, in Canada, 69% of new cancer cases and 80% of deaths due to cancer occur among those who are at least 60 years old); increasing tobacco use in recent decades has led to greater incidence of cancer of the lung and certain other sites; changes in diet, decreasing physical activity and increasing obesity have most likely contributed to an increase in various forms of cancer. Table B.3 shows the estimated percentages of cancer deaths attributable to various causes in people under the age of 65 years in the United States of America. These estimates probably apply to most industrialized countries.

Table B.3: Causes of cancer deaths in the USA, under age 65 years [83]

Cause of cancer (or contributory factor)	Best estimate	Range of acceptable estimates
Tobacco	30	25-40
Alcohol	3	2-4
Diet	35	10-70
Reproductive and sexual behavior	7	1-13
Occupation	4	2-8
Pollution	2	1-5
Industrial by-products	1	1-2
Medicines and medical procedures	1	0.5-3
Geophysical factors	3	2-4
Infection	10	1-?

A striking feature of cancer is its geographical and temporal variability. The population of a particular place at a specific time exhibits a certain pattern of cancer, with more cases of one type and fewer of another, as can be seen in Figure B.6. In another place, or at another time, the pattern of cancer in the population will be different (for instance, stomach cancer is especially frequent in Japan, colon cancer is prominent in the United States, and skin cancer is common in Australia).

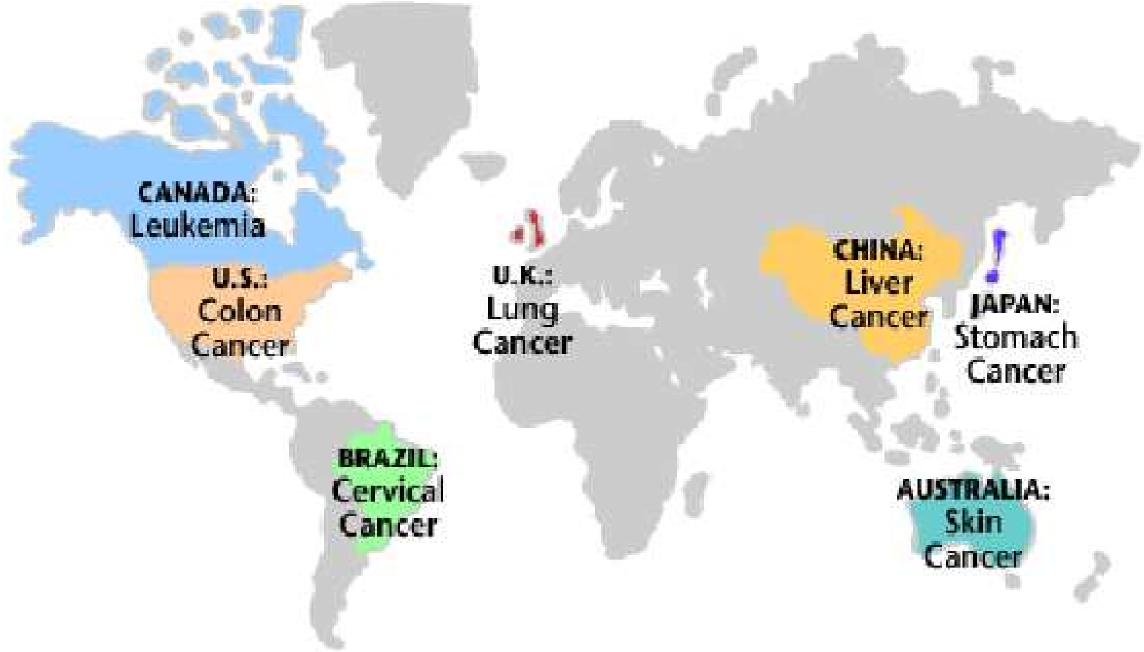

Figure B.6: Regions of highest incidence of cancer. Image comes from a National Cancer Institute tutorial (`http://pres2.nci.nih.gov/sciencebehind/cancer/cancer26.htm`).

In theory, differences in heredity or environmental risk factors might be responsible for the different cancer rates observed in different countries. Studies on people who have moved from one country to another suggest that exposure to risk factors for cancer vary by geographic location. For example, in Japan, the rate of colon cancer is lower and the rate of stomach cancer is higher than in the United States. But this difference has been found to gradually disappear in Japanese families that have moved to the United States. This suggests that the risk of developing cancer is not determined primarily by heredity. The change in risk for cancer for Japanese families could involve cultural or environmental factors predominant in one location and not in the other. This is illustrated by the following examples.

Carcinogens risks, though encountered almost universally, are not the same in all parts of the world. In developed countries, for example, the extensive use of X-rays for diagnostic and therapeutic purposes is generally well accepted, even though the radiation may contribute to the development of certain types of cancer, especially leukemia. In the same countries, food-handling methods -another lifestyle factor- minimize accumulation of the mould that produces aflatoxin, which is a liver carcinogen [129]. In many African countries, by contrast, there is little or no danger from medical X-radiation, but people continue to store food under conditions that favor the production of aflatoxin. Exposure to non-ionizing ultraviolet radiation in sunlight gives rise to the common forms of skin cancer in Caucasian populations [128]. Burning from solar radiation is associated with the rarer, but more fatal, melanoma. Individuals with light complexions are especially at risk.

B.5 Cancer diagnosis and treatments

B.5.1 Diagnosis

The diagnosis of cancer is not a straightforward task because the presence of symptoms and signs related to this disease (unexplained weight loss, fever, fatigue, pain, changes of the skin) does not necessarily mean that cancer is present and they are not always recognized as being significant by people, sometimes being dismissed if they have an obvious case or are only temporary. The diagnosis of cancer is made after a number of clinical tests have been performed. These tests can include visual physical inspection, medical image acquisitions and blood/urine (and other substances) tests. The tests involved will depend on which cancer is suspected.

After cancer has been diagnosed, doctors assign a *stage* to the cancer to determine how far the disease has progressed. This staging is based on the conclusions furnished by the tests about the size of the tumor, the invasion into surrounding tissues and if cancer has been metastasized to other regions of the body or to regional lymph nodes. The stage of disease has four levels. An invasive *neoplasm* confined entirely to the organ of origin is said to be *localized.* A neoplasm that has extended beyond the limits of the organ of origin, either directly into surrounding organs or tissues or into regional lymph nodes, is said to be *regional.* A neoplasm that has spread to parts of the body remote from the primary tumor, either by direct extension or by discontinuous metastasis, is said to be *distant.* When information is not sufficient to assign a stage, a neoplasm is said to be *unstaged.* For some cancers and diagnosis years, the extent of disease information can also be converted to Stages 0-IV as defined by the American Joint Committee on Cancer [13]. The patient's chances for survival are better when cancer is detected at a lower stage number (see Figure B.7), because it can be treated while it is small and is less likely to have spread to other parts of the body. In fact, cancers that can be detected by *screening* (regular screening examinations by a health care professional or self-examinations) account for about half of all new cancer cases. In the United States, the 5-year relative survival rate for these cancers is about 82%. If all these cancers were diagnosed at a localized stage through regular cancer screenings, 5-year survival would increase to about 95%.

B.5.2 Treatments

After the staging of the cancer, physicians must take a decision on the treatment planning of the disease that it would depend on the type of cancer found.

Treatments for cancer have also gone through a slow process of development through history. Even though medicine progressed and flourished in some ancient civilizations, there was little progress in cancer treatment. The approach to cancer was Hippocratic

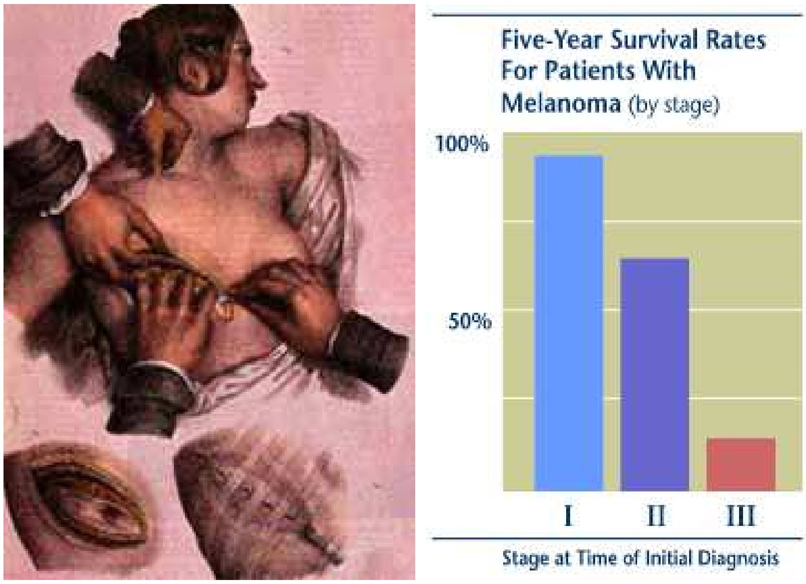

Figure B.7: Left: example of old primitive surgery in a breast cancer. Right: Relationship between the stage of the detected cancer and the survival rate.

(or Galenic) for the most part and their views set the pattern for cancer management for centuries. They considered the patient incurable after a diagnosis of cancer had been made, although Galen did write about surgical cures for breast cancer if the tumor could be completely removed at an early stage. Surgery then was very primitive with many complications, including blood loss. It was not until the 19th and early 20th centuries that major advances were made in general surgery and specifically in cancer surgery.

In 1896, W.C. Roentgen (1845-1923), presented the *X-ray*, *X* being the algebraic symbol for an unknown quantity. Within months, systems were being devised to use X-rays for diagnosis, and within 3 years radiation was used in the treatment of cancer. At the beginning of the 20th century, shortly after radiation began to be used for diagnosis and therapy, it was discovered that radiation could cause cancer as well as cure it. At the present time, advances in technology make it possible to focus radiation more precisely than in the past, helping to treat only the area involved by the cancer. Radiation is focused to avoid the normal tissues as much as possible, thus expecting to increase the effectiveness and reduce the side effects of radiation therapy. Studies are in progress to find out which radiation techniques are best suited for specific categories of patients (conformal proton beam radiation therapy, stereotactic radiation therapy, hyperthermia, boron neutron capture therapy, ...)

During World War II, the U.S Army was studying a number of agents related to *mustard gas* in order to develop more effective agents and to develop protective measures. In the course of that work, a compound called *nitrogen mustard* was studied and found to have substantial activity against a cancer of the lymph nodes called *lymphoma*. This agent served as the model for a long series of similar but more effective agents that killed rapidly proliferating cancer cells by damaging their DNA.

Since then, other researchers discovered drugs that blocked different functions involved in cell growth and replication. The era of *chemotherapy* had begun. Over the years, the development and use of chemotherapy drugs have resulted in the successful treatment of many people with cancer. Now several approaches are being studied to improve the activity and reduce the undesirable side effects of chemotherapy (new drugs and its combinations, new delivery techniques, novel approaches to targeting drugs more specifically at the cancer cells to produce fewer side effects, ...).

By the middle of the 20th century, scientists had in their hands the instruments needed to begin solving the complex problems of chemistry and biology presented by cancer. DNA was found to be the basis of the genetic code that gives orders to all cells. After learning how to translate this code, scientists were able to understand how genes worked and how they could be damaged by mutations becoming possible to localize the exact site of the damage to a specific gene. Medical scientists are progressively identifying the genes that are damaged by chemicals or radiation and the genes that, when inherited, can lead to cancer. This scientists' understanding of the biology of cancer cells has led to the development of biologic agents that mimic some of the natural signals that the body uses to regulate growth. This cancer treatment is called *biologic therapy*. Some of these biologic agents are given to patients to imitate or influence the natural immune response either by directly altering the cancer cell growth or acting indirectly to help healthy cells control the cancer.

Cancer is not an irreversible death sentence that does not describe a single disease but rather more than 100 types of disease, some of which are fully curable. The treatments of even the more lethal types continually improve, and that every day scientists understand a little more about cancer cause, growth, and spread. These advances have allowed lots of people to gain the battle against cancer and to continue their life in an almost normal fashion. Anyway, the adoption of a healthy lifestyle, including a healthy diet, physical exercise, appropriate body weight, and avoidance of risk-associated behaviors can lead to a long active life.

APPENDIX C

Details of segmentation methods

In this Appendix, further details about different parts of the segmentation methods used in this work are presented. In Section C.1, the theory of 2D active contours, their numerical implementation and their conversion to 3D are described in order to complement Section 4.2.3. The next part of the Appendix details the numerical implementation of the Gradient Vector Flow (Section C.2).

C.1 Deformable models

C.1.1 2D active contours theory

In the initial formulation [139], the evolution of a *snake* (or active contour) is expressed as an energy minimization problem. The optimal contour position, corresponding to a correct segmentation, is the one which minimizes the energy. The energy is decomposed into an internal energy, which is minimum for a regular contour (energy related to the physical behavior of the contour), and an external energy, which is minimum at the searched contour points (energy related to the reliability to the data to model). If the parametric deformable contour is noted as $\mathbf{X}(s) = (X(s), Y(s)), s \in [0, 1]$, the evolution equation can be formulated as follows:

$$E(\mathbf{X}) = E_{int}(\mathbf{X}) + E_{ext}(\mathbf{X}) \tag{C.1}$$

The internal energy is expressed as a combination of the first and second order derivatives:

$$E_{int}(\mathbf{X}) = \frac{1}{2}\int_0^1 \alpha(s)\left|\frac{\partial \mathbf{X}}{\partial s}\right|^2 + \beta(s)\left|\frac{\partial^2 \mathbf{X}}{\partial s^2}\right|^2 ds \tag{C.2}$$

where $\alpha(s)$ and $\beta(s)$ are the elasticity and rigidity parameters, respectively, and they are usually constant. Such parameters adjust the model evolution in such a way that a high value of α tends to shorten the snake and to eliminate loops. On the other hand, a high value of β penalizes the high curvature regions, thus smoothing the contour.

The external energy is computed by means of an integration on the contour of a potential function which must be minimum at the contour points:

$$E_{ext}(\mathbf{X}) = \int_0^1 P(\mathbf{X}) ds \tag{C.3}$$

where P is frequently obtained from the image gradient.

It can be shown that this problem consists in computing the contour that minimizes the energy function and it is equivalent to find the solution of the Euler-Lagrange equation [139]:

$$\mathbf{F}_{int}(\mathbf{X}) + \mathbf{F}_{ext}(\mathbf{X}) = \mathbf{0} \tag{C.4}$$

with

$$\mathbf{F}_{int}(\mathbf{X}) = \frac{\partial}{\partial s}\left(\alpha(s)\frac{\partial \mathbf{X}}{\partial s}\right) - \frac{\partial^2}{\partial s^2}\left(\beta(s)\frac{\partial^2 \mathbf{X}}{\partial s^2}\right) \tag{C.5}$$

and

$$\mathbf{F}_{ext}(\mathbf{X}) = -\nabla P(\mathbf{X}) \tag{C.6}$$

In order to solve this optimization problem, the time t is added as a variable of the function $X(s,t)$ to make the equation dynamic. Therefore, the solution is the equilibrium state of:

$$\gamma\frac{\partial \mathbf{X}}{\partial t} = \mathbf{F}_{int}(\mathbf{X}) + \mathbf{F}_{ext}(\mathbf{X}) \tag{C.7}$$

As the solution of this equation is stabilizing, the derivative with respect to the time disappears, obtaining the desired solution of C.4.

An alternative to the energy formulation is to directly model the problem by means of a dynamic force equation. The internal forces are the same, but on the other hand, the external forces are not necessarily derived from a potential, thus being a more general formulation than the energy one.

Finally, some initial and limit conditions are added to the problem:

$$\begin{cases} \mathbf{X}(s,t=0) = \mathbf{X}_0(s) & \text{initial condition} \\ \mathbf{X}(0,t) = \mathbf{X}(1,t) & \text{first limit condition} \\ \frac{\partial \mathbf{X}}{\partial s}(0,t) = \frac{\partial \mathbf{X}}{\partial s}(1,t) & \text{second limit condition} \end{cases} \tag{C.8}$$

C.1.2 Numerical implementation of 2D active contours

The solution of the equation that controls the evolution of the deformable model can be obtained by means of several methods such as finite elements. In the presented work, the finite elements in time method has been employed due to its quickness and simplicity.

Therefore, the procedure starts from a contour defined by a vector X of n samples, with n being constant. This vector contains the sample coordinates in the simplest case, even if it could also contain the discretization of other physical characteristics associated to the model such as elasticity, rigidity, ... Here, they are considered as being constant. Then, for a given spatial sample step h, $X = (x_i)$ is expressed with $x_i = (x(ih), y(ih))$.

In this moment, the following hypothesis is assumed: the total energy of the model is the sum of the energies associated to each one of its samples; and they can be decomposed in an external energy term (related to the image) and an internal energy one (related to the stress and twisting suffered by each contour point). It can be expressed as follows:

$$E_{total} = \sum_{i=1}^{n} E_{int}(i) + E_{ext}(i). \tag{C.9}$$

The external energy can be obtained from a pre-computed image of energies. It must be pointed out that the position of each contour element is not discretized and can take any value, thus the corresponding energy must be computed by means of an interpolation of the nearest discrete position values. This interpolation is very critical because it will assure a smooth convergence of the contour towards the solution, avoiding an oscillation between two discrete values of the energy.

In a similar way, a simple expression of the model internal energy can be obtained from the sample values:

$$E_{int}(i) = \alpha\frac{|x_i - x_{i-1}|^2}{2h^2} + \beta\frac{|x_{i-1} - 2x_i + x_{i+1}|^2}{2h^4}. \tag{C.10}$$

Consequently, the solution of the Euler-Lagrange equation C.4 is equivalent to solve the matrix equation $AX + F_{ext}(X) = 0$, where A is the $n \times n$ penta-diagonal matrix:

$$\begin{vmatrix} 2\alpha+6\beta & -\alpha-4\beta & \beta & 0 & 0 & \cdots \\ -\alpha-4\beta & 2\alpha+6\beta & -\alpha-4\beta & \beta & 0 & \\ \beta & -\alpha-4\beta & 2\alpha+6\beta & -\alpha-4\beta & \beta & \\ 0 & \beta & -\alpha-4\beta & 2\alpha+6\beta & -\alpha-4\beta & \\ 0 & 0 & \beta & -\alpha-4\beta & 2\alpha+6\beta & \\ \vdots & & & & & \ddots \end{vmatrix} \tag{C.11}$$

If a temporal (τ time steps) discretization of the model evolution is added to the spatial discretization, the temporal derivative can be approximated in Equation C.7 by means of a difference between successive steps:

$$\frac{X^t - X^{t-1}}{\tau} + AX^t = F_{ext}(X^{t-1}), \tag{C.12}$$

the evolution of the deformable contour being controlled, from its initial state X^0, by the following equation:

$$X^t = (Id + \tau A)^{-1}\left(\tau F_{ext}(X^{t-1}) + X^{t-1}\right). \tag{C.13}$$

The advantage of this expression is that the inversion of the matrix $(Id+\tau A)$ must only be computed once, since it does not include any dynamic term. On the other hand, the choice of the temporal step τ asks for a trade-off that guarantees the model convergence without excessively decreasing its evolution speed.

C.1.3 Extension from 2D to 3D: deformable surfaces.

The extension from a 2D contour to a 3D deformable surface can be achieved as follows [55]:

$$\begin{array}{rlll}\mathbf{S}: & [0,1]^2 & \rightarrow & \mathbb{R}^3 \\ & (r,s) & \rightarrow & \mathbf{S}(r,s) = (X(r,s), Y(r,s), Z(r,s))\end{array} \tag{C.14}$$

Therefore, the energy equation has the same shape than the one used to define the deformable contours (equation C.1):

$$E(\mathbf{S}) = E_{int}(\mathbf{S}) + E_{ext}(\mathbf{S}) \tag{C.15}$$

The 2-order Tikhonov stabilizator is usually chosen as the internal energy:

$$E_{int}(\mathbf{S}) = \frac{1}{2}\int_{[0,1]^2} \alpha \left(\left| \frac{\partial \mathbf{S}}{\partial r} \right|^2 + \left| \frac{\partial \mathbf{S}}{\partial s} \right|^2 \right) + \beta \left(\left| \frac{\partial^2 \mathbf{S}}{\partial r \partial s} \right|^2 + \left| \frac{\partial^2 \mathbf{S}}{\partial r^2} \right|^2 + \left| \frac{\partial^2 \mathbf{S}}{\partial s^2} \right|^2 \right) drds \tag{C.16}$$

In a similar way, the external energy is expressed as follows:

$$E_{ext}(\mathbf{S}) = \int_{[0,1]^2} P(\mathbf{S}) drds \tag{C.17}$$

It can be shown that a surface that minimizes this energy defines an equilibrium state of:

$$\gamma \frac{\partial \mathbf{S}}{\partial t} = \mathbf{F}_{int}(\mathbf{S}) + \mathbf{F}_{ext}(\mathbf{S}) \tag{C.18}$$

with:

$$\mathbf{F}_{int}(\mathbf{S}) = \alpha \nabla^2 \mathbf{S} - \beta \nabla^2 (\nabla^2 \mathbf{S}) \tag{C.19}$$

where ∇^2 is the Laplacian operator, and:

$$\mathbf{F}_{ext}(\mathbf{S}) = -\nabla P(\mathbf{S}) \tag{C.20}$$

The problem of the limit conditions is more complex than in the case of deformable contours because different choices can be performed. Such choices define the surface topology (spherical, cylindric or toroidal). Finally, these equations must be discretized and one common choice to achieve it is by means of finite difference methods.

C.2 Numerical implementation of the Gradient Vector Flow

The vectorial diffusion equation 4.5, that specifies the GVF, given the weighting functions, can be implemented by means of a finite difference framework. In the case of the chosen weighting functions, the equation to solve is the following:

$$\begin{aligned} u_t(x,y,t) &= \mu \nabla^2 u(x,y,t) - [u(x,y,t) - f_x(x,y)]\cdot \\ &\quad [f_x(x,y)^2 + f_y(x,y)^2] \end{aligned} \tag{C.21}$$

$$\begin{aligned} v_t(x,y,t) &= \mu \nabla^2 v(x,y,t) - [v(x,y,t) - f_y(x,y)]\cdot \\ &\quad [f_x(x,y)^2 + f_y(x,y)^2] \end{aligned} \tag{C.22}$$

The solution in stationary stage of these parabolic linear equations is the solution of the Euler equations 4.5. Since these equations are not coupled, they can be separately solved as scalar differential equations with partial derivatives in u and v.

The equations C.21 and C.22 are known as the *generalized diffusion equations* and have been widely used in different fields such as the heat conduction or fluid theory. The equations can be expressed in an easier fashion:

$$u_t(x,y,t) = \mu \nabla^2 u(x,y,t) - b(x,y)u(x,y,t) + c^1(x,y) \tag{C.23}$$

$$v_t(x,y,t) = \mu \nabla^2 v(x,y,t) - b(x,y)v(x,y,t) + c^2(x,y) \tag{C.24}$$

where

$$b(x,y) = f_x(x,y)^2 + f_y(x,y)^2 \tag{C.25}$$

$$c^1(x,y) = b(x,y)f_x(x,y) \tag{C.26}$$

$$c^2(x,y) = b(x,y)f_y(x,y) \tag{C.27}$$

In order to obtain f_x and f_y, any classical gradient computation method can be used. Afterwards, the $b(x,y)$, $c^1(x,y)$ and $c^2(x,y)$ coefficients can be computed and they remain fixed during the iterative procedure.

The indices i, j and n correspond to x, y and t, Δx and Δy being the distance between pixels, and Δt being the time step between iterations, the partial derivatives shall solve the iterative solution as follows:

$$u_t = \frac{1}{\Delta t}(u_{i,j}^{n+1} - u_{i,j}^{n}) \tag{C.28}$$

$$v_t = \frac{1}{\Delta t}(v_{i,j}^{n+1} - v_{i,j}^{n}) \tag{C.29}$$

$$\nabla^2 u = \frac{1}{\Delta x \Delta y}(u_{i+1,j} + u_{i,j+1} + u_{i-1,j} + u_{i,j-1} - 4u_{i,j}) \tag{C.30}$$

$$\nabla^2 v = \frac{1}{\Delta x \Delta y}(v_{i+1,j} + v_{i,j+1} + v_{i-1,j} + v_{i,j-1} - 4v_{i,j}). \tag{C.31}$$

By replacing these approximations in C.23 and C.24, the iterative solution of the GVF is:

$$\begin{aligned} u_{i,j}^{n+1} &= (1 - b_{i,j}\Delta t)u_{i,j}^{n} + \\ &+ r(u_{i+1,j}^{n} + u_{i,j+1}^{n} + u_{i-1,j}^{n} + u_{i,j-1}^{n} - 4u_{i,j}^{n}) + \\ &+ c_{i,j}^{1}\Delta t \end{aligned} \tag{C.32}$$

$$\begin{aligned} v_{i,j}^{n+1} &= (1 - b_{i,j}\Delta t)v_{i,j}^{n} + \\ &+ r(v_{i+1,j}^{n} + v_{i,j+1}^{n} + v_{i-1,j}^{n} + v_{i,j-1}^{n} - 4v_{i,j}^{n}) + \\ &+ c_{i,j}^{2}\Delta t \end{aligned} \tag{C.33}$$

where

$$r = \frac{\mu \Delta t}{\Delta x \Delta y}. \tag{C.34}$$

The convergence of the described iterative procedure is guaranteed by a classic result from the numerical method theory. Assuming b, c^1 and c^2 bounded, Equations C.32 and C.33 are stables if the Courant-Fiedrichs-Lewy constraint on the step size ($r \leq 1/4$) is accomplished. As Δx, Δy and μ are usually fixed, from the definition of r in C.34 it can be obtained that, in order to guarantee the GVF convergence, the time step must satisfy the following constraint:

$$\Delta t \leq \frac{\Delta x \Delta y}{4\mu}. \tag{C.35}$$

APPENDIX D

Semi-interactive segmentation of tumors

D.1 Introduction

The registration methodology we have introduced has as limitation that the regions placed inside or near the main structures will be deformed according to the registration computed for the latter. A critical example of this situation occurs when a tumor is located inside the lungs and there is a large volume difference between CT and PET images (due to the respiration motion). In this case, the tumor is registered according to the transformation computed for the lungs, becoming banana-shaped, as shown in Figure D.1. The aim of this stage is to show how this undesired effect can be avoided since it is fundamental to assure that the information about geometry and location of the tumors is not lost in the registration process.

D.2 Introducing tumors in the registration process

The algorithm we propose consists in adding the semi-interactive segmentation of the tumors in the registration process. The interaction consists for the physician in defining a landmark in the tumor of interest (in both CT and PET images). This semi-interactive approach has been chosen due to the complexity of a fully automatic tumor segmentation method, mainly in CT images. In addition, this very reduced interaction is well accepted by the users, and even required.

Next, both selected points are used as the input to a relaxation region growing algorithm [57] to segment the tumors. Lung segmentation in CT and PET images is achieved using the procedure introduced in Chapter 4 and refined by the results of tumor segmentation.

Then, a first registration phase based on the CT and PET tumor centers is applied, providing a rigid transformation that assures that the tumors are linearly registered.

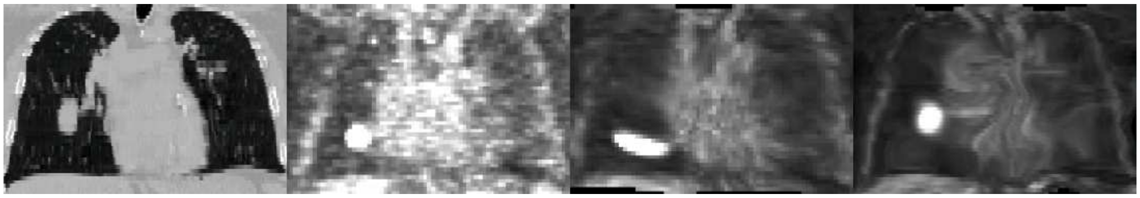

Figure D.1: Improvement of the registration in the tumor area. From left to right: CT and PET original images; PET image registered without tumor constraints; PET image registered with tumor constraints.

The next step concerns the non-linear registration phase of the images. The proposed non-linear registration method using Free Form Deformations (FFD) was developed in order to account for movement of the lungs during the respiration cycle (and of other organs in the considered regions). However, it does not include any constraints derived from tumors.

To avoid the incorrect tumor transformation produced by these techniques (see Figure D.1), we propose to combine two FFD grids: one obtained from a non-linear registration between tumor surfaces, and the other one computed between CT and PET lungs. This combination is achieved by means of a trade-off between lung and tumor grids that depends on the distance from a given control point to the tumor boundaries and it constitutes an efficient and original feature of the proposed approach.

Finally, a FFD registration, optimizing a mutual information criterion, is applied between the whole intensity images. It is initialized with the grid computed between the structures. The objective of this stage is to provide a deformation for the points far away from the segmented features and to correct possible errors induced by the segmentation phase.

D.3 Results and conclusions

The proposed method improves the accuracy of registration of CT and PET images with pathologies. The fact of adding a semi-interactive stage is not a disadvantage because physicians prefer to control this crucial step. Moreover, with a simple gesture, the algorithm benefits from medical and expert knowledge and the results are notably improved, as shown in Figure D.1.

The proposed algorithm has been tested on 5 pairs of CT and PET images with good results for all cases.

APPENDIX E

Description of brain internal structures by means of spatial relations for MR image segmentation

This chapter presents a method for segmenting internal brain structures in MR images. It introduces prior information in an original way through descriptions of the spatial arrangement of structures by means of spatial relations, which are represented in the fuzzy set framework. The method is hierarchical as the segmentation of a given structure is based on the previously segmented ones. The processing of each structure is decomposed into two stages: an initialization stage which makes extensive use of prior knowledge and a refinement stage using a 3D deformable model. The deformable model is guided by an external force representing the combination of a classical data term derived from an edge map and a force corresponding to a given spatial relation. We propose different ways to compute a force from a fuzzy set representing a relation or a combination of relations. Results obtained for the lateral ventricles, the third ventricle, the caudate nuclei and the thalami are promising. The proposed combination of spatial relations and deformable models has proved to be very useful to segment parts of the structures were no visible edges are present, improving the segmentation accuracy.

E.1 Introduction

The segmentation of brain internal structures such as the ventricles and the deep grey nuclei (caudate nucleus, putamen, globus pallidus, thalamus) has many medical applications such as morphometric studies, 3D visualization, surgical planning, anatomical support to functional studies ... However, their automatic segmentation in MR images remains a challenging task due to the image low-contrast and in some cases the lack of strong edges between some structures.

Several approaches dedicated to internal brain structures segmentation have been recently published. Most approaches rely either on a digital atlas which is registered with the image to be recognized [22 ; 72 ; 310] or/and on deformable templates [219 ;

141 ; 260 ; 214] usually based on a statistical shape training. The main drawbacks of these approaches are the difficulty to deal with the anatomical variability among subjects and their computational cost.

Our approach uses descriptions of brain structures by means of spatial relations to constrain the segmentation procedure and a 3D deformable model to refine and to regularize the result. Spatial relations are less variable than the structures themselves which justifies to rely on them to constrain the search. Pitiot et al. [214] proposed an expert-knowledge guided segmentation system, combining distance relations with a deformable model for brain structures segmentation and showed improved segmentation results compared to the use of a deformable template. They combined both explicit (distance constraints) and implicit knowledge (shape constraints). In our case, we employ only explicit knowledge expressed through different kinds of spatial relations, including distances but also adjacency and directional relations. The relations are represented in a fuzzy set framework and are employed at three different stages of the process: to produce regions of interest (ROI) that will restrain the segmentation, to select regions that fulfill a description and to constrain the deformable model. The idea of using spatial relations in brain structures segmentation was first introduced by Géraud [99 ; 22]. Nevertheless, in this system, ROI were built using a digital atlas, which may lead to some problems due to anatomical variability among subjects. Moreover, this approach did not include a regularization phase which may compromise the segmentation of low-contrast structures. Another drawback of this strategy is the computational cost of the registration.

We propose a hierarchical procedure in which the segmentation of a given object makes use of information derived from previously obtained structures. After some preprocessing steps, the procedure is initialized by the segmentation of the lateral ventricles, which are the easiest brain internal structures to segment. Each structure is then segmented in two stages. The first step consists in a rough segmentation that will serve as initialization of the deformable model. First we compute a fuzzy region of interest (ROI) from spatial relationships guaranteeing that the object is included in it. After an automatic thresholding, we extract different regions of the expected radiometric class. Regions satisfying the description of the object to segment are then automatically selected and merged to produce an initial segmentation. In a second step, this initial result is refined and regularized using a deformable model.

The chapter is organized as follows. In Section E.2, we show how the arrangement of brain structures is described by means of spatial relations, how these relations are represented and used in the segmentation process. Then, in Section E.3, we present the deformable model and the methods to compute an external force from the spatial relations. Finally some results are presented in Section E.4.

E.2 Spatial Relations

Spatial relations are used extensively in linguistic descriptions found in neuroanatomy textbooks. These descriptions correspond to structural relations between brain structures and are likely to be quite stable among subjects. They are naturally used by the neuroanatomist when studying an image. In this part, we first show how brain structures can be described using spatial relations and how this description can be formalized. We then introduce methods to represent spatial relations, based on the fuzzy set framework. Finally, we explain how those relations are used in the segmentation procedure.

E.2.1 Description of brain structures using spatial relations

In collaboration with a neuroanatomist (D. Hasboun, CHU La Pitié-Salpêtrière), we proposed a description of brain structures using spatial relations. It consists of a hierarchy of objects sharing relationships. Different levels of the hierarchy are linked by inclusion relations (e.g. the putamen is part of the basis nuclei which are part of the telencephalon), while objects of the same level are linked by spatial relationships. We use an anatomical hierarchy derived from the one proposed in Neuronames [1] [32]. The relationships are a computational formalization of linguistic descriptions given by the neuroanatomist. They include four types of relations: direction, adjacency, distances and symmetry. The 6 directional relations correspond to the 3 dimensions of the space: "above, below, in front of, behind, lateral, medial". The relations "lateral" and "medial", which are commonly used in anatomical descriptions, replace relations "left" and "right". This vocabulary is useful because the brain is approximately symmetrical with respect to the mid-sagittal plane, and by using these expressions, both hemispheres can be described in the same way. "Lateral" means "orthogonally and away from the mid-sagittal plane" while "medial" means "orthogonally and towards the mid-sagittal plane". Adjacency relations describe structures that are touching each other. Symmetry relations link homologous structures in both hemispheres. Finally, even though distance relations such as "close to", "far from" are not present in the original anatomical description, they have proved useful for the segmentation and have thus been added to the description. Here are some examples of anatomical descriptions using spatial relations:

- direction: the thalamus is lateral to the third ventricle and below the lateral ventricle;
- distance: the lateral ventricles are far from the brain surface;
- adjacency: the thalamus is adjacent to the third ventricle;
- symmetry: homologous structures of both hemispheres (e.g. left and right thalami) are approximately symmetrical with respect to the mid-sagittal plane.

The anatomical description is formalized using a structure called a *synthetic hierarchical graph* (SHG). It is an attributed hierarchical graph, i.e. a set of graphs called *levels* such that the nodes of two consecutive levels are linked by inclusion relations. Each level has the structure of an attributed graph: the nodes correspond to brain structures and the edges to spatial relations between them. The SHG corresponding

---

[1] http://rprcsgi.rprc.washington.edu/neuronames/

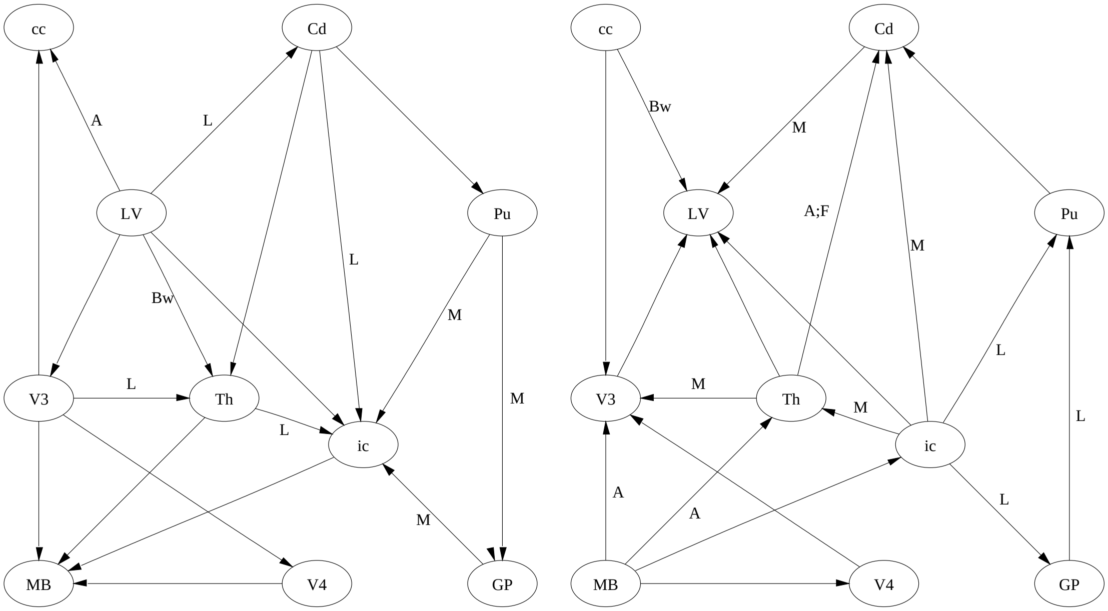

Figure E.1: A fraction of the third level of the *synthetic hierarchical graph* describing brain structures. The following abbreviations are used for brain structures: cc - corpus callosum, LV - lateral ventricle, V3 - third ventricle, V4 - fourth ventricle, MB - mesencephalon, Cd - caudate nucleus, Pu - putamen, GP - globus pallidus, Th - thalamus, ic - internal capsule. Spatial relations are denoted as follows: I - medial, E - lateral, H - above, B - below, Av - in front of, Ar - behind. An edge between two structures indicates an adjacency relation. If the edge is attributed, there is an additional directional relation. The target object is at the end of the arrow: e.g. the relation $LV \xrightarrow{H} cc$ means that "the corpus callosum is above the lateral ventricle". To avoid conflicting edges and to enhance visualization, the graph is shown on two different figures, each one representing a fraction of the edges.

to brain structures contains 4 levels. A fraction of the third level, which contains the structures we want to segment (ventricles and grey nuclei), is shown as an example in Figure E.1. Higher levels correspond to superstructures such as the telencephalon or the diencephalon. The lower level (level 4) corresponds to the subdivisions of structures such as, for example, the different horns of the lateral ventricle. The graph presented here has been used to represent brain anatomy but can be potentially used to describe any structured scene.

E.2.2 Representation of spatial relations

To handle imprecision, spatial relationships are represented in a fuzzy set framework and can refer to fuzzy objects as well as to crisp ones. This imprecision may come from either the processing of images or from the nature of the relations under consideration (e.g. directional relationships are intrinsically imprecise). Two kinds of fuzzy approaches can be used to represent spatial relations: one can define either a fuzzy set representing the degree of satisfaction of the relation with respect to a reference object in each point of the 3D space or a value representing the satisfaction of the relation between two given objects. The first approach presents several advantages: it allows the comparison of any target object with the reference one at a low computational cost, just by comparing the target and the fuzzy set, fusion operators can be used to combine spatial relations, the fuzzy set can also be considered as a ROI in which the target object should be found. The second approach consists in a direct comparison between objects and it can only be applied to the selection of regions.

Directions and distances have been represented using the first approach as in Bloch et al [22]. Directional relationships are represented by computing a fuzzy dilation of the reference object by a structuring element representing the direction under consideration. For distances, fuzzy sets representing linguistic descriptions such as A *is near* B or A *is at about 10 mm from* B are constructed on the set of distances $\mathbb{R}^+$. By combining them with distance maps, fuzzy sets in the 3D space are built. Examples of such fuzzy sets can be found in Figure E.3. Adjacency and symmetry relations are represented using the second approach. An adjacency degree is defined using the method proposed by Bloch et al [23]. In the case of non-overlapping binary objects, this degree is computed as a function of the distance between objects. The symmetry measure [63] is defined as a measure of comparison between a given object and its symmetrical image with respect to a given plane, which, in our case, is the brain symmetry plane. This plane, which is a good approximation of the mid-sagittal plane, is found by maximizing a symmetry measure [285]. However, in our current implementation, symmetry relations are not used in the segmentation because brain hemispheres are treated separately. Only the brain symmetry plane is used, in order to separate the hemispheres. Nevertheless, as these relations can be integrated in the approach straightforwardly, we choose to present them in the chapter.

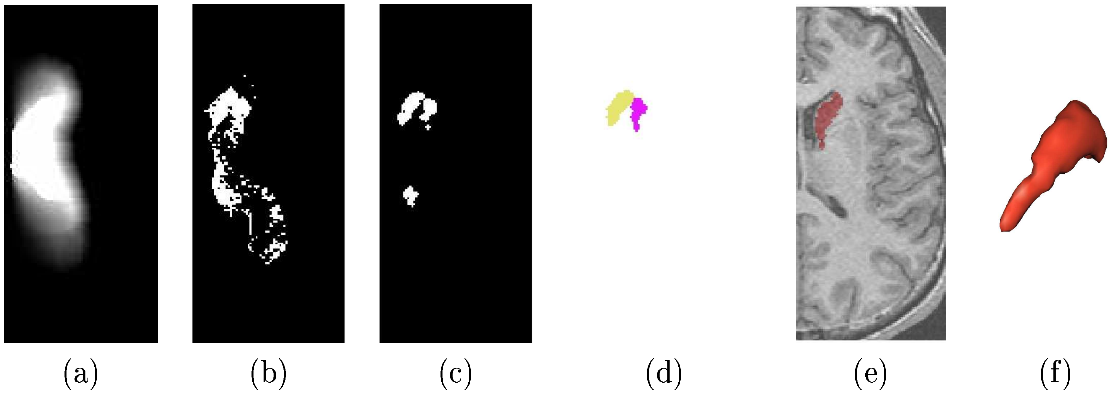
(a) (b) (c) (d) (e) (f)

Figure E.2: Rough segmentation of the caudate nucleus (axial slices): (a) region of interest (ROI) corresponding to a conjunctive fusion with t-norm “product” of spatial relations: “lateral to the lateral ventricle” and “near the lateral ventricle”; (b) automatic thresholding in the ROI; (c) morphological opening of the previous result; (d) separation of the caudate and a fraction of the putamen; (e) rough segmentation; (f) simplex mesh corresponding to this rough segmentation.

E.2.3 Spatial relations application

Spatial relations are used in three different ways during the segmentation process: to define regions of interest (ROI), to select objects corresponding to a given description and to control the evolution of the deformable model. Let us first recall that each structure is segmented in two steps: a rough segmentation and a final segmentation. The first two applications of spatial relations occur only in the first step and are presented here while the third one, employed in the final segmentation, will be presented with the deformable model.

The first application of spatial relations concerns the construction of regions of interest to restrict the search of the structure to be segmented. When several spatial relations appear in the description of a structure, these relations are combined by means of fusion operators between fuzzy sets [20]. This is done using either a *t-norm* such as "minimum" or "product" in case of a conjunctive fusion. For a disjunctive fusion, a *t-conorm* will be adopted. This fusion operation provides a new fuzzy set which is used as a ROI to restrict the search of a given structure.

The second application is related to the selection of regions which have been labelled in the ROI. These regions are either connected components extracted after automatic thresholding or obtained from a watershed segmentation on the distance map to the contour of the class (the h-minima algorithm is used to remove irrelevant minima [82]) in case where different touching objects cannot be disconnected. When the selection involves distances and directions, we compute the degree to which a region satisfies the relation represented by a fuzzy set, using a measure of satisfiability [31]. When the selection involves adjacencies and symmetries, a measure is directly available.

In order to clarify these two applications, we present an example corresponding to the rough segmentation of the caudate nucleus. First, using the "product" t-norm, we compute a ROI which corresponds to the following conjunctive fusion: "lateral to the lateral ventricle" and "near the lateral ventricle" (Figure E.2(a)). An automatic thresholding is then performed in the ROI (Figure E.2(b)). The threshold value is found by using an estimation of the radiometric characteristics of the grey nuclei due to Poupon [218], which estimates the radiometry of the grey and white matter by the method of Mangin et al [185]. These values are not critical as the segmentation will be refined with the deformable model. After morphological opening (Figure E.2(c)), the largest connected component, which corresponds to the caudate nucleus and a part of the putamen, is selected. Afterwards, the possible holes are filled by means of a morphological closing. A watershed segmentation on the distance map to the contour allows to separate the caudate nucleus from the putamen (Figure E.2(d)). We then select the regions corresponding to the description of the caudate nucleus: these are the regions adjacent to the lateral ventricle and satisfying the previously fused relation. We obtain an initial segmentation (Figures E.2(e) and (f)).

E.3 Refinement using a 3D deformable model

For most structures, the result obtained from the previous stage cannot be considered as a final result (see for example Figures E.2(e) and (f)). In particular, the lack of regularization term may lead to imperfect boundaries. These problems are overcome using a deformable model.

E.3.1 Simplex mesh deformable model

All the structures in which we are interested have the topology of a sphere (except the third ventricle). To achieve a correct segmentation, we need to maintain their topology through the deformation process. This is performed with a discrete model based on simplex meshes. Simplex meshes, introduced by Delingette [75], are topologically dual to triangulations and have a constant vertex connectivity. The segmentation obtained at the first stage is transformed to a triangulation using an isosurface algorithm based on tetrahedra [213]. It is decimated and converted to a simplex mesh by the dual operation (Figure E.2(f)). Finally, its topological quality is optimized to make faces regular.

Evolution

The evolution of the deformable surface $\mathbf{X}$ is described by the following dynamic force equation:

$$\gamma \frac{\partial \mathbf{X}}{\partial t} = \mathbf{F}_{int}(\mathbf{X}) + \mathbf{F}_{ext}(\mathbf{X})$$

where $\mathbf{F}_{int}$ is the internal force that specifies the regularity of the surface and $\mathbf{F}_{ext}$ is the external force that drives the surface towards image edges. The chosen internal force is:

$$\mathbf{F}_{int} = \alpha \nabla^2 \mathbf{X} - \beta \nabla^2 (\nabla^2 \mathbf{X})$$

where α and β respectively control the surface tension (prevent it from stretching) and rigidity (prevent it from bending) and ∇^2 is the Laplacian operator. It is then discretized on the simplex mesh using the finite difference method [306].

External Force

In our case, the external force is not only derived from image edges but also constrains the deformable model to satisfy the description of the structure. It can be written as a linear combination:

$$\mathbf{F}_{ext} = \lambda \mathbf{v} + \mu \mathbf{F}_R$$

where $\mathbf{v}$ is a Gradient Vector Flow (GVF) field introduced by Xu et al. [307] and $\mathbf{F}_R$ is the force attached to the spatial relationships described in Section E.3.2. A GVF field $\mathbf{v}$ is computed by diffusion of the gradient vector of a given edge map and is defined as the equilibrium solution of the following diffusion equation:

$$\begin{cases} \frac{\partial v}{\partial t} = g(\|\nabla f\|)\nabla^2 v - h(\|\nabla f\|)(v - \nabla f) \\ v(x,y,z,0) = \nabla f(x,y,z) \end{cases} \tag{E.1}$$

where f is an edge map. In Section E.3.3, we show how to construct an edge map suited to internal brain structures. Such a definition gives the GVF a large capture range and allows the model to progress into boundary concavities. The functions g and h are weighting functions which can be chosen as follows:

$$\begin{cases} g(r) = e^{-\frac{r}{\kappa}^2} \\ h(r) = 1 - g(r) \end{cases} \tag{E.2}$$

E.3.2 Deriving external forces from spatial relations

While in the two cases presented in Section E.2.3 spatial relations were only involved in the initialization process, they can also be used to constrain the final segmentation. Applications of spatial relations in imaging available in the literature [15 ; 22 ; 210] make use of the relations only in the recognition phase, the segmentation part being achieved by classical techniques. Even in applications concerning segmentation, like in Bloch et al. [22], spatial relations are not used to find the contour of the objects but, in that case, to select a radiometric class. However, in our case, the main difficulty lies in the lack of visible edges. For this reason, we propose to introduce spatial relations in a deformable model, through the definition of an external force derived from the fuzzy set. To our knowledge, the only combination of spatial relations and deformable models can be found in Pitiot et al [214]. However, the authors only consider the case of distance relations. Our approach, deriving a force from a fuzzy set, applies to any spatial relation that can be represented in this fuzzy set framework, including directional and distance relations.

The idea of deriving a force from a fuzzy set has already been used by Xu et al. [306] to reconstruct the cortical surface using a deformable model. But, in that case, the sets represented radiometric classes (of gray and white matters) derived from a fuzzy segmentation instead of spatial relationships. The authors used a balloon force, the magnitude of which was computed from the fuzzy sets:

$$w_p(x,y,z) = \begin{cases} 0 \quad \texttt{if } |2\mu_{wm} + \mu_{gm} - 1| \leq \delta \\ 2\mu_{wm} + \mu_{gm} - 1 \quad \texttt{elsewhere} \end{cases} \tag{E.3}$$

where μ_{wm} is the membership function of the white matter, μ_{gm} of the gray matter, and δ is a threshold. The direction of evolution ("inflate" or "deflate" the surface) is naturally determined in the previous equation. Indeed, w_p is positive when the surface lies in the white matter, equal to zero when it is in the gray matter and negative when it is in the cerebro-spinal fluid or the background. In our case, to build a force corresponding to a given spatial relation R represented by a fuzzy set of membership function μ_R, we could choose $w_p(x,y,z) = 1 - \mu_R$. However, unlike in the previous case, there is no way to determine whether the surface should be "inflated" or "deflated", w_p being positive. Thus, a balloon force does not appear to fit our needs. In the following, we propose three different ways to compute a force from a fuzzy set R of membership function μ_R.

In order to attract the deformable model in a region where the spatial relation is satisfied, the force should possess the following properties: be equal to zero where the relation holds (i.e. in the kernel of R), be non-zero elsewhere, be directed towards the points where the relation is satisfied and have a norm proportional to $1-\mu_R$. If we used directly $P_R = 1-\mu_R$ as a potential, the corresponding force $\mathbf{F}_R = -\nabla P_R$ would be obviously zero outside the support of R. This can be easily solved by adding to the potential the distance from the support, then defining:

$$P_R^1(x,y,z) = 1-\mu_R(x,y,z) + d_{supp(R)}(x,y,z) \tag{E.4}$$

where $d_{supp(R)}$ is the distance from the support of R. With the following normalization, we obtain a force fulfilling our previous properties:

$$\mathbf{F}_R^1 = -(1-\mu_R)\frac{\nabla P_R^1(x,y,z)}{\|\nabla P_R^1(x,y,z)\|} \tag{E.5}$$

A second way to define such a force would be to use a distance force [56] replacing the edge map with our fuzzy set. One has then to replace the classical distance with a distance from a fuzzy set, e.g. the morphological distance obtained by fuzzy dilation of the reference object [21]. However, this distance has a very high computational cost. Instead of that, we propose to use the distance to the kernel of R which is a binary object:

$$P_R^2(x,y,z) = g(d_{Ker(R)}(x,y,z)) \tag{E.6}$$

where $d_{Ker(R)}(x,y,z)$ is a distance map to the kernel of R and g is a non-decreasing function, e.g. $g(x) = -ke^{-x^2}$ or $g(x) = -1/x$. The force $\mathbf{F}_R^2$ is derived through Equation E.5.

A third possibility is to use a gradient vector diffusion technique such as the Gradient Vector Flow (GVF). Again we have to replace the edge map with a fuzzy set, replacing f with μ_R in Equation E.1. However, the force would be non-zero in the kernel of R which is a non desirable property. This can be solved using the following normalization:

$$\mathbf{F}_R^3 = (1-\mu_R)\frac{\mathbf{u}}{\|\mathbf{u}\|} \tag{E.7}$$

where $\mathbf{u}$ is the GVF computed from the fuzzy set R.

Although they are similar, the 3 previous forces do not have exactly the same properties. In the particular case of a fuzzy set with local maxima outside its kernel, $\mathbf{F}_R^1$ and $\mathbf{F}_R^3$ would be directed towards these maxima whereas $\mathbf{F}_R^2$ would point towards the kernel of R. Figure E.3 shows an example of each of these forces. One can see that $\mathbf{F}_R^1$ and $\mathbf{F}_R^3$ share a similar behavior. In particular, they are orthogonal to isolevels of R. This is not the case for $\mathbf{F}_R^2$ which is always directed towards the kernel. The computational cost of $\mathbf{F}_R^1$ and $\mathbf{F}_R^2$ is very low (5 seconds for a 128x128x124 image on a PC Pentium III 1Ghz). The computation time is higher for $\mathbf{F}_R^3$ (3 minutes), while being still acceptable. $\mathbf{F}_R^2$ should not be applied in case of fuzzy sets with maxima outside their kernel. It was not the case in our experiments and all forces have lead to extremely similar results. Finally, even though $\mathbf{F}_R^1$ and $\mathbf{F}_R^3$ are similar, $\mathbf{F}_R^3$ introduces a regularization which could be useful. It is also worth noting that all these results are valid in the case of a binary set instead of a fuzzy one. In that particular case, forces $\mathbf{F}_R^1$ and $\mathbf{F}_R^2$ would be equal as the kernel of a binary set is equal to its support.

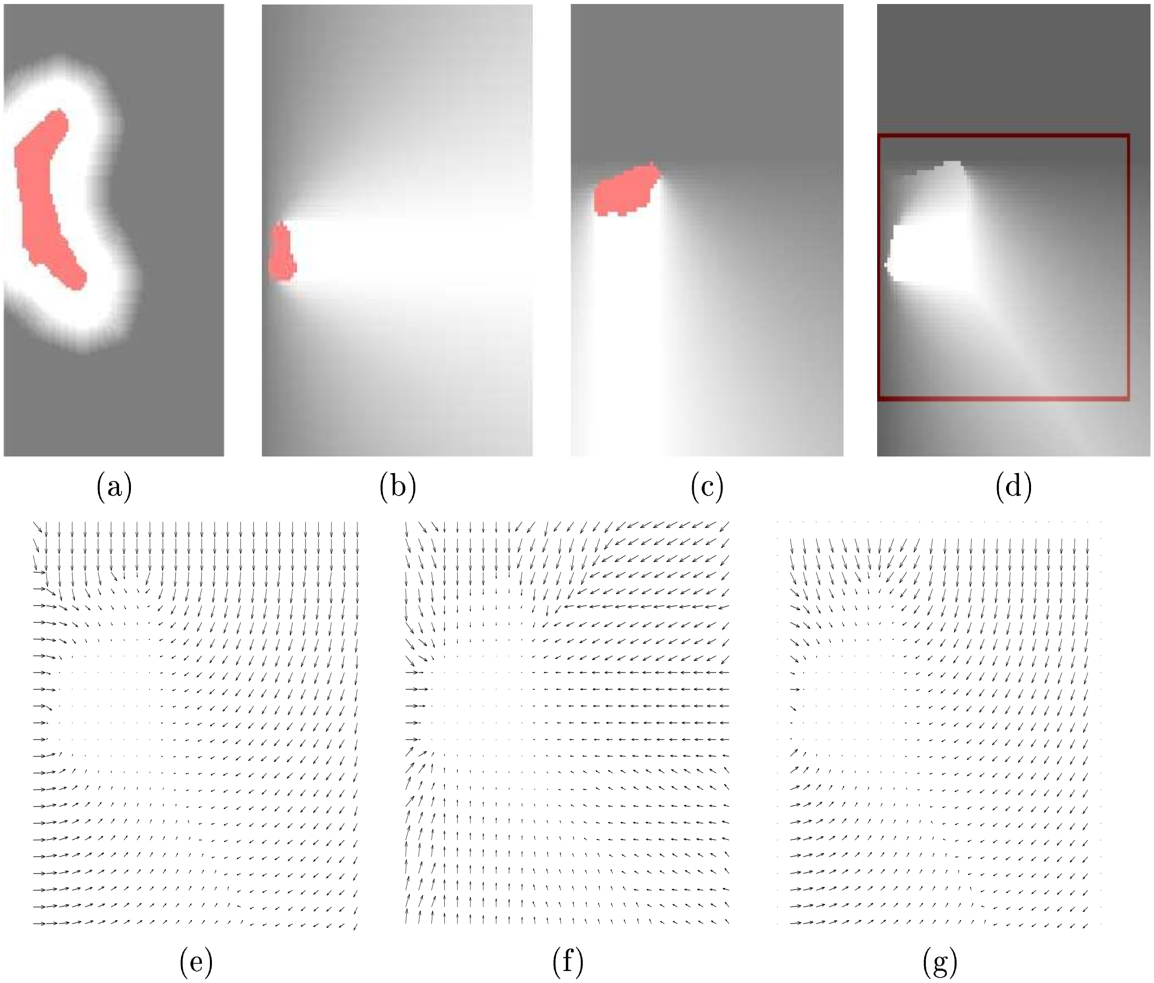

(a) (b) (c) (d)

(e) (f) (g)

Figure E.3: Slices of fuzzy sets representing spatial relations and the derived external force (only the part corresponding to the left hemisphere is shown): (a) distance: “close to the lateral ventricle”, (b) direction: “lateral to the third ventricle”, (c) direction: “below the lateral ventricle”, (d) conjunctive fusion of the two previous directions, (e) external force corresponding to the fusioned relation, computed using the first method $\mathbf{F}^1_R$ (for visualization purposes a 1/3 under-sampling has been performed and we only show the part of the previous image corresponding to the rectangle shown in (d)), (f) idem with the second method $\mathbf{F}^2_R$, (g) idem with the third method $\mathbf{F}^3_R$. Bright areas correspond to high values.

E.3.3 Edge map computation

Two main problems appear when computing an edge map associated to grey nuclei in MRI: the noise and the lack of contrast of the grey/white interface. Linear spatial filtering which is usually associated to Canny-Deriche edge detectors is inadequate in this case as it would mix contours of thin elongated objects such as those we are interested in. Anisotropic diffusion [100] is an efficient way to remove noise in homogeneous regions while preserving and even enhancing edges. However, due to the very tiny transition for some of the grey nuclei, this edge enhancement is insufficient.

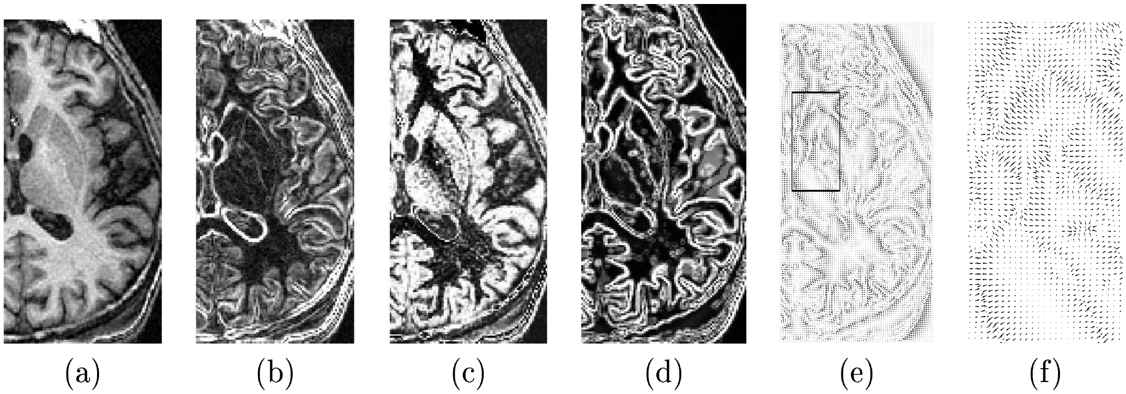

Figure E.4: Edge map for the caudate nucleus (axial slices): (a) original image, (b) gradient computed on original image, (c) probability map, (d) edge map: gradient computed on probability map after anisotropic diffusion, (e) Gradient vector flow (GVF) computed on the previous edge map, (f) zoom on a portion of the GVF.

We propose to use prior information on nuclei grey levels to enhance edges, computing the gradient on a probability map indicating for each voxel its membership to a given structure. This probability is computed as a distribution $P(x) = p(I(x))$ where I is our image. Its gradient is related to the gradient of I by $\nabla P(x) = p'(I(x))\nabla I(x)$. This means that edge enhancement will occur in the neighborhood of the extrema of p'. If we choose p to be a Gaussian function $G_{m,\sigma}$ of mean m and standard-deviation σ, edges will be enhanced in the neighborhood of $m \pm \sigma$. Parameters m and σ are estimated for each grey nucleus using the same method as in Section E.2.3. To remove the noise, we finally apply an anisotropic diffusion on the probability map. Applying it on the map instead of the original image has the additional advantage to normalize the image, allowing to chose the same diffusion parameter for all images. Figure E.4 presents an edge map computed for the caudate nucleus and the corresponding GVF.

E.4 Results and Conclusion

All our experiments have been performed on T1-weighted MR images [2]. Some preprocessing steps are needed. First, we correct the image for intensity non-uniformity [183]. Then, the brain is extracted using a robust method based on morphological operations [185]. This allows us to eliminate radiometric classes that are of no interest to our application (scalp, air, skull…). However, whereas we systematically use the non-uniformity correction before extracting the brain, we do not suggest to use it for the grey nuclei because their contrast seems to be altered by this correction. Finally, we compute the brain symmetry plane [285].

We obtained good results for the ventricular system, the caudate nuclei and the thalami on a database containing 10 images (an example is shown in Figure E.5). The ventricles are not very difficult to segment as they present a high contrast with

---

[2] These images have a size of 256x256x124.

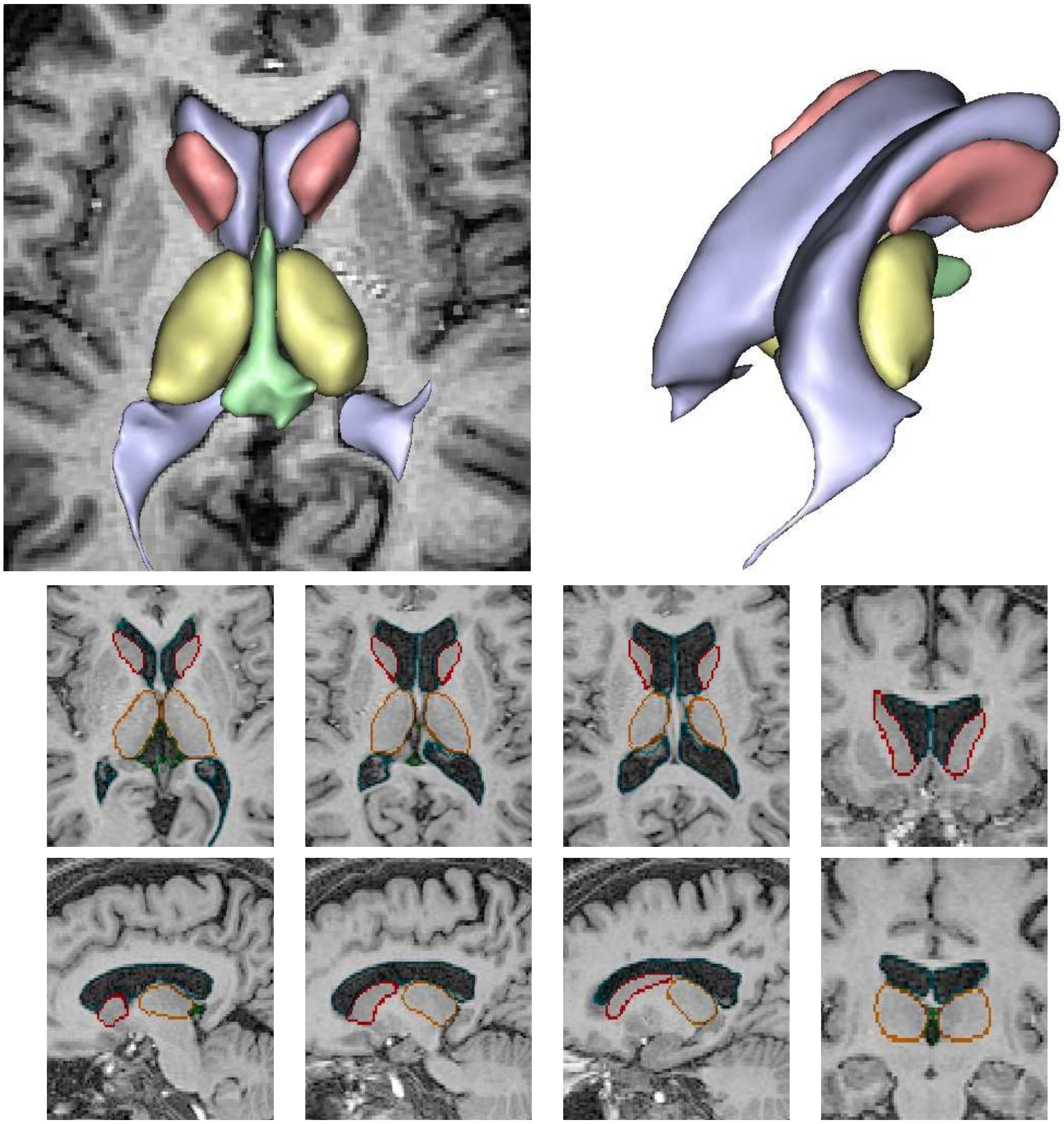

Figure E.5: Results obtained for the lateral ventricles, the third ventricle, the caudate nuclei and the thalami. Top: 3D rendering superimposed on an axial slice. Bottom: structure contours superimposed on axial, sagittal and coronal slices. 3D images have been visualized using the Anatomist software (www.anatomist.info), developed at S.H.F.J, Orsay, France.

surrounding structures. Only their separation is a bit more tricky, but this problem is solved by the watershed computed on the distance map to the contour. The ventricles, which are segmented first, are then used as a reference to segment the other structures. The lower part of the caudate nucleus is difficult to segment, due to the lack of gradients, and the trade-off between GVF and the spatial relations has shown to be useful in that case as can be seen in Figure E.6. We are currently working on a more extensive validation of the method. The lower part of the thalamus is also difficult and in that case, the relation with respect to the third ventricle has helped

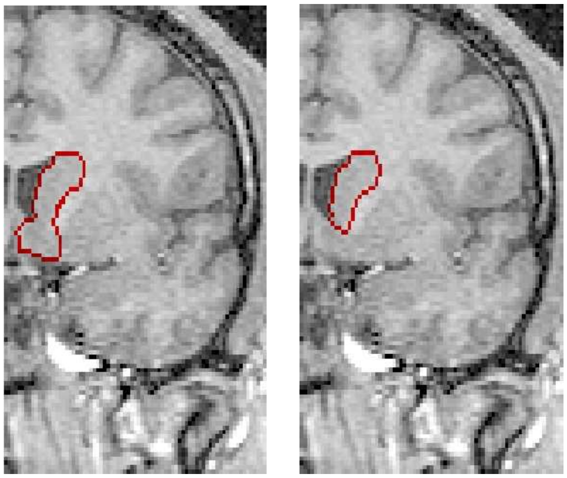

Figure E.6: Influence of spatial relations on the evolution of the deformable model: segmentation of the caudate nucleus. The force corresponding to spatial relations prevents the model from evolving beyond the lower limit of the structure. Left: result obtained without spatial relation. Right: result obtained with the spatial relation.

to produce an acceptable rough segmentation. In order to compare our method to others, a quantitative validation is needed. At last, whereas the tuning of parameters has not been very difficult, a full study of their influence will be performed soon.

We proposed a method combining prior information derived from spatial relations and deformable models to segment brain internal structures in MRI. This information correspond to a description of brain anatomy and can be represented by a *synthetic hierarchical graph*. The combination of spatial relations and the deformable model is done through the introduction of a new external force. We proposed three methods to construct such a force. Good results have been obtained for the ventricular system, the caudate and the thalamus. We are now working on applying the method to other structures. They can include other grey nuclei such as the putamen and the globus pallidus but also white matter structures which are usually not segmented. Some limits of these structures are not visible on the MRI and in that case, spatial relations could be of great help. Mid-term perspectives of this work include the simultaneous segmentation of structures, which could lead to a greater robustness for structures such as the caudate nucleus, and also the combination of spatial relations and shape constraints in the deformable model.

List of Publications

Technical rapports

Camara, O., Bloch, I., Frouin, V., Foehrenbach, H., De Druille, O., Rigo, P., Marchandise, X., and Stévenet, J.F., Développement et l'évaluation d'une méthodologie de recalage élastique d'images multimodalités (TDM, IRM, TEP) pour le diagnostic oncologique de différents segments anatomiques (cou, thorax et abdomen), *Action Concertée Incitative (ACI), Technologies pour la santé. Project: ONCOMATCHING*, 2001.

Patents

Bloch, I., Delso, G., and Camara, O., Registration of thoracic and abdominal imaging modalities, *U.S. Provisional Patent Application No. 60/369,681*, 2003. In collaboration with Segami SARL.

International Journals

Bloch, I., Colliot, O., Géraud T., and Camara, O., Fusion of Spatial Relationships for Guiding Recognition, with Examples in Brain Structure Recognition, *ICAPR Special Issue of Pattern Recognition Letters*, 2004 (In Press).

Camara, O., Colliot, O., and Bloch, I., Computational modelling of thoracic and abdominal regions by means of spatial relationships, *Real-Time Imaging*, 2004 (In Press).

Peer-reviewed international conferences

Camara, O., Delso, G., Colliot, O., Bloch, I., Frouin, V., Delzescaux, T., Briandet, P., Stévenet, J.F., Bernard, C., Foehrenbach, H., Marchandise, X., and Rigo, P., Recalage non-linéaire à posteriori et évaluation d'images TEP au FDG-18 d'émission corps entier et d'images TDM thoraciques et abdominales, In *Proc. 42ème Colloque de médecine nucléaire de langue française, SFBMN'04*, 2004.

Camara, O., Delso, G., Colliot, O., Bloch, I., Frouin, V., Delzescaux, T., Briandet, P., Stévenet, J.F., Bernard, C., Foehrenbach, H., Marchandise, X., and Rigo, P., Software-based non-linear registration and evaluation of 18F-FDG whole-body emission PET with thoracic and abdominal CT. Alternative or complementary solution to combined

PET/CT scanners, In *Proc. European Association of Nuclear Medicine, EANM'04*, 2004.

Colliot, O., Camara, O., and Bloch, I., Integration of fuzzy structural information into deformable models, In *Proc. Information Processing and Management of Uncertainty in Knowledge-Based Systems. IPMU'04*, 2004.

Colliot, O., Camara, O., Dewynter, R., and Bloch, I., Description of brain internal structures by means of spatial relations for MR image segmentation, In *Proc. The International Society of Optical Engineering. SPIE'04 Medical Imaging*, 2004.

Camara, O., Colliot, O., Delso, G., and Bloch, I., Apport de contraintes anatomiques au recalage non linéaire d'images TDM et TEP dans les régions thoraciques et abdominales, In *Reconnaissance des Formes et Intelligence Artificielle RFIA'04*, Toulouse, France, 2004, pp.797-806.

Colliot, O., Camara, O., and Bloch, I., Combinaison de relations spatiales et de modèles déformables pour la segmentation de structures cérébrales internes en IRM, In *Reconnaissance des Formes et Intelligence Artificielle RFIA'04*, Toulouse, France, 2004, pp.563-572.

Camara, O., Delso, G., and Bloch, I., Free Form Deformations Guided by Gradient Vector Flow: a Surface Registration Method in Thoracic and Abdominal PET-CT Applications, In *Proc. 2nd International Workshop on Biomedical Image Registration, WBIR'03*, Philadelphie, USA, 2003.

Camara, O., Colliot, O., Delso, G., and Bloch, I., 3D nonlinear PET-CT image registration algorithm with constrained Free-Form Deformations, In *Proc. 3rd IASTED International Conference on Visualization, Imaging, and Image Processing, VIIP'03*, Benalmadena, Spain, 2003.

Camara, O., Delso, G., and Bloch, I., Evaluation of a thoracic elastic registration method using anatomical constraints in oncology, In *Proc. 2nd Joint Conference of the IEEE Engineering in Medicine and Biology Society and the Biomedical Engineering Society, IEEE EMBS-BMES'02*, Houston, USA, 2002.

Camara, O., Delso, G., Frouin, V., and Bloch, I., Improving thoracic elastic registration in oncology by using anatomical constraints, In *Proc. 6th Medical Image Understanding and Analysis, MIUA'02*, Portsmouth, UK, 2002.

Bibliography

[1] J.L.R. Andersson and L. Thurfjell. A multivariate approach to registration of dissimilar tomographic images. *European Journal of Nuclear Medicine*, 26(7):718–733, 1999.

[2] C.R. Appledorn. A new approach to the interpolation of sampled data. *IEEE Transactions on Medical Imaging*, 15:369–376, 1996.

[3] N. Arad, N. Dyn, D. Riesfeld, and Y. Yeshwin. Image Warping by Radial Basis Functions: Application to Facial Expressions. *Computer Vision, Graphics and Image Processing: Graphical Models and Image Processing*, 56(2):161–172, 1994.

[4] S.G. Armato, III and H. MacMahon. Automated lung segmentation and computer-aided diagnosis for thoracic CT scans. In *Computer Assisted Radiology and Surgery (CARS'03)*, 2003.

[5] M.A. Audette, F.P. Ferrie, and T.M. Peters. An algorithmic overview of surface registration techniques for medical imaging. *Medical Image Analysis*, 4:201–217, 2000.

[6] R. Bajcsy. Digital Anatomy Atlas and Its Registration to MRI, fMRI, PET: The Past Presets a Future. In *Workshop in Biomedical Image Registration (WBIR'03)*, pages 201–211, 2003.

[7] R. Bajcsy and S. Kovacic. Multiresolution elastic matching. *Computer Vision, Graphics and Image Processing*, 46:1–21, 1989.

[8] R. Bajcsy, R. Lieberson, and M. Reivich. A computerized system for the elastic matching of deformed radiographic images to idealized atlas images. *Journal of Computer Assisted Tomography*, 7(4):618–625, 1983.

[9] R.A. Banvard and M.J. Ackerman. The Third Visible Human Project Conference Proceedings. Technical report, National Library of Medicine, Bethesda, Maryland USA, 2000.

[10] R. Bar-Shalom, Z. Keidar, L. Guralnik, N. Yefremov, J. Sachs, and O. Israel. Added value of fused PET/CT imaging with FDG in diagnostic imaging and management of cancer patients [abstract]. *Journal of Nuclear Medicine*, 43(32P):117, 2002.

[11] C. Barillot. Fusion de données appliquée à la modélisation de structures cérébrales. Technical report, Laboratoire SIM faculté de médecine, Université de Rennes I, France, 1999.

[12] C. Barillot. Deformable Registration. invited lecture. In *Information Processing in Medical Imaging (IPMI'01)*, 2001.

[13] O.H. Beahrs, D.E. Henson, R.V. Hutter, and M.H. Myers. *Manual for Staging of Cancer*. American Joint Committee on Cancer, Philadelphia (PA), USA, 3rd edition, 1988.

[14] R. R. Beichel, R. B. Zotter, C. Janko, K. Palagyi, E. Sorantin, G. Werkgartner, H. Bischof, and M. Sonka. Liver segment approximation in CT data for surgical resection planning. In *SPIE Conference on Medical Imaging: image processing*, 2004.

[15] F. Le Ber and L. Mangelick. A Formal Representation of Landscape Spatial Patterns to Analyze Satellite Images. *AI Applications*, 12(1-3):51–59, 1998.

[16] P. Besl and N. McKay. A method for registration of 3D shapes. *IEEE Transactions on Pattern Analysis and Machine Intelligence*, 18(14):239–256, 1992.

[17] M. Betke, H. Hong, D. Thomas, C. Prince, and J. P. Ko. Landmark Detection in the Chest and Registration of Lung Surfaces with an Application to Nodule Registration. *Medical Image Analysis*, 7(3):265–281, 2003.

[18] T. Beyer, D.W. Townsend, T. Brun, P.E. Kinahan, M. Charron, R. Roddy, J. Jerin, J. Young, L. Byars, and R. Nutt. A combined PET/CT scanner for clinical oncology. *Journal of Nuclear Medicine*, 41(3):1369–1379, 2000.

[19] R. Bissett, K. Leszczynski, S. Loose, S. Boyko, and P. Dunscombe. Quantitative vs. Subjective Portal Verification using Digital Portal Images. *International Journal of Radiation Oncology, Biology, Physics*, 34(2):489–495, 1989.

[20] I. Bloch. Information combination operators for data fusion: A comparative review with classification. *IEEE Transactions on Systems, Man, and Cybernetics*, 26(1):52–67, 1996.

[21] I. Bloch. On Fuzzy Distances and their Use in Image Processing under Imprecision. *Pattern Recognition*, 32(11):1873–1895, 1999.

[22] I. Bloch, T. Géraud, and H. Maître. Representation and Fusion of Heterogeneous Fuzzy Information in the 3D Space for Model-Based Structural Recognition - Application to 3D Brain Imaging. *Artificial Intelligence Journal*, 148:141–175, 2003.

[23] I. Bloch, H. Maître, and M. Anvari. Fuzzy Adjacency between Image Objects. *International Journal of Uncertainty, Fuzziness and Knowledge-Based Systems*, 5(6):615–653, 1997.

[24] T. Blodgett, T. Beyer, G. Antoch, S. Mueller, L. Freudenberg, and T. Akhurst. The effect of respiration motion on PET/CT image quality. In *Conference of the Society of Nuclear Medicine (SNM'02)*, page 58, 2002.

[25] J.L. Boes and C.R. Meyer. Multi-variate mutual information for registration. In *International Conference on Medical Image Computing and Computer-Assisted Intervention (MICCAI'99)*, pages 606–612, 1999.

[26] S. Bonnet, A. Koening, S. Roux, P. Hugonnard, R. Guillemaud, and P. Grangeat. Dynamic X-ray computed tomography. In *Proceedings of the IEEE*, volume 91, pages 1574–1587, 2003.

[27] F.L. Bookstein. Principal Warps: Thin-plate splines and the decomposition of deformations. *IEEE Transactions on Pattern Analysis and Machine Intelligence*, 11(6):567–585, 1989.

[28] G. Borgefors. Distance transformations in arbitrary dimensions. *Computer Vision,Graphics and Image Processing*, 27:321–345, 1984.

[29] G. Borgefors. Hierarchical Chamfer Matching: A Parametric Edge Matching Algorithm. *IEEE Transactions on Pattern Analysis and Machine Intelligence*, 10:849–865, 1988.

[30] L. Boucher, S. Rodrigue, R. Lecomte, and F. Bénard. Respiratory Gating for 3-Dimensional PET of the Thorax: Feasibility and Initial Results. *The Journal of Nuclear Medicine*, 45(2):214–219, 2004.

[31] B. Bouchon-Meunier, M. Rifqi, and S. Bothorel. Towards General Measures of Comparison of Objects. *Fuzzy Sets and Systems*, 84(2):143–153, September 1996.

[32] D.M. Bowden and R.F. Martin. NeuroNames Brain Hierarchy. *Neuroimage*, 2:63–83, 1995.

[33] R.N. Bracewell. *The Fourier Transform and Its Applications*. McGraw-Hill, New York, USA, 1965.

[34] M. Bro-Nielsen and C. Gramkow. Fast fluid registration of medical images. In *Visualization in Biomedical Computing (VBC'96)*, pages 267–276, 1996.

[35] M. Bro-Nielsen, C. Gramkow, and S. Kreiborg. Non-rigid Image Registration Using Bone Growth Model. In *Joint Conference Computer Vision, Virtual Reality and Robotics in Medicine and Medical Robotics and Computer-Assisted Surgery (CVRMed-MRCAS'97)*, pages 3–12, 1997.

[36] C. Broit. *Optimal Registration of Deformed Images*. PhD thesis, Computer and Information Science Dept., University of Pennsylvania, Philadelphia, PA, 1981.

[37] L.G. Brown. A Survey of Image Registration Techniques. *ACM Computing Surveys*, 24(4):325–376, Dec 1992.

[38] R.D. Bucholz, K.R. Smith, J. Henderson, and L. McDurmont. Intraoperative localization using a three dimensional optical digitizer. In *Medical robotics and computer assisted surgery*, pages 283–290, 1994.

[39] P.J. Burt. Fast filter transforms for image processing. *Computer Vision, Graphics and Image Processing*, 16:20–51, 1981.

[40] T. Butz and J.P. Thiran. Affine registration with feature space mutual information. In *International Conference on Medical Image Computing and Computer-Assisted Intervention (MICCAI'01)*, pages 549–556, 2001.

[41] T. Butz and J.P. Thiran. Feature-space Mutual Information for Multi-modal Signal Processing with Application to Medical Image Registration. In *European Signal Processing Conference (EUSIPCO'02)*, volume 1, pages 3–10, 2002.

[42] J. Cai, J.C. Chu, D. Recine, M. Sharma, C. Nguyen, R. Rodebaugh, V.A. Saxena, and A. Ali. Ct and PET Lung Image Registration and Fusion in Radiotherapy Treatment Planning using the Chamfer-Matching Method. *International Journal of Radiation Oncology, Biology, Physics*, 43(4):883–891, 1989.

[43] I.C. Carlsen and H.A. Wischmann. Multi-resolution elastic registration of PET-CT images. In *Conference of the Society of Nuclear Medicine (SNM'03)*, 2003.

[44] V. Caselles, R. Kimmel, and G. Sapiro. Geodesic active contours. In *International Conference on Computer Vision (ICCV'95)*, pages 694–699, 1995.

[45] P. Castellanos, P.L. del Angel, and V. Medina. Deformation of MR images using a local linear transformation. In *SPIE Conference on Medical Imaging: image processing*, volume 4322, pages 909–916, 2001.

[46] M. Charron, T. Beyer, P.E. Kinahan, C.C. Meltzler, M.A. Dachille, and D.W. Townsend. Whole-Body FDG PET and CT imaging of malignancies using a combined PET/CT scanner [abstract]. *Journal of Nuclear Medicine*, 40(5):256P, 1999.

[47] C. Chefd'Hotel, G. Hermosillo, and O. Faugeras. Flows of Diffeomorphisms for multimodal image registration. In *IEEE International Symposium on Biomedical Imaging (ISBI'02)*, 2002.

[48] C.T. Chen, C.A. Pelizzari, G.T.Y. Chen, M.D. Cooper, and D.N. Levin. Image Analysis of PET Data with the Aid of CT and MR Images. In *Information Processing in Medical Imaging (IPMI'87)*, pages 601–611, 1987.

[49] G. T. Y. Chen and C. A. Pelizzari. Image correlation techniques in radiation therapy planning. *Computerized medical imaging and graphics*, 13(3):235–240, 1989.

[50] R. Chin, Jr., R. Ward, J.W. Keyes, R.H. Choplin, J.C. Reed, S. Wallenhaupt, A.S. Hudspeth, and E.F. Haponik. Mediastinal staging of non-small-cell lung cancer with positron emission tomography. *American Journal of Respiratory and Critical Care Medicine*, 152(6):2090–2096, 1995.

[51] G.E. Christensen, M.I. Miller, U. Grenander, and M.W. Vannier. Individualizing Neuroanatomical Atlases Using a Massively Parallel Computer. *IEEE Computer*, 29(1):32–38, 1996.

[52] G.E. Christensen, R.D. Rabbitt, and M.I. Miller. 3D Brain Mapping using a Deformable Neuroanatomy. *Physics in Medicine and Biology*, 39:609–618, 1994.

[53] G.E. Christensen, R.D. Rabbitt, M.I. Miller, S.C Joshi, U. Grenander, T.A. Coogan, and D.C. van Essen. Topological properties of smooth anatomic maps. In *Information Processing in Medical Imaging (IPMI'95)*, pages 101–112, 1995.

[54] H. Chui and A. Rangarajan. A feature registration framework using mixture models. In *Workshop on Mathematical Methods in Biomedical Image Analysis (MMBIA'00)*, pages 190–197, 2000.

[55] L.D. Cohen. On active contour models and balloons. *CVGIP: Image Understanding*, 53(2):211–218, 1991.

[56] L.D. Cohen and I. Cohen. Finite Element Methods for Active Contour Models and balloons for 2D and 3D images. *IEEE Transactions on Pattern Analysis and Machine Intelligence*, 15(11):1131–1147, 1993.

[57] L.D. Cohen and I. Cohen. Seeded region growing. *IEEE Transactions on Pattern Analysis and Machine Intelligence*, 16:641–647, 1994.

[58] A. Colin. *Etude de méthodes de recalage et de fusion d'images 3D du cerveau. Application au suivi d'une pathologie cérébrale.* PhD thesis, Université d'Auvergne, Clermont Ferrand, France, 1997.

[59] A. Collignon, F. Maes, D. Delaere, D. Vandermeulen, P. Suetens, and G. Marchal. Automated multimodality image registration using information theory. In *Information Processing in Medical Imaging (IPMI'95)*, pages 263–264, 1995.

[60] D. Collins, T. Peters, W. Dai, and A. C. Evans. Model-based segmentation of individual brain structures from MRI data. *Visualization in Biomedical Computing*, 1808:10–23, 1992.

[61] D.L. Collins, P. Neelin, T.M. Peters, and A.C. Evans. Automatic 3D intersubject registration of MR volumetric data in standarized Talairach space. *Journal of Computer Assisted Tomography*, 18(2):192–205, 1994.

[62] O. Colliot. *Représentation, évaluation et utilisation de relations spatiales pour l'interprétation d'images. Application à la reconnaissance de structures anatomiques en imagerie médicale.* PhD thesis, Telecom Paris, 2003.

[63] O. Colliot, I. Bloch, and A.V. Tuzikov. Characterization of approximate plane symmetries for 3D fuzzy objects. In *Information Processing and Management of Uncertainty in Knowledge-Based Systems (IPMU'02)*, volume 3, pages 1749–1756, 2002.

[64] O. Colliot, O. Camara, R. Dewynter, and I. Bloch. Description of brain internal structures by means of spatial relations for MR image segmentation. In *SPIE Conference on Medical Imaging: image processing*, 2004.

[65] O. Colliot, A.V. Tuzikov, R.M. Cesar, and I. Bloch. Approximate Reflectional Symmetries of Fuzzy Objects with an Application in Model-Based Object Recognition. *Fuzzy Sets and Systems*, 147:141–163, 2004.

[66] T.F. Cootes, D. Cooper, C.J. Taylor, and J. Graham. Active shape models - their training and application. *Computer Vision Image Understanding*, 61(1):38–59, January 1995.

[67] T.F. Cootes, G.J. Edwards, and C.J. Taylor. Active Appearance Models. *IEEE Transactions on Pattern Analysis and Machine Intelligence*, 23(6):681–685, 2001.

[68] C. Couinaud. *Le foie: études anatomiques et chirurgicales.* Masson, Paris, France, 1957.

[69] A.D.J. Cross and E.R. Hancock. Graph matching with a dual-step EM algorithm. *IEEE Transactions on Pattern Analysis and Machine Intelligence*, 20(11):1236–1253, 1998.

[70] E. D'Agostino, F. Maes, D. Vandermeulen, and P. Suetens. A viscous fluid model for multimodal non-rigid image registration using mutual information. In *International Conference on Medical Image Computing and Computer-Assisted Intervention (MICCAI'02)*, pages 23–26, 2002.

[71] C. Davatzikos. Spatial Normalization of 3D Brain Images Using Deformable Models. *Journal of Computer Assisted Tomography*, 20(4):656–665, 1996.

[72] B.M. Dawant, S.L. Hartmann, J.P. Thirion, F. Maes, D. Vandermeulen, and P. Demaerel. Automatic Segmentation of Internal Structures of the Head using a Combination of Similarity and Free-Form Transformations: Part I, Methodology and Validation on Normal Subjects. *IEEE Transactions on Medical Imaging*, 18(10), 1999.

[73] D. Delbeke. Oncological Applications of FDG PET Imaging. *Nuclear Medicine*, 40(10):1706–1714, 1999.

[74] H. Delingette. Simplex meshes: a general representation for 3D shape reconstruction. Technical Report 2214, INRIA, 1994.

[75] H. Delingette. General object reconstruction based on simplex meshes. *International Journal of Computer Vision*, 32(2):111–146, 1999.

[76] T. Delzescaux, H. Foehrenbach, and V. Frouin. A performance study for whole-body helicoidal CT/PET-FDG a posteriori registration using rigid and non-rigid FFD-based methods. In *Conference of the Society of Nuclear Medicine (SNM'03)*, 2003.

[77] R. Deriche. Using Canny's criteria to derive a recursively implemented optimal edge detector. *International Journal of Computer Vision*, 1(2):167–187, 1987.

[78] J. Deubler and J.C. Olivo. A wavelet-based multiresolution method to automatically register images. *Journal of Mathematical Imaging and Vision*, 7:199–209, 1997.

[79] A.P. Dhawan, L.K. Arata, A.V. Levy, and J. Mantil. Iterative Principal Axes Registration Method for Analysis of MR-PET Brain Images. *IEEE Transactions on Medical Imaging*, 42(11):1079–1087, 1995.

[80] G.T. Diamandopoulos. Cancer: An historical perspective. *Anticancer Research*, 16(4A):1595–1602, 1996.

[81] E. Dizendorf, I.F. Ciernik, B. Baumert, G.K. von Schulthless, U.M. Luetolf, and H.C. Steinert. Impact of integrated PET/CT scanning ion external beam radiation treatment planning [abstract]. *Journal of Nuclear Medicine*, 43(33P):118, 2002.

[82] P. Dokladal, I. Bloch, M. Couprie, D. Ruijters, R. Urtasun, and L. Garnero. Topologically controlled segmentation of 3D Magnetic Resonance Images of the head by using morphological operators. *Pattern Recognition*, 2003.

[83] R. Doll and R. Peto. The causes of cancer: quantitative estimates of avoidable risks of cancer in the united states today. *Journal of the National Cancer Institute*, 66:1191–1308, 1981.

[84] I. Dryden and K. Mardia. *Statistical Shape Analysis.* John Hopkins University Press, New York, USA, 1998.

[85] R. Duda, P.E. Hart, and D. G. Stork. *Pattern Classification.* Wiley, New York, USA, 2nd edition, 2001.

[86] B.A. Dwamena, S.S. Sonnad, J.O. Angobaldo, and R.L. Wahl. Metastases from non-small cell lung cancer: mediastinal staging in the 1990s–meta-analytic comparison of PET and CT. *Radiology*, 213(2):530–536, 1999.

[87] Y.E. Erdi, K. Rosenzweig, A.K. Erdi, H.A. Macapinlac, Y.C. Hu, L.E. Braban, J.L. Humm, O.D. Squire, C.S. Chui, S.M. Larson, and E.D. Yorke. Radiotherapy treatment planning for patients with non-small cell lung cancer using positron emission tomography (PET). *Radiotherapy and Oncology*, 62(1):51–60, 2002.

[88] A.C. Evans, C. Beil, S. Marrett, C.J. Thompson, and A. Hakjm. Anatomical-functional correlation using an adjustable MRI-based region of interest atlas with positron emission tomography. *Journal of Cerebral Blood Flow and Metabolism*, 8:513–530, 1988.

[89] O. Faugeras. *Three-Dimensional Computer Vision: a Geometric Viewpoint.* MIT Press, Cambridge, Massachussets, USA, 1993.

[90] J. Feldmar and N. Ayache. Rigid, affine and locally affine registration of free-form surfaces. *International Journal of Computer Vision*, 18(2):99–119, 1996.

[91] J. Feldmar, J. Declerck, G. Malandain, and N. Ayache. Extension of the ICP Algorithm to Nonrigid Intensity-Based Registration of 3D volumes. *Computer Vision Image Understanding*, 66(2):193–206, May 1997.

[92] J. Ferlay, F. Bray, P. Pisani, and D.M. Parkin. GLOBOCAN: Cancer incidence, mortality and prevalence worldwide, Version 1.0. In *IARC CancerBase No. 5.* International Agency for Research on Cancer, Lyon, France, 2000.

[93] J. Fitzpatrick, J. West, and C.R. Maurer, Jr. Predicting error in rigid-body, point-based registration. *IEEE Transactions on Medical Imaging*, 17:694–702, 1998.

[94] J.M. Fitzpatrick, D.L.G. Hill, Y. Shyr, J. West, C. Studholme, and C.R. Maurer, Jr. Visual Assessment of the Accuracy of Retrospective Registration of MR and CT Images of the Brain. *IEEE Transactions on Medical Imaging*, 17(4):571–585, 1998.

[95] M. Fornefett, K. Rohr, and H.S. Stiehl. Radial basis functions with compact support for elastic registration of medical images. *Image and Vision Computing*, 19:87–96, 2001.

[96] D. Freedman and P. Diaconis. On the histogram as a density estimator: L2 theory. *Zeitschrift fur Wahrscheinlichkeitstheorie und verwandte Gebiete*, 57:453–476, 1981.

[97] S. Gambhir, J. Czernin, J. Schwimmer, D.H. Silverman, R.E. Coleman, and M.E. Phelps. A tabulated summary of the FDG-PET literature. *The Journal of Nuclear Medicine*, 42(5 (Suppl)):1S–93S, 2001.

[98] J.C. Gee, L. le Bricquer, C. Barillot, D.R. Haynor, and R. Bajcsy. Bayesian approach to the brain image matching problem. In *SPIE Conference on Medical Imaging: image processing*, volume 2434, pages 145–156, 1995.

[99] T. Géraud. *Segmentation des structures internes du cerveau en imagerie par résonance magnétique tridimensionnelle.* PhD thesis, Telecom Paris, 1998.

[100] G. Gerig, O. Kubler, R. Kikinis, and F.A. Jolesz. Nonlinear anisotropic filtering of MRI data. *IEEE Transactions on Medical Imaging*, 11(2):221–232, June 1992.

[101] P. Gerlot and Y. Bizais. Image registration: a review and a strategy for medical application. In *Information Processing in Medical Imaging (IPMI'88)*, pages 81–89, 1988.

[102] B.K. Ghaffary and A.A. Sawchuk. A survey of new techniques for image registration and mapping. In *Proceedings of the SPIE: Applications of Digital Image Processing*, volume 432, pages 222–239, 1983.

[103] G.W. Goerres, E. Kamel, T.N.H. Heidelberg, M.R. Schwitter, C. Burger, and G.K. von Schulthess. PET-CT image co-registration in the thorax: influence of respiration. *European Journal of Nuclear Medicine*, 29(3):1337–1343, 2002.

[104] G.W. Goerres, G.K. von Schulthess, and T.F. Hany. Positron Emission Tomography and PET CT of the head and neck: FDG uptake in normal anatomy, in benign lesions, and in changes resulting from treatment. *American Journal of Roentgenology*, 179(5), 2002.

[105] G.H. Golub and C.F. van Loan. *Matrix computations*. Wiley, Baltimore, MD, USA, 3rd edition, 1996.

[106] C.S. Goodman. Introduction to health care technology assessment. Technical report, National Library of Medicine/NICHSR, 1998.

[107] A. Goshtaby. Registration of images with geometric distortions. *IEEE Transactions on Geoscience and Remote Sensing*, 26:60–64, 1988.

[108] G.J. Grevera and J.K. Udupa. An objective comparison of 3D image interpolation methods. *IEEE Transactions on Medical Imaging*, 17:642–652, 1998.

[109] A. Guimond, A. Roche, N. Ayache, and J. Meunier. Multimodal Brain Warping Using the Demons Algorithm and Adaptative Intensity Corrections. *IEEE Transactions on Medical Imaging*, 20:58–69, 2001.

[110] N. Gupta, J. Rogers, G. Graeber, M. Szwerc, and D. Mullett. Augmenting staging and diagnostic accuracy of whole body PET-FDG imaging using CT/PET fusion algorithm. In *Conference of the Society of Nuclear Medicine (SNM'02)*, page 305, 2002.

[111] R.L. Harder and R.N. Desmarais. Interpolation Using Surface Splines. *Journal of Aircraft*, 9(2):189–191, 1972.

[112] R. Hardy. Multiquadric Equations of Topography and Other Irregular Surfaces. *Journal of Geophysical Research*, 76(8):1905–1915, 1971.

[113] T. Hartkens, D.L.G. Hill, A.D. Castellano-Smith, D.J. Hawkes, C.R. Maurer, Jr., A.J. Martin, W.A. Hall, H. Liu, and C.L. Truwit. Using points and surfaces to improve voxel-based non-rigid registration. In *International Conference on Medical Image Computing and Computer-Assisted Intervention (MICCAI'02)*, pages 565–572, 2002.

[114] T. Hartkens, D. Rueckert, J.A. Schnabel, D.J. Hawkes, and D.L.G. Hill. VTK CISG Registration Toolkit: An open source software package for affine and non-rigid registration of single- and multimodal 3D images. In *Bildverarbeitung für die Medizin (BVM'02)*, 2002.

[115] P. Hellier. *Recalage non rigide en imagerie cérébrale: méthodes et validation.* PhD thesis, Université de Rennes I, France, 2000.

[116] P. Hellier, C. Barillot, I. Corouge, B. Gibaud, G. Le Goualher, D.L. Collins, A. Evans, G. Malandain, N. Ayache, G.E. Christensen, and H.J. Johnson. Retrospective Evaluation of Intersubject Brain Registration. *IEEE Transactions on Medical Imaging*, 22(9):1120–1130, September 2003.

[117] P.F. Hemler, P.A. van den Elsen, T.S. Sumanaweera, S. Napel, J. Drace, and J.R. Adler. A quantitative comparison of residual error for three different multimodality registration techniques. In *Information Processing in Medical Imaging (IPMI'95)*, pages 251–262, 1995.

[118] C. Hernandez-Esteban. *Modélisation d'objects 3D par fusion silhouettes-stéréo à partir de séquences d'images en rotation non calibrées.* PhD thesis, Telecom Paris, 2004.

[119] D.L.G. Hill, P.G. Batchelor, M. Holden, and D.J. Hawkes. Medical image registration. *Physics in Medicine and Biology*, 46:R1–R45, 2001.

[120] D.L.G. Hill and D.J. Hawkes. Voxel similarity measures for automated image registration. In *Visualization in Biomedical Computing (VBC'94)*, pages 205–216, 1994.

[121] D.L.G. Hill, D.J. Hawkes, N.A. Harrison, and C.F. Ruff. A strategy for automated multimodality image registration incorporating anatomical knowledge and imager characteristics. In *Information Processing in Medical Imaging (IPMI'93)*, pages 182–196, 1993.

[122] C.K. Hoh, M. Dahlbom, G. Harris, Y. Choi, R.A. Hawkins, M.E. Phelps, and J. Maddahi. Automated Iterative Three-Dimensional Registration of Positron Emission Tomography Images. *Journal of Nuclear Medicine*, 34(11):2009–2018, 1993.

[123] M. Holden, D.L.G. Hill, E.R.E. Denton, J.M. Jarosz, T.C.S. Cox, T. Rohlfing, J. Goodey, and D.J. Hawkes. Voxel similarity measures for 3D serial MR brain image registration. *IEEE Transactions on Medical Imaging*, 19(2):94–102, 2000.

[124] M. Holden, J.A. Schnabel, and D.L.G. Hill. Quantifying small changes in brain ventricular volume using non-rigid registration. In *International Conference on Medical Image Computing and Computer-Assisted Intervention (MICCAI'01)*, pages 49–56, 2001.

[125] D.R. Holmes, III, J.J. Camp, and R.A. Robb. Evaluation of search strategies and cost functions in optimizing voxel-based image registration. In *SPIE Conference on Medical Imaging: Image Display*, volume 2707, pages 554–562, 1996.

[126] B.K.P. Horn. Closed-form solution of absolute orientation using unit quaternions. *Journal of the Optical Society of America*, 4:629–642, 1987.

[127] B.K.P. Horn and B.G. Schunck. Determining optical flow. *Artificial Intelligence*, 17:185–203, 1981.

[128] IARC. Solar and Ultraviolet Radiation. In *Monographs on the Carcinogenic Risk of Chemicals to Humans, Vol. 55*. International Agency for Research on Cancer, Lyon, France, 1992.

[129] IARC. Some Naturally Occurring Substances: Food Items and Constituents, Heterocyclic Aromatic Amines, and Mycotaxins. In *Monographs on the Carcinogenic Risk of Chemicals to Humans, Vol. 56*. International Agency for Research on Cancer, Lyon, France, 1993.

[130] A.A. Ioannides, L.C. Liu, J. Kwapien, S. Drozdz, and M. Streit. Coupling of regional activations in a human brain during an object and face affect recognition task. *Human Brain Mapping*, 11(2):77–92, 2000.

[131] J. Jacq and C. Roux. Registration of non-segmented images using a genetic algorithm. In *Computer Vision, Virtual Reality and Robotics in Medicine*, volume 905, pages 205–211, 1995.

[132] P. Jannin, J.M. Fitzpatrick, D.J. Hawkes, X. Pennec, R. Shahidi, and M.W. Vannier. White paper: Validation of Medical Image Processing in Image-guided Therapy. In *Computer Assisted Radiology and Surgery (CARS'02)*, pages 299–305, 2002.

[133] M. Jenkinson and S. Smith. A global optimization method for robust affine registration of brain images. *Medical Image Analysis*, 5(2):143–156, 2001.

[134] G. Jerusalem, V. Warland, F. Najjar, P. Paulus, M.F. Fassotte, G. Fillet, and P. Rigo. Whole-body 18F-FDG PET for the evaluation of patients with Hodgkin's disease and non-Hodgkin's lymphoma. *Nuclear Medicine Communications*, 20(1):13–20, 1999.

[135] G. Jumarie. A new information theoretic approach to the entropy of non-random discrete maps relation to fractional dimension and temperature of curves. *Chaos, Solitions, Fractals*, 8(6):953–970, 1997.

[136] G.C. Kagadis, K.K. Delibasis, G.K. Matsopoulos, N.A. Mouravliansky, P.A. Asvestas, and G.C. Nikiforidis. A comparative study of surface- and volume-based techniques for the automatic registration between CT and SPECT brain images. *Medical Physics*, 29(2):201–213, 2002.

[137] E. Kamel, G. W. Goerres, C. Burger, G.K. von Schulthess, and H.C. Steinert. Recurrent laryngeal nerve palsy in patients with lung cancer: Detection with PET/CT image fusion – Report of 6 cases. *Radiology*, 224:153–156, 2002.

[138] I.L. Kaplan and L.C. Swayne. Composite SPECT-CT Images: Technique and Potential Applications in Chest and Abdominal Imaging. *American Journal of Roentgenology*, 152:865–866, 1989.

[139] M. Kass, A. Witkin, and D. Terzopoulos. Snakes: Active Contour Models. *International Journal of Computer Vision*, 1(4):321–331, 1987.

[140] Z. Keidar. Hybrid imaging using PET/CT with F-18-FDG in suspected recurrence of lung cancer: diagnostic value and impact on patient management [abstract]. *Journal of Nuclear Medicine*, 43(32P):114, 2002.

[141] A. Kelemen, G. Szekely, and G. Gerig. Elastic Model-Based Segmentation of 3D Neuroradiological Data Sets. *IEEE Transactions on Medical Imaging*, 18(10), October 1999.

[142] P.E. Kinahan, D.W. Townsend, and T. Beyer. Attenuation correction for a combined 3D PET/CT scanner. *Medical Physics*, 25:2046–2053, 1998.

[143] R.J. King. *Cancer Biology.* Prentice Hall, 2nd edition, 2000.

[144] Z.F. Knops, J.B.A. Maintz, M.A. Viergever, and J.P.W. Pluim. Normalized Mutual Information Based PET-MR Registration Using K-Means Clustering and Shading Correction. In *Workshop in Biomedical Image Registration (WBIR'03)*, pages 31–39, 2003.

[145] K.F. Koral, S. Lin, J.A. Fessler, M.S. Kaminski, and R.L. Wahl. Preliminary results from intensity-based CT-SPECT fusion in I-131 anti-B1 monoclonal-antibody therapy of lymphoma. *Cancer*, 80(12):20–27, 1997.

[146] E. Kramer, M. Noz, G. Maguire, Jr., J. Sanger, and C. Walsh. Fusing of Immunoscintigraphy SPECT with CT or MRI for Improved Multimodality Image Interpretation. In *Conference of the IEEE Engineering in Medicine and Biology Society (IEEE EMBS'92)*, pages 1805–1806, 1992.

[147] D.W. Kufe, R.E. Pollock, R.R. Weichselbaum, R.C. Bast, Jr., T.S. Gansler, J.F. Holland, and E. Frei, III. *Cancer Medicine.* American Society and BC Decker, Inc., 6th edition, 2003.

[148] J.M. Kuhnigk, H. Hahn, M. Hindennach, V. Dicken, S. Krass, and H.O. Peitgen. Lung lobe segmentation by anatomy-guided 3D watershed transform. In *SPIE Conference on Medical Imaging: image processing*, 2003.

[149] B.J. Kuipers and T.S. Levitt. Navigation and Mapping in Large-Scale Space. *Artificial Intelligence Magazine*, 9(2):25–43, 1988.

[150] S. Lavallée. Registration for computer-integrated surgery: methodology, state of the art. In R. H. Taylor, S. Lavallée, G. C. Burdea, and R. Mosges, editors, *Computer-integrated surgery, Technology and clinical applications*, chapter 5, pages 77–97. MIT Press, Cambridge, MA, 1996.

[151] S. Lavallée and R. Szeliski. Recovering the position and orientation of free-form objects from image contours using 3D distance maps. *IEEE Transactions on Pattern Analysis and Machine Intelligence*, 17(4):378–390, 1995.

[152] D. Le. *Détection et correction des mouvements du patient dans les séquences d'images médicales*. PhD thesis, Institut National Agronomique, Paris-Grignon, France, 1995.

[153] T. Lehmann, A. Sovakar, W. Schmitt, and R. Repges. A Comparison of Similarity Measures for Digital Substraction Radiography. *Computers in Biology and Medicine*, 27(2):151–167, 1997.

[154] T.M. Lehmann, C. Gönner, and K. Spitzer. Survey: interpolation in medical image processing. *IEEE Transactions on Medical Imaging*, 18:1049–1075, 1999.

[155] T.M. Lehmann, C. Gönner, and K. Spitzer. Addendum: B-spline interpolation in medical image processing. *IEEE Transactions on Medical Imaging*, 20:660–665, 2001.

[156] D. Lemoine, C. Barillot, B. Gibaud, and E. Pasqualini. An Anatomical-based 3D Registration System of Multimodality and Atlas Data in Neurosurgery. In *Information Processing in Medical Imaging (IPMI'91)*, pages 154–164, 1991.

[157] H. Lester and S.R. Arridge. Combining fluid deformations and spline warps: Fully automatic non-linear registration with a large number of landmarks. In *Computer Assisted Radiology and Surgery (CARS'97)*, 1997.

[158] H. Lester and S.R. Arridge. Summarising fluid registration by thin-plate spline warps with many landmarks. In *Medical Image Understanding and Analysis (MIUA'97)*, 1997.

[159] H. Lester and S.R. Arridge. A survey of hierarchical non-linear medical image registration. *Pattern Recognition*, 32:129–149, 1999.

[160] B. Likar and F. Pernus. A hierarchical approach to elastic registration based on mutual information. *Image and Vision Computing*, 19:33–44, 2001.

[161] S. Lim, Y. Jeong, and Y. Ho. Automatic segmentation of the liver in CT images using the watershed algorithm based on morphological filtering. In *SPIE Conference on Medical Imaging: image processing*, 2004.

[162] T. Lindeberg. Scale-space theory: a basic tool for analyzing structures at different scales. *Journal of Applied Statistics*, 21(2):224–270, 1994.

[163] F. Liu, B. Zhao, P. Kijewski, M. Ginsberg, L. Wang, and L. Schwartz. Automatic liver contour segmentation using GVF snake. In *SPIE Conference on Medical Imaging: image processing*, 2004.

[164] M.H. Loew. Medical Imaging Registration Study Project. In *Report of NASA Image Registration Workshop*, November 1997.

[165] W.E. Lorensen and H.E. Cline. Marching cube, a high resolution 3D surface reconstruction algorithm. In *International Conference on Computer Graphics and Interactive Techniques (SIGGRAPH'87)*, volume 21, pages 163–169, 1987.

[166] J. Lötjönen and T. Mäkelä. Elastic matching using a deformation sphere. In *International Conference on Medical Image Computing and Computer-Assisted Intervention (MICCAI'01)*, pages 541–548, 2001.

[167] J.M.P. Lotjonen. Segmentation of MR Images using Deformable Models: Application to Cardiac Images. *International Journal of Bioelectromagnetism*, 3(2):37–45, 2001.

[168] B. Ma, A. Hero, J. Gorman, and O. Michel. Image registration with minimum spanning tree algorithm. In *IEEE International Conference on Image Processing (ICIP'00)*, 2000.

[169] J. MacQueen. Some methods for classification and analysis of multivariate observations. In *Proceedings of the Fifth Berkeley Symposium on Mathematical Statistics and Probability*, volume 1, pages 281–297, 1967.

[170] F. Maes. *Segmentation and Registration of Multimodal Medical Images: from Theory, Implementation and Validation to a Useful Tool in Clinical Practice.* PhD thesis, Katholieke Universiteit Leuven, Belgium, 1998.

[171] F. Maes, A. Collignon, D. Vandermeulen, G. Marchal, and P. Suetens. Multimodality image registration by maximization of mutual information. *IEEE Transactions on Medical Imaging*, 16:187–198, 1997.

[172] F. Maes, D. Vandermeulen, G. Marchal, and P. Suetens. Clinical relevance of fully automated multimodality image registration by maximization of mutual information. In *Proceedings Image Registration Workshop*, pages 323–330, 1997.

[173] F. Maes, D. Vandermeulen, and P. Suetens. Comparative evaluation of multiresolution optimization strategies for multimodality image registration by maximization of mutual information. *Medical Image Analysis*, 3(4):373–386, 1999.

[174] G.Q. Maguire, Jr., M.E Noz, H. Rusinek, J. Jaeger, E.L. Kramer, J.J. Sanger, and G. Smith. Graphics Applied to Medical Image Registration. *IEEE Computer Graphics and Applications*, 11:20–27, 1991.

[175] J.B.A. Maintz. *Retrospective Registration of Tomographic Brain Images.* PhD thesis, Utrecht University, The Netherlands, 1996.

[176] J.B.A. Maintz, P.A. van den Elsen, and M.A. Viergever. Comparison of edge-based and ridge-based registration of CT and MR brain images. *Medical Image Analysis*, 1:151–161, 1996.

[177] J.B.A. Maintz and M.A. Viergever. A Survey of Medical Image Registration. *Medical Image Analysis*, 2(1):1–36, 1998.

[178] T. Makela, Q. C. Pham, P. Clarysse, J. Nenonen, J. Lotjonen, O. Sipila, H. Hanninen, K. Lauerna, J. Knuutti, and I. E. Magnin. A 3-D model-based registration approach for the PET, MR and MCG cardiac data fusion. *Medical Image Analysis*, 7(3):377–389, 2003.

[179] S. Makhija, N. Howden, R. Edwards, J. Kelley, D.W. Townsend, and C.C. Meltzer. Positron emission tomography/computed tomography imaging for the detection of recurrent ovarian and fallopian tube carcinoma: a retrospective review. *Gynecologic Oncology*, 224:153–156, 2002.

[180] G. Malandain and J.M. Rocchisani. Matching of 3D medical images with a potential based method. Technical Report 1890, INRIA, 1993.

[181] R. Malladi, J.A. Sethian, and B.C. Vemuri. Shape modelling with front-propagation: a level set approach. *IEEE Transactions on Pattern Analysis and Machine Intelligence*, 17(2):158–175, 1995.

[182] S.G. Mallat. A theory for multiresolution signal decomposition: the wavelet representation. *IEEE Transactions on Pattern Analysis and Machine Intelligence*, 11(7):674–693, 1989.

[183] J.F. Mangin. Entropy minimization for automatic correction of intensity non uniformity. In *Workshop on Mathematical Methods in Biomedical Image Analysis (MMBIA'00)*, pages 162–169, 2000.

[184] J.F. Mangin, I. Bloch, J. Lopez-Krahe, and V. Frouin. Transformations du Chanfrein dans des images 3D anisotropes. Technical report, Telecom Paris, 1994.

[185] J.F. Mangin, O. Coulon, and V. Frouin. Robust brain segmentation using histogram scale-space analysis and mathematical morphology. In *International Conference on Medical Image Computing and Computer-Assisted Intervention (MICCAI'98)*, pages 1230–1241, 1998.

[186] S. Marsland and C.J. Twining. Constructing data-driven optimal representations for iterative pairwise non-rigid registration. In *Workshop in Biomedical Image Registration (WBIR'03)*, pages 50–60, 2003.

[187] M. Martinelli, D.W. Townsend, C. Meltzer, and V.V. Villemagne. Survey of Results of Whole Body Imaging Using the PET/CT at the University of Pittsburgh Medical Center Facility. *Clinical Positron Imaging*, 3(4 (Suppl)):167–169, 2000.

[188] D. Mattes. Automatic Multimodality Image Registration with Deformations. Technical report, Thesis for the degree of MS in Electrical Engineering, University of Washington Medical Center, Seattle, 2000.

[189] D. Mattes, D.R. Haynor, H. Vesselle, T.K. Lewellen, and W. Eubank. Nonrigid multimodality image registration. In *SPIE Conference on Medical Imaging: image processing*, volume 4322, pages 1609–1620, 2001.

[190] D. Mattes, D.R. Haynor, H. Vesselle, T.K. Lewellen, and W. Eubank. PET-CT Image Registration in the Chest Using Free-form Deformations. *IEEE Transactions on Medical Imaging*, 22(1):120–128, 2003.

[191] C.R. Maurer, Jr., G.B. Aboutanos, B.M. Dawant, R.J. Maciunas, and J.M. Fitzpatrick. Registration of 3-D Images Using Weighted Geometrical Features. *IEEE Transactions on Medical Imaging*, 15(6):836–849, 1996.

[192] C.R. Maurer, Jr., J.M. Fitzpatrick, M.Y. Wang, R.L. Galloway, Jr., R.J. Maciunas, and G.S. Allen. Registration of head volume images using implantable fiducial markers. *IEEE Transactions on Medical Imaging*, 16:447–462, 1997.

[193] X. Meihe, R. Srinivasan, and W.L. Nowinski. A fast mutual information method for multi-modal registration. In *Information Processing in Medical Imaging (IPMI'99)*, volume 1613, pages 466–471, 1999.

[194] C.R. Meyer, J.L. Boes, B. Kim, P.H. Bland, K.R. Zasadny, P.V. Kison, K. Koral, K.A. Frey, and R.L. Wahl. Demonstration of accuracy and clinical versatility of mutual information for automatic multimodality image fusion using affine and thin-plate spline warped geometric deformations. *Medical Image Analysis*, 1:195–206, 1996.

[195] M.I. Miller, G.E. Christensen, Y.A. Amit, and U. Grenander. Mathematical Textbook of Deformable Neuroanatomies. *Medical Sciences*, 90:11944–11948, 1993.

[196] J. Montagnat. *Modèles déformables pour la segmentation et la modélisation d'images médicales 3D et 4D.* PhD thesis, INRIA Sophia-Antipolis, 1999.

[197] O. Musse. *Contribution à la mise en correspondance non rigide d'images médicales: une approche paramétrique hiérarchique sous contraintes topologiques.* PhD thesis, Université Strasbourg 1, France, 2000.

[198] Y. Nakamoto, M. Osman, C. Cohade, L.T. Marshall, J.M. Links, S. Kohlmyer, and R.L. Wahl. PET/CT: comparison of quantitative tracer uptake between germanium and CT transmission attenuation-correction images. *Journal of Nuclear Medicine*, 43(9):1137–1143, 2002.

[199] P. Neelin, J. Crossman, D.J. Hawkes, Y. Ma, and A.C. Evans. Validation of an MRI/PET landmark registration method using 3D simulated PET images and

point simulations. *Computerized medical imaging and graphics*, 17(4/5):351–356, 1993.

[200] H. Neemuchwala, A. Hero, and P. Carson. Feature coincidence trees for registration of ultrasound breast images. In *IEEE International Conference on Image Processing (ICIP'01)*, 2001.

[201] C. Nikou, F. Heitz, and J.P. Armspach. Robust voxel similarity metrics for the registration of dissimilar single and multimodal images. *Pattern Recognition*, 32:1351–1368, 1999.

[202] M. Osman, C. Cohade, J. Leal, and R. Wahl. Direct comparison of FDG PET and PET/CT imaging in staging and restaging patients with lung cancer [abstract]. *Journal of Nuclear Medicine*, 43(151P):548, 2002.

[203] M.M. Osman, C. Cohade, Y. Nakamoto, L.T. Marshall, J.P. Leal, and R.L. Wahl. Clinically significant inaccurate localization of lesions with PET/CT: frequency in 300 patients. *The Journal of Nuclear Medicine*, 44:240–243, 2003.

[204] M.M. Osman, C. Cohade, and R.L. Wahl. Respiratory motion artifacts on PET emission images obtained using CT attenuation correction on PET-CT. In *Conference of the Society of Nuclear Medicine (SNM'02)*, page 305, 2002.

[205] H. Park, H.B. Peyton, and C.R. Meyer. Construction of an Abdominal Probabilistic Atlas and its Application in Segmentation. *IEEE Transactions on Medical Imaging*, 22(4):483–492, 2003.

[206] J.A. Parker, R.V. Kenyon, and D.E. Troxel. Comparison of interpolating methods for image resampling. *IEEE Transactions on Medical Imaging*, 2:31–39, 1983.

[207] E.I. Parsai, K.M. Ayyangar, R.R. Dobelbower, and J.A. Siegel. Clinical Fusion of Three-Dimensional Images using Bremsstrahlung SPECT and CT. *The Journal of Nuclear Medicine*, 38(2):319–324, 1997.

[208] C.A. Pelizzari, G.T.Y. Chen, D.R. Spelbring, R.R. Weichselbaum, and C.T. Chen. Accurate Three-Dimensional Registration of CT, PET and/or MR Images of the Brain. *Journal of Computer Assisted Tomography*, 13(1):20–26, 1989.

[209] G.P. Penney, J. Weese, J.A. Little, P. Desmedt, D.L.G. Hill, and D.J. Hawkes. A comparison of similarity measures for use in 2D-3D medical image registration. *IEEE Transactions on Medical Imaging*, 17:586–595, 1998.

[210] A. Perchant and I. Bloch. A New Definition for Fuzzy Attributed Graph Homomorphism with Application to Structural Shape Recognition in Brain Imaging. In *IEEE Instrumentation and Measurement Technology Conference proceedings*, volume 3, pages 1801–1806, 1999.

[211] D. Perperidis, A. Rao, R. Mohiaddin, and D. Rueckert. Non-rigid Spatio-Temporal Alignment of 4D Cardiac MR Images. In *Workshop in Biomedical Image Registration (WBIR'03)*, pages 191–200, 2003.

[212] C. Petitjean. *Recalage non rigide d'images par approches variationnelles statistiques: Application à l'analyse et à la modélisation de la fonction myocardique en IRM.* PhD thesis, Université René Descartes, Paris V, France, 2003.

[213] B. Piquet, C. T. Silva, and A.E. Kaufman. Tetra-Cubes: an algorithm to generate 3D isosurfaces based upon tetrahedra. In *Brazilian Symposium on Computer Graphics and Image Processing (SIBGRAPI'96)*, volume 21, pages 205–210, 1996.

[214] A. Pitiot, H. Delingette, N. Ayache, and P.M. Thompson. Expert knowledge guided segmentation system for brain MRI. In *International Conference on Medical Image Computing and Computer-Assisted Intervention (MICCAI'03)*, pages 644–652, 2003.

[215] J.P.W. Pluim and J.M. Fitzpatrick. Image Registration. *IEEE Transactions on Medical Imaging*, 22(11):1341–1343, November 2003.

[216] J.P.W. Pluim, J.B.A. Maintz, and M.A. Viergever. Image Registration by Maximization of Combined Mutual Information and Gradient Information. *IEEE Transactions on Medical Imaging*, 19(8):809–814, 2000.

[217] J.P.W. Pluim, J.B.A. Maintz, and M.A. Viergever. Mutual-Information-Based Registration of Medical Images: A Survey. *IEEE Transactions on Medical Imaging*, 22(8):986–1004, August 2003.

[218] F. Poupon. *Parcellisation systématique du cerveau en volumes d'intérêt. Le cas des structures profondes.* PhD thesis, INSA Lyon, Lyon, France, Dec. 1999.

[219] F. Poupon, J.F. Mangin, D. Hasboun, C. Poupon, I. Magnin, and V. Frouin. Multi-object deformable templates dedicated to the segmentation of brain deep structures. In *International Conference on Medical Image Computing and Computer-Assisted Intervention (MICCAI'98)*, pages 1134–1143, 1998.

[220] M.J.D. Powell. An efficient method for finding the minimum of a function of several variables without calculating derivatives. *The Computer Journal*, 7:155–162, 1964.

[221] W.K. Pratt. *Digital Image Processing.* Wiley, New York, USA, 2nd edition, 1991.

[222] C. Pérault, A. Loboguerrero, J.C. Liehn, and F. Batteux. Automatic Superimposition of CT and SPECT Immunoscintigraphic Images in the Pelvis. In *Visualization in Biomedical Computing (VBC'92)*, volume 1808, pages 235–240, 1992.

[223] W. Press, S. Teukolsky, W. Vetterling, and B. Flannery. *Numerical Recipes in C*. Cambridge University Press, Cambridge, England, 2nd edition, 1992.

[224] J. Kautsky R. Turcajová. A hierarchical multiresolution technique for image registration. In *Proceedings of the SPIE Mathematical Imaging: Wavelets Applications in Signal and Image Processing*, 1996.

[225] A. Rangarajan, H. Chui, and J.S. Duncan. Rigid point feature registration using mutual information. *Medical Image Analysis*, 4:1–17, 1999.

[226] N. Ritter, R. Owens, J. Cooper, R.H. Eikelboom, and P.P. van Saarloos. Registration of stereo and temporal images of the retina. *IEEE Transactions on Medical Imaging*, 18(2):404–418, 1999.

[227] A. Roche. *Recalage d'images médicales par inférence statistique*. PhD thesis, Université de Nice-Sophia Antipolis, France, 2001.

[228] A. Roche, G. Malandain, X. Pennec, and N. Ayache. The Correlation Ratio as a New Similarity Measure for Multimodal Image Registration. In *International Conference on Medical Image Computing and Computer-Assisted Intervention (MICCAI'98)*, pages 1115–1124, 1998.

[229] A. Roche, X. Pennec, M. Rudolph, D.P. Auer, G. Malandain, S. Ourselin, L.M. Auer, and N. Ayache. Generalized Correlation Ratio for Rigid Registration of 3D Ultrasound with MR Images. In *International Conference on Medical Image Computing and Computer-Assisted Intervention (MICCAI'00)*, pages 567–577, 2000.

[230] C.E. Rodriguez-Carranza and M.H. Loew. A weighted and deterministic entropy measure for image registration using mutual information. In *SPIE Conference on Medical Imaging: image processing*, volume 3338, pages 155–166, 1998.

[231] C.E. Rodriguez-Carranza and M.H. Loew. Global optimization of weighted mutual information for multimodality image registration. In *SPIE Conference on Medical Imaging: image processing*, volume 3338, pages 89–96, 1999.

[232] P. Rogelj and S. Kovacic. Point Similarity Measure Based on Mutual Information. In *Workshop in Biomedical Image Registration (WBIR'03)*, pages 112–121, 2003.

[233] P. Rogelj, S. Kovacic, and J.C. Gee. Validation of a non-rigid registration algorithm for multi-modal data. In *SPIE Conference on Image Processing*, volume 4684, 2002.

[234] T. Rohlfing and C.R. Maurer. Intensity-Based Non-Rigid Registration Using Adaptive Multilevel Free-Form Deformation with an Incompressibility Constraint. In *International Conference on Medical Image Computing and Computer-Assisted Intervention (MICCAI'01)*, pages 111–119, 2001.

[235] K. Rohr. *Landmark-Based Image Analysis: Using Geometric and Intensity Models*, volume 21 of *Computational Imaging and Vision Series.* Kluwer Academic Publishers, Dordrecht Boston London, 2001.

[236] K. Rohr, M. Fornefett, and H.S. Stiehl. Approximating thin-plate splines for elastic registration: integration of landmark errors and orientation attributes. In *Information Processing in Medical Imaging (IPMI'99)*, volume 1613, pages 252–265, 1999.

[237] K. Rohr, H.S. Stiehl, R. Sprengel, W. Beil, T.M. Buzug, J. Weese, and M.H. Kuhn. Nonrigid registration of medical images based on anatomical point landmarks and approximating thin-plate splines. In *Aacheren Workshop Bildverarbeitung für die Medizin*, pages 41–46, 1996.

[238] A. Rosenfeld and J.L. Pfaltz. rDistance Functions on Digital pictures. *Pattern Recognition*, 1:33–61, 1968.

[239] N. Rougon, C. Petitjean, and F. Prêteux. Variational non rigid image registration using exclusive f-information. In *IEEE International Conference on Image Processing (ICIP'01)*, 2003.

[240] D. Rueckert, M.J. Clarkson, D.L.G. Hill, and D.J. Hawkes. Non-rigid registration using higher-order mutual information. In *SPIE Conference on Medical Imaging: image processing*, volume 3979, pages 438–447, 2000.

[241] D. Rueckert, A.F. Frangi, and J.A. Schnabel. Automatic Construction of 3-D Statistical Deformation Models of the Brain Using Nonrigid Registration. *IEEE Transactions on Medical Imaging*, 22(8):1014–1025, 2003.

[242] D. Rueckert, I. Somoda, C. Hayes, D. Hill, M. Leach, and D. Hawkes. Nonrigid Registration Using Free-Form Deformations: Applications to Breast MR Images. *IEEE Transactions on Medical Imaging*, 18(8):712–721, 1999.

[243] D. Ruprecht and H. Muller. Image warping with scattered data interpolation. *IEEE Computer Graphics and Applications*, 15(2):37–43, 1995.

[244] D. Sarrut. *Recalage multimodal et plate-forme d'imagerie médicale à accès distant.* PhD thesis, Université Lumiére Lyon 2, France, 2000.

[245] D. Sarrut and S. Miguet. Fast 3D image transformations for registration procedures. In *IEEE International Conference on Image Processing (ICIP'99)*, pages 446–452, 1999.

[246] M. Sato, A. E. Hassanien, and M. Nakajima. Non-linear registration of medical images using Cauchy-Navier splines transformation. In *SPIE Conference on Image Processing*, pages 3661–3677, 1999.

[247] M. Schmitt and J. Mattioli. *Morphologie mathématique.* Logique mathématiques informatiques. Masson, Paris, 1993.

[248] J.A. Schnabel, D. Rueckert, M. Quist, J.M. Blackall, A.D. Castellano-Smith, T. Hartkens, G.P. Penney, W.A. Hall, H. Liu, C.L. Truwit, F.A. Gerritsen, D.L.G. Hill, and D.J. Hawkes. A Generic Framework for Non-Rigid Registration Based on Non-Uniform Multi-level Free-Form Deformations. In *International Conference on Medical Image Computing and Computer-Assisted Intervention (MICCAI'01)*, pages 573–581, 2001.

[249] J.A. Schnabel, C. Tanner, A. Castellano-Smith, M.O. Leach, C. Hayes, A. Degenhard, R. Hose, D.L.G. Hill, and D.J. Hawkes. Validation of Non-Rigid Registration using Finite Element Methods. In *Information Processing in Medical Imaging (IPMI'01)*, volume 2082, pages 344–357, 2001.

[250] J.A. Schnabel, C. Tanner, A.D. Castellano-Smith, A. Degenhard, M.O. Leach, D.R. Hose, D.L.G. Hill, and D.J. Hawkes. Validation of Nonrigid Image Registration Using Finite-Element Methods: Application to Breast MR Images. *IEEE Transactions on Medical Imaging*, 22(2):238–247, February 2003.

[251] A.M. Scott, H.A. Macapinlac, C.R. Divgi, and J.J Zhang. Clinical Validation of SPECT and CT/MRI Image Registration in Radiolabeled Monoclonal Antibody Studies of Colorectal Carcinoma. *The Journal of Nuclear Medicine*, 35(12):1976–1984, 1994.

[252] D. W. Scott. *Multivariate Density Estimation.* Wiley, New York, USA, 1992.

[253] T. Sederberg and S. Parry. Free form deformation of solid geometric models. In *International Conference on Computer Graphics and Interactive Techniques (SIGGRAPH'86)*, volume 20, pages 151–160, 1986.

[254] W.P. Segars. *Development and Application of the New Dynamic NURBS-based Cardiac-Torso (NCAT) Phantom.* PhD thesis, The University of North Carolina, USA, 2001.

[255] W.P. Segars and B.M.W. Tsui. Study of the efficacy of respiratory gating in myocardial SPECT using the new 4D NCAT Phantom. *IEEE Transactions on Nuclear Science*, 49(3):675–679, 2002.

[256] D. Selle, B. Preim, A. Schenk, and H.O. Peitgen. Analysis of Vasculature for Liver Surgical Planning. *IEEE Transactions on Medical Imaging*, 21(11):1344–1357, 2002.

[257] J. Serra. *Image Analysis and Mathematical Morphology.* Academic Press, London, 1982.

[258] R. Shahidi, L. Clarke, and R.D. Bucholz et al. White paper: Challenges and opportunities in computer-assisted interventions. *Computer Aided Surgery*, 6(3):176–181, January 2001.

[259] C. E. Shannon. A mathematical theory of communication. *Bell System Technology Journal*, 27:379–423, 623–656, 1948.

[260] D. Shen, E.H. Herskovits, and C. Davatzikos. An Adaptative-Focus Statistical Shape Model for Segmentation and Shape Modeling of 3D Brain Structures. *IEEE Transactions on Medical Imaging*, 20(4), April 2001.

[261] F. Shtern and D. Winfield. Report of the joint working group on image-guided diagnosis and treatment. Technical report, U.S. Public Health Service's Office on Woman's Health and National Cancer Institute, Washington, D.C., April 1999.

[262] K. Sjögreen, M. Ljungberg, K. Erlandsson, L. Floreby, and S.E. Strand. Registration of Abdominal CT and SPECT Images Using Compton Scatter Data. In *Information Processing in Medical Imaging (IPMI'97)*, volume 1230, pages 232–244, 1997.

[263] P.J. Slomka, D. Dey, C. Przetak, U.E. Aladl, and R.P. Baum. Automated 3-Dimensional Registration of Stand-Alone 18F-FDG Whole-Body PET with CT. *The Journal of Nuclear Medicine*, 44(7):1156–1167, 2003.

[264] J.P.P. Starink and E. Baker. Finding point correspondence using simulated annealing. *Pattern Recognition*, 28:231–240, 1995.

[265] H.C. Steinert, T.F. Hany, E. Kamel, D. Lardinois, W. Weder, and G.K. von Schulthess. Impact of integrated PET/CT scanning on preoperative staging of lung cancer [abstract]. *Journal of Nuclear Medicine*, 43(151P):547, 2002.

[266] J. Stough, S.M. Pizer, E.L. Chaney, and M. Rao. Clustering on Image Boundary Regions for Deformable Model Segmentation. In *IEEE International Symposium on Biomedical Imaging (ISBI'04)*, 2004.

[267] C. Studholme. Simultaneous Population Based Image Alignment for Template Free Spatial Normalisation of Brain Anatomy. In *Workshop in Biomedical Image Registration (WBIR'03)*, pages 81–90, 2003.

[268] C. Studholme, V. Cardenas, and M. Weiner. Multi scale image and multi scale deformation of brain anatomy for building average brain atlases. In *SPIE Conference on Medical Imaging: image processing*, volume 4322, pages 557–568, 2001.

[269] C. Studholme, D. Hill, and D. Hawkes. An overlap invariant entropy measure of 3D medical image alignment. *Pattern Recognition*, 32:71–86, 1999.

[270] C. Studholme, D.L.G. Hill, and D.J. Hawkes. Multiresolution voxel similarity measures for MR-PET registration. In *Information Processing in Medical Imaging (IPMI'95)*, pages 287–298, 1995.

[271] C. Studholme, D.L.G. Hill, and D.J. Hawkes. Incorporating connected region labelling into automated image registration using mutual information. In *Workshop on Mathematical Methods in Biomedical Image Analysis (MMBIA'96)*, pages 23–31, 1996.

[272] H. Sturges. The choice of a class-interval. *Journal of the American Statistical Association*, 21:65–66, 1926.

[273] Y.C. Tai, K.P. Lin, C.K. Hoh, S.C.H. Huang, and E.J. Hoffman. Utilization of 3D Elastic Transformation in the Registration of Chest X-ray CT and Whole-Body PET. *IEEE Transactions on Nuclear Science*, 44(4):1606–1612, 1997.

[274] J. Talairach, G. Szikla, and P. Tournoux. *Atlas d'anatomie stéréotaxique du télencéphale.* Masson, Paris, 1967.

[275] P. Thévenaz, T. Blu, and M. Unser. Image Interpolation and Resampling. In I. Bankman, editor, *Handbook of Medical Image Processing.* Academic Press, New York, USA, 2003.

[276] P. Thévenaz and M. Unser. Optimization of Mutual Information for Multiresolution Image Registration. *IEEE Transactions on Image Processing*, 9(12):2083–2099, 2000.

[277] J. Thirion. Non-rigid matching using Demons. In *International Conference on Computer Vision and Pattern Recognition (CVPR'96)*, pages 245–251, 1996.

[278] J.P. Thirion. Image matching as a diffusion process: an analogy with Maxwell's demons. *Medical Image Analysis*, 2(3):243–260, 1998.

[279] D.W. Thompson. *On Growth and Form.* Cambridge University Press, Cambridge, England, 1917.

[280] S. Timoshenko and J.N. Goodier. *Theory of elasticity.* McGraw-Hill, New York, USA, 1951.

[281] L. Tomatis, A. Aitio, N. E. Day, E. Heseltine, J. Kaldor, A. B. Miller, D. M. Parkin, and E. Riboli. Cancer: Causes, Occurrence and Control. In *IARC Scientific Publication No. 100.* International Agency for Research on Cancer, Lyon, France, 1990.

[282] D. Tomazevic, B. Likar, and F. Pernus. "Gold Standard" 2D/3D Registration of X-ray to CT and MR Images. In *International Conference on Medical Image Computing and Computer-Assisted Intervention (MICCAI'02)*, pages 461–468, 2002.

[283] D.W. Townsend, J.P.J. Carney, J.T. Yap, and N.C. Hall. PET/CT Today and Tomorrow. *The Journal of Nuclear Medicine*, 45(1 (Suppl)):4S–14S, 2003.

[284] T.G. Turkington, R.J. Jaszczak, C.A. Pelizzari, C.C. Harris, J.R. MacFall, J.M. Hoffman, and R.E. Coleman. Accuracy of registration of PET, SPECT and MR images of a brain phantom. *Journal of Nuclear Medicine*, 34(9):1587–1594, 1993.

[285] A.V. Tuzikov, O. Colliot, and I. Bloch. Evaluation of the symmetry plane in 3D MR brain images. *Pattern Recognition Letters*, 24(14):2219–2233, oct 2003.

[286] S. Ukil and J. M. Reinhardt. Smoothing lung segmentation surfaces in 3D x-ray CT images using anatomic guidance. In *SPIE Conference on Medical Imaging: image processing*, 2004.

[287] M. Unser, A. Aldroubi, and M. Eden. B-spline signal processing: Part I-theory. *IEEE Transactions on Signal Processing*, 41(2):821–832, 1993.

[288] M. Unser, A. Aldroubi, and M. Eden. The L2 polynomial spline pyramid. *IEEE Transactions on Pattern Analysis and Machine Intelligence*, 15(4):364–379, 1993.

[289] I. Vadja. *Theory of Statistical Inference and Information.* Kluwer Academic Publishers, Dordrecht, The Netherlands, 1989.

[290] P.E. Valk, E. Abella-Columna, M.K. Haseman, T.R. Pounds, R.D. Tesar, R.W. Myers, H. B. Greiss, and G. A. Hofer. Whole-body PET imaging with [18F]fluorodeoxyglucose in management of recurrent colorectal cancer. *Archives of Surgery*, 134(5):503–511, 1999.

[291] P.A. van den Elsen, E.J.D. Pol, and M.A. Viergever. Medical image matching - a review with classification. *IEEE Engineering in medicine and biology*, 12(1):26–39, 1993.

[292] P. Viola. *Alignment by maximization of mutual information.* PhD thesis, MIT, Cambridge, Massachussets, USA, 1995.

[293] D. Vranjesevic, J.E. Filmont, J. Meta, D.H. Silverman, M.E. Phelps, J. Rao, P. E. Valk, and J. Czernin. Whole-body (18)F-FDG PET and conventional imaging for predicting the outcome in previously treated breast cancer patients. *The Journal of Nuclear Medicine*, 43(3):325–329, 2002.

[294] H.N. Wagner. Fused Image Tomography: An Integrating Force. *Nuclear Medicine*, 40(8):13N–32N, 1999.

[295] R.L. Wahl, L.E. Quint, R.D. Cieslak, A.M. Aisen, R.A. Koeppe, and C.R. Meyer. Anatometabolic tumor imaging: fusion of FDG PET with CT or MRI to localize foci of increased activity. *The Journal of Nuclear Medicine*, 34:1190–1197, 1993.

[296] W. Wells. Statistical approaches to feature-based object recognition. *International Journal of Computer Vision*, 21(1):63–98, 1997.

[297] E. Weng, L. Tran, S. Rege, A. Safa, A. Sadeghi, G. Juillard, R. Mark, S. Santiago, C. Brown, and M. Mandelkern. Accuracy and clinical impact of mediastinal lymph node staging with FDG-PET imaging in potentially resectable lung cancer. *American Journal of Clinical Oncology*, 23(1):47–52, 2000.

[298] J. West, J.M. Fitzpatrick, M.Y. Wang, B.M. Dawant, C.R. Maurer, Jr., R.M. Kessler, R.J. Maciunas, C. Barillot, D. Lemoine, A. Collignon, F. Maes,

P. Suetens, D. Vandermeulen, P.A. van den Elsen, P.F. Hemler, S. Napel, T.S. Sumanaweera, B. Harkness, D.L.G. Hill, C. Studholme, G. Malandain, X. Pennec, M.E. Noz, G.Q. Maguire, Jr., M. Pollack, C.A. Pellizari, R.A. Robb, D. Hanson, and R.P. Woods. Comparison and evaluation of retrospective intermodality brain image registration techniques. In *SPIE Conference on Medical Imaging: image processing*, volume 2710, pages 332–347, 1996.

[299] WHO. The World Health Report 2001. Technical report, World Health Organization, Geneva, Switzerland, 2001.

[300] R. Wiemker, K. Rohr, L. Binder, R. Sprengel, and H.S. Stiehl. Application of elastic registration to imagery from airbone scanners. In *Congress of the International Society for Photogrammetry and Remote Sensing (ISPRS'96)*, pages 949–954, 1996.

[301] M.A. Wirth. *A nonrigid approach to medical image registration: matching images of the breast.* PhD thesis, Faculty of Engineering, RMIT University, Melbourne, Victoria, Australia, 1999.

[302] G. Wollny and F. Kruggel. Computational cost of nonrigid registration algorithms based on fluid dynamics. *IEEE Transactions on Medical Imaging*, 21:946–952, 2002.

[303] J.C.H. Wong, C. Studholme, D.J. Hawkes, and M.N. Maisey. Evaluation of the limits of visual detection of image misregistration in a brain fluorine-18 fluorodeoxyglucose PET-MRI study. *European Journal of Nuclear Medicine*, 24:642–650, 1997.

[304] R.P. Woods, S.R. Cherry, and J.C. Mazziotta. Rapid automated algorithm for aligning and reslicing PET images. *Journal of Computer Assisted Tomography*, 16:620–633, 1992.

[305] R.P. Woods, J.C. Mazziotta, and S.R. Cherry. MRI-PET registration with automated algorithm. *Journal of Computer Assisted Tomography*, 17:536–546, 1993.

[306] C. Xu. *Deformable Models with Application to Human Cerebral Cortex Reconstruction in Magnetic Resonance Images.* PhD thesis, Johns Hopkins University, 2000.

[307] C. Xu and J.L. Prince. Snakes, Shapes and Gradient Vector Flow. *IEEE Transactions on Image Processing*, pages 359–369, March 1998.

[308] C. Xu and J.P. Prince. Gradient Vector Flow: A New External Force for Snakes. In *International Conference on Computer Vision and Pattern Recognition (CVPR'97)*, pages 66–71, 1997.

[309] C. Xu and J.P. Prince. Generalized Gradient Vector Flow External Forces for Active Contours. *Signal Processing, An International Journal*, 71(2):131–139, December 1998.

[310] J.H. Xue, S. Ruan, B. Moretti, M. Revenu, and D. Bloyet. Knowledge-based segmentation and labelling of brain structures from MRI images. *Pattern Recognition Letters*, 22:395–405, 2001.

[311] H. Yeung, H. Schider, and S. Larson. Utility of PET/CT for assessing equivocal PET lesions in oncology-initial experience [abstract]. *Journal of Nuclear Medicine*, 43(32P):115, 2002.

[312] J.N. Yu, F.H. Fahey, H.D. Gage, C.G. Eades, B.A. Harkness, C.A. Pelizzari, and J.W. Keyes, Jr. Intermodality, Retrospective Image Registration in the Thorax. *The Journal of Nuclear Medicine*, 36(12):2333–2338, 1995.

[313] V. Zagrodsky, R. Shekhar, and J.F. Cornhill. Multi-function extension of simplex optimization method for mutual information-based registration of ultrasound images. In *SPIE Conference on Medical Imaging: image processing*, volume 4322, pages 508–515, 2001.

[314] Z. Zhang. Iterative point matching for registration of free-form curves and surfaces. *International Journal of Computer Vision*, 13(2):119–152, 1994.

[315] X. Zhou, T. Hara, H. Fujita, T. Hayashi, N. Murata, S. Kobayashi, R. Yokoyama, T. Kiryu, and H. Hosh. Automated segmentations of skin, soft tissue and skeleton from torso CT images. In *SPIE Conference on Medical Imaging: image processing*, 2004.

[316] B. Zitova and J. Flusser. Image registration methods: a survey. *Image and Vision Computing*, 21:977–1000, 2003.

[317] I.G. Zubal, C.R. Harrell, E.O. Smith, Z. Rattner, G.R. Gindi, and P.B. Hoffer. Computerized Three-dimensional Segmented Human Anatomy. *Medical Physics*, 21(2):299–302, 1994.